Strength degradation of carbon-carbon composites for aircraft brakes

Leigh, Benjamin David

Award date:
1999

Awarding institution:
University of Bath

STRENGTH DEGRADATION OF CARBON-CARBON COMPOSITES FOR AIRCRAFT BRAKES

submitted by Benjamin David Leigh

for the degree of PhD

of the University of Bath

1999

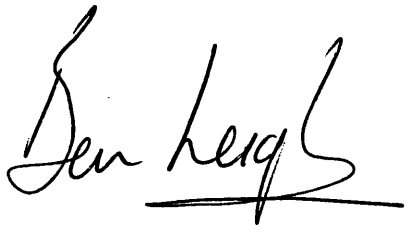

ProQuest LLC
789 East Eisenhower Parkway
P.O. Box 1346
Ann Arbor, MI 48106-1346

ACKNOWLEDGEMENTS

Brian McEnaney for invaluable direction and advice during the course of the project.

All the staff and students of the Department of Materials Science at the University of Bath for help, advice and encouragement.

Dr Ron Fisher, Mr David Johnson and all the staff of Dunlop Limited, Aviation Division for useful advice and discussion.

The EPSRC and Dunlop Limited, Aviation Division for the financial support of the project.

All my family and friends for their constant support and encouragement.

Rebecca Marsden for being everything.

This thesis is dedicated to the memory of

Ernest Kenneth Eastabrook

"It is better to know some of the questions
than to know all of the answers."

James Thurber

ABSTRACT

The objectives of this study were to study the mechanisms of degradation of the mechanical properties of carbon-carbon composite aircraft brake discs. The project has been carried out in association with Dunlop Limited, Aviation Division in the framework of an EPSRC CASE studentship. The study therefore focuses on the commercial disc material produced by Dunlop, but also includes research on model materials designed to represent parts of the structure of the commercial material. The commercial material is a laminated carbon-carbon composite containing poly(acrylonitrile) (PAN) derived carbon fibres in both continuous fibre and chopped fibre forms, in a chemical vapour infiltrated (CVI) matrix.

Optical microscopy of ex-service discs showed that in some, significant evidence of oxidative attack was present. This material was also found to have reduced density and significantly reduced mechanical properties, and hence it is suggested that oxidation is responsible for the premature failure of some brake discs. However, the extent of oxidation could not be related to the age of the disc. Testing of whole discs demonstrated that failure occurred by delamination of the plies in the composite close to the load bearing face of the tenons. Whether this is the failure mechanism of discs in service is impossible to assess as discs suffer gross secondary damage upon failure which destroys any useful evidence of the failure mechanism.

Physical examination of ex-service discs also showed that in some cases material had been worn from the load bearing faces of the tenons and hence the area bearing the shear forces between the tenons and the swept area of the disc is reduced. It is proposed that this is another mechanism by which brake discs can fail. Optical microscopy revealed that the surface of the tenons was covered with a film of carbon material. Mechanical tests showed that surface films can be formed under conditions of blunt indentation and compression. It was also found that these films are only loosely bound to the substrate. It is therefore suggested that the tenons could wear by a cyclic process of film formation and detachment. This wear mechanism is unusual as it does not involve any sliding contact.

Flexure testing was used to assess the effect of low levels of oxidation (up to 6 % weight loss) on the mechanical properties of model carbon-carbon composites with

structures based on parts of the structure of the commercial material. Testing laminated carbon-carbon composites in a conventional flexural manner is complicated by the fact that failure by interlaminar shear is difficult to avoid. This is a reflection of the high tensile strength and low interlaminar shear strength of these materials. This type of failure was avoided by arranging the specimens such that there was no coincidence of shear forces and weak planes. This was achieved by testing the specimen on its side in a test called edgewise flexure.

Optical microscopy demonstrated that the effect of oxidation on the microstructure was to erode the fibre-matrix interface causing the formation of crescent-shaped porosity. This is due to the combined effects of structural disorder, residual stresses, and the presence of small scale manufacture-induced porosity and catalytic impurities in these regions.

Edgewise flexural testing of the unoxidised model materials indicated that the mechanical properties are improved to the greatest extent by the inclusion of well oriented continuous fibre. However, this is due to the contributions of both the fibres and the surrounding matrix, the latter showing considerable structural orientation with the fibre direction. Poorly oriented fibre layers (both in continuous and staple forms) were found to have inferior mechanical properties. Analysis of the fracture paths demonstrated that in well oriented fibre layers the crack passed across fibres and through natural weaknesses such as low density regions, whereas in poorly oriented fibre layers the crack passed between adjacent matrix sheaths. Some evidence for pseudo-plastic behaviour was found in poorly oriented staple fibre layers.

Oxidation had a deleterious effect on the mechanical properties of all the model materials and in general the strongest materials demonstrated the greatest decreases for a given weight loss. This is a direct result of the weakening of the fibre-matrix bond which also caused an increase in the amount of fibre pullout observed in the fracture surfaces. The weakest material, which consisted mostly of poorly oriented fibre layers, showed only small reductions in mechanical properties and this suggests that the performance of this material is relatively unaffected by the strength of the fibre-matrix bond. This is consistent with the observation that the crack path is between matrix sheaths. All the materials performed well when compared with others in the open literature, although this is attributed to the differences between the materials and the novelty of the test, with the latter possibly being most significant.

CONTENTS

SECTION A

SECTION B

Section A

Introduction and Background

1. INTRODUCTION

1.1. Background

Carbon-carbon composites form a subgroup of the family of composite materials, a class of almost infinite variety. Composite literally means "made up of distinct parts or elements", and it is the inclusion of more than one constituent which allows unique optimisation of the properties of the composite material. Composite materials are in widespread everyday use, and one of the most common is concrete. Here crushed rock is added to cement to both improve the compressive strength and to reduce the cost of the material. Even the painting of a metallic component to inhibit corrosive attack can be thought of in terms of creating a composite between the metal and the polymeric paint.

"It is a common principle that two or more components may be profitably combined to form a composite material so as to make best use of the more favourable properties of the components while simultaneously mitigating the effects of some of their less desirable characteristics"[1]. It is this principle which forms the foundation of all composite engineering.

Most structural composite materials consist of two main parts; a matrix and a reinforcement. Usually the reinforcement is in the form of fibres, but even here there is tremendous scope for variation with countless fibrous arrangements or architectures being possible. The primary function of the matrix is to act as a binder for the reinforcement, holding the fibres together and keeping them aligned in the desired directions. Applied loads are therefore transferred through the matrix to the fibres, allowing them to support compressive loads. The matrix should also allow the fibres to act individually by separating them, and provide some kind of protection from physical and chemical damage.

Carbon-carbon composites are relatively unusual in that both the reinforcement and the matrix are composed of elemental carbon, albeit often in different forms. The myriad of forms in which carbon can exist is mainly a result of the ease with which carbon catenates (bonds to itself). Diamond and graphite are the two well known forms (Figure 1), however the recent discovery of spherical (fullerenes) and cylindrical (nanotubes) forms has opened up whole new areas of research.

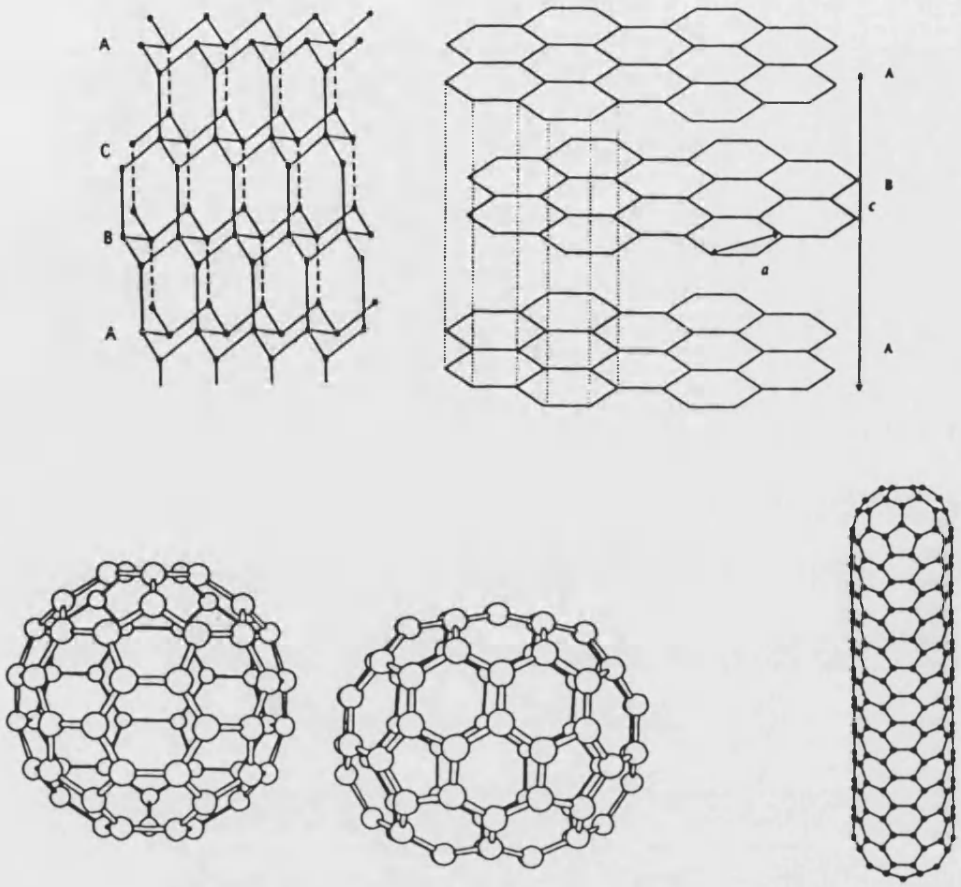

Figure 1. The structure of various forms of carbon; diamond, graphite, fullerenes (C_{60} and C_{70}) and nanotubes[2].

A layer of carbon atoms in a extended hexagonal array is known as a graphene plane and it is this which is the basis of the crystal structure of graphite. In effect this structure is two dimensional and in order to become graphite a stack of graphene planes must be formed where the third dimension has order, i.e. there is regular registry between adjacent planes. Within the planes the bonding is trigonal sp^2 hybridised σ bonding with delocalised π bonding. The nature of bonding between planes in graphite is the subject of some debate, but has historically been described as of the van der Waals interaction type. This difference in the nature of intra- and inter-layer bonding gives rise to the highly anisotropic properties of graphite. The inter-layer bonding is relatively weak, and this allows relative motion between layers to

occur quite easily. The ease with which this occurs leads to the application of graphite as a lubricant and also allows structures to form where graphene planes are roughly parallel and equidistant, but are misaligned in the *c* direction[3]. This form of carbon has been called "turbostratic" and the interlayer spacing in these materials is generally greater than that of perfect graphite (3.35 Å). In most carbon materials, the regions of relatively ordered turbostratic or graphitic carbon are surrounded by carbonaceous material in which the graphene plane are neither parallel nor equally spaced, i.e. there is no third dimension order. These areas of material exhibiting three dimensional order are called crystallites. In some carbon materials these crystallites can be oriented such that the impression given is of much greater range of order than in the single crystallites. This is the basis of the model proposed by Franklin[4] for the division of carbons in those which are graphitising and those which are non-graphitising. Here crystallite orientation can be induced in graphitising carbons while it cannot in non-graphitising carbons. Clearly then, a wide range of structures can be produced from relatively pure carbon and indeed some of these structures can be changed by suitable thermochemical treatments. In carbon-carbon composites further variation is possible by virtue of the fact that more than one carbon type is present. Hence the properties of carbon-carbon composites cover a wide range, and can be optimised for many different applications.

Carbon-carbon composites were first considered for practical use in inter-continental ballistic missiles in the late 1950s and subsequently developed by the U. S. Air Force for the space plane programme, and by NASA for the Apollo missions[5]. Further intensive research was stimulated by the inception of the Space Shuttle programme[6]. However in these cases the primary area of interest was in using carbon-carbon composites as heat shields.

In Europe carbon-carbon composites were developed as friction materials in response to demand from the development of Concorde. The first trials of carbon-carbon composite braking systems took place in 1973 using a VC10 aircraft. A year later, the brakes were fitted to Concorde and hence went into commercial service. At the time, the cost of the material prohibited its use on aircraft with the exception of military jets, and Concorde. However, further developments and subsequent reductions in cost have meant that the use of carbon-carbon composites is economically viable on many commercial airliners. Carbon-carbon composite brakes are currently fitted on all of

the Airbus family (A300, A310 and A320) as well as Boeing 747-400, 757, 767, and the McDonnell Douglas MD-11. Their use can represent significant weight savings (approximately 900 kg on a Boeing 747-400[7]) as well as extended service lives over their sintered metal equivalents.

Carbon-carbon composites also find commercial use as rocket nozzles and racing car brakes and clutches. The market share for each of the major production areas is shown in Table 1. In 1990 the total market for carbon-carbon composite products was worth around £100 m.[7] with the only published market survey[8] predicting an annual growth of 11% towards £200 m. by the turn of the century. However, more contemporary sources indicate that these predictions are somewhat pessimistic, quoting an annual turnover of approximately £600 m. in 1996[9].

Application	Percentage of total	
	Volume	Value
Aircraft brakes	63	31
Rocket nozzles	14	31
Nose cones and ablatives	11	37
Other	12	1

Table 1. Breakdown of carbon-carbon composite market by application[7].

Around 75% of the world demand for carbon-carbon composites is from the USA due to large defence and aerospace industries. The three biggest producers of carbon-carbon composites are Hitco, formerly a division of British Petroleum, the Bendix Division of Allied-Signal and the French company SEP. Other significant producers include Avco, Dunlop, FMI, Goodrich, Kaiser Aerotech, Schunk and Sigri.

1.2. Context of work

As with many areas of scientific research, much of the work on carbon-carbon composites has been commercially driven. Hence the main areas of investigation have addressed the problems associated with the practical use of carbon-carbon composites, namely the long and costly manufacturing process, and the degradation of the material in service.

Cost is still the principal factor in restricting the use of carbon-carbon composites. Typically carbon-carbon composites cost between £100 to £1000 kg^{-1} with aircraft brake materials being amongst the cheapest, and those used in rocket nozzles being the most expensive. This is due to the complex three-dimensional structure, and high density of these materials. Table 2 shows a breakdown of the cost of a mid-range-price carbon-carbon composite (£300 kg^{-1}) and it is clear that a large proportion of the total is derived from manufacturing costs. Consequently, a great deal of research has targeted possible alternatives to the manufacturing routes currently employed, with the dual objectives of reducing cost and increasing production lead time. The second of these is significant since the production time for carbon-carbon composite material can be several months. This means the manufacturer does not have the ability to respond quickly to changes in demand.

	Percentage of cost
Carbon fibres	17
Weaving	17
Matrix precursor	2
Fabrication	40
Protective coating	12
Pre-tax profits	12

Table 2. Breakdown of costs for a mid-priced carbon-carbon composite[7].

Since carbon-carbon composites uniquely maintain a high degree of structural integrity at temperatures in excess of 2000 °C, they are often employed in applications which exploit this property. However, in many of these applications the material is exposed to oxidising atmospheres whilst at elevated temperatures. While this is not a great drawback for one-use components such as missile nose cones and rocket nozzles, it represents a serious problem in multi-use components such as aircraft brake discs. Here it is an economic necessity for the disc to have an extended service life, and therefore oxidation inhibition is another area which has been subject to scrutiny. Despite the emphasis on the development of oxidation resistant systems for the commercial marketplace, the mechanisms of oxidation and the effects of oxidation on

the properties if carbon-carbon composites are still relatively poorly understood. It seems that empirical solutions to the problems have been found without fully understanding the nature of the problem itself. This is not as great an oversight as it would at first seem since by the nature of the material the problem is very complex. The oxidation mechanism is likely to be influenced by many factors including the chemical nature of both the matrix and the fibre, the microstructure and macrostructure of the composite and the oxidation conditions. The body of available reference texts tend to suggest solutions to specific problems, and from this general rules of thumb have been derived. However to be sure of their accuracy tests under the specific conditions of interest still have to carried out.

1.3. Project objectives

The objective of this project is to study the mechanisms of degradation of the mechanical properties of carbon-carbon composite aircraft brake discs as a result of exposure to service conditions. The project has been carried out in association with Dunlop Aviation Limited in the framework of an EPSRC CASE studentship award. The study therefore focuses on the commercial disc material produced by Dunlop Ltd. but it also includes work on simpler model materials based on elements of the structure of the commercial material.

The friction and wear of the commercial material has been investigated in a previous project[9] and whilst this project is closely related to the previous one, it is intended to concentrate more on the causes of mechanical failure of the disc material in service. This will involve the following:

a) Testing of ex-service material of various ages to assess the extent of the reduction of mechanical properties.
b) Microstructural analysis of ex-service material and comparison with literature sources to identify likely degradation mechanisms.
c) Analysis of possible disc failure mechanisms.
d) Design of model materials representing parts of the disc material structure.
e) Design of mechanical test method sensitive enough to monitor changes in mechanical properties.
f) Investigation into the effects of oxidation on the mechanical properties of the model carbon-carbon composites.

1.4. Thesis structure

The thesis is divided into two sections. Section A contains the introduction, background and literature review. This consists of five chapters which are concerned with the important basic knowledge required for full understanding of the work described in Section B. This introduction constitutes Chapter 1 and is followed by a brief introduction to aircraft brakes in Chapter 2. Chapter 3 is an introduction to carbon-carbon composites and Chapters 4 and 5 discuss the oxidation of carbon and carbon-carbon composites respectively. Section B contains the information concerned with the experimental programmes undertaken during the project. Chapter 6 contains information gained while characterising the commercial material and Chapter 7 presents the results of compressive testing of the commercial material. A discussion of the failure mechanisms of aircraft brake discs is contained within Chapter 8 along with results from tests which have suggested a novel wear mechanism which could go some way to explaining premature disc failure. In Chapter 9 the model materials are characterised using similar techniques to those used in Chapter 6. Chapter 10 presents the result of flatwise flexure testing of the model materials and concludes that the method is not suitable for measuring property changes in these materials. The results of testing unoxidised model materials in edgewise flexure are presented in Chapter 11, and in Chapter 12 the results of similar testing on oxidised materials is presented. The conclusions of the work are made in Chapter 13 and in Chapter 14 suggestions are made for useful directions of further investigation. Chapter 15 contains the reference list.

2. AIRCRAFT BRAKES

2.1. Requirements of the braking system

When discussing aircraft design, much emphasis is placed on the criteria for the selection of one design over any other. Factors such as the cruising speed, payload capability and range tend to justifiably dominate discussion. The design of the braking system is a small but crucial part of the overall aircraft design. Improvements in brake efficiency can allow greater payloads to be safely carried and may also allow large aircraft to utilise short, previously unusable runways.

The requirements of any braking system are obvious. Principally the system should be capable of stopping the vehicle within the shortest possible distance[10]. Also, the braking characteristics of the system should be unaffected by factors such as atmospheric conditions, braking conditions and system age. On top of this, the system should be designed so as to require minimal maintenance[11].

The materials used in the braking system are required to perform three main functions. Firstly they must act as friction components to provide the torque required to stop the aircraft. Secondly they must act as a heat sink to absorb the thermal energy produced by conversion from the kinetic energy of the aircraft, and finally, they must act as structural elements to transfer the torque to the tyre and undercarriage[12]. In aircraft braking systems, all these requirements can be satisfied by carbon-carbon composites.

The most severe braking situation is known as a rejected take-off (RTO). In this case the brakes must be able to stop a fully laden aircraft from an aborted take-off. In the case of a Boeing 767 the take-off speed is 320 kmh^{-1} and the aircraft weighs approximately 170 tonnes. This represents roughly 670 MJ of kinetic energy, the majority of which must be dissipated by the brakes in 30 s during an RTO.

Aircraft brakes are multiple disc systems, essentially consisting of a stack of discs where alternate discs rotate with the wheel, while the others are held stationary by the undercarriage. Rotating discs are called rotors and are attached to the inner surface of the wheel rim by a series of engaging crenellations, where projections on the outer circumference of the disc known as tenons fit in to grooves in the hub. Stators are held stationary by tenons on their inner circumference which engage with grooves in the torque tube which is part of the undercarriage. The use of a tenon system to

transfer torque permits the discs to slide along the torque tube and hub allowing the system to accommodate changes in disc thickness as a result of wear. Figure 2 shows a cutaway view of a typical aircraft brake assembly. The interleaved stators and rotors form an annular overlapping area known as the swept area. The stators on each end of the stack (or heatpack) have only one swept area and are termed single stators, while all others are known as double stators. During a braking action, the stack of rotors and stators are pushed together by a series of hydraulic pistons, causing the swept areas of adjacent discs to come into contact. It is the friction caused across these areas of contact which generates the braking force.

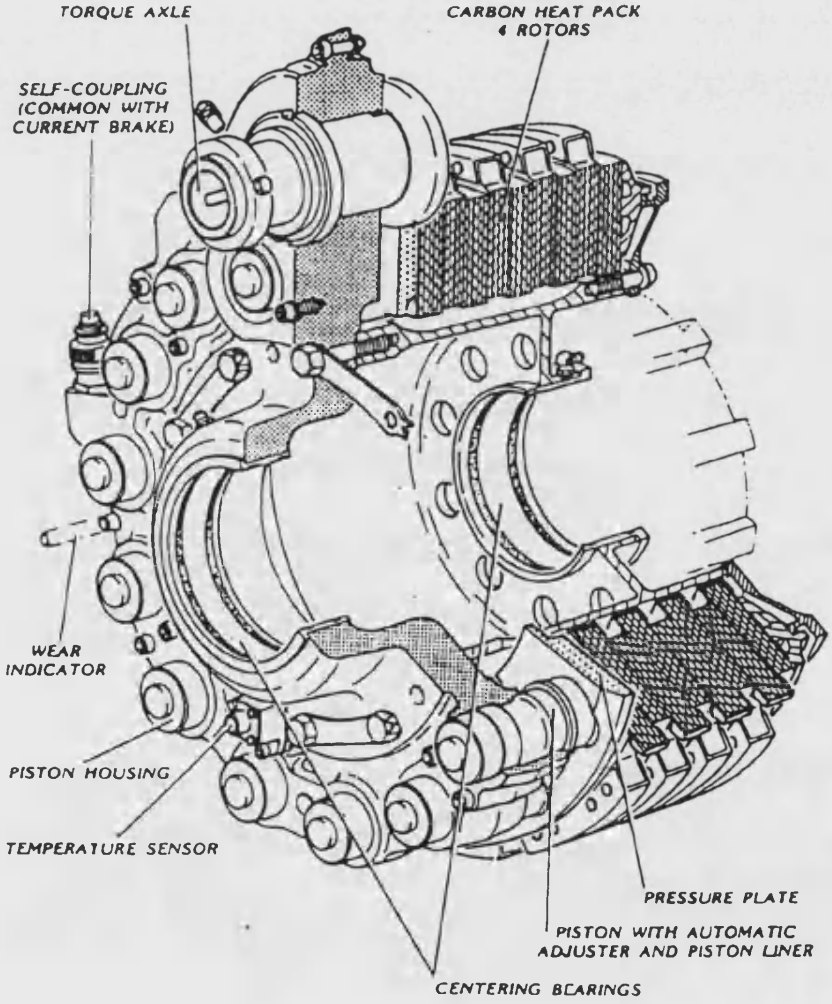

Figure 2. Cutaway of a typical aircraft brake[13].

2.2. Frictional aspects of braking

Oddly, for a material which finds use as a friction material, the frictional characteristics of carbon-carbon composites form only part of the selection criteria along with their thermal properties and low densities. However some work has been done to determine the friction characteristics for carbon-carbon composites under a wide range of braking conditions. Typically the coefficient of friction (μ) under static or low sliding speed conditions is of the order of 0.2, but when the brake is hot μ is typically 0.3 and can be as high as 0.6. It is for this reason that carbon-carbon braking systems used in racing cars have an effective temperature range of 400-600 °C. Absorbed water can act as an efficient lubricant causing the coefficient of friction to be as low as 0.1. This is the origin of the term "morning sickness" which is used by pilots to describe the poor performance of the brakes after an overnight stop in a humid environment.

2.3. Wear of friction materials

After the considerations based on thermal properties and weight savings due to low density, the attractiveness of carbon-carbon composites for use in aircraft brakes is further enhanced by their long service lives. The brakes fitted to the Boeing 767-300 typically yield 3000 landing per overhaul (LPO) which compares very favourably with the 1500 LPO for their steel equivalents. This long service interval is due to the extraordinarily low wear rates which can be achieved by judicial control of the way in which the brakes are used.

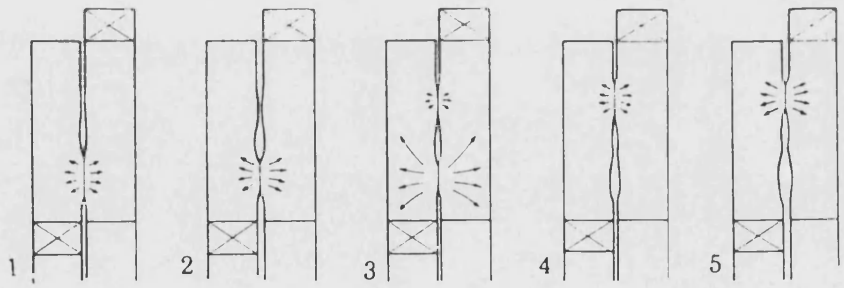

Figure 3. Bands of contact established during braking as a result of thermo-elastic and wear effects (after Stimpson *et al*[14] and Savage[7]).

The frictional contact of brakes is a thermo-elastic and wear phenomenon. Figure 3 shows the sequence of events which occurs during a braking action. Initially only local asperities make contact and work done at these point causes local expansion. The rotation of one of the surfaces causes the formation of a narrow annular band of contact. Further work and expansion take place until heat flow, wear at the band of contact and changes in mechanical loading from adjacent discs cause a new band of contact to be established. Work diminishes at the original contact and the material cools and contracts. Since wear has taken place the original band of contact is unlikely to become re-established for some time. This model was reported in publications by Barber[15] and Kennedy *et al*[16] and has been observed to take place on carbon-carbon composite brakes.

The low observed wear rates are due to a cyclic wear and regeneration process in which fine debris is deformed to produce a thin film on the friction surface. This film delaminates from the substrate and is crushed into fine debris which is reapplied to the wear face to regenerate the film. This process is shown schematically in Figure 4.

It has been shown that the wear behaviour of carbon-carbon composite aircraft brakes is highly dependent on the energy involved in the specific braking action. Broadly speaking, braking actions can be divided into high and low energy conditions. High energy conditions are produced during landing and low energy conditions are produced during the application of the brakes while the aircraft manoeuvres on the ground, commonly called "taxi snubs" or simply "snubs". Landing conditions produce low wear rates and low coefficients of friction. This is because there is sufficient energy involved to allow the film regeneration process to occur. However, taxi snubs result in high wear rates and high coefficients of friction. It has been found that the wear rate under these conditions can be significantly reduced by pre-heating the brakes to above 100 °C[9]. Also it was found that the fibre architecture of a given carbon-carbon composite system (for example PAN/CVI) did not significantly alter the friction and wear properties whereas the manufacturing parameters such as final heat treatment temperature were found to be highly influential by altering the thermal properties of the composite.

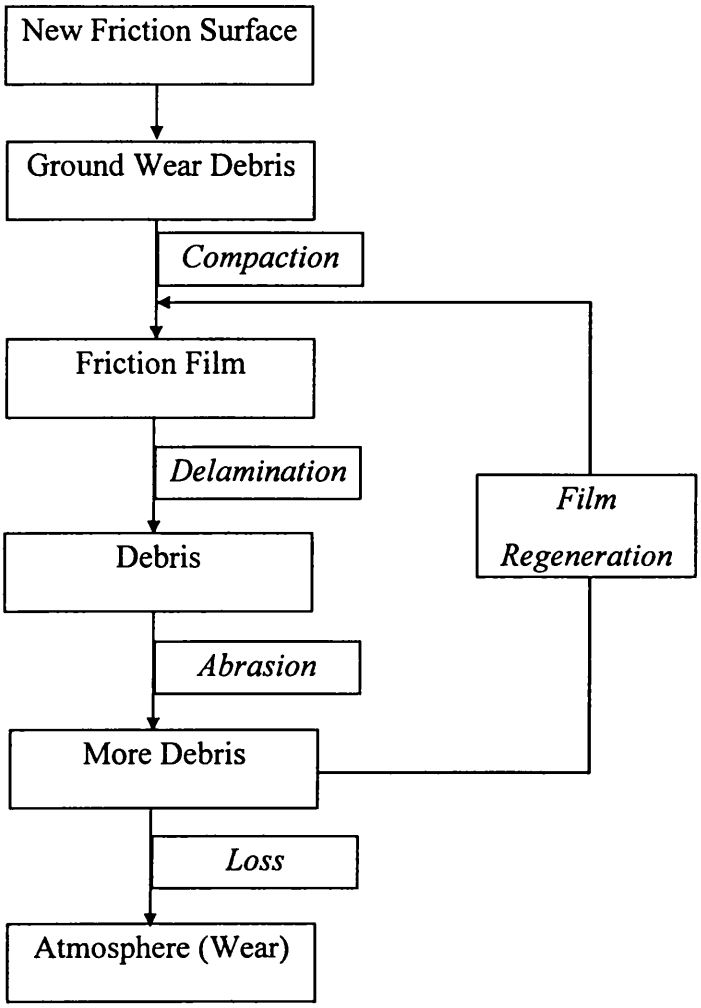

Figure 4. Wear mechanism for carbon-carbon composite materials (after Savage[7] and Awasthi *et al*[12]).

2.4. Thermal considerations

Clearly the primary design criteria for an aircraft braking system it to stop the aircraft by absorbing its kinetic energy. Since most of this energy is converted to heat, the consideration of the thermal aspects of braking is of the utmost importance. The most severe requirement of the system is to be capable of withstanding RTO conditions at the end of its service life[17]. Interestingly, the constraining factors are not mechanical, but thermal. It has been reported that after approximately 2000 landings the brake has insufficient thermal capacity to absorb the heat generated in an RTO without melting the surrounding structures[18]. Due to the compact nature of aircraft brakes, and their location within the hub of the wheel, the transfer of heat to the atmosphere is poor. It

would seem obvious to design systems of air scoops and cooling channels into the discs and undercarriage to aid this transfer of heat, however the passage of air over the brakes when hot causes accelerated rates of oxidation. Oxidation is by far the greater of the two problems and therefore brakes are designed with thermal capacity rather than heat transfer as a priority.

The frictional and wear characteristics of a brake also depend greatly on the interface temperature, or the temperature of the surfaces of the discs which are in sliding contact. Obviously, the measurement of such temperatures presents a great number of technical challenges and so often they are estimated using mathematical modelling. There is very little published work which documents brake interface temperatures, however figures of 3000 °C have been reported[12].

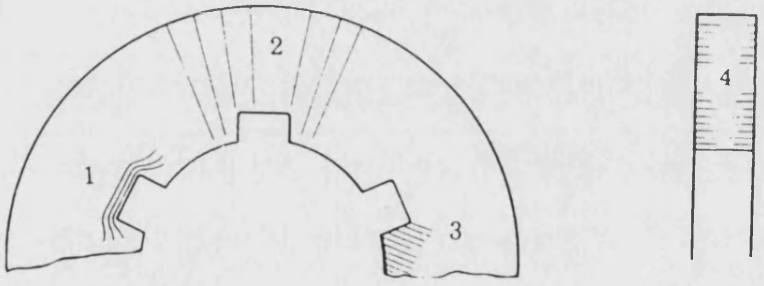

Figure 5. Preferred fibre directions; 1: flow around notches (strength), 2: radially at surface (heat flow), 3: 45° to shear at slot (strength), 4: normal to disc surface (heat flow)[14].

2.5. Brake disc design

The design of the braking system is a far from simple task. All of the factors outlined in the previous sections must be taken into consideration. As in all composite materials, the properties of a carbon-carbon composite are strongly influenced by the fibre architecture. However due to the nature of the material the fibre architecture not only affects the mechanical properties, but also the thermal properties. Hence there

are two criteria which the fibre arrangement has to satisfy. Figure 5 shows the preferred fibre directions for a carbon-carbon composite brake disc. Strength criteria dictate the 1st and 3rd fibre directions where the flow of the fibre around notches in the 1st direction gives effective mechanical reinforcement of the junction between the tenon and the swept area. The fibres in the 3rd direction are arranged at 45° to the plane of potential shear failure between the tenon and the swept area. Thermal considerations dictate the 2nd and 4th directions where good flow of heat is required both across the swept area and into the body of the disc from the friction surfaces where the highest temperatures are experienced. Clearly it would be very difficult, not to mention expensive, to satisfy all these conditions with a single fibre architecture. Therefore the fibre architectures used tend to be a compromise which satisfies all the criteria to some extent, while remaining within the manufacturing state of the art and minimising cost.

3. CARBON-CARBON COMPOSITES

3.1. Introduction

As has been explained in Chapter 1, carbon-carbon composites are a family of materials with almost infinite variety. This is due to the large number of independent variables which affect the properties of the composite. These variables can be split into four areas; fibre type, matrix type, fibre architecture and processing conditions. By careful manipulation of these variables the properties of the composite produced can be tailored to a specific application.

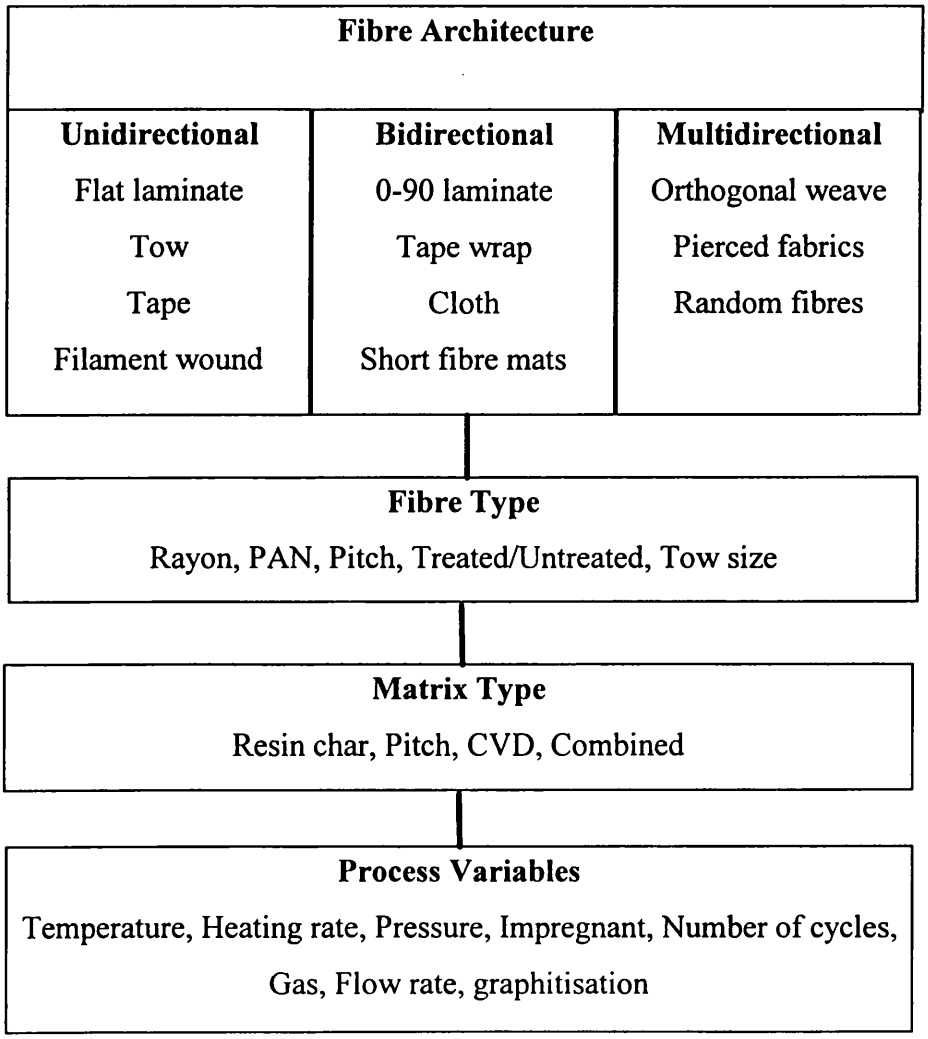

Figure 6. Representation of some of the choices facing the designer using carbon-carbon composite materials (after Thomas[19]).

3.2. Carbon fibres

The term carbon fibre is used to denote fibres which are at least 92 wt.% carbon in composition[20]. As with the finished composite, an immense variety is available and in some cases the properties of a fibre can be altered by heat treatments leading to even greater variety.

3.2.1. Manufacture

Carbon fibres have been inadvertently produced from natural fibres such as cotton for millennia. The first recorded intentional conversion was in 1878 by Thomas Eddison who converted cotton and later bamboo to carbon for use as filaments in electric lamps. Nowadays the majority of commercial carbon fibres are derived from poly(acrylonitrile) (PAN) with lesser amounts produced from pitch and small quantities produced from rayon. In addition to this, carbon filaments, sometimes called vapour grown carbon fibres, can be grown on the surface of catalyst particles if they are brought into contact with a carbonaceous gas at high temperature. Whichever production route is used, in order for the resulting fibres to achieve good mechanical properties it is a requirement for the orientation of the graphene layers to be oriented parallel with the fibre axis. In this case, the fibre exploits the high strength of the graphene structure along the *a*-axis.

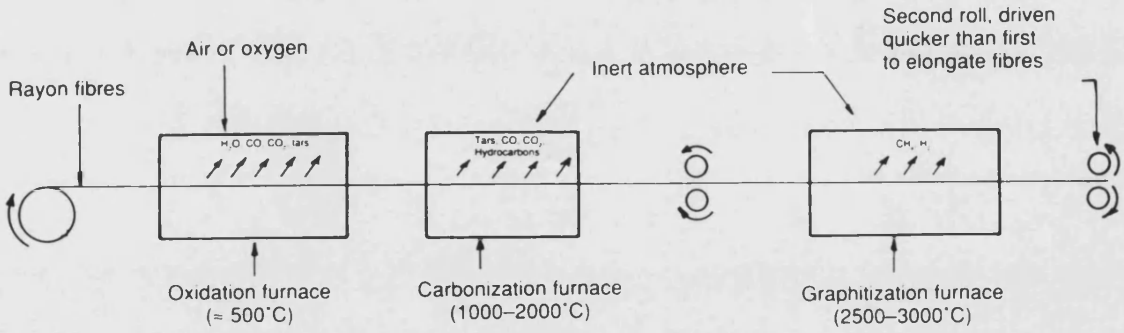

Figure 7. The basic route for the production of carbon fibres from rayon[21].

Amongst the first carbon fibres to be produced commercially, in 1959 by the Union Carbide Company, were those derived from rayon. The basic steps involved in producing carbon fibres from rayon are shown in Figure 7. The first processing step typically takes place at about 300 °C and involves polymer stabilisation and the

formation of cross links. Chemical pre-treatments can be used to reduce the time required for this step from several hours to a few minutes. During this oxidative stage between 50 and 60 % of the fibre mass is lost to decomposition products such as H_2O, CO and CO_2. The next step, carbonisation, usually takes place up to around 1500 °C and after this stage the mass yield is between 20 and 25 %. The fibres have a reasonably isotropic structure at this stage with poorly aligned graphene layers and as a result poor mechanical properties. Stretching during the subsequent graphitisation stage significantly improves both the strength and modulus of the fibres produced, but is an expensive process. The resulting fibre is easily recognisable by its crenellated surface. The poor yield, relatively poor mechanical properties, and necessity for an expensive graphitisation step for these fibres has meant that they have not been generally competitive for commercial use.

Pitches are complex mixtures of polyaromatic molecules. The pitch used as a precursor for the production of carbon fibres can be a petroleum pitch (a residue obtained from the distillation of crude oil), a coal tar pitch or any other pitch[22]. Unless carefully heat treated, pitches are usually isotropic and as these pitches are thermoplastic they can be melt spun into fibres relatively easily. These fibres are carbonised by heating to above 1000 °C while maintaining their shape. To achieve this the fibre must first be stabilised by oxidisation in air at approximately 300 °C. The isotropic structure of these fibres means that they are of low strength and low modulus. The mechanical properties are not much improved even when they are carbonised at high temperatures. Improvements can be induced by mechanical stretching at temperatures of between 2700 and 3000 °C, however this is a costly and impractical process[23].

Processes have been developed to convert pitches into a mesophase or liquid crystal system. When commercial pitches are heated to around 400 °C dehydrogenation condensation reactions take place producing planar aromatic molecules which aggregate to form the mesophase. As the mesophase content reaches 40 % a phase inversion occurs and it becomes the continuous phase. The mesophase pitch product is then melt spun into fibres and processed by oxidation in air at about 250 °C followed by carbonisation and graphitisation at about 2500 °C. Processing mesophase pitch ought to represent a method of producing high performance, low cost carbon fibres. However, there is a major drawback associated with the melt spinning process.

Melt spinning involves passing the melt through a capillary and cooling it on exit so that it solidifies and forms a continuous fibre. The processing conditions have to be precisely controlled such that the fibre does not disintegrate into droplets or break by excessive tension from the winding spool. Mesophase pitch is particularly difficult to melt spin due to the extreme temperature dependence of its viscosity. Hence, in all but the very high modulus fibre market, mesophase pitch fibres have difficulty competing with other types of fibre.

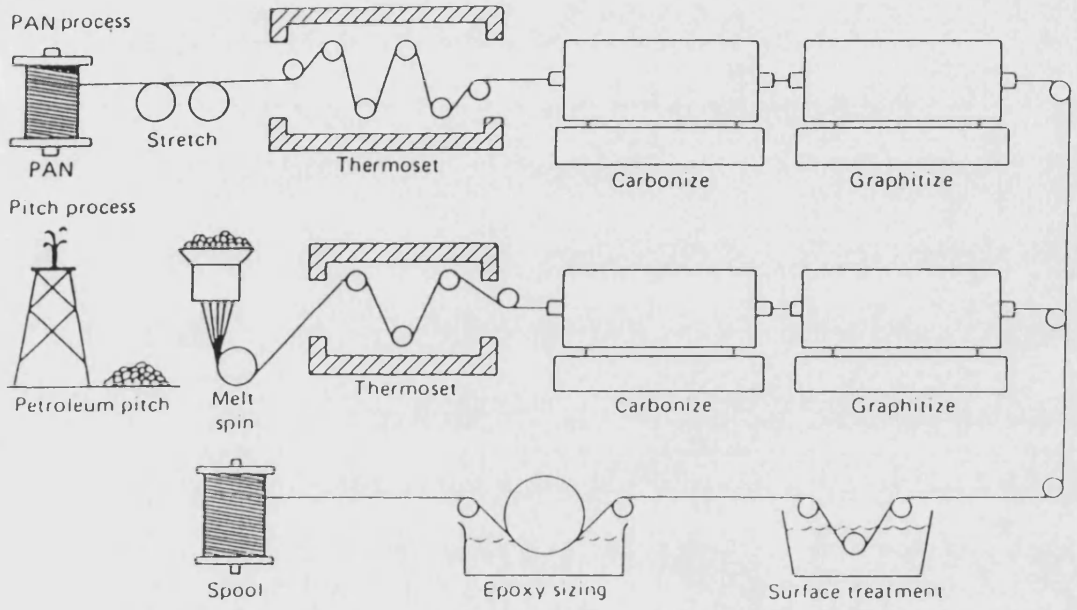

Figure 8. Comparison of the processing routes for pitch and PAN derived carbon fibres[7].

Poly(acrylonitrile) (PAN) is one of the most commonly used precursors in the manufacture of carbon fibres. This is partly due to the wide range of properties which can be obtained from the same base polymer by alteration of the processing conditions. During the 1960s it was discovered that the PAN structure could be stabilised by an oxidation process and subsequently carbonised to produce carbon fibres with properties superior to those of rayon based fibres. A comparison of the processing routes for pitch and PAN based carbon fibres is shown in Figure 8. The main difference is that the orientation of the structure of the fibre occurs naturally in

mesophase pitch whereas it is imparted to PAN by stretching prior to oxidation (rayon is oriented by stretching during graphitisation).

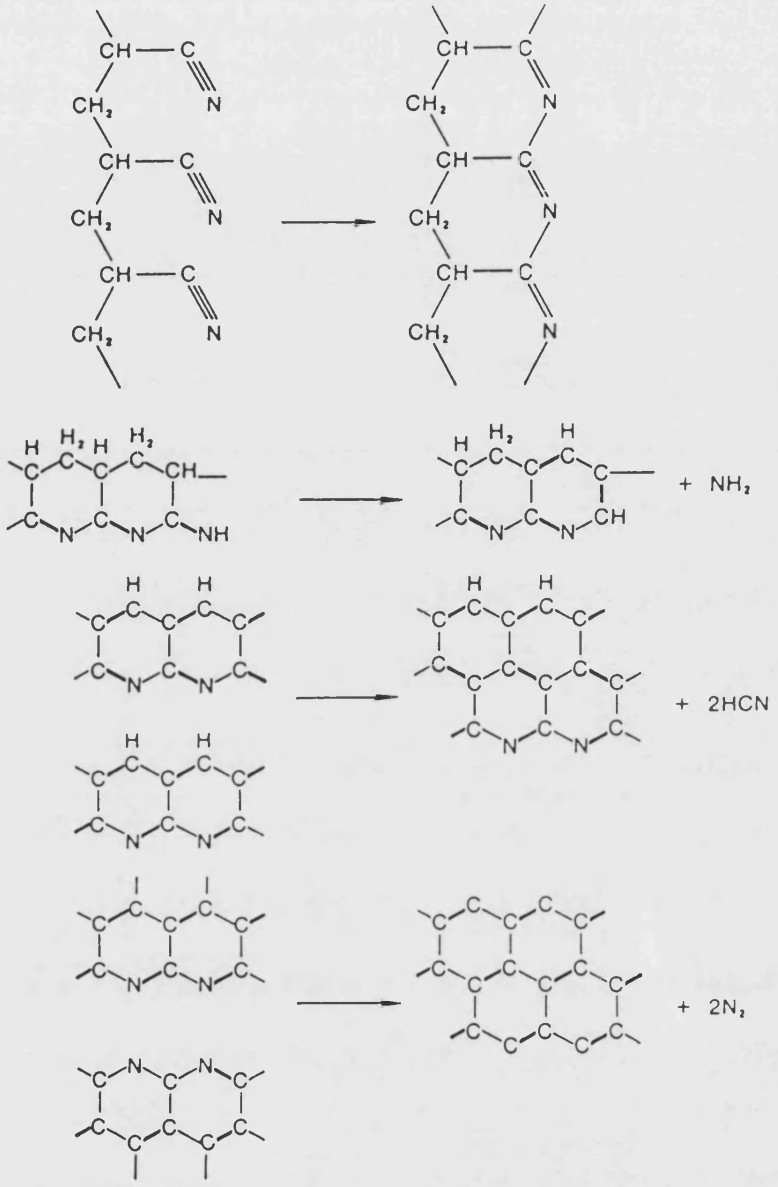

Figure 9. A much simplified representation of the conversion of PAN to carbon[24].

PAN can be spun into well oriented polymer fibres and stabilised by heating in an oxygen containing atmosphere to about 250 °C. Carbonisation follows and converts the fibre into a structure where more than 92 % by weight is carbon. A much simplified schematic diagram showing the chemistry of the conversion of PAN to carbon is shown in Figure 9. Although the processes of oxidation and stabilisation are complex, there are two important features. Firstly, the reaction of the nitrile groups to

form a closed ring structure, and second the fact that oxygen aids cross-linking. The nitrile group reaction is the essential PAN stabilisation stage, as it allows the polymer to degrade during the carbonisation stage without collapse of the fibre or loss of orientation[25].

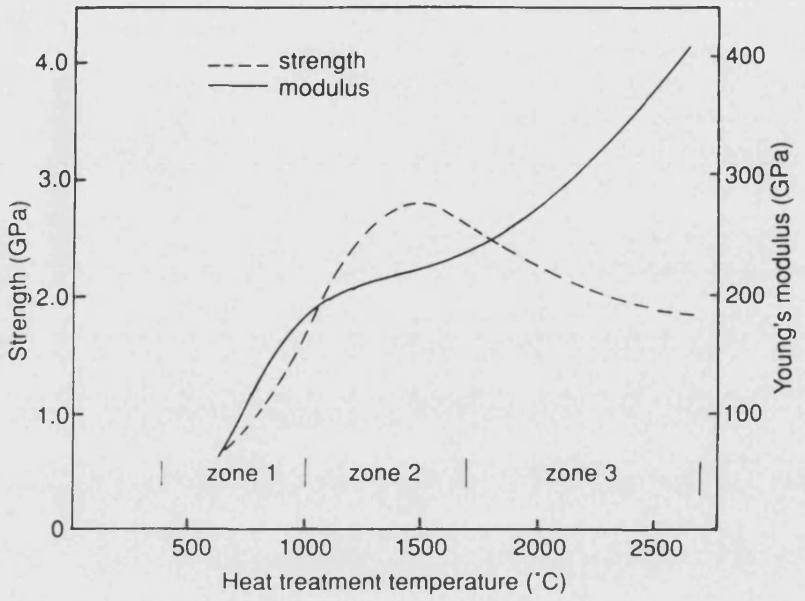

Figure 10. Effect of Heat treatment temperature on strength and modulus of PAN based carbon fibres[7].

The properties of the PAN based carbon fibre can be significantly altered by the carbonisation temperature, and the heat treatment temperature. Broadly, the fibres are divided into three categories by their modulus. Low modulus (LM) fibres have a Young's modulus of 190-220 GPa whereas intermediate modulus (IM) fibres have a modulus in the range 220-250 GPa. IM fibres are of high quality, have high strength and strain to failure, and are used extensively in the manufacture of aircraft and racing cars. High modulus fibres (HM) have a modulus in the range 360-400 GPa and achieve high stiffness at the expense of strength and strain to failure. The way in which the heat treatment temperature affects strength and modulus is shown in Figure 10. Zone 1 represents carbonisation in which the major chemical changes to the fibre occur. The fibre loses around 50 % by weight although the fibres are not physically degraded. This process is complete at 1000 °C, and although residual nitrogen remains in the structure, the modulus at this stage (around 200 GPa) means that these

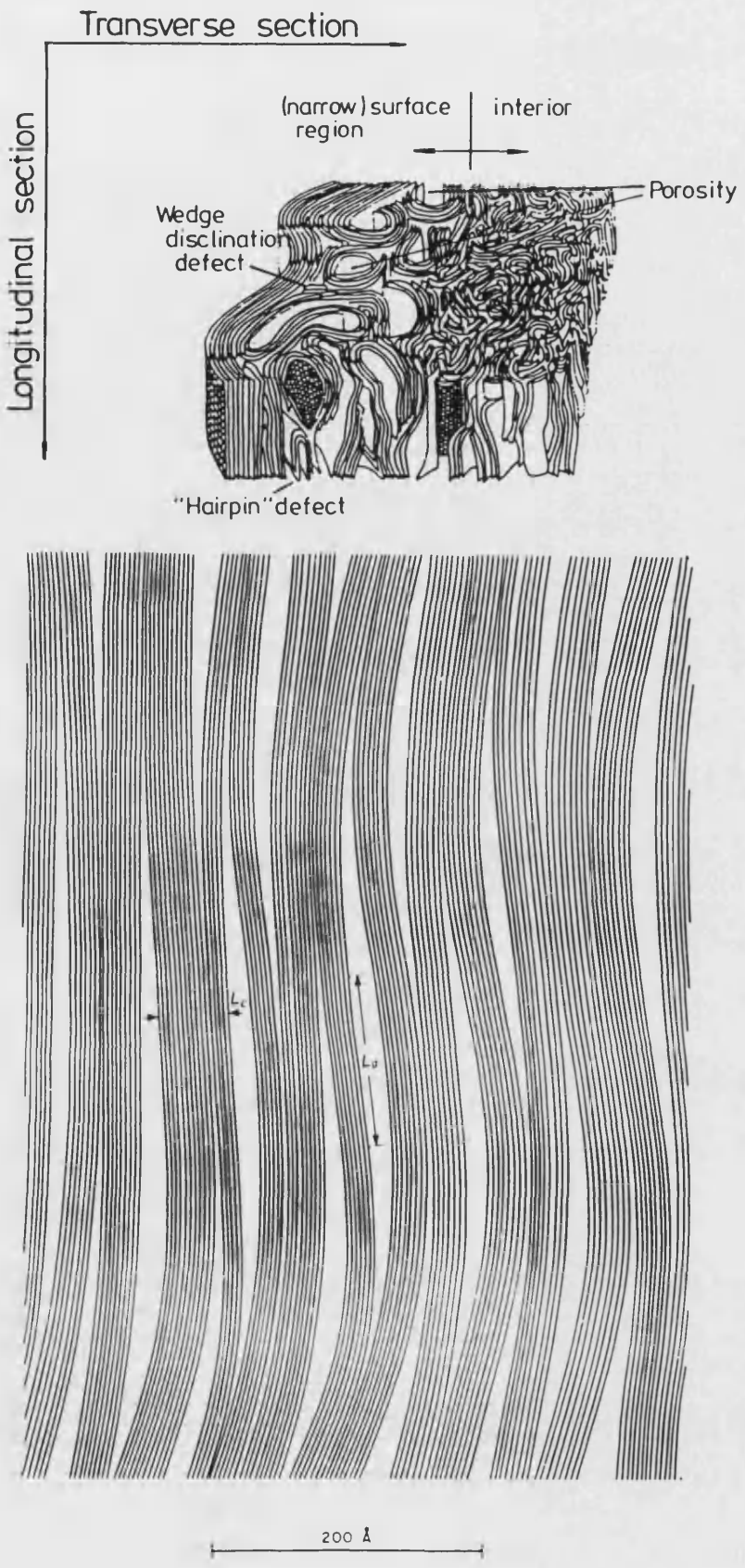

Figure 11. Schematic diagram showing the arrangement of the graphene layers in a high strength ex-PAN carbon fibre[26] and a longditudinal section of a similar fibre[27].

fibres can be commercially exploited as LM carbon fibres. In zone 2 the residual nitrogen is lost and graphite crystallites grow and align, causing a gradual increase in modulus and turnover in strength. Heat treatment to higher temperatures can cause further crystallite growth and alignment and hence higher moduli.

The structure of a high strength PAN based carbon fibre is shown schematically in Figure 11. There is a thin surface layer in which the graphene layers are aligned with the axis of the fibre and also its surface, while in the interior the structure is less ordered. Longditudinally the structure is one of long graphene planes which are in registry in parts forming graphite crystallites with the dimensions L_c and L_a as shown.

3.2.2. Mechanical properties

As has already been discussed, the properties of carbon fibres can vary tremendously. Table 3 shows some typical properties of carbon fibres made from isotropic pitch, mesophase pitch and PAN. Many of the properties of carbon fibres are related to its structure and hence interrelated. In general the following trends are observed as the degree of orientation of the graphene planes with the fibre axis increases[22];

- increase in tensile modulus
- decrease in strain to failure
- decrease in compressive strength
- increase in shear modulus
- increase in degree of anisotropy
- decrease in electrical resistivity
- increase in thermal conductivity
- increase in coefficient of thermal expansion
- increase in density
- increase in thermal stability (oxidation resistance)
- increase in chemical stability
- increase in cost

	Isotro-pic pitch	Mesophase pitch			PAN		
		Low modulus	High modulus	Ultra high modulus	LM	IM	HM
Tensile strength GPa	1	1.4	1.7	2.2	3.3	4.5	2.4
Tensile modulus GPa	41	160	380	725	230	270	390
Strain to failure %	2.5	0.9	0.4	0.3	1.4	1.8	0.6
Density gcm^{-2}	1.6	1.9	2.0	2.15	1.76	1.8	1.9
Fibre diameter μm	8.5	11	10	10	8	6.5	5
Carbon assay %	99	>97	>99	>99	92	96	100

Table 3. Typical properties of carbon fibres derived from various precursors (after Savage[7]).

3.2.3. Fibre surfaces

The properties of the surface of carbon fibres is of paramount importance, particularly for the composite engineer, since it is the surface which is required to bond with the other phase of the composite material. This bonding can take the form of physical interlocking with fibre surface roughness and chemical bonding. After low temperature carbonisation the highly disordered structure of carbon fibres contains open porosity and surface activity. Thus after exposure to moist air they contain chemisorbed oxygen and basic oxides which can subsequently react with matrix materials. To improve interfacial bonding surface treatments are necessary which although not well understood, seem to have at least three main effects;

a) surface cleaning by removal of weakly adherent debris
b) modification of surface morphology to give an increased keying effect
c) formation of chemical subgroups at the fibre surface.

It is known that the interface between fibre and matrix is of great importance. In addition to altering the way in which the matrix and fibre bond, it is often at the interface that chemical impurities are found. These are usually left over from the

processing of the fibre. These impurities can have a marked effect on the chemical properties of the composite particularly as they are often employed in high temperature applications. For example alkali metals are known to catalyse the reaction of oxygen and carbon and these are commonly found on the surface of fibres. Hence oxidation often occurs at the fibre-matrix interface which is the most critical part of the composite structure.

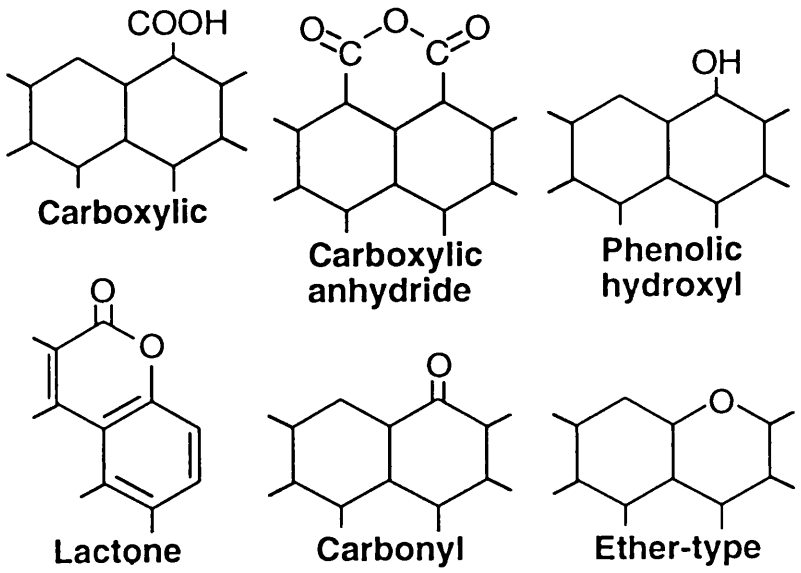

Figure 12. Carbon surface structures containing oxygen[28].

3.3. Types of carbon-carbon composite

The vast choice of carbon fibres currently available means that hundreds of types of carbon-carbon composite are possible even if all other processing variables are kept constant. The options available to the composite designer have been shown in Figure 6 and some of these will be discussed in more detail in this section.

3.3.1. Fibre lay-up

As would be expected, fibre lay-up is known to be one of the strongest influences on the properties of the finished composite. Often the optimum design of the fibre architecture is not practically possible and so compromise is inevitable. The fibre lay-up has to be such that it provides the best properties in the composite, that it remains spatially stable during the formation of the matrix, and that the fibres can be easily handled. Usually this means that the fibres are formed in some way into a cloth.

Hence much of the technology and nomenclature of fibre lay-up is borrowed from the textile industry.

Carbon fibres are generally supplied on a spool as a tow. A tow is a group of continuous aligned fibres. The size of the tow is a measure of the number of fibres within it. Tows can range in size from 1 k to 320 k, i.e. 1000 to 230000 fibres in each bundle. Tows can be used directly in filament winding operations or as continuous unidirectional fibre in a cloth, although in this case they must be laterally stabilised by mechanical connection to another layer. More commonly, however, tows are twisted into yarns which can then be woven, braided or knitted into a wide variety of cloths.

An important consideration when selecting a cloth structure is the flexibility of the cloth. A flexible cloth is required for the laying up of complex shapes such as compound curves. If the cloth has only to conform to simple curves and flat surfaces then the choice of cloth is dictated by the required fibre directions and proportions. In all the cases mentioned thus far it has been assumed that the cloth is a two-dimensional structure. However it is possible, if difficult, to weave, braid and knit in three dimensions. Here the fibres are woven to close to the shape of the finished product or an intermediate stage before the matrix is added. This is most easily achieved in rectilinear shapes and those with rotational symmetry such as cones and cylinders.

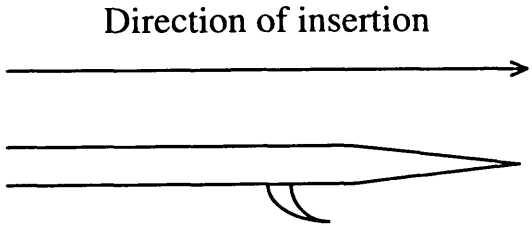

Figure 13. Diagram of a barbed needle used for the interlinking of cloth layers.

It is possible to achieve a pseudo-three-dimensional fibrous structure from a stack of two-dimensional cloth by needling or stitching. In this process two or more layers of cloth are joined mechanically by linking fibres from adjacent layers. This is achieved by passing barbed needles such as that shown in Figure 13 through the layers of cloth which are to be joined. The barb collects some fibres from the first layer and drags them through to the last layer, thus forming a mechanical link. This process can be

used to aid the handling of delicate cloths by joining them to a more robust backing layer.

In addition to the continuous fibre reinforcements, the option of short fibre reinforcement is also available. Although short carbon fibres can be used in reinforced plastics such as moulding compounds, in carbon-carbon composites they are most commonly used in the form of felts. A felt is a tangled mat of short fibres where the fibre volume fraction is low. Some alignment can be achieved by a process known as carding, which is akin to brushing or combing. And the thickness of the felt can be increased by folding and needling.

3.3.2. Manufacturing routes

In order to turn a fibre preform into a usable product the fibres must be held in place by a matrix phase. For the product to be a carbon-carbon composite the matrix phase must be almost entirely carbon. There are two main routes to the introduction of the matrix to the fibre preform. The matrix carbon can either be atomically deposited from the gas phase, or formed by the thermal decomposition of a liquid polymer.

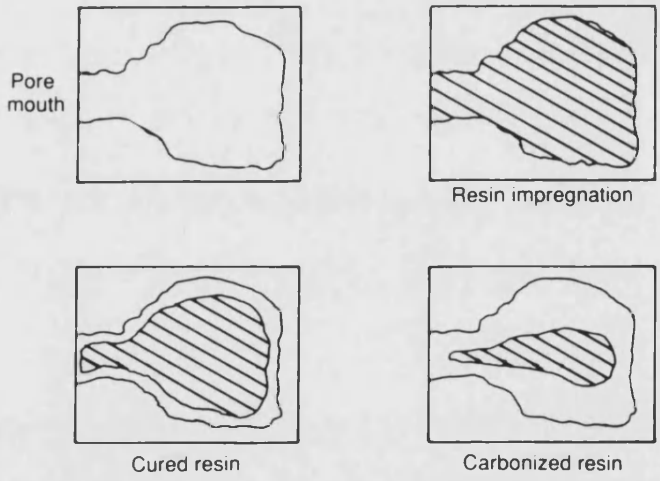

Figure 14. Schematic mechanisms of shrinkage during curing and pyrolysis[29].

Two groups of precursors are used in the liquid phase route, thermosets and thermoplastics. Thermosetting resins are used in carbon-carbon composites because they are relatively easy to use to impregnate the fibres, and a large base of knowledge exists from their use in the reinforced plastic composites industry. The resins are

introduced to the fibre preform often with pressurised assistance, and then cured to form a rigid solid. The cured resin is then pyrolised to form a carbonaceous matrix. A volumetric shrinkage is associated with both the curing and pyrolysis steps (Figure 14). This shrinkage can cause stresses in the matrix and the fibres, and porosity in the finished composite. Residual porosity is reduced by iterations of the impregnation and pyrolysis cycles. The carbon yield from these resins is typically around 50 to 60 % by weight and the density of the matrix material formed is roughly 1.5 to 1.6 gcm^{-3}. The low density of these carbons indicates their non-graphitic structure. However, in the vicinity of fibres grapthitisation of the matrix can be induced by shrinkage stresses. These factors can limit the density of the final composite, but there are still many applications for these materials.

The use of pitch as a precursor in the formation of carbon products is not a new idea but an extension of the technology used in the graphite electrode processing industry. The major drawback, however, with using pitch is the difficulty associated with categorisation, and hence quality control of the final product. This variability does allow the production of a wide variety of matrix microstructures by the manipulation of the processing conditions and careful choice of the pitch used. Due to their thermoplastic nature, the carbonisation of pitches is often associated with severe bloating and the loss of low molecular weight compounds. This can be overcome by the use of an oxidative process which cross-links the pitch. However the true potential of pitch based materials can only be realised by the application of high pressure during carbonisation. This process is known as hot isostatic pressure impregnation carbonisation, or HIPIC. The use of pressures around 100 MPa can improve the carbon yield of a given pitch from 50 % to 90 %. Sadly, the use of this method is limited by the size and cost of the equipment required despite the fact that it is probably one of the best production methods for thick sectioned, high density artefacts such as rocket nozzles. A great deal of work is being carried out to investigate the suitability of pitches as a matrix precursor for carbon-carbon composites. The aim is to reduce processing costs by realising the advantages of the high carbon yield and the ease of graphitizability of these materials.

The other major production route for the matrix of carbon-carbon composites is via the gas phase. Here carbon is deposited on the fibre preform by the decomposition of a carbon rich gas. This process is called chemical vapour infiltration (CVI) or

sometimes chemical vapour deposition (CVD). Since this is the method by which the composites used in this investigation were made, this method will be discussed in detail in the next section.

3.3.3. Production of PAN/CVI carbon-carbon composites

The CVI process involves the formation of a solid product from the nucleation and growth of the material from the gas phase. This can be achieved either by the reaction or decomposition of gaseous species whilst in proximity with the fibrous substrate. This allows close control of the microstructure, and hence properties, of the solid deposit. CVI as a method has the added advantage that the same technique can be used to deposit many wear and oxidation resistant coatings. In general, CVI carbon-carbon composites possess excellent mechanical properties due to the slow and controllable way in which the matrix is formed. However, in order to achieve high densities the reaction rate and hence the deposition rate have to be very low. This means that the energy inputs required are high and so the finished products are often expensive.

The CVI process, although simple in essence, is in fact very complex. Thermodynamics can be used to predict the onset of carbon deposition for a given reaction. Equation 1 shows the reaction for the decomposition of methane to give

$$CH_4\,(g) \rightarrow C\,(s) + 2H_2\,(g) \qquad \textit{Equation 1}$$

solid carbon and hydrogen. Methane is one of the most stable hydrocarbons and temperatures in excess of 550 °C are required before the deposition of carbon is thermodynamically favourable.

The kinetics of deposition reactions are very complex, but a model has been developed by Spear[30], in which the reaction is broken down into seven distinct steps.

1. Forced flow of reactant gasses into reaction vessel,
2. Diffusion of reactants through laminar flow boundary layers around substrate,
3. Adsorption of reactants on surface of substrate,
4. Reaction of adsorbed reactants to give solid products and adsorbed gaseous products,

5. Desorption of adsorbed gaseous products,
6. Diffusion of gaseous products through the boundary layer region,
7. Forced flow of the gaseous products through reaction vessel exit.

The complexity of the interactions at each of these steps means that the exact nature and influence of each individual process it not explicitly understood. However it is known that at low temperatures and pressures the surface reaction step tends to dominate the overall reaction rate. Whereas at high temperatures and pressures the process is diffusion controlled. The rate controlling step is of particular importance when the solid is to be deposited inside the pore structure of a porous solid as is the case with a fibre preform.

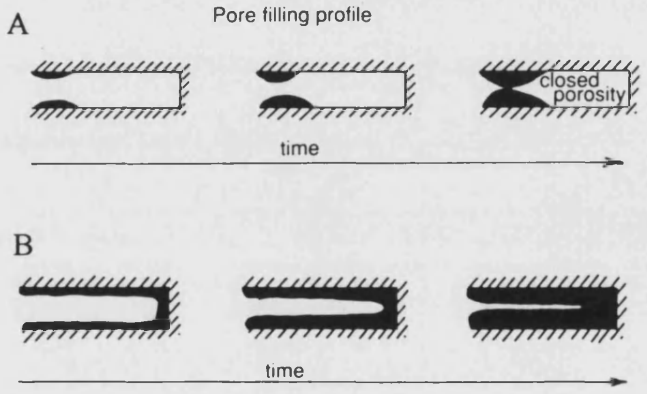

Figure 15. Schematic diagrams showing the influence of reaction kinetics on the pattern of deposition; a) surface reaction rate >> diffusion rate, b) diffusion rate >> surface reaction rate[7].

In order to achieve a fully dense product the pore structure must remain open at all times, since once porosity becomes closed material is no longer deposited inside it. It is for this reason that in isothermal CVI, the deposition has to be under reaction rate control. Figure 15 shows the effect of altering the relative diffusion and reaction rates. The pore structure can also be kept open by inducing the matrix carbon to be deposited preferentially in a specific area. By applying a pressure or temperature gradient through the thickness of the fibre preform, the matrix can be induced to grow from one face to the other. However these methods are more complex than isothermal CVI and

are not as suitable for large production runs. Hence their limited use in the commercial production of carbon-carbon composites.

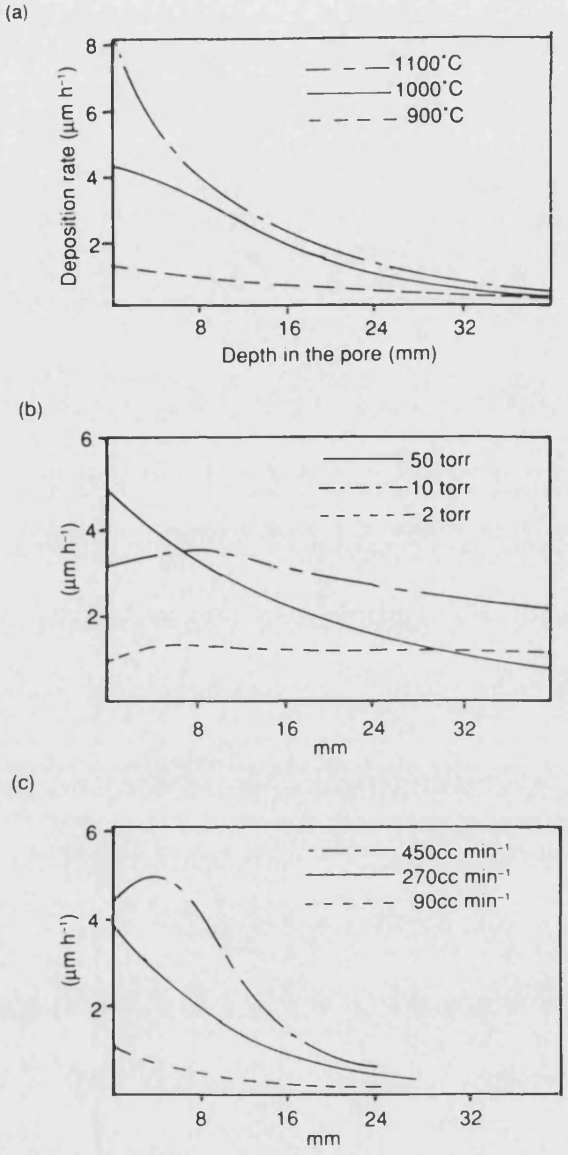

Figure 16. Experimental deposition rate versus pore depth profiles showing the influence of a) temperature, b) pressure, and c) flow rate[7].

Isothermal CVI relies on tight control of the reaction conditions to produce a dense, high quality product. Figure 16 shows the influence of temperature, pressure and flow rate on the deposition rate at various depths within a pore. The three graphs clearly show that it is not possible to get a higher deposition rate deeper within the pore and so the best that can be aimed at by the engineer is a deposition rate which is approaching independence from pore depth. This can be aided by designing the fibre

preform so that deep narrow pores are avoided. However, it is for this reason that during CVI densification the product is often removed from the furnace and the surface machined off to reopen closed porosity, before continuing with the CVI process.

There are three main microstructures which can be formed by CVI carbon; smooth laminar, rough laminar, and isotropic. These can be easily characterised by examination by optical microscopy using crossed polars which allow the optical activity of the material to be assessed. Isotropic material has no optical activity whereas laminar material forms the characteristic Maltese Cross pattern. Rough laminar also has annular features around the fibres and has been found to be the preferred microstructure since isotropic material is of low density and smooth laminar material is prone to thermal stress microcracking. Isothermal CVI tends to produce smooth laminar material since raising the reaction temperature to induce the rough laminar structure causes the formation of undesirable closed porosity.

All of the methods used to densify carbon-carbon composites are slow and inefficient processes, and as a result many carbon-carbon composite items are manufactured using a combination of production routes. For example, it is common for carbon-carbon composites fabricated by the pyrolysis of thermosetting resins to be further densified using CVI.

3.4. Properties of carbon-carbon composites

Much of the knowledge of the mechanical properties of carbon-carbon composites is still based on that of polymeric matrix composites. Although similar in their concept, there are fundamental differences between these materials. Also much of the theoretical modelling of the mechanical properties requires assumptions to be made and this inevitably causes inaccuracy when a comparison is made between theoretical and practical results.

The use of carbon-carbon composites in military applications has added to the natural commercial secrecy surrounding many developments in their technology. Also, being a relatively new area of research has meant that the rate of practical development has far outstripped the theoretical understanding of many of the more technical aspects of the science. For example, the understanding of the relationships between structure and

properties is relatively sketchy, particularly when compared with that of the polymer matrix composite systems.

3.4.1. General properties

It has already been discussed that the properties of carbon-carbon composites are highly dependent on the processing route and conditions. The chemical changes which occur during processing cause complex effects in the composite. The pyrolysis of an organic precursor involves a large volumetric shrinkage which induce large stresses in the structure of the composite which can lead to damage and hence alter the mechanical properties. Unlike polymer matrix composites the matrix phase cannot always be considered to be isotropic in the case of carbon-carbon composites. The matrix is deposited after the fibres, and so the degree of anisotropy is strongly influenced by the fibre lay-up.

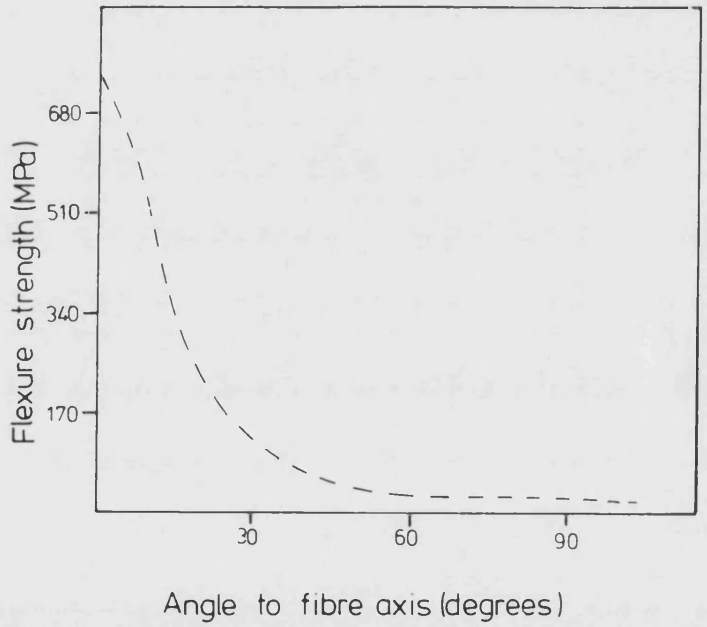

Figure 17. Effect of angle between fibre axis and load axis on the strength of a unidirectional carbon-carbon composite[7].

As with all fibre reinforced materials, the properties of carbon-carbon composites show a marked anisotropy as a result of the fibrous reinforcement. Maximum stress theory states that the tensile strength of unidirectional fibres will be achieved if the angle between the fibre axis and the applied load is no more than 4°. If the angle is

between 4° and 24° the strength is governed by the shear strength and above 24° the strength approaches that of the matrix[31]. This effect is shown graphically in Figure 17. Obviously there are very few situations where unidirectional reinforcement is used and so the calculation of the theoretical properties of carbon-carbon composites is difficult. The properties also depend on the fibre content and direction. Typical values of tensile strength for unidirectional, bidirectional and 3-directional carbon-carbon composites are shown in Table 4. The mechanical properties of the matrix carbon are poor in comparison to those of the fibre in the axial direction, and the transverse properties of the fibre are also poor. This gives rise to considerable anisotropy in the mechanical properties of many carbon-carbon composites. The tensile strength of a unidirectional composite can be described by a simple rule of mixtures, although in practical situations is it almost impossible to realise the theoretically determined strength. This is due to poor fibre-matrix bonding, inherent brittleness and the distribution of large scale and irregular porosity. Generally carbon-carbon composites only achieve between 50 and 60 % of their theoretical strength.

Composite Type	Tensile strength (MPa)		
	x-direction	y-direction	z-direction
Unidirectional fibres in the x-direction	770	25	25
Bidirectional fibres in the x-y plane	330	330	25
3-directional orthogonal weave, bundle size ratios x:y:z = 2:2:3	175	175	250

Table 4. Effect of fibre bundle orientation on the tensile strength of carbon-carbon composites.

It is difficult to manufacture a fully dense carbon-carbon composite and so these materials should strictly be regarded as three phase materials where the three phases are matrix, fibre and porosity. Obviously the effect of the porosity depends upon its size, shape and distribution. The combination of these factors affects the way in

which differences in porosity content influence the properties of the material. In general these effects are shown by a plot of the measured property as a function of porosity content. Two points on this plot are fixed regardless of the other factors. First the property at zero percent porosity content is equal to the property of the fully dense material, and second, the material must have zero property at 100 % porosity since effectively there is no material under test. The nature of the function linking these two points is dependent on both the material and the property under investigation.

One of the simplest analyses assumes that the relationship between property and porosity content takes the form of an exponential decay of the type described by Equation 2. This model has been shown to be relatively applicable to the variation of strength with porosity content. The constant *b* in the equation describes the curvature of the relationship where large values of *b* indicate a highly curved relationship. In this case the effect of small amounts of porosity has a large effect on the property such that much of the property of the fully dense material is lost by the inclusion of only a little porosity. Figure 18 shows the effect of porosity on the strength of three carbon-carbon composites with different matrices.

$$P_x = P_0 e^{(-bx)} \qquad \textit{Equation 2}$$

Where P_x = Value of the property at x % porosity

P_0 = Value of the property for fully dense material

b = Numerical constant

x = Percentage porosity

In some cases *b* can also be related to the nature of the porosity. In the case of strength, the effect of thin, sharp edged, transverse porosity will be great despite the low volumetric percentage of such pores. Hence this could be expected to produce a high value of *b*. In contrast, the effect of spherical porosity would have a much less severe effect on strength and so would yield a low value of *b*. However, since stress concentrations would still occur even around spherical porosity, low levels of porosity would still have a disproportionately large effect, i.e. 10 % porosity would cause a greater than 10 % reduction in strength. Porosity which had no effect of shape, size

and distribution would caused an exactly proportional reduction in property and hence could be regarded as *ideal*[32]. Although this concept is somewhat theoretical it does describe the relationship between density and porosity content.

This simple model does not adequately describe some observed behaviour because it takes no account of the type of porosity. For many physical properties, the size, location and shape of the porosity are as important as the volume fraction. In addition, the size, position and shape of the porosity will not be uniform, but rather will form distributions. Hence as strict treatment of the relationship between a physical property and the porosity content is rather complex. There is no reason why the dependence should not take the form of a more complex curve or even a step function. One interesting dependence is that of the coefficient of thermal expansion (CTE) of nuclear graphites as a function of porosity content. Here the CTE is seen to be relatively independent of porosity content suggesting that the property is reliant only on the retention of a continuous three-dimensional network of material.

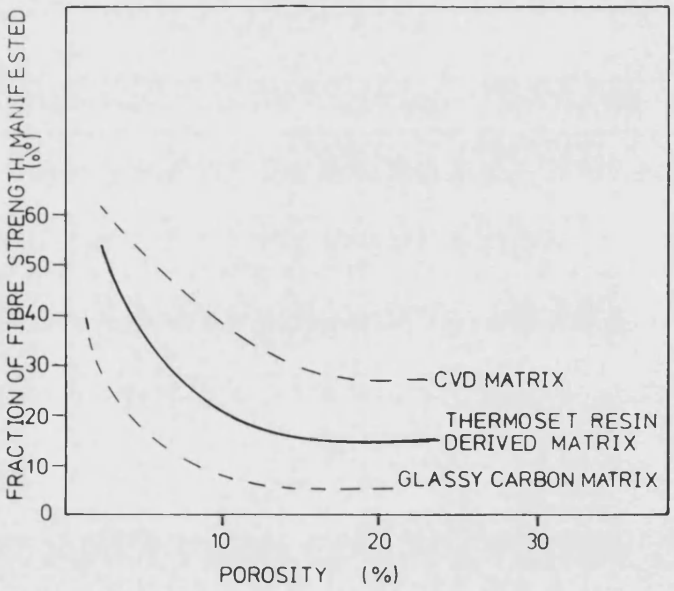

Figure 18. Effect of porosity on the strength of carbon-carbon composites[33].

Since many carbon-carbon composites including those used in this study, are used in aircraft brakes, Table 5 shows a comparison of some of the properties of carbon-carbon composites and other candidate disc materials. The figures shown here should be take as a guide since for all three materials a range of figures can be achieved. It is clear that the carbon-carbon composite has inferior properties in most of the listed

categories. However, it is in the specific properties (i.e. those where weight is accounted for) that the carbon-carbon composite scores well. It must be remembered that these materials were originally developed because of their outstanding specific properties which are a function of their low densities.

	Carbon-carbon	Steel	Copper
Tensile strength / MPa	66	410	240
Strain to failure / %	0.55	33	40
Density / kgm^{-3}	1800	7900	8900
Specific heat capacity / $Jg^{-1}K^{-1}$	1.42	0.59	0.42
Thermal conductivity / $Wm^{-1}K$	10 - 150	59	346
Coefficient of thermal expansion / 10^{-6} K^{-1}	0 - 8	14	18

Table 5. Some properties of aircraft disc brake materials (after Stimpson and Fisher[14]).

The other major reason for the use of carbon-carbon composites is the retention of their mechanical properties far in excess of the maximum useful temperatures of other materials[34]. The maximum temperature for the use of carbon materials is limited by the onset of creep at about 2000 °C[35]. The flexural modulus of carbon-carbon composites has been shown to decrease with increasing temperature however for some more graphitic carbon-carbon composites the modulus has been shown to increase up to temperatures of around 1000 °C before decreasing. This effect is analogous to that observed in polycrystalline graphites where the initial increase is attributed to closure of thermal stress cracks. There is no great temperature dependence of the strength of carbon-carbon composites with temperature, however both shallow minima[36] and maxima[37] have been reported. Also it is generally accepted that the strength of carbon fibres and carbon-carbon composites decreases at temperatures above around 2000 °C[38].

3.4.2. Creep and fatigue

The creep of carbon-carbon composites is characterised by an initial transient period followed by a steady state creep rate which increases progressively between about 2000 °C and 2600 °C.

Although there is little published work on the fatigue properties of carbon-carbon composites, what there is suggests that the fatigue properties are excellent. An infinite fatigue life is predicted at around 45 % of the static strength[39]. There is doubt over the cyclic opening and closing of pores and whether this phenomenon can indeed continue indefinitely. In long term fatigue tests the pore volume fraction is seen to increase arising from the loss of matrix material in small particles. This is known as "dusting out".

3.4.3. Toughness and fracture

An important property of any engineering material is its toughness which describes its resistance to crack growth. High toughness is necessary since it causes a progressive and hence non-catastrophic failure mechanism. Toughness is achieved by designing the material such that it contains features which allow the dissipation of energy during crack growth. In ductile materials this mechanism is plastic deformation at the crack tip. This is shown schematically in Figure 19. In carbon-carbon composites both the fibre and matrix are brittle, but by carefully designing the composite, and in particular the fibre-matrix interface, it can achieve a toughness far higher than either constituent.

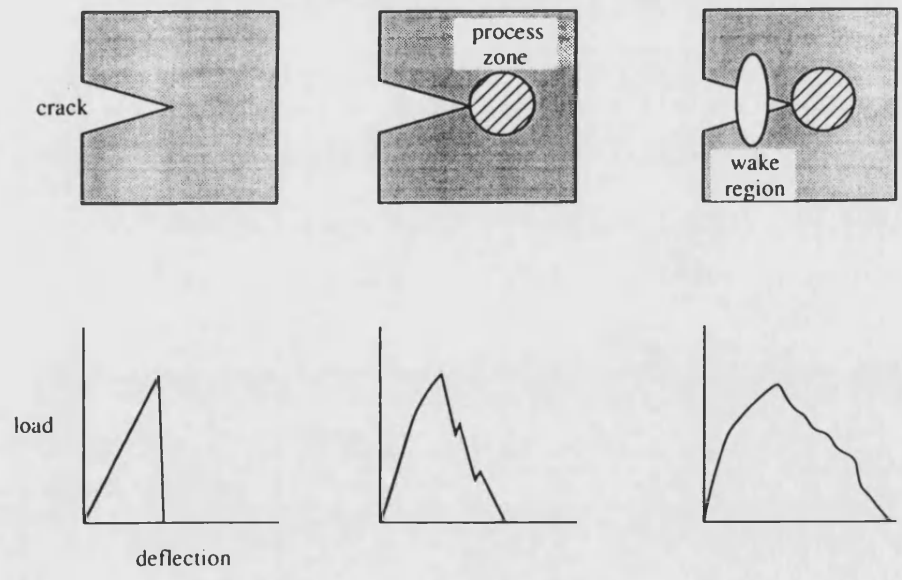

Figure 19. Fracture mechanisms and load versus deflection curves for brittle, semi-brittle and ductile materials[34]

The propagation of a crack through a carbon-carbon composite is similar to that observed in reinforced plastics. The mechanism consists of five distinct steps;

1. First matrix cracking
2. Fibre-matrix debonding
3. Crack bridging
4. Fibre fracture
5. Fibre pull-out

First matrix cracking occurs when the failure strain of the matrix material is reached, since the failure strain of carbon fibres are generally greater than the matrix carbon the cracking initiates in the matrix. This is characterised by an abrupt change in slope of a stress versus strain curve, however since carbon-carbon composites are heavily pre-cracked bodies as a result of their manufacture, this feature is often absent. In the

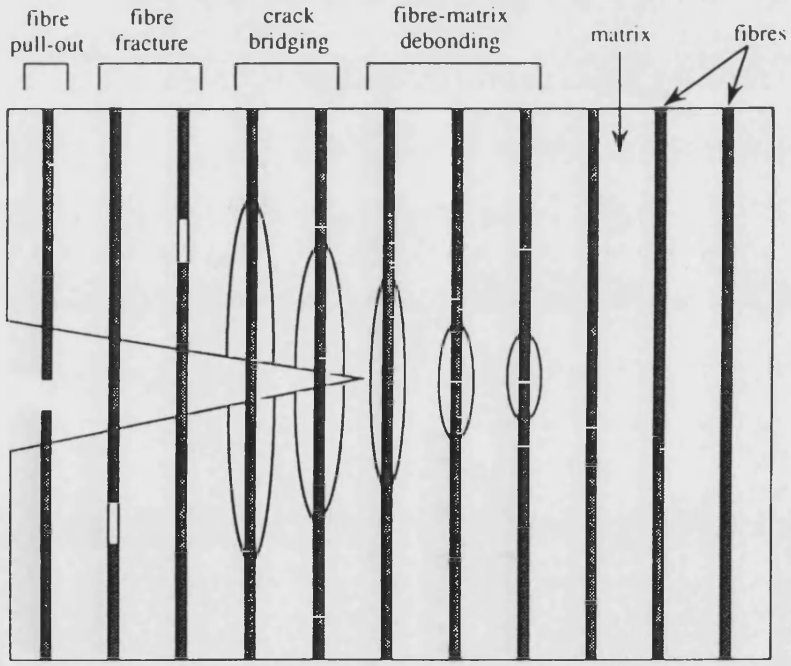

Figure 20. Micromechanical fracture processes in a unidirectional composite[34].

process zone ahead of the crack tip, the shear stresses are such that interfacial debonding occurs. The control of this process is of paramount importance in determining the toughness characteristics of a composite system. If the interfacial

bond is weak there is insufficient load transfer between the matrix and the fibre and the composite is weak. If the bond is strong there is minimal interfacial debonding and the composite becomes brittle. The process of debonding is one of the principal mechanisms of energy absorption during crack growth and hence toughening. This and the following stages are shown in Figure 20.

Advancement of the crack leaves crack-bridging fibres which may contribute to toughening in three ways, by further debonding, by frictional resistance to elongation of the fibres, and by reducing the stress intensity at the crack tip. Further crack growth causes fibre fracture. Upon fracture the fibre relaxes its axial stress which causes a transverse expansion. If the fibre fractures some distance from the axis of the crack the fibre snaps back within its matrix socket. Further crack opening pulls these fibres out from their sockets which requires energy on order to overcome the frictional forces between the fibre and the matrix socket. Measurement of the length of fibre pullout of a fractured specimen can therefore provide some information about the strength of the fibre-matrix bond.

4. OXIDATION OF CARBON

4.1. Introduction

As has been demonstrated, carbon-carbon composites are ideal for use as a structural materials at elevated temperatures, and particularly in inert or ablative atmospheres. However they are often employed in situations where they are exposed to atmospheres containing oxygen. Therefore an understanding of the causes and effects of oxidation is an essential part of the design process.

The oxidation of carbon-carbon composites is complicated by numerous microstructural considerations and so this chapter considers the simpler case of the oxidation of carbon materials in general before Chapter 5 discusses oxidation of carbon-carbon composites.

4.2. Mechanisms and kinetics

The kinetics of the reactions between carbon and oxidising species are complex and often difficult to understand fully. However, in order to understand the reactions which occur during the service life of a carbon-carbon composite component, knowledge of the reactions is important.

The surface of carbon materials play a key role in determining the extent and pattern of oxidation which will occur[40]. In general terms physical or chemical disorder tends to increase the chance of oxidative reactions occurring. Topographically, the favoured reaction sites are found at the prismatic edges of carbon layers and defects within the basal plane.

Carbonaceous materials are not usually perfectly graphitic. They contain hetroatoms such as hydrogen, oxygen, sulphur and phosphorus, and crystallographic defects such as dislocations, vacancies, stacking faults and crystal boundaries. It has been shown that the reactivity of carbon materials depends upon the extent and range of the order in the structure. High degrees of long range order tend to give low reactivities, and vice versa. A measure of the relative reactivities of similar carbons can be gained by measuring the active surface area (ASA). This indicates the area which is initially available for reaction, and is distinct from the total surface area (TSA). Comparison

of the TSA and ASA gives an idea of the number of active sites per unit area of a carbon material.

There are five basic kinetic steps which make up carbon oxidation reactions and these are shown below;

1. Mass transfer by diffusion of the gaseous reactants from the bulk gas to the carbon surface
2. Adsorption of the reactant on the carbon surface
3. Occurrence of chemical rearrangements and reactions on the surface and formation of adsorbed products
4. Desorption of products
5. Mass transport by diffusion of the gaseous products away from the carbon surface and into the bulk gas

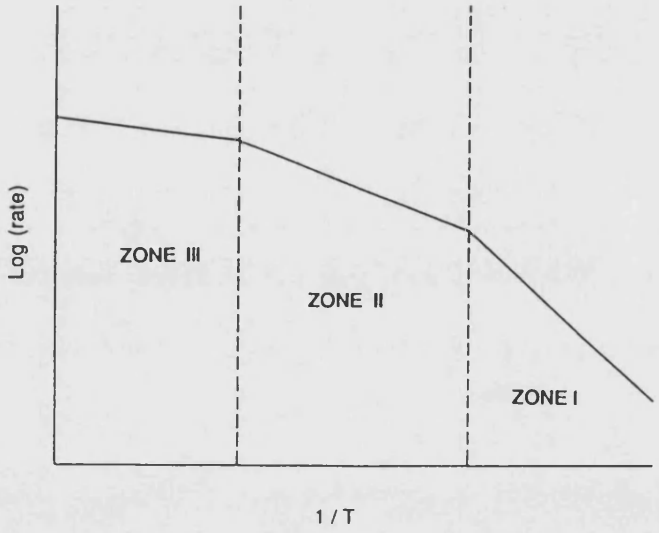

Figure 21. Schematic Arrhenius plot for the gasification of carbon[41].

The rate of this whole process is determined by the single slowest step known as the RDS (rate determining step). This step is dependent in turn on process parameters, temperature, pressure and sample size, and carbon properties such as porosity, active site concentration, and catalytic impurities. The consideration of the RDS is

particularly important in non-homogeneous materials and those which are porous. In the case of porous materials the kinetics of mass transfer are very different from those at the external surface.

The oxidation of carbon is often referred to as occurring in one of three zones depending on the nature of the RDS. Zone 1 describes the situation where the RDS is that of the chemical reaction between the carbon and the oxidising species. Because of this it is also referred to as oxidation under chemical control. Zone 3 denotes the condition where the RDS is the diffusion of the gaseous species to and from the surface of the material, and is also known as oxidation under diffusion control. Zone 1 occurs at low temperatures and Zone 3 at high temperatures. Between these zones exists Zone 2. Here the rate of reaction is determined at the surface of the sample by chemical reaction rates and by diffusion of active gases to the internal surfaces of pores. Figure 21 shows a schematic Arrhenius plot for the gasification of carbon, indicating the three reaction zones. The three zones of reaction can also be separated

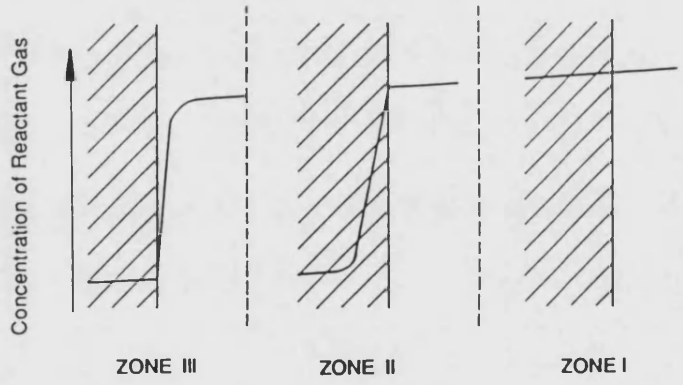

Figure 22. Diagram showing the concentration profiles of the reactant gas in the three rate controlling zones[41].

by examining the concentration of the reactant gas across the surface region of the sample. This is shown in Figure 22. In Zone 1 the concentration is constant in the bulk gas and the sample at all depths, since the reaction is under chemical control. In Zone 2 the concentration falls away within the sample as a function of depth. Here the

oxidation within the pore system is under diffusion control. In Zone 3 the concentration falls away at the surface of the sample since even the oxidation of the exterior of the sample is under diffusion control.

It is an important factor to note that the reactivity of a given carbon is dependant on the reactive species used. Also it does not necessarily follow that the order of reactivity of a group of carbons will remain unchanged if alternative oxidising species are used. This is clear if the active site model is considered. The reactions between carbon and two gases, carbon dioxide and molecular oxygen, are shown below;

$$C + CO_2 \rightarrow 2CO \qquad \textit{Equation 3}$$

$$C + O_2 \rightarrow CO_2 \qquad \textit{Equation 4}$$

Clearly Equation 3 requires only a single active site whereas Equation 4 contains an intermediate stage where two adjacent active sites are necessary. So in this example the reactivity of the same carbon is different when the oxidising species oxygen and carbon dioxide are used.

4.3. Significant gasification reactions of carbon

Carbon gasification reactions form the basis of many industrial processes, such as the combustion of coal and the production of synthetic gas, fuel gases and activated carbons[42]. Many of these reactions are desirable and have been used for centuries, however some of them are negative side-effects of the use of carbonaceous materials at elevated temperatures.

Of all the gasification reactions, probably the most important is the reaction of oxygen and carbon. This occurs in the combustion of coal to produce heat and as such has its origins in antiquity. For the use of carbon at high temperature in oxygen-containing atmospheres (e.g. air) it is a significant and undesirable reaction. For this reason it will be discussed in more detail in Section 4.3.1. The other significant reaction under these conditions is that between carbon and carbon dioxide and this too will be discussed in a separate section (4.3.2.).

$$C + H_2O \rightarrow CO + H_2 \qquad \textit{Equation 5}$$

Of the other significant reactions of carbon, that involving steam is of the most industrial relevance. It is used in the gasification of coal, activation of carbon, regeneration of coked catalysts, water-gas manufacture and in nuclear technology[40]. It also has deleterious effects on carbon-carbon composites particularly those used in rocket motors where steam and hydrogen are present. Following gasification by steam (Equation 5), a number of secondary reactions can occur. These are shown below;

$$CO + H_2O \rightarrow CO_2 + H_2 \qquad \textit{Equation 6}$$

$$C + CO_2 \rightarrow 2CO \qquad \textit{Equation 7}$$

$$C + 2H_2 \rightarrow CH_4 \qquad \textit{Equation 8}$$

$$3H_2 + CO \rightarrow CH_4 + H_2O \qquad \textit{Equation 9}$$

Some or all of these reactions may be of importance in determining the rate and nature of the overall gasification process and they have been extensively studied[43,44,45]. Of those listed the two most important are the water-gas shift reaction (Equation 6) and the Boudouard reaction (Equation 7). Two distinct mechanisms for the reaction between carbon and steam have been proposed which explain the rate of the reaction by different inhibition mechanisms;

Mechanism 1

$$C_f + H_2O\,(g) \rightarrow C(O) + H_2 \qquad \textit{Equation 10}$$

$$C(O) \rightarrow CO\,(g) \qquad \textit{Equation 11}$$

$$H_2\,(g) + C_f \leftrightarrow C(H_2) \qquad \textit{Equation 12}$$

Mechanism 2

$$C_f + H_2O\,(g) \leftrightarrow C(O) + H_2 \qquad \textit{Equation 13}$$

$$C(O) \rightarrow CO\,(g) \qquad \textit{Equation 14}$$

Where C_f represents a vacant active site, C(O) represents an active site occupied by an adsorbed oxygen atom, and $C(H_2)$ represents an active site occupied by an adsorbed hydrogen molecule. The first mechanism predicts inhibition by hydrogen adsorption on active sites, while the second predicts inhibition by removal of the C(O) complex by hydrogen. It is as yet unclear which mechanism is correct.

Gasification of coal can release oxides of nitrogen which can further react with the coal in a number of ways to form nitrogen gas and oxides of carbon.. This is also one of the reactions by which nitrogen oxides can be removed from industrial waste gas flows.

Carbon can also react with atomic hydrogen. The reaction between carbon and hydrogen (Equation 8) is the least favourable of the gasification reactions of carbon and in the absence of a catalyst, requires even higher temperatures and pressures than the endothermic steam reaction[46]. It is of industrial significance in the production of methane. At 1000 °C and 1 atm pressure the equilibrium concentration of methane is only about 1 %, and so to improve the methane yield high pressures are required. Table 6 shows the standard enthalpies of reaction at 298 K for some common gasification reactions.

Reaction	ΔH^{o} ($kJmol^{-1}$)
$C + CO_2 \rightarrow 2CO$	170.7
$C + H_2O \rightarrow CO + H_2$	130.3
$C + O_2 \rightarrow CO_2$	-393.4
$C + 2H_2 \rightarrow CH_4$	-74.8

Table 6. Standard reaction enthalpies at 298 K for common gasification reactions[40].

There are many other carbon gasification reactions which are of some commercial interest such as those listed below;

$$C + SO_2 \rightarrow CO, CO_2, COS \qquad \textit{Equation 15}$$

$$C + 2F_2 \rightarrow CF_4 \qquad \textit{Equation 16}$$

$$2C + N_2 \rightarrow C_2N_2 \qquad \textit{Equation 17}$$

4.3.1. Reaction of carbon and oxygen

As has been previously discussed, the combustion of carbon in oxygen containing atmospheres has been one of the most important reactions in the history of mankind. Despite this the reaction between carbon and molecular oxygen is still not fully

understood. It is of particular importance in the field of aircraft brakes since the brakes are open to the ambient atmosphere which comprises approximately 20 % oxygen. There are two primary reactions which can occur;

$$C + O_2 \rightarrow CO_2 \qquad \textit{Equation 18}$$

$$C + {}^1/_2O_2 \rightarrow CO \qquad \textit{Equation 19}$$

The two oxidation reactions above have associated standard enthalpy changes at 298 K of -393 and -111 $kJmol^{-1}$ respectively. The relationship between these two reactions and the mechanisms which control them has been the subject of intense scrutiny for over fifty years. It has been generally concluded that the ratio of carbon monoxide to carbon dioxide produced increases with increasing reaction temperature. Indeed this fact was reported by workers such as Arthur[47] as early as 1951. Recent work has concluded that oxidation of carbon in fluidised sand beds occurs via an intermediate carbon monoxide with this gas being further oxidised to carbon dioxide[48]. This work also highlights the difficulties associated with ascertaining whether carbon monoxide is formed since its conversion to carbon dioxide can often be very rapid and occur close to the surface of the carbon. It has also been found that radicals can be very important in this reaction[49]. The interaction of these radicals with the carbon is affected by the medium in which the oxidation occurs, and this may account of some of the apparently anomalous results which have been presented. For example in a fluidised sand bed the close proximity of the sand provides a large surface area on which the radicals can recombine and this inhibits the oxidation of carbon monoxide.

Clearly the oxidation of carbon is far from simple and it is further complicated when the carbon material is porous as in the case of a carbon-carbon composite, since the kinetics of mass transport in pores is very involved. However it is known that at low pressures the reaction does proceed at a measurable rate at temperatures above about 300 °C. In air practical carbons are seen to oxidise measurably above about 450 °C with a marked increase in reaction rate above about 750 °C as the reaction switches from Zone 1 to Zone 2.

It is worth pointing out that since the oxidation reactions of carbon all result in gaseous products, the extent of oxidation can easily be calculated by a mass comparison (Equation 20).

$$\%_{OX} = \frac{M_u - M_o}{M_u} \qquad \textit{Equation 20}$$

Where $\%_{OX}$ = Percentage oxidation

M_u = Unoxidised mass

M_o = Oxidised mass

This is commonly expressed as a percentage, and although useful as a rough guide, it gives no information as to the location, type, mode or mechanism of the oxidation which has caused it. This is of particular significance in composite materials where the location and shape of the porosity caused by oxidation has a great bearing on the mechanical properties. The effects are similar to those caused by manufacture induced porosity which have been discussed in Section 3.4.1.

4.3.2. Reaction of carbon and carbon dioxide

This reaction would seem to be of little relevance for carbon materials used in ambient atmospheres since these contain only about 0.03 % carbon dioxide. However, the reaction is a significant second stage in the reactions between carbon and oxygen, and carbon and steam, and an understanding of it is therefore also of importance.

This reaction is known as the Boudouard reaction (Equation 7) and involves an enthalpy change of approximately 171 $kJmol^{-1}$. This is therefore an endothermic reaction. This is a very important fact if a controlled reaction rate is required since it is much easier to control an endothermic reaction than it is to control an exothermic one. At the same temperature the reaction proceeds at a rate which is several orders of magnitude slower than the carbon and oxygen reaction unless a catalyst is present[46]. In general catalysts are required to produce significant Boudouard reaction rates at temperatures below 900 °C. The reverse reaction involving the dissociation of carbon monoxide has been shown to occur on many catalytically active metal surfaces at temperatures as low as 500 °C[50]. The study of the catalysed Boudouard reaction has been the subject of many studies particularly those concerned with the reaction

kinetics and the rate equations[43,44,45,51,52]. This interest primarily stemmed from the nuclear industry where graphite is used as a moderator in the core of nuclear reactors where carbon dioxide is used as the circulating coolant. However, this condition is subject to the added complication that oxidation can also be caused radiolytically.

5. OXIDATION OF CARBON-CARBON COMPOSITES

The oxidation of carbon-carbon composites bears much relation to that of pure carbon. However, the reactivity of the surface of a carbon material is dependant on many factors such as microstructure, macrostructure, inclusion of hetroatoms, presence of catalysts and the nature and structure of the pore network. All of these features are present in carbon-carbon composites to a much greater extent than is found in near-perfect graphite. In this respect the oxidation of carbon-carbon composites is more closely related to the oxidation of nuclear graphites, which in essence are particulate carbon-carbon composites.

5.1. Effect of oxidation on microstructure

Since the oxidation reactions of carbon are gasification reactions, it is obvious that a microstructural consequence of them is the creation of porosity. The nature and location of this porosity is highly dependent on the type and structure of the unoxidised composite. It can also dictate the rate of reaction particularly at high temperatures (Zones 2 and 3) since under these conditions the RDS is mass transfer[53]. Two things are required for any reaction to occur; reactant species, and energy. In the case of the oxidation of carbon the reactant species are the oxidising gas, and the active carbon site. Almost all of the active sites in a carbon-carbon composite exist within the pore network purely because this is where most of the surface area lies. Within closed porosity oxidation can only occur between the carbon and the pore-filling gas. Therefore there is only minimal oxidation in these regions. However, closed porosity may become open as oxidation proceeds. At low temperatures the reaction is controlled by the chemical interaction and therefore the most important influence is the distribution of active sites. The reactivity of an active site is primarily dependent on the degree of structural disorder, i.e. defect concentration. However it must be borne in mind that the activation energy for the reaction (energy barrier) can be significantly lowered in the presence of a catalyst. Goto *et al*[54] showed that for a carbon fibre-glassy carbon composite the oxidation first takes place at the fibre-matrix interface, and proceeds through the optically anisotropic and graphitic matrix and finally into the isotropic matrix. This first step is probably governed by the presence of impurities, disrupted structure and the ease of

mass transport. The ease of mass transport arises from the fact that the oxidation of the interface begins where the interface intersects the specimen surface. Thence the fibre-matrix interface porosity developed as a result of oxidation is always open. The continuation of oxidation in the graphitic and non isotropic matrix is a function of the high active site concentration in these regions. Their presence is due to the high stress concentrations produced by the shrinkage of the carbon during manufacture. Finally the reaction proceeds into the glassy, isotropic carbon. This region is least likely to react since it contains fewer active sites and the porosity is almost all closed.

By heat treating the composite after production to high temperatures some of the structural defects, and hence active sites, can be removed from the structure by atomic rearrangement. It has been found that the onset of oxidation for composites heat treated to 2700 °C is up to 200 °C higher than for those heat treated to 1000 °C[55]. The heat treatment temperature (HTT) has also been found to affect the location of the oxidation. For a PAN/CVI composite heat treated to 1100 °C the oxidation occurred preferentially in the matrix, but with a higher HTT (2000 °C) the fibre-matrix interface was oxidised first[56]. It was also reported that the rate of oxidation was not necessarily the sum of the rates of oxidation of the component parts. The rate of oxidation of another PAN/CVI carbon-carbon composite in air has also been shown to be dependent on the extent of oxidation[57]. The results suggested a three stage regime with a constant oxidation rate up to 25 % burn off, a higher but constant rate between about 40 % and 70 %, and a final stage where the rate is proportional to the remaining mass of the composite. It was found that the first stage corresponded to the fibres being attacked creating tunnels in the composite. In the second stage steady state was established and in the third all the fibrous material had been removed, and only the CVI carbon remained. The production of tunnels into the composite by this mechanism is of great significance since it completely changes the nature of the pore network and hence mass transfer within the material. A similar effect has been found in a composite with ex-acrylic fibres and a pyrocarbon matrix, however in this case the preferential oxidation of the fibres was ascribed to catalytic activity[58].

This tunnelling effect highlights another important factor which is the fibre lay-up. Since oxidation often occurs at the fibre-matrix interface and proceeds into the fibres the resulting porosity takes the form of the fibre lay-up. Therefore control of the oxidative process can be influenced by the design of the fibre architecture. For

example, continuous fibres will tend to allow ingress of the oxidising species well into the bulk of the material whereas shorter fibres may restrict the mass transport processes. Interestingly a recent paper suggested that the development of porosity within the fibres was beneficial in retarding oxidation. This was attributed to local stress graphitisation around the pores within the fibres which results in the carbon at the fibre-matrix interface being more oxidation resistant[59].

In essence then, oxidative attack can preferentially remove carbon from any area of the composite depending on the structure, pore network and available catalyst. However, by examination of oxidised material it is possible to identify the oxidised regions by the appearance of porosity which cannot be attributed to the manufacture process.

5.2. Effect of oxidation on mechanical properties

The effect of oxidation on the mechanical properties has much industrial relevance, since carbon-carbon composites are used as structural components often in oxidising atmospheres. Despite this however, there is little information in the open literature on this topic. There is some information on similar topics pertaining to nuclear graphite and this information suggests that the effects of oxidation are significant. As previously mentioned, the oxidation of nuclear graphites is complicated by the fact that oxidation can occur by both thermal and radiolytic mechanisms. However Brocklehurst[60] summarised the effects as shown in Figure 23. The main conclusion which can be drawn from this work is that the effect of thermal oxidation on the mechanical properties of graphite is severe. For example, the strength is seen to decline to around 50 % of its unoxidised value at only about 5 % oxidation. Similar trends to these have been found by other researchers[61,62,63].

What little information on the effects of oxidation on the mechanical properties of carbon-carbon composites exists in the public domain suggests similar trends to those observed in nuclear graphites. Some research indicates that the effect of 20 % weight loss are reductions of 75 %, 64 % and 57 % in Young's modulus, flexural strength and work of fracture respectively[64,65,66]. The relationships are seen to have forms similar to those found for nuclear graphites, i.e. exponential. This implies that the oxidation is having a more than proportional effect and hence most of the mechanical properties are lost in the early stages of oxidation. Typically a given mechanical property for a composite is reduced by half at about 10 % weight loss. This indicates that low levels

of oxidation are having a marked effect on stress transfer within the composite and this is consistent with the oxidative attack being concentrated at the fibre-matrix interface which is the critical region for stress transfer.

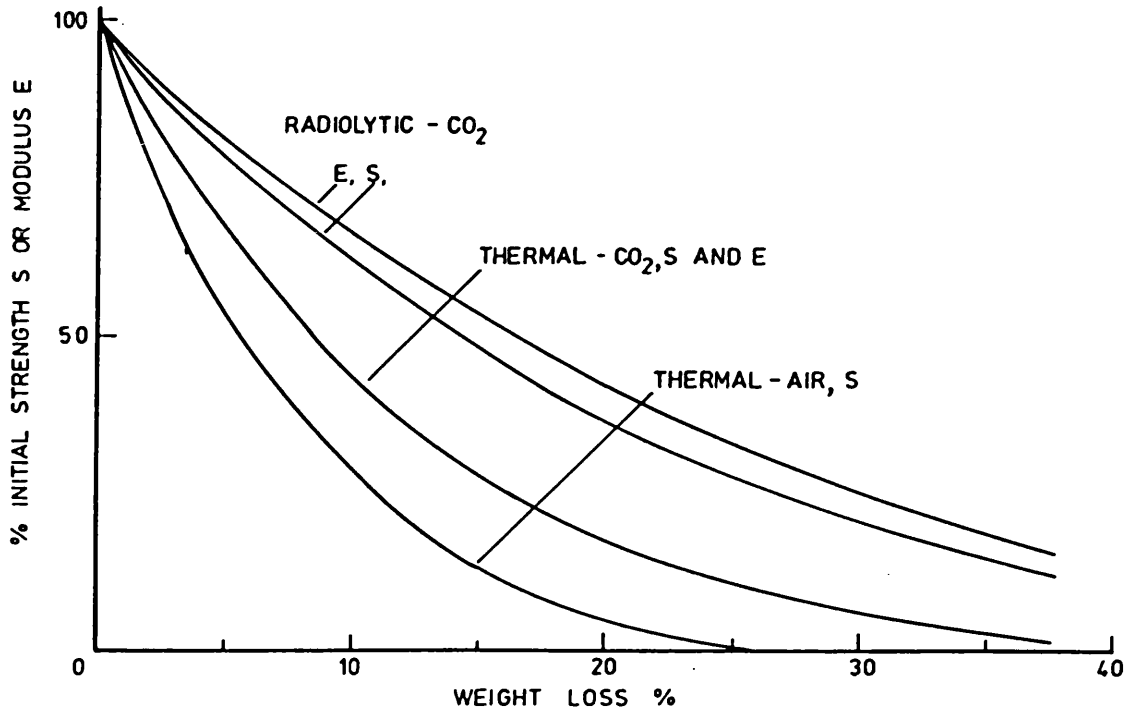

Figure 23. Comparison of the effect of thermal and radiolytic oxidation on the strength and modulus of graphite[60] (Radiolytic CO_2[67,68], Thermal CO_2[69,70] and Thermal air[71]).

Confusingly however, there is some work which suggests that the mechanical properties of a brittle PAN/Pitch carbon-carbon composite could be significantly improved by low levels of oxidation[72]. As a result of oxidation the fracture mode in three point bending was observed to change from a brittle mechanism to a more progressive one. Also the flexural strength and failure strain improved by 85 % and 120 % at a weight loss of 1.4 %. It was suggested that this was due to greater utilisation of the fibre strength. Greater weight loss was found to reduce the mechanical properties of the composite in accordance with other work.

5.3. Catalysis

It is well known that many metal salts, oxides and other compounds have a marked catalytic effect on the oxidation reactions of carbon. This is pertinent to the study of carbon-carbon composites from two perspectives. Firstly, impurities may well be present in the composite as a result of the manufacturing processes and their distribution can affect the location and effect of oxidation on the properties. Secondly, the impurities can be introduced to the material during the service life of the component. It is suspected that the severe oxidation encountered in carbon-carbon aircraft brakes by some operators was due to ingress of the detergents used to clean commercial aircraft. These detergents contain significant quantities of the types of metal salts which have been shown to strongly catalyse the oxidation of carbon.

McKee[76] has conducted much research on this topic and the results of some of this work are shown in Table 7. This table shows the ignition temperature of graphite in flowing oxygen, and uses this as an indication of the catalytic effect of the metal. Clearly there is a marked lowering of the ignition temperature with lead causing a reduction of 358 °C to 382 °C. Some of the metals such an iron, cobalt and manganese, were seen to loose their reactivity as the reaction progressed and this is taken to mean that the metal is a more effective catalyst than the oxide. Conversely some oxides are more effective than their metals (MoO_2 and V_2O_5). It has also been suggested that only those metals which can oscillate between two states of oxidation can catalyse the oxidation of graphite[73].

5.4. Oxidation protection

In order to fully realise the potential of carbon-carbon composites particularly in applications where high temperatures are experienced such as aircraft brakes, practical oxidation protection is critical[74]. Oxidation protection can be achieved in two ways, either by negative catalysis (inhibition) or by the creation of a barrier to the diffusion of the oxidative species. The addition of inhibitors such as compounds of phosphorus and boron, can easily be achieved during manufacture and have been found to significantly reduce the rate of oxidation of graphite[75]. For example the rate of oxidation at 800 °C in air, was found to be reduced by a factor of about 5 by the addition of 3 % by weight of boron oxide (B_2O_3). Inhibitors tend to be most effective at low temperatures i.e. where the reaction is under chemical control. This is

generally achieved by the inhibitors occupying the active sites on the surface of the carbon and hence not permitting reactions to occur. However at higher temperatures where diffusion is the RDS the diffusion barrier method is more effective.

Catalyst	wt % as metal	Ignition Temp. (°C)
Pb	0.15	382
V	0.20	490
Mn	0.45	523
Co	0.33	525
Cr	0.95	540
Cu	0.20	570
Mo	0.15	572
Ag	0.16	585
Cd	0.21	590
Fe	0.13	593
Pt	0.03	602
Ni	0.45	613
Ir	0.40	638
Rh	0.20	622
Ru	0.30	640
Pd	0.30	659
Ce	0.72	692
Zn	50.00	700
W	0.02	718
Hg	0.10	720
Sn	0.10	738
None		740

Table 7 Catalytic activity of oxides in graphite oxidation[76].

There has been much work in the field of high temperature oxidation protection of carbon-carbon composites. The method involves applying a coating to the composite to prevent the physical proximity of the oxidative gas and the carbon. The selection of

a suitable coating is not as simple as finding a material which is impermeable to oxygen (or carbon dioxide etc.). The coating must remain coherent under all of the conditions likely to be experienced by the component during its service life. The biggest problem is to avoid cracking of the barrier layer or separation of it from the substrate. Cracking has been shown to catastrophically reduce the effectiveness of a coating as even very small cracks allow rapid diffusion of gases[77].

Cracking is often the result of thermal mismatches between the coating and the substrate. Since carbon-carbon composites experience large amplitude thermal cycles during their service these thermal expansion mismatches are very significant[78]. Table 8 shows the coefficients of thermal expansion (CTE) for some candidate engineering ceramics. The CTE for carbon-carbon composites are typically between 0 and 1 $\times 10^6$ K^{-1}.

Material	CTE ($\times 10^6$ K^{-1})	Material	CTE ($\times 10^6$ K^{-1})
SiO_2	0.65	HfB_2	7.60
Si_3N_4	3.00	ZrB_2	8.30
SiC	5.00	Y_2O_3	8.60
AlN	6.00	TiO_2	8.80
HfN	6.30	Al_2O_3	9.60
HfC	7.00	ThO_2	10.40
ZrC	7.50	HfO_2 (stab)	10.50
ZrN	7.50	ZrO_2 (stab)	13.40

Table 8. Coefficients of thermal expansion (CTE) for selected engineering ceramics[79].

Silica cannot be used directly at service temperatures since it reacts with the carbon to cause oxidation as shown in Equation 21.

$$SiO_2 + 3C \rightarrow SiC + 2CO \qquad \textit{Equation 21}$$

The next best materials are silicon nitride and silicon carbide, but these have CTE values between 5 and 10 times that of the carbon-carbon composite. Thus it is

difficult to apply these materials without them cracking. Some systems use a combination of ceramics to achieve the best coating. An example of a combined system is the SiC/B_2O_3 system. Here the silica provides most of the protection while the boron oxide phase can fill the thermal mismatch cracks by becoming molten at the operating temperature. The nature of the crack filling (i.e. by a liquid phase) limits the use of this system to relatively low temperatures since at high temperatures the boron oxide phase becomes volatile. There is also a suggestion that oxygen can diffuse through the boron oxide when it is molten giving rise to oxidation beneath the protective layer[77].

In addition to the chemical and kinetic requirements of oxidation inhibitors is the commercial requirement that they be easily applied. Many ceramic barrier systems have the advantage that they can be easily applied by modification of the feeder gases in a CVI process. Hence much of the reported work is based on vapour deposition routes. However, for aircraft brake applications CVI has the major drawback that the coating cannot be applied to selective surfaces, i.e. non friction surfaces. Consequently most antioxidant systems a applied through painting or spraying procedures, as a post-treatment after final densification[74].

Section B

Experimental Programme

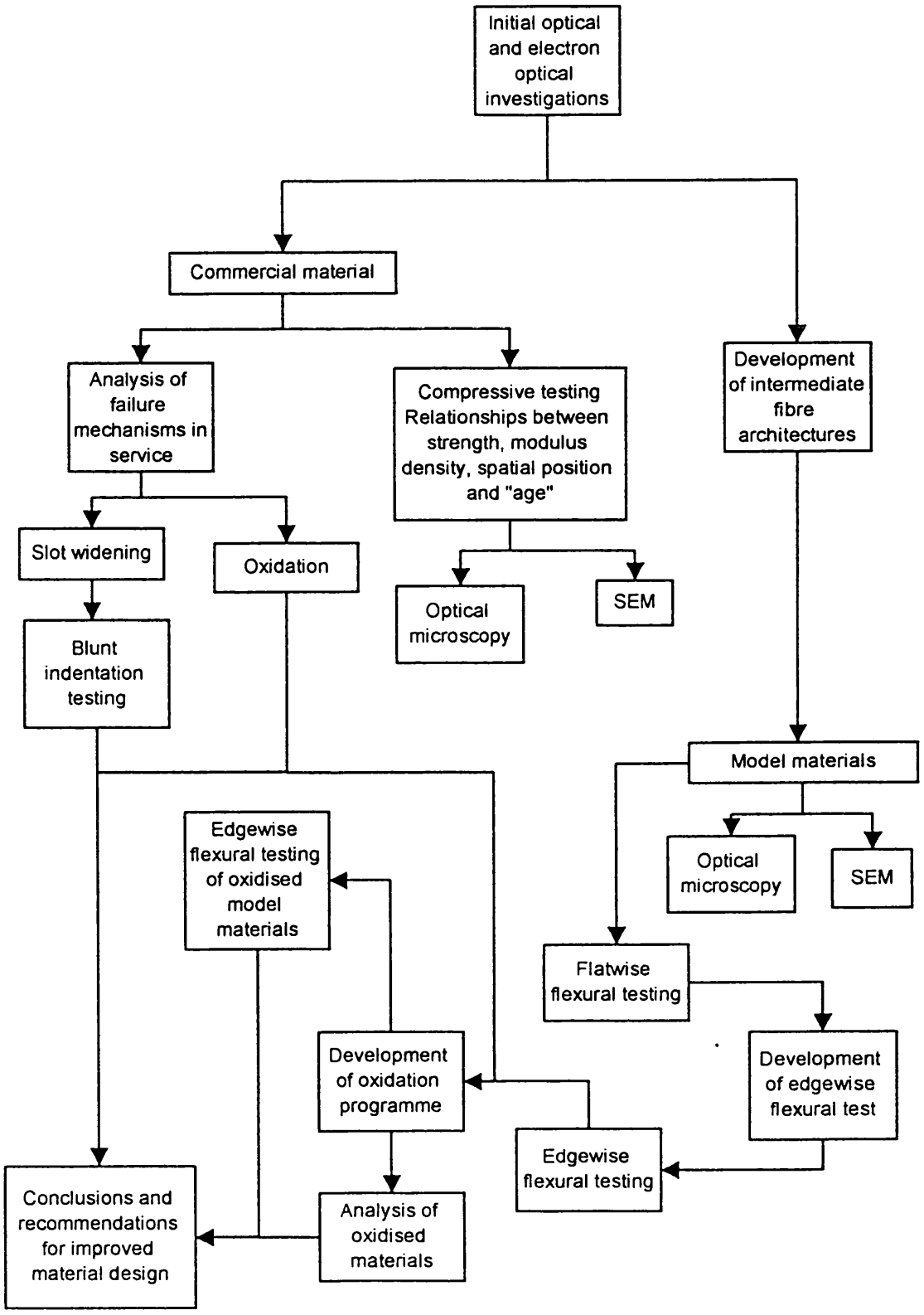

Schematic diagram showing the experimental programme and the relationships between the various investigations of which it was formed.

6. CHARACTERISATION OF COMMERCIAL MATERIAL

Before any investigation could be made of the properties of the commercial material it was first necessary to understand the microstructure. To this end several investigative techniques were employed. So that the microstructure and features observed in this chapter may be related to the manufacturing process, a brief description of the manufacture of the commercial Dunlop disc material is also given.

6.1. Manufacture of the commercial material

The material produced by Dunlop for use in aircraft brakes consists of poly(acrylonitrile) (PAN) fibres in a chemical vapour infiltration (CVI) matrix. The production of PAN fibres is discussed in Section 3.2.1., and those used by Dunlop are made from textile grade PAN. Briefly the process involves two stages, stabilisation and carbonisation. Stabilisation occurs by oxidation and is necessary to prevent the structure of the fibre collapsing during carbonisation.

The stabilised fibres are used in the form of a two layer cloth. One of the layers consists of continuous unidirectional fibre, and the other of a material called felt or staple. The felt has a complex structure which is manufactured in several stages. First, a 320k tow of stabilised PAN fibres is crimped and stretch broken. These fibres are then cut to length, mechanically fluffed and then, in a process akin to that used in spinning, they are carded. Carding involves brushing the fibres such that they are entangled and roughly aligned but have a element of three-dimensional structure. At this stage the cloth is very weak and has a variable fibre density. The cloth is then folded back on itself several times and passed through rollers to build up the fibre density and to reduce density variations. This thicker cloth is needled together using barbed needles so that it can be handled more easily. This is now known as felt and can be used in the production of the final cloth. It is a three-dimensional semi-random short fibre arrangement with a fibre volume fraction of around 5 %. The structure cannot be defined as truly random since the fibres do have a certain degree of alignment as a result of the carding process.

The felt is then combined with a layer consisting of unidirectional continuous fibre and these two layers are needled together. This two layer cloth is now ready to be carbonised and laid-up and is called Dunlop aligned mat (DAM). The cloth is

carbonised at a temperature between 1000 and 1500 °C and during this stage loses about 50 % by mass as a result of volatilisation of water, ammonia, hydrogen cyanide, carbon monoxide, nitrogen and methane.

To form the brake disc, the cloth is cut to shape, and laid up in a jig using mass as a measure of the final desired fibre density. The exact nature of the lay-up pattern is commercially sensitive, however the pattern does vary depending on the aircraft for which the disc is required. In all cases the cloth is laid parallel to the wear face. The cloth preform is then compressed in the jig, and placed into the CVI furnace. The carbonaceous matrix is then deposited by the cracking of methane gas by the CVI process. Often several time intervals in the CVI furnace are required to build up the required density. Finally the composite is heat treated to around 2500 °C to improve its properties.

This process produces a material with a bulk density in the range 1.75 to 1.95 g cm^{-3} and thermal conductivity between 55 and 75 $Wm^{-1}K^{-1}$. Both of these physical properties form part of the quality control criteria and failure to meet the lower limit results in rejection of the batch.

6.2. Optical microscopy

Optical microscopy is perhaps one of the simplest investigative techniques which may be used to elucidate the microstructure of carbon-carbon composites. The success of the technique is largely dependent on the selection and execution of an appropriate sample preparation regime. Therefore the preparation techniques used are described in some detail in the following section.

The use of reflected light microscopy can reveal many features such as fibres, matrix, pores and cracks, and can resolve features as small as about 1 μm. However the amount of information which can be gained can be hugely increased by examination between crossed polars. This is due to the birefringence of graphite, and allows assessment of the microstructure in terms of optical activity or optical texture. Birefringence describes the difference in refractive index between the ordinary and extraordinary light rays within a material[80]. This causes optical extinction in regions which are isotropic and hence optically inactive. The additional use of a sensitive tint (1λ) plate shifts the colour of extinction for black to red and also enables the distinction between similar bright regions depending on the orientation of the crystal

planes within these regions with respect to the optical axis of the system. These regions appear either yellow or blue as shown in Figure 24.

The use of a sensitive tint plate also allows discrimination between isotropic regions and porosity since isotropic regions appear monochromatic (red, yellow or blue) whereas porosity appears black as it reflects little or no light.

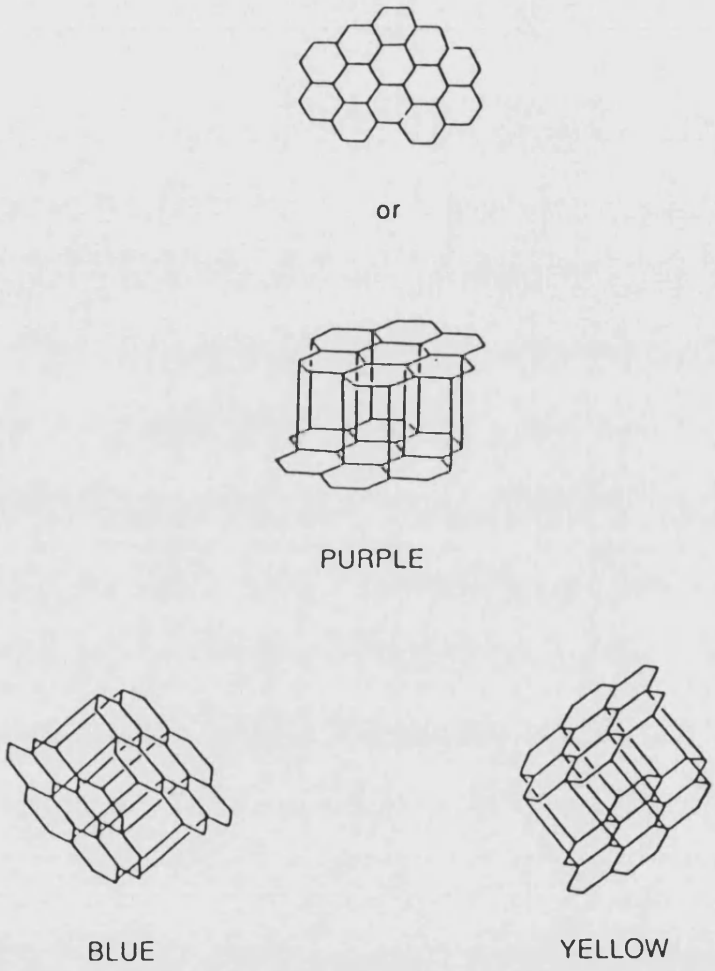

Figure 24. Interpretation of interference colours produced in optical microscopy[7].

If a monochromatic, optically active region, is rotated through 360 ° two positions of maximum and minimum light intensity are observed, which appear red. Between these positions the region appears either yellow or blue depending on the phase difference between the ordinary and extraordinary light rays[81]. Figure 25 shows the effect of using the optical techniques described here. The first image (a) is a bright-

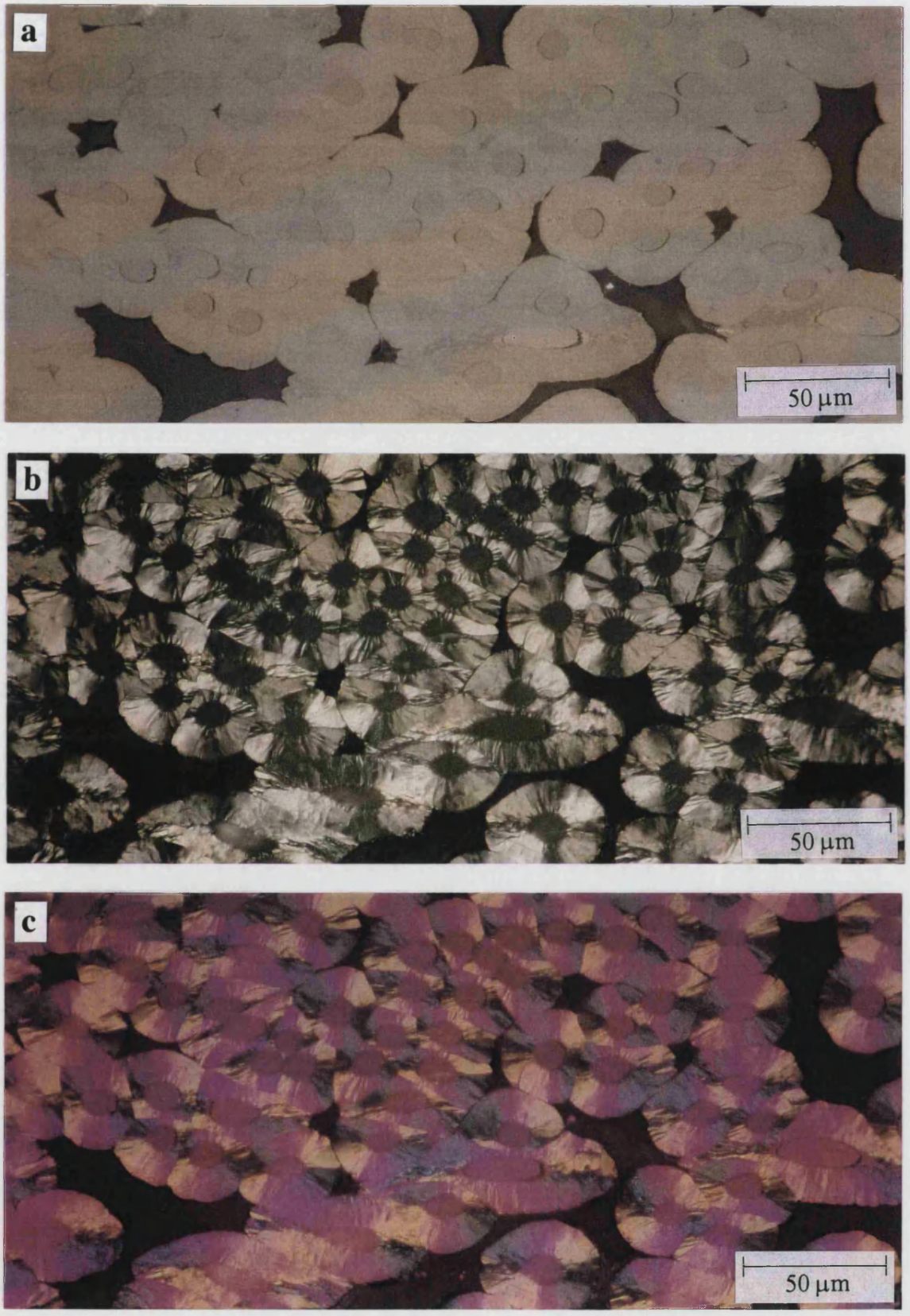

Figure 25. Three images of a carbon-carbon composite in a) bright-field, b) crossed polars, and c) crossed polars and a sensitive tint plate.

field image of a carbon-carbon composite. The second photograph (b) shows the same region but with the use of crossed polars, and the third (c) shows the effect of the additional use of a sensitive tint plate.

In some cases optical microscopy was combined with computer image analysis for quantitative interpretation of microstructures. The PC-based Optimas image analysis system was used for this purpose. Unfortunately the system was only capable of working with greyscale images and this meant that distinction between fibres and matrix was impossible. However, it was possible to measure porosity and to increase the contrast between carbon and the pores which were filled with the mounting resin, a fluorescing dye was added to the resin. When viewed using ultraviolet light, the carbon appeared relatively dark while the resin occupying pores fluoresced strongly and hence appeared bright.

6.2.1. Sample preparation

To gain the most information from optical microscopy there are three requirements of the preparation, that the sample be optically flat, scratch free and representative of the bulk structure. The last of these criteria is important since in achieving optical flatness, usually by grinding, it is easy to damage the sample and its microstructure, and hence be misinformed by the optical analysis. The successful preparation routine contained three steps; sample selection and coarse preparation, mounting, and polishing.

The first stage or coarse preparation, consisted of the selection of the specimen and the trimming of it to fit a standard mould in which it was to be mounted. This involved the use of various machinery such as abrasive cut-off wheels (Buehler Abrasimet 2 and Struers Exotom) and diamond saws (Tycet Tyslide) as well as more agricultural methods such as manual hacksawing. At all stages care was exercised to avoid the introduction of preparation artefacts such as cracks and impurities into the sample. The sample was then washed in an ultrasonic bath using acetone, and dried before mounting.

Mounting the sample is required so that delicate parts of its structure are not damaged during the subsequent polishing stages. Ideally the mounting media should fill all the porosity in the sample to provide support. The filling of porosity also makes polishing easier since pores can trap polishing media and cause scratches in the polished face.

To this end a cold setting, low viscosity resin was used. In preparation for mounting the sample was placed on its side (i.e. with the face which was to be polished in the vertical plane) in an open-topped mould and positioned inside a transparent vacuum chamber. The chamber was then evacuated to 10 kPa in order to draw out the air inside the open porosity. While the chamber was being evacuated the resin was prepared. The resin used was a two part epoxy (Strures Epothin) which was mixed in accordance with the manufacturers instructions. At this point the fluorescing dye (Struers Epodye) was added if it was required. The mounting resin was introduced to the mould via a tube fitted with a tap, which passed through a sealed port in the vacuum chamber. The resin was drawn up the tube by the action of atmospheric pressure on the resin reservoir. Once the sample was completely covered it was allowed to stand, still under vacuum, so that the resin could fully penetrate the pore network. During this phase the vacuum was carefully controlled to avoid boiling of the hardener in the resin. As the vacuum was reduced back to atmospheric pressure, so the resin was pushed further into the pore network. The mould was then removed from the chamber and the sample repositioned with the face of interest downwards. The mould was then placed in a pressure bomb and pressurised to 300 kPa and kept at 40 °C for 24 hours to cure the resin. By this method it was found that the resin fully penetrated the pore network to a depth of more than 5 mm into the sample. Once the resin had fully cured the sample was removed from the mould and prepared for polishing.

Polishing is required to produce a flat smooth surface for optical analysis. To achieve this a polishing routine was developed for use specifically with carbon-carbon composites. The details of this routine are given in Table 9. There are three stages in any polishing routine; planar grinding, sample integrity and polishing. The first stage involves turning a sample surface which is usually rough and uneven, into a flat surface. This is achieved by fairly coarse grinding using silicon carbide paper. Although this produces a flat surface it also usually causes damage to the sample. Indeed in the preparation of some materials the energies involved can induce structural changes in the sample. However the damaged region is thin and can be removed by slower and less severe grinding using much finer abrasive media. Ideally this stage should produce a surface which is completely free of optically visible scratches. At this point the sample is in a condition suitable for optical analysis. A further polishing

stage can be employed to improve the surface further and to produce some surface relief which is particularly useful if differential interference contrast (DIC) microscopy is to be used. However for the work presented in this thesis this final stage was frequently found to be unnecessary.

Polishing Stage	Surface	Abrasive Media	Load per Sample (lb)	Wheel Speed (rpm)	Head Rotation	Process Time (min)
Planar Grinding	Abrasive paper	P320 SiC + water	5	150	Compli-mentary	Until plane
Sample Integrity	5.2p Perforated Texmet	9 μm diamond in oil	5	240	Compli-mentary	4
	5.1 Texmet	0.05 μm α Al_2O_3 sol-gel seeded	10	100	Contra	6
Polishing	PS4 Chemo-met	0.05 μm colloidal SiO_2	2.5	100	Compli-mentary	3

Table 9. Polishing route used to prepare samples for optical microscopy.

6.2.2. Results

Figure 26 shows a low magnification micrograph of a section through the commercial material and some of the larger scale structures in the composite are visible. The most obvious of these is the laminated nature of the material. Near to the bottom of the picture is a layer of continuous fibre layer in which the fibre direction is close to parallel to the polished surface. Closer to the top of the picture is another layer of continuous fibre but in this case the fibre direction is closer to perpendicular to the polished surface of the sample. The fibres in this layer are shown in section and so they should appear round, however the magnification is not high enough to distinguish individual fibres. Between these layers is a typical layer of staple material. It is clear

from this micrograph that these staple layers contain an appreciable amount of porosity, which appears as dark areas, whereas the continuous fibre layers appear to contain very much less. Overall the composite appears purple with small patches of yellow and blue. These patches occur in the Maltese Cross pattern in each matrix sheath which surrounds every fibre. The fibres appear as a plain purple indicating that the structure does not have any distinct large scale order. Both of these features are shown more clearly at higher magnification as in Figure 27.

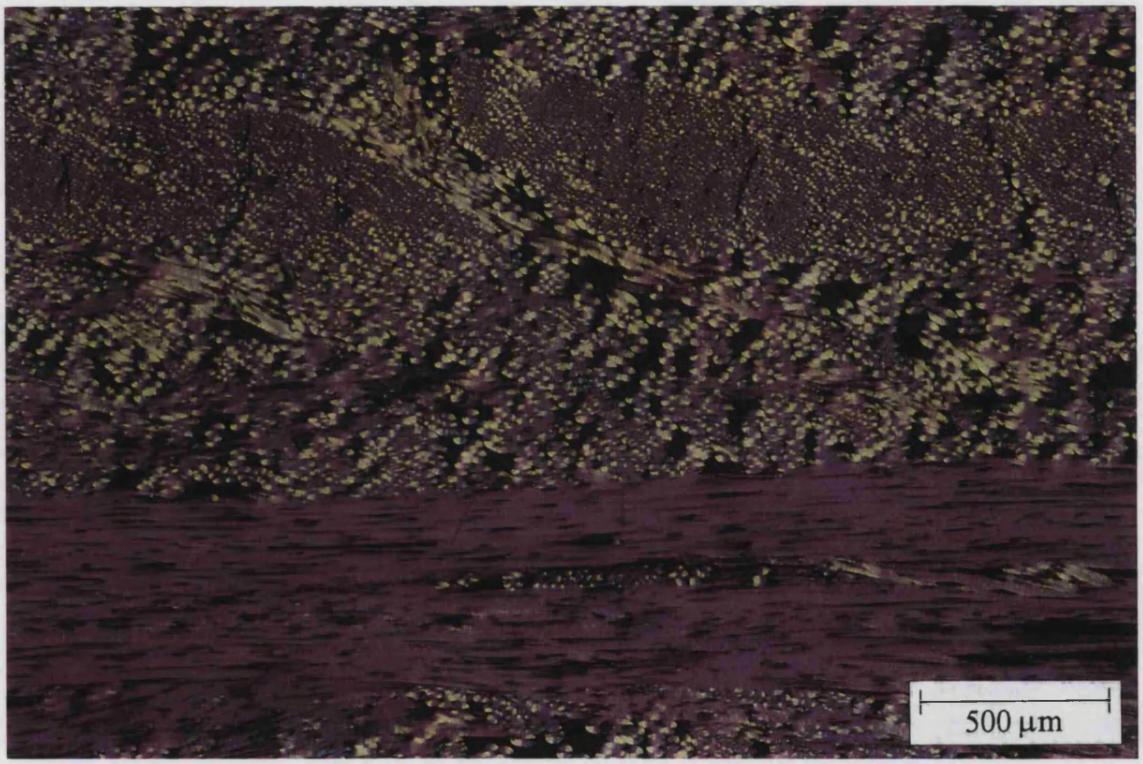

Figure 26. Low magnification optical micrograph of the commercial material.

The classic form of the Maltese Cross can be seen in the matrix material surrounding fibres in the staple fibre layer shown at the top of Figure 27. The three colours (purple, yellow and blue) can be seen and their occurrence indicates a high degree of order in the structure of the carbon in these regions. In fact the Maltese Cross pattern is present in the matrix carbon in the continuous fibre regions but due to the low thickness of the matrix in these region it is very difficult to see clearly. The reason that the matrix sheaths are so thin in these areas is that the fibres are closely packed together and hence there is little space in which the matrix can be deposited. Evidence for the close packing of continuous fibres is given in the bottom half of Figure 27.

The fibre in these layers is supplied in large tows which are spread out and laid together to form a sheet of parallel fibres. The low fibre density region and void running from the bottom right hand corner of Figure 27 is evidence that during laying up, adjacent tows do not always join together well. This creates a gap between the fibre tows which is often too wide for the matrix carbon to completely fill and a void is created.

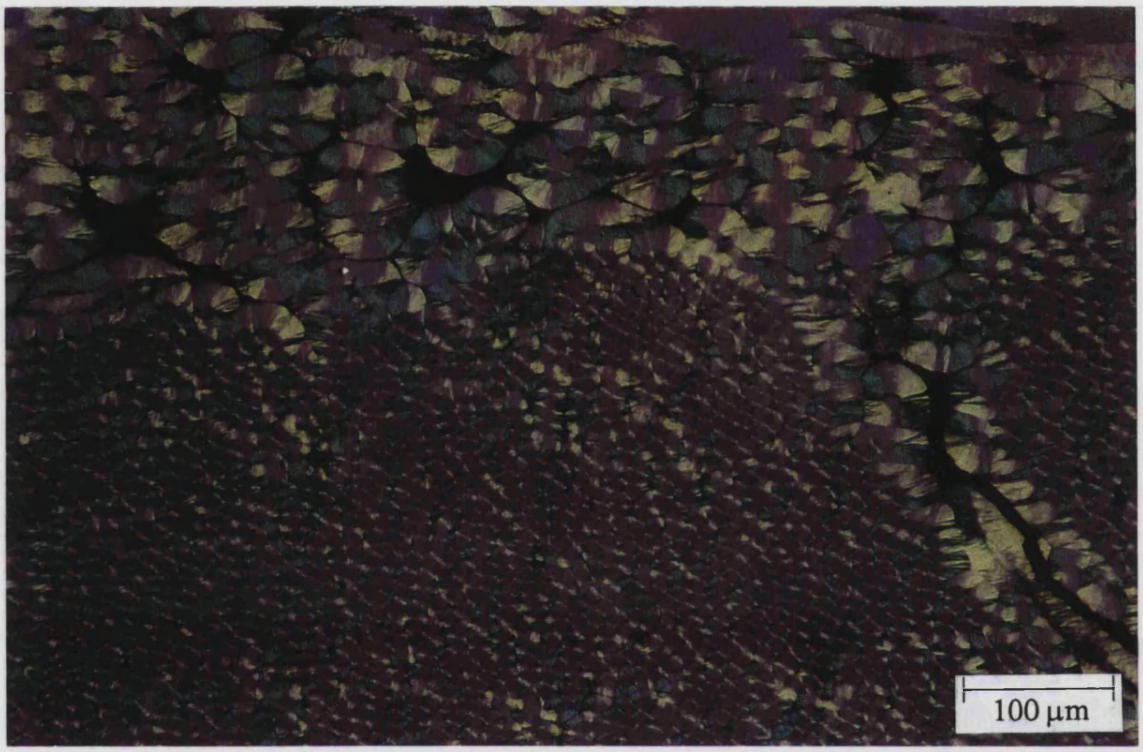

Figure 27. Photomicrograph of the commercial material showing the densely packed fibres in the continuous fibre layer at the bottom and the Maltese Cross pattern in the matrix of the staple fibre layer at the top.

The final major feature which was observed during the optical analysis of the commercial material was a stitch. An example of a typical stitch is shown in Figure 28. Here the stitch is shown in section and is close to the edge of the sample which is at the top of the figure. The micrograph clearly shows the gross disruption to the fibrous structure of the continuous fibre layer as a result of the stitching process and demonstrates the way stitches form a mechanical link between adjacent cloth layers. In this case it can also be deduced that the stitching has dragged fibres from the staple

layer below into and through the continuous fibre layer above implying that the needle passed through the cloths in an upwards direction.

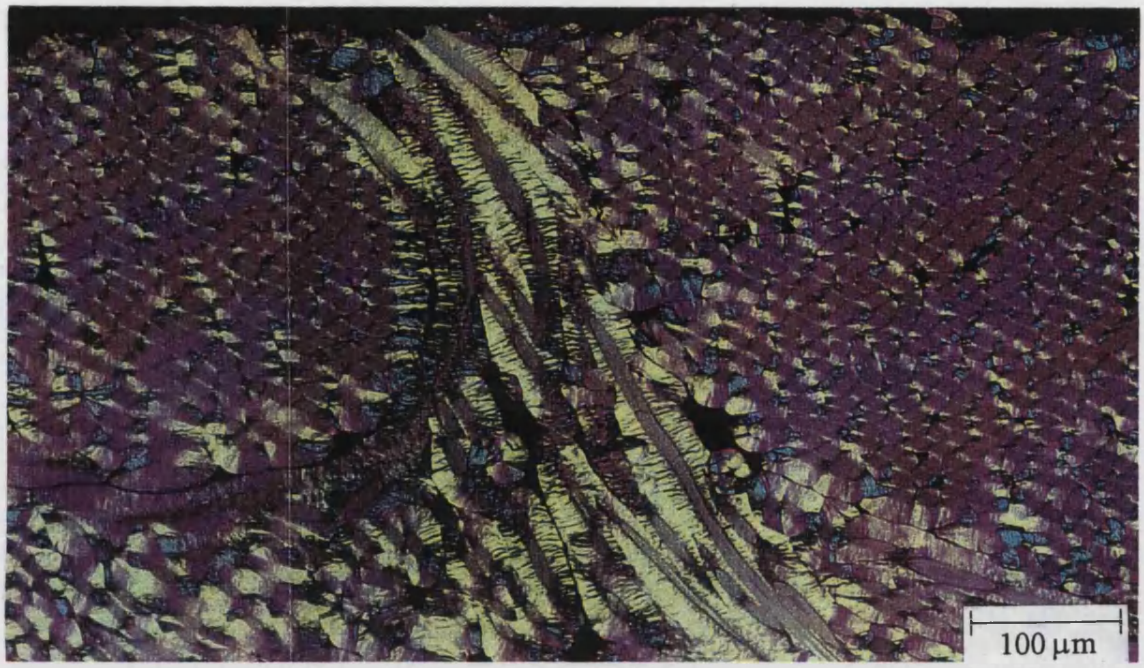

Figure 28. Typical stitch in the commercial material shown in section.

6.3. Scanning electron microscopy

Scanning electron microscopy (SEM) is another useful analytical tool which is in widespread use. The theory of electron microscopy and associated techniques can be extremely involved although there are a number of instructive texts to which the reader is directed[82,83,84,85,86]. The operation of the SEM is analogous to that of an optical microscope with the exception that a beam of electrons replaces the beam of light. This allows the resolution of much smaller features and consequently the use of much higher magnifications. The disadvantage of using electrons is that the sample must be electrically conductive. If it is not the sample becomes charged as a result of the incident electron beam and the image is distorted. Conductivity is usually achieved by the addition of a thin coating of gold which is sputtered onto the surface of the sample. However carbon-carbon composites are naturally electrically conductive and therefore a coating is not required. The sample must also be non-volatile since the SEM operates under vacuum.

That the samples need not be coated so that they are electrically conductive greatly simplifies sample preparation. Basically the only restriction is on the sample size

which can be examined as it must be small enough to physically fit in the vacuum chamber of the SEM. Rough and uneven surfaces can also be examined very easily in the SEM which is particularly useful when investigating the morphology of fracture surfaces. The only problems arise when investigating unsupported, high aspect ratio (i.e. long and thin) pieces of material such as individual fibres. These can tend to oscillate while under the operating conditions of the SEM causing blur on the image produced.

Mounting was not necessary unless the sample was to be polished in which cases the routine detailed in Section 6.2.1. was used. The sample was attached to the microscope stage using adhesive pads or putty and then earthed to the stage using conductive paint or putty. Examination was carried out using two microscopes, a JEOL T-330 and a JEOL 6310. The second of these was fitted with equipment for elemental determination by energy dispersive analysis of x-rays (EDAX) which allowed the detection of impurities in the carbon-carbon composite materials.

6.3.1. Results

It was found that while electron microscopy was a simple analytical technique which revealed some interesting features of the composite, it did pose some unexpected problems associated with the specimen preparation. SEM is a surface topographical technique, i.e. it detects and visualises surface roughness and three dimensional features. Therefore the SEM analysis of samples which had been polished in preparation for optical microscopy and were hence flat, revealed very little about the structure. Indeed the only features which were easily distinguishable were the regions of resin which filled the pores in the composite during mounting. By contrast the analysis of surfaces of the material prepared by milling showed very few features at all and the structure of the composite was indistinct. The reason for this was that a film of carbonaceous material had been formed over the surface of the sample during milling. This is a well known effect generally associated with sliding wear conditions and produces a flat, smooth surface which obscures the structure of the underlying material. It was found that this film could be removed and the structure of the composite underneath revealed by chemical etching using chromic acid. A sample of the commercial material was exposed to concentrated chromic acid for several minutes

before being thoroughly washed and dried. This sample was then loaded into the SEM and analysed.

The structure of the material was shown most clearly in staple fibre layers although the microstructural features could be seen to some extent in all regions. Figure 29 shows a single fibre in its sheath of matrix. The fibre shown here exhibits a rather atypical structure in that the top half appears to contain fine texture, while the bottom half, separated from the top by a horizontal groove, has an indeterminate structure. In most cases the fibres showed little structure but if any they tended to resemble the top half of the fibre shown here. This suggests that the fibres have little or no long range order and that as a result the crystallites within them are very small. This figure shows very clearly that the matrix has a concentric lamella structure indicating that it has been deposited in layers which are wrapped around the fibres. This evidence of long range order in the matrix agrees well with that from optical microscopy.

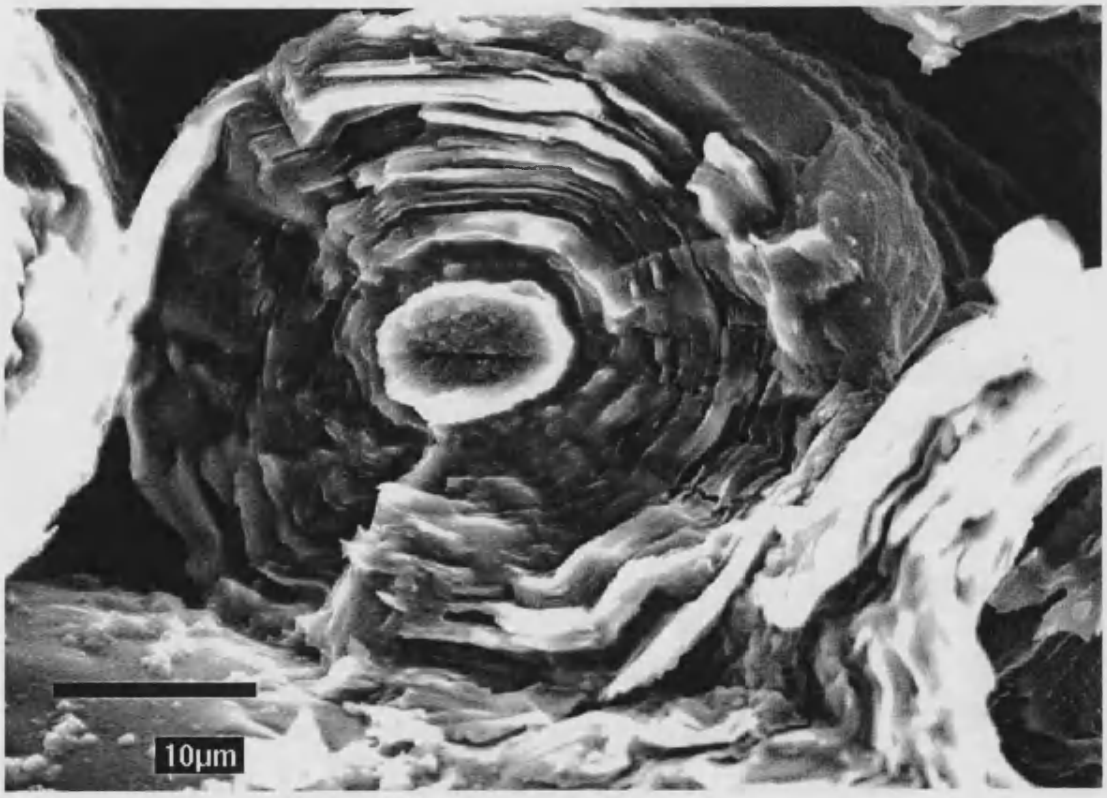

Figure 29. SEM image of a fibre and matrix sheath after etching with chromic acid showing the concentric lamella structure of the matrix.

6.4. X-ray diffraction

X-ray diffraction (XRD) is another analytical tool which can reveal useful information about the atomic structure of a material. It is widely used in the investigation of crystalline solids, and can be used to reveal information about diverse areas such as chemical composition and stress distribution. There have been many books which describe in detail the use of x-ray diffraction and the interpretation of the results[87,88,89]. The figures which are usually quoted from x-ray diffraction experiments are $d_{(002)}$ (interlayer spacing), L_c (stack height) and L_a (stack width). These values can be calculated using the equations below.

$$d_{(002)} = \frac{\lambda}{2\sin\theta_{(002)}} \qquad \textit{Equation 22}$$

$$L_a = \frac{1.84\lambda}{2\beta_{(10)}\cos\theta_{(10)}} \qquad \textit{Equation 23}$$

$$L_c = \frac{0.9\lambda}{2\beta_{(002)}\cos\theta_{(002)}} \qquad \textit{Equation 24}$$

Where :

λ	=	Incident x-ray wavelength (Å)
$\beta_{(10)}$	=	Half height width of the (10) peak (radians)
$\beta_{(002)}$	=	Half height width of the (002) peak (radians)
$\theta_{(10)}$	=	The Bragg angle for the (10) peak (°)
$\theta_{(002)}$	=	The Bragg angle for the (002) peak (°)

X-ray diffraction was carried out using a Phillips PW1710 x-ray diffractometer which could use both powdered and bulk samples.

6.4.1. Results

Figure 30 shows the x-ray diffraction pattern for a sample taken from a new Dunlop brake disc. The graph shows plots of the total counts as a function of double the diffraction angle on both linear and logarithmic scales. It is immediately apparent that the logarithmic plot shows more detail, however the linear plot is useful for highlighting the unmistakable intensity of the diffraction peaks.

The (002) peak dominates the graph and occurs at $2\theta \approx 27°$. On the left side of this peak a much smaller peak can be seen ($2\theta \approx 24°$). This is also from the (002) planes and is hence always associated with the main (002) peak. These two peaks result from the fact that the x-ray source used is not strictly monochromatic. Sometimes main peaks can be seen to split into two and this is caused by a doublet in the primary source wavelength ($K_{\alpha 1}$ and $K_{\alpha 2}$). However in this case the second peak arises from the unfiltered presence of K_β. It is however very unusual to be able to see the smaller of the two peaks as it is normally swamped by the larger (as the ratio of K_α to K_β is 600:1).

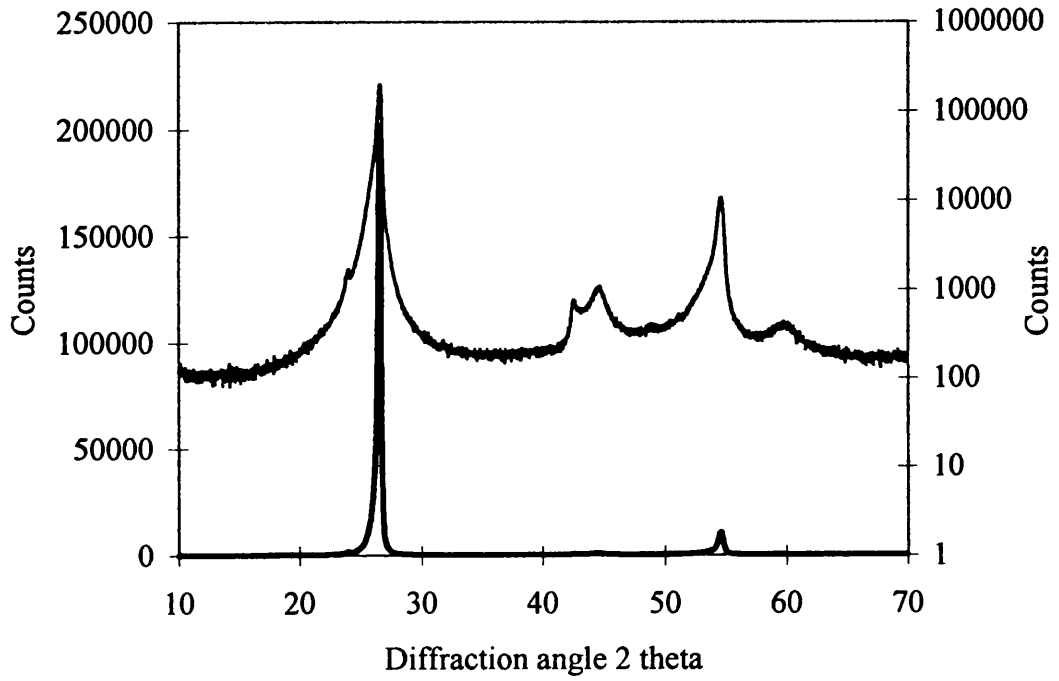

Figure 30. X-ray diffraction pattern for a sample taken from a new Dunlop brake disc.

Further peaks are visible at $2\theta \approx 43°$, 45 ° and 54 ° and these correspond to reflections from (100), (101) and (004) planes respectively. The ratio of the peaks to the background noise (which is shown more clearly on the logarithmic scale) gives an indication of the crystallinity of the sample, and it can be seen that the disc material is quite crystalline. This confirms the findings from the optical microscopy which showed that the material was optically active.

X-ray diffraction curves have also been plotted for the component parts of the disc material, i.e. heat-treated PAN based carbon fibres and CVI carbon from the matrix[9]. These are shown in Figure 31 and Figure 32. These plots show that the CVI has a highly graphitic structure, more than the composite and that the fibres are more amorphous. This is shown by the lower and broader peaks in the fibre XRD trace. These findings are in good agreement with those of the optical microscopy. Mathematical analysis of these traces only served to further confirm that the CVI carbon was highly crystalline, the fibres consisted of very small crystallites and hence appeared pseudo-amorphous, and the composite material was a mixture of these two.

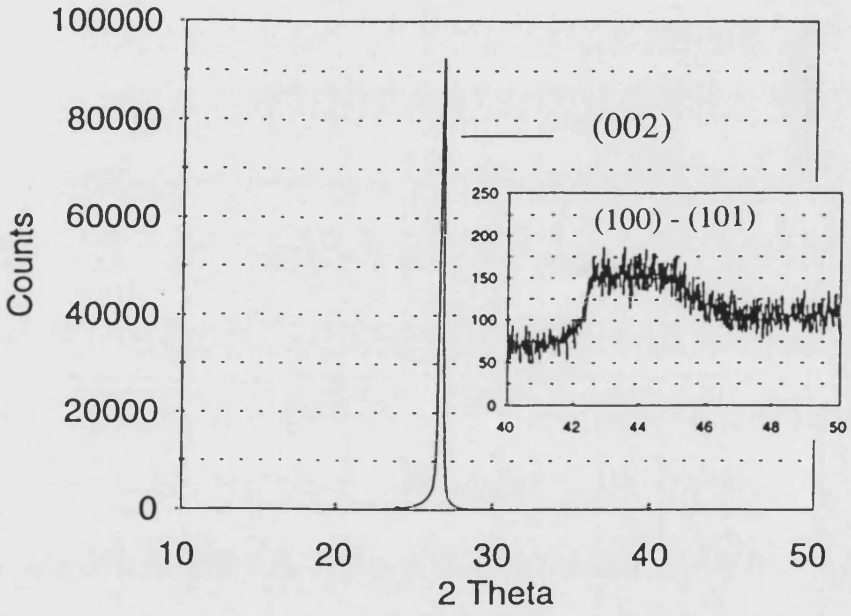

Figure 31. X-ray diffraction pattern for graphitised CVI carbon[9].

Material	$d_{(002)}$ / (Å)	L_a / (Å)	L_c / (Å)
Composite	3.38	208	247
CVI carbon	3.37	300	330
PAN fibres	3.42	75	6

Table 10. Results of analysis of x-ray diffraction traces (*after Hutton*[9]).

The results of the analysis are shown in Table 10. One interesting point of note from this analysis is the value of L_c for the fibres. This is approximately 6 Å and the interlayer spacing ($d_{(002)}$) is 3.42 Å. This means that the crystallites consist of only two or three graphene planes, and this explains why the fibres appear amorphous when examined by optical microscopy.

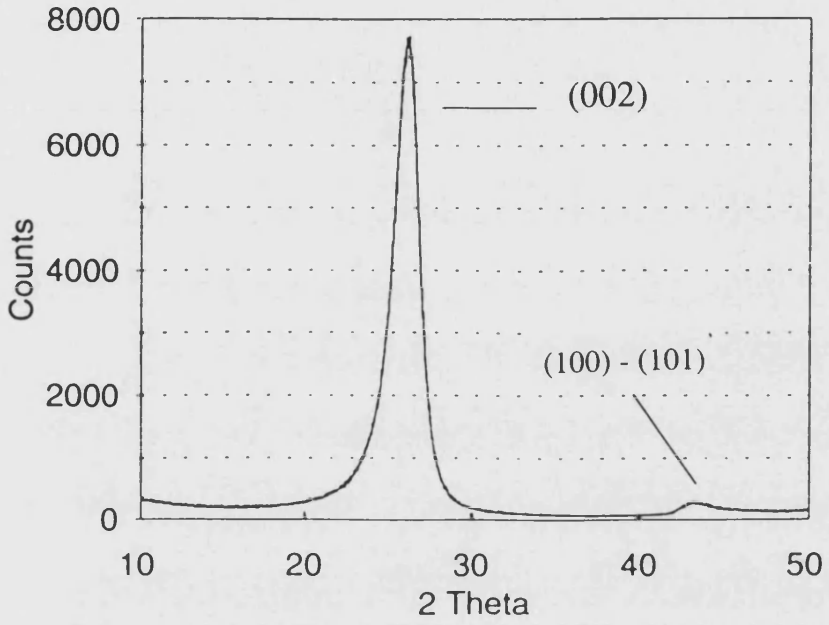

Figure 32. X-ray diffraction pattern for heat-treated PAN based carbon fibres[9].

6.5. Thermogravimetric analysis

Thermogravimetric analysis (TGA) is a method by which reaction kinetics can be determined. The technique consists of heating a sample at a constant rate and monitoring its mass as the reaction proceeds. This was carried out as part of a previous project on the Dunlop disc material[9] and the results are reproduced here for the sake of completeness. Also the results give some useful insights into the kinetics of the oxidation reaction of the Dunlop material.

6.5.1. Results

TGA traces were produced for the Dunlop carbon-carbon composite brake material and its component parts. The testing was conducted using a SETARAM TG-92 thermogravimetric analyser. Samples were heated in air at 10 °C per minute to about

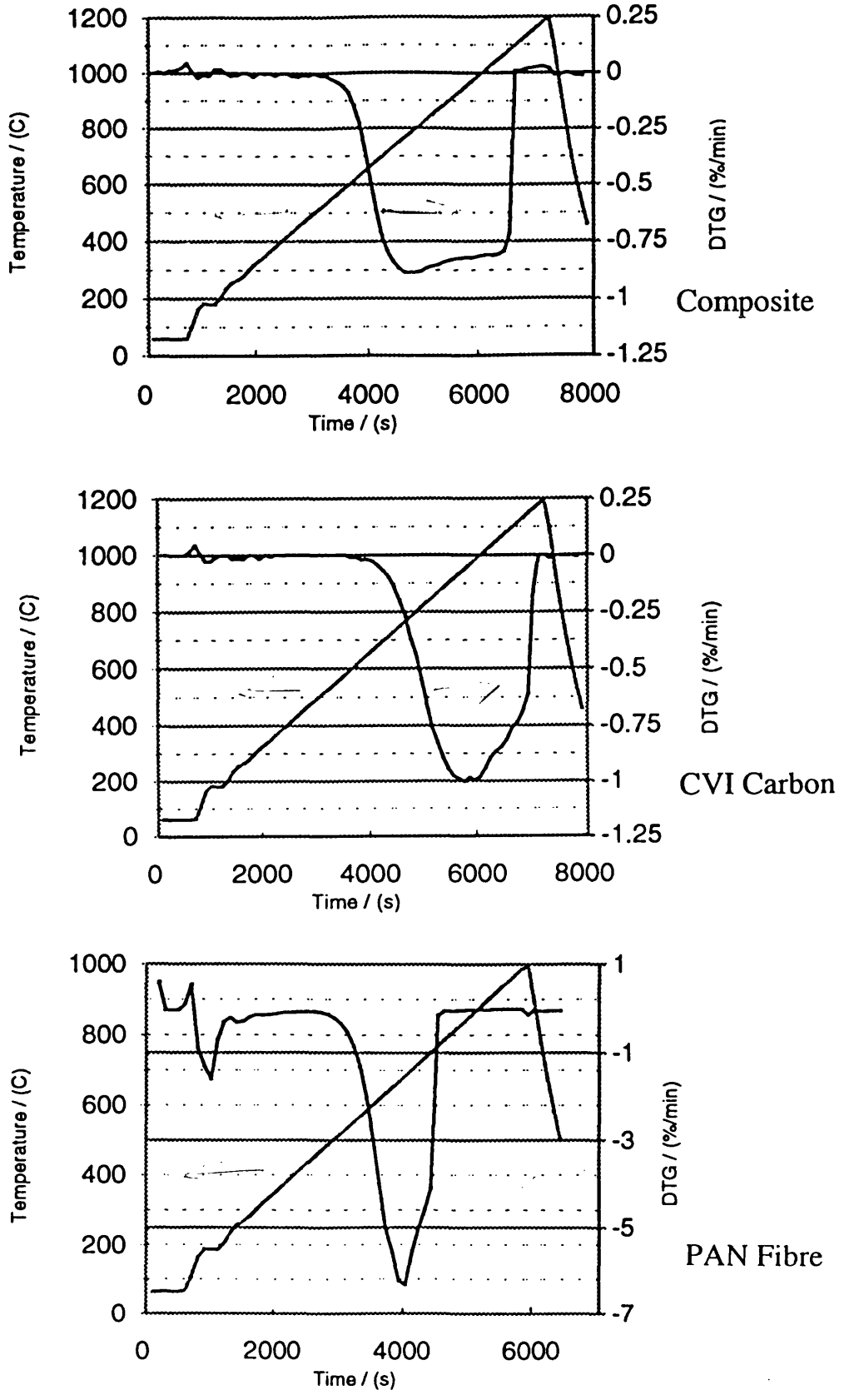

Figure 33. TGA traces for the Dunlop composite and its component parts[9].

1100 °C. The results are shown in Table 11 and Figure 33. It is clear that, as with the XRD data, the TGA shows that the properties of the composite are a combination of those of the fibres and the CVI carbon. Also the temperatures of onset and peak rate of oxidation are lower for the fibres than the matrix. This implies that at a given temperature the rate of oxidation of the fibre is higher than that of the matrix, i.e. it would be expected that the fibre would be oxidised preferentially.

Material	Temperature of oxidation onset / (°C)	Temperature of peak oxidation rate / (°C)
Dunlop composite	540	800
CVI carbon	611	1067
PAN fibres	510	770

Table 11. Results of TGA on sample of Dunlop composite material and its component parts (*after Hutton*[9]).

7. COMPRESSIVE TESTING OF COMMERCIAL MATERIAL

7.1. Introduction

The main thrust of this work was to discover what mechanisms occurred during the life of a carbon-carbon composite brake disc which could cause the mechanical properties of the material to be reduced. An obvious starting point for the work was to examine and compare the structure and properties of new and old discs and identify the differences between them. However there are a number of problems with this approach. Firstly it is impossible to assess the "age" of a disc without destroying it. In this case the term "age" is used to represent how far along the time-line between first application and failure the disc is. Commonly the age of a disc is expressed as the number of landing cycles which it has achieved. However two nominally identical discs may have potential service lives of 1000 and 10000 landing cycles. If they are both tested when they have achieved 900 landing cycles the first is very close to the end of its life whereas the second is almost new. This makes the comparison of the properties of discs where only the landing cycle count is known somewhat meaningless. However discs which have achieved 5000 landing cycles are likely, but not certain, to be "older" than discs which have achieved 1000 landing cycles. Also the assessment of the properties and structure of failed discs (i.e. those at the end of their life) is fraught with difficulties. Failure of an aircraft brake disc is generally catastrophic in terms of the individual disc involved. There is gross damage to much of the disc as a result of the large amount of energy concerned with the failure process. Indeed much of the material at the inner and outer circumferences of the disc is ground to dust and lost to atmosphere. Sadly these parts are often those of most interest. The part of the disc which remains intact is also frequently damaged and this can obviously affect the results of mechanical testing since pre-existing damage will reduce the strength of a sample. Microstructural analysis of test samples made from failed discs prior to test can reveal the extent of the damage although one can never be certain that the sample which is under examination is representative of the sample group. Clearly it is impossible to assess damage within the sample without destroying it.

Second is the problem of selecting a mechanical test method which is appropriate to the material under investigation. A first glance it would seem that most test methods

would be adequate, however all have positive and negative features. The design of an appropriate test method forms another large part of this project. Aside from the practical difficulties of performing the test is the problem of insuring that the test is sensitive enough to detect small changes in the mechanical properties. For example, if it was found that the disc failed by delamination as a result of weakening of the interlaminar bonding, then a test sensitive to this property is appropriate, i.e. an interlaminar shear test.

Finally, there is the difficulty of finding ex-service material which shows a deterioration of its mechanical properties. The problem of strength loss during service life is reasonably uncommon and the discs which do exhibit strength loss tend to fail before they are removed from the aircraft and can be tested. Therefore the supply of returned discs which, when tested, show strength loss is unreliable at best.

7.2. Compressive testing

Tensile testing of materials has inherent difficulties associated with gripping the specimen and consequent failure outside the gauge length and so was rejected as an initial test method. Shear testing can be conducted in a number of ways; compressive loading of notched specimens, short span three point bending and double punch shear, but it was felt that all of these methods were over elaborate for the purposes of the initial investigations. Of the available test methods compressive testing was immediately attractive due to its practical simplicity and the plain shape of the samples required. The rectilinear shape of the sample was important since all of the samples used were machined by hand and simple shapes can be machined more easily and reliably. Also the test rig required was simple, readily available and easy to use.

7.2.1. Test method

Testing was carried out using the guidelines set out in the standard DD ENV 658-2[90]. Strictly, this standard applies only to testing of ceramic matrix composites with continuous fibre reinforcement, however it was the most relevant of the available standards and was hence used as a guide.

The test method consists of loading a low aspect ratio, rectilinear sample between flat and parallel platens while recording the applied load and the displacement of the platens relative to each other. The sample dimensions are chosen to avoid the possibility of buckling of the sample and the recommended aspect ratio is between 2:1

and 2.5:1. Also it is suggested that the thickness of the sample be a whole number of plies and that the selected plies should be representative of the bulk structure of the composite. These criteria and the thickness of the commercial material which was available dictated fairly exactly the sample size.

Tests were conducted using an Instron 1195 testing machine fitted with a load versus time chart recorder. Since the crosshead of the machine is under displacement control and hence moves at constant speed, this chart can be easily converted into a stress versus strain plot. The sample was loaded between two steel platens which were assessed for parallelism and found to be parallel to within 0.02 mm at their outer edges. The platens were circular with a diameter of approximately 50 mm which meant that the parallelism of the platens over the contact area was within tolerances (0.01 mm). The crosshead speed was selected so that the test was completed within 1 minute as recommended. A 100 kN load cell was used and the crosshead speed was 0.5 mm per minute.

7.2.2. Material selection

Discs with a variety of service histories were selected for testing ranging from new to over 5000 landing cycles. All the discs were stators from Boeing 757 aircraft and all had nominally the same structure. In two cases samples were taken from more than one disc from the same heatpack (the term heatpack being used to describe the stack of discs attached to the same wheel) were tested in order to assess the strength variation between discs which had nominally experienced the same conditions during their service lives. The origin of each of the sample groups is shown in Table 12.

As can be seen the discs ranged from new to over 5000 landing cycles old, however the failed disc which must be at the end of its service life, has experienced only 3758 landing cycles. Therefore there is some debate as to which of these two sample groups is "older".

7.2.3. Specimen preparation

The dimensions of the specimen were chosen so as to conform to the standards, and the actual dimensions are given in Table 13. In this case the thickness (h) is taken as the dimension across the composite plies, and the length (l) and width (b) are taken in the plane of the plies. This is shown schematically in Figure 34.

Sample Group	Disc Number	Service History
A	E081852S	As received
B	E062816S	Approx. 2000 landings
C	E050749S	5042 landings
D	Failed #1	3758 landings (tenon failure)
E	E050450S	5042 landings
F	Failed #2	3758 landings (tenon failure)

Table 12. Origin of the sample groups used in the compressive testing programme.

	Dimension / (mm)
Length (l)	20.00
Mean thickness (h)	10.00
Mean width (b)	10.00

Table 13. Nominal dimensions of the compressive test specimens.

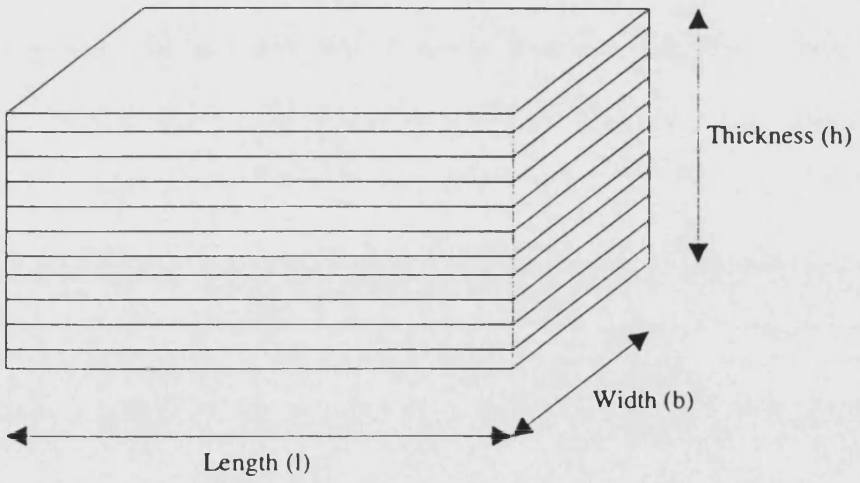

Figure 34. Schematic diagram of compressive test specimen.

The maximum thickness of the specimen was limited by the thickness of the worn, ex-service discs and so 10 mm was as large as was practically possible. Obviously the larger the specimen the more of the material which is sampled and so the results are more representative of the bulk. The square section and aspect ratio criteria then dictated the other dimensions of the specimens. The sample dimensions used allowed the samples to include approximately 10 cloth plies.

The discs were cut into blocks using a combination of saws and cut-off wheels and the individual samples were marked out on the surface. At this point each specimen was given a unique identifier so that not only could it be traced to a specific disc, but also its spatial origin within the disc was known. Each of these large blocks was milled using a tungsten carbide tool to a thickness of 10 mm in such a way that the resultant material was symmetrical about the centre line of the disc. This eliminated a further possible source of variation. The blocks were cut up into oversize samples and milled to the final shape. Care was taken to cause as little damage to the specimens as possible during the machining process. This was achieved by milling ever smaller amounts from the surface as the final dimension was approached.

The specimens were then weighed, measured and tested for parallelism and perpendicularity. The width and thickness of the samples which were used for calculations were the arithmetic means of measurements taken at the middle and each end of each sample.

The density of each sample was simply calculated using Equation 25, and the strength of the specimens were calculated using Equation 26.

$$\rho = \frac{m}{b \times h \times l} \qquad \textit{Equation 25}$$

$$\sigma = \frac{W}{b \times h} \qquad \textit{Equation 26}$$

Where : ρ = density

m = mass

σ = compressive strength

W = peak compressive load

7.3. Mechanical results

7.3.1. Relationship between strength and density

Obviously there should be a relationship between the density and the strength of the material. Changes of density from sample to sample are caused by variations in the percentage content of the three constituents of the material, namely CVI carbon, fibre derived carbon and porosity. The densities of the two types of carbon are similar and so the system is effectively two phase, carbon and porosity. Hence density is directly related to porosity. There should therefore be an inverse relationship between porosity content and strength. However, as was discussed earlier, it is not just the volume of the porosity which is of significance but also its size, shape and position. There are two different populations of porosity in the material, that arising from manufacture and that arising as a result of service. New material will only contain porosity from the former source whereas ex-service material will contain a mixture of both. Hence when plotting density versus strength it is important that the data from new and ex-service material be considered as coming from distinct populations.

Figure 35 shows the relationship between density and strength for the commercial material tested in compression in both the new and ex-service conditions. If the results are considered as a whole it is clear that there is a positive relationship between density and strength as expected, although there is an appreciable amount of scatter. There would seem to be little difference between the new and ex-service material except for the fact that the new material tends to be of higher density, and hence higher strength.

Separating the two sets of data and adding linear best fit lines to them highlights an important difference. The slope of the best fit line for new material is significantly shallower than that for ex-service material. This implies that a low density is more deleterious if it occurs as a result of service induced porosity, than if it is a result of manufacture. In other words the effects on compression strength are different for the two types of porosity, which confirms the presence of two distinct populations of porosity. Conveniently this fits the expected model for the behaviour of the material, however the evidence is far from conclusive. This point is emphasised by the R^2 values for the two lines which are approximately 0.5 and 0.2.

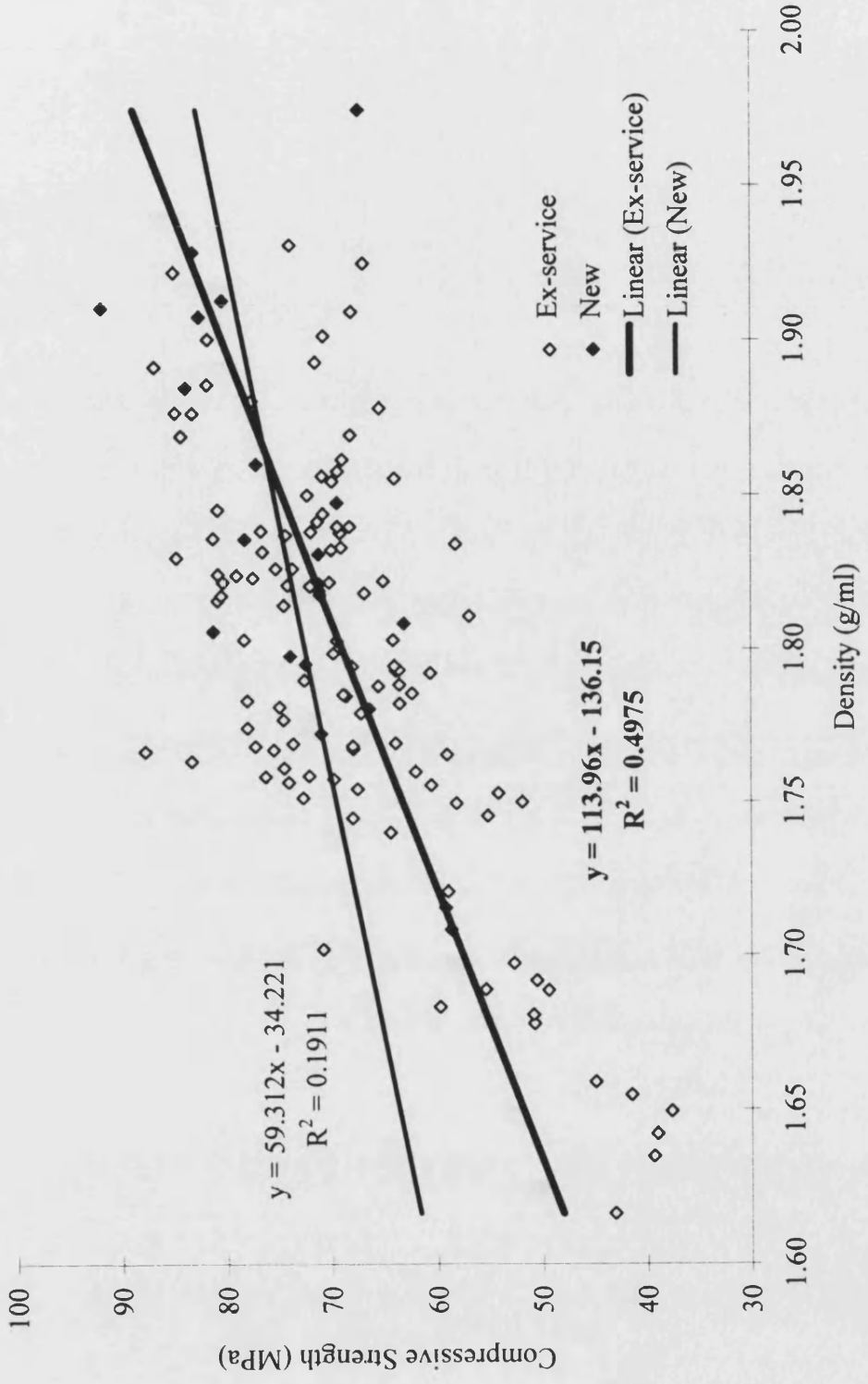

Figure 35. Graph showing the correlation between density and strength for the commercial material.

7.3.2. Relationship between strength and position in disc

It was deemed important to determine whether the effects of service on the strength and density of the commercial disc material were uniform throughout the disc or whether there were spatial effects. By using unique identifiers for each sample and recording its original position in the disc it was possible to investigate correlations between these two variables. Theoretically the density of a new disc is completely uniform, and indeed the fibre density is strictly controlled so that its distribution is uniform. However CVI carbon is known to be deposited preferentially at the free surface of the disc during manufacture. Because of the way in which the discs are stacked during CVI the free surfaces are the inside and outside circumferences. Hence the density of the resulting material does tend to be slightly higher in these regions. To try to avoid unacceptable variation, the discs are made oversize, and the edges machined away during the finishing process. Therefore the expected trend is for the density to be fairly uniform with slight increases at the inside and outside circumferences possible.

When the results were plotted as three-dimensional bar graphs some interesting trends became apparent. An example of the bar graphs is shown in Figure 36. Firstly the density and compressive strength of all the sample groups showed no consistent trends with regard to the position of the sample around the disc. This is hardly surprising since the discs are rotationally symmetrical and hence it would be expected the any trends would be also be rotationally symmetrical.

Since the samples for each group were cut out in arrays four samples wide, each group could be interpreted as having four subgroups from four distances from the inside circumference. This assumption allows the calculation of mean strength and densities to be calculated for each subgroup and hence the data to be plotted on conventional two-dimensional graphs.

The plots of density versus position are shown in Figure 37. It is clear that for all sample groups excluding those which were from discs which had failed (D and F) the density is fairly constant with a slight rise at the outside circumference. This is as expected. The reason that there is no observed increase in density at the inner circumference is that the position of the samples from the inner circumference is actually much further from the preformed inner circumference than the comparable case at the outside. The discs are manufactured in the form of a ring of material and

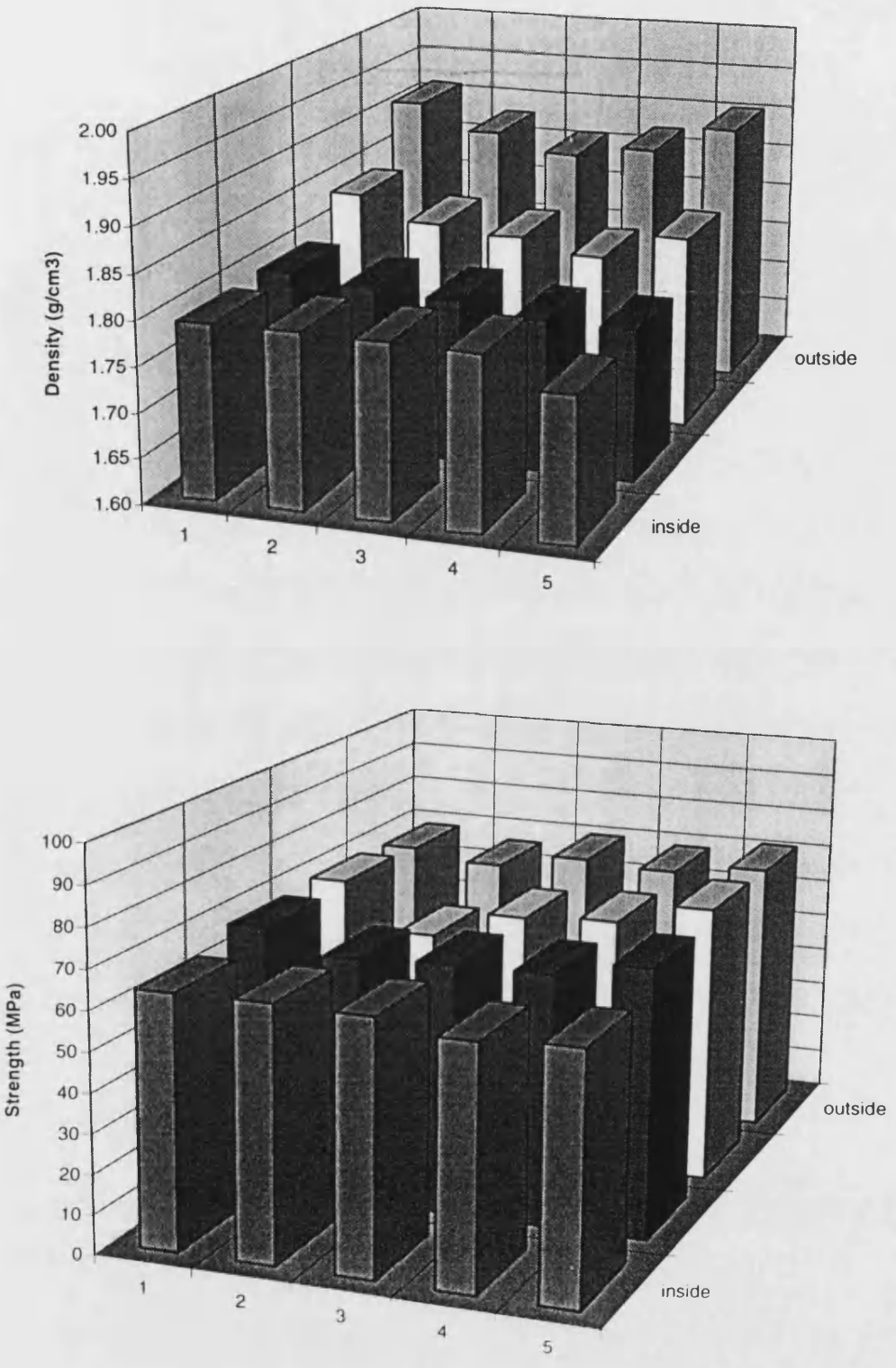

Figure 36. Charts showing density (top) and compressive strength (bottom) as a function of the spatial origin of the sample for sample group B.

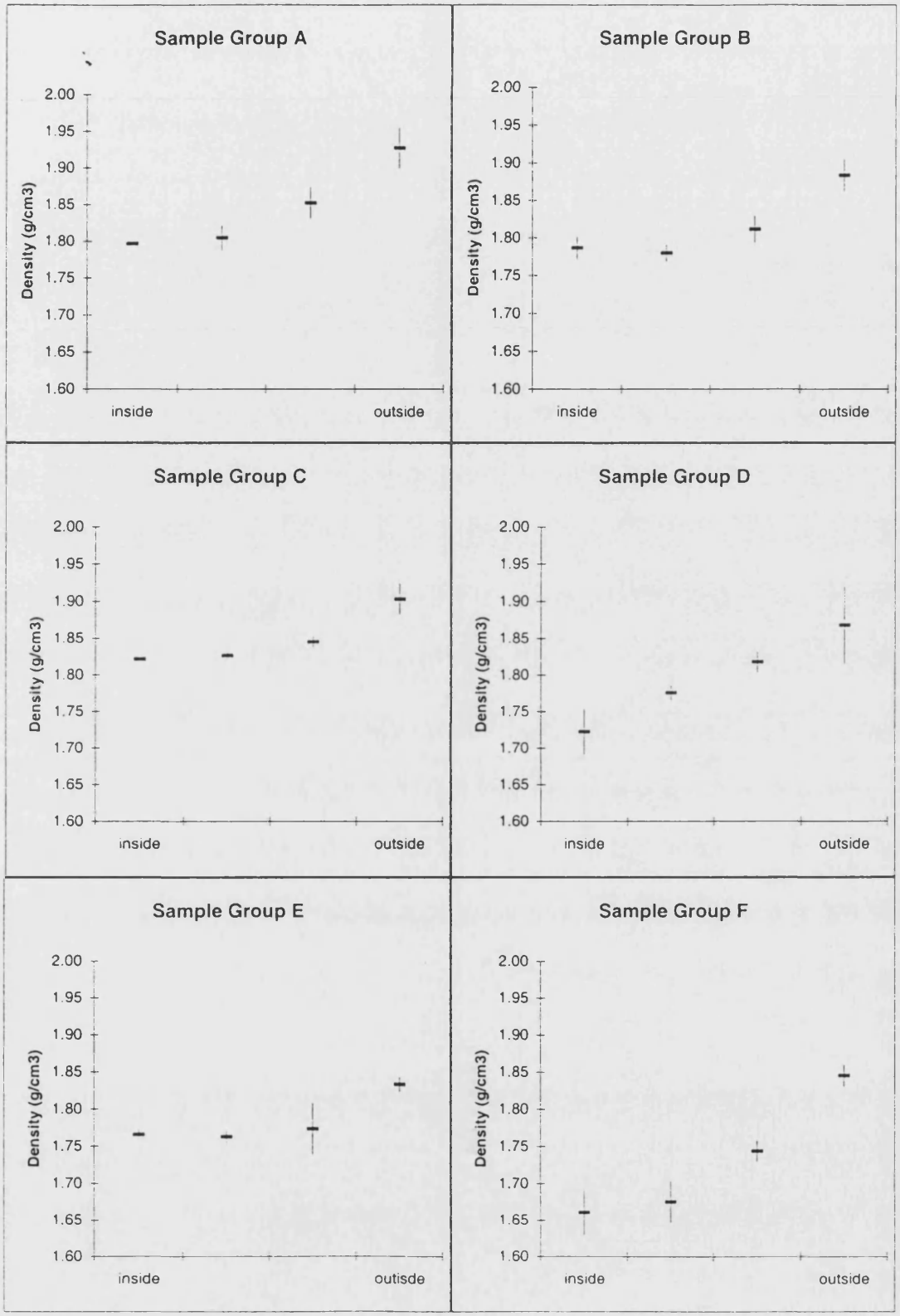

Figure 37. Density versus position for all six sample groups shown as a mean value for each position (error bars represent ± one standard deviation).

are subsequently machined to produce the friction surfaces, tenons and other features. It is the edges of this ring which are of increased density. Samples could only be cut from the swept area which is close to the outer edge but some distance from the inner edge. Hence while much of the high density material at the outside edge survives machining, nearly all of that at the inner edge is lost.

In the two groups of samples from failed discs (D and F) a decrease in density can be seen at the inner circumference. Importantly it is in this region that failure of the disc occurs. It could be that the material becomes less dense in this region during the life of the disc and since low density means low strength, the disc fails. However there is no evidence of this effect in the other ex-service discs. Alternatively, the process of failure could cause gross damage to the material causing cracking which would reduce the density. So it is impossible to conclude from this evidence whether the low density at the inside edge of failed discs is the cause or an artefact of failure.

7.3.3. Variation of strength and density with material age

The difficulty of assessing the "age" of ex-service material has already been discussed in some detail, however the number of landing cycles is the only logical measure which can be used. Therefore new material is assumed to be the "youngest" and failed material the "oldest" with non-failed material being graded in between according to the number of landing cycles achieved.

To estimate to effect of age on density and compression strength, mean values for these characteristics were calculated for each sample group. A summary of the results is given in Table 14. Examining the data in this table does not give any clear indication about the effect of age on density and compressive strength. However when the data are plotted in graphical form it is possible to identify broad trends.

The graphs (Figure 38) show a broad downward trend in both strength and density with increasing age although the evidence for this is somewhat tenuous. The ages of the two discs from the same heatpack have been adjusted so that the error bars, which represent one standard deviation, can be separated. Linear best fits to these data do show inverse relationships although the gradient of the lines are very shallow, however this is partly due to the large scale of the x-axis. The values of R^2 for the best fit lines show that they are poor fits to the data, $R^2 = 0.51$ for the density data and $R^2 = 0.13$ for the strength data.

Sample group	"Age"	Group size	Density / gcm^{-3}	Compressive strength / MPa
A	New	16	1.86 ± 0.06	75.90 ± 7.76
B	≈ 2000 l	20	1.82 ± 0.04	65.47 ± 3.62
C	5042 l	24	1.85 ± 0.03	74.71 ± 4.56
D	Failed	24	1.80 ± 0.06	74.18 ± 10.54
E	5042 l	24	1.78 ± 0.03	71.61 ± 6.28
F	Failed	24	1.73 ± 0.08	55.08 ± 10.32

Table 14. Summary of results of compression testing (values given are mean ± one standard deviation).

7.3.4. Variation of strength and density between nominally identical discs

It was mentioned earlier that assessing the "age" of ex-service material is impossible because the total life of a given disc is unknown until it fails. This creates great difficulty in quantifying the effect of age on the physical properties of the material. There is also the consideration that two discs from the same heatpack, and hence subject to the same service conditions, do not necessarily exhibit identical service lives. Indeed it would be odd for all the discs in a heatpack to fail simultaneously. This is another source of variation in the data. The effect is highlighted by the graphs in Figure 38, and in particular by the densities of the 5042 landing discs. These data which one would expect to be similar, are in fact very different. There is no overlap of the error bars which represent ± 1 standard deviation, which suggests that the data comes from different sources. Although this is just an example it does serve to highlight what is a serious problem with testing ex-service material; namely that the variation between discs can easily mask any underlying trends as a result of service life.

7.4. Analysis of material and failure mechanisms

Although the effect of service conditions on the strength and density of the material which was tested was minimal it was deemed possible that changes in microstructure might be observed. To this end samples with representative properties from each group were mounted and polished using the techniques described in Section 6.2.

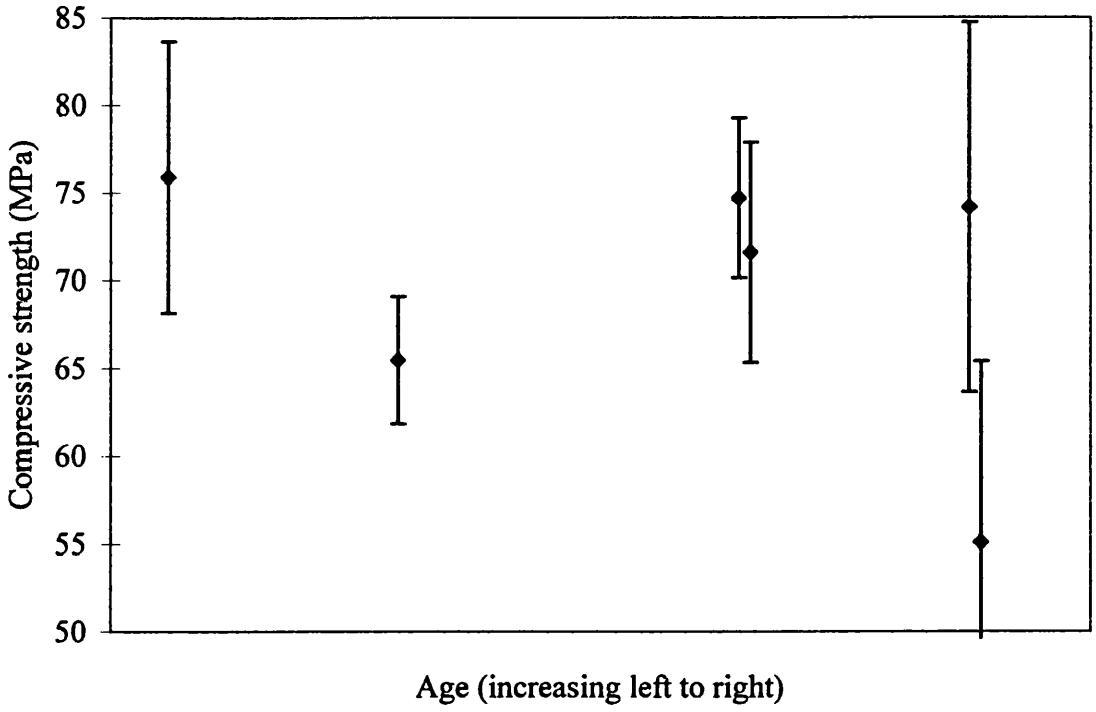

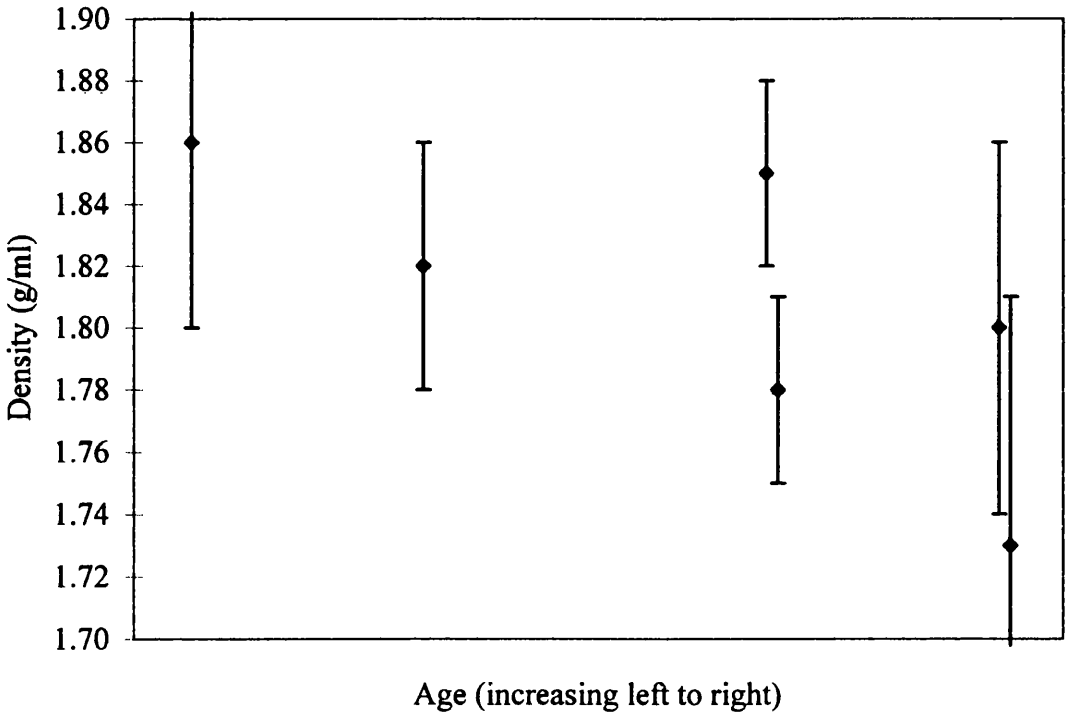

Figure 38. Graphs showing the effect of "age" on the strength and density of commercial material. Points are mean values and error bars represent ± 1 standard deviation.

7.4.1. Microstructural analysis of materials

After testing all the samples were examined by eye to trace the macroscopic crack path. Subsequently chosen samples were mounted and polished such that optical microscopy revealed the crack path in all the layers of the material, i.e. the edge of the sample was prepared.

By carefully avoiding areas which failed during the test the pre-test condition of the material could be assessed. Unfortunately the material from all the groups appeared very similar. The exception to this was the material from the failed discs. Here the material exhibited extra porosity over and above that which was normally present. Two types of extra porosity were observed an these are shown in Figure 39. Some porosity was concentrated between matrix sheaths (A) and was similar to that

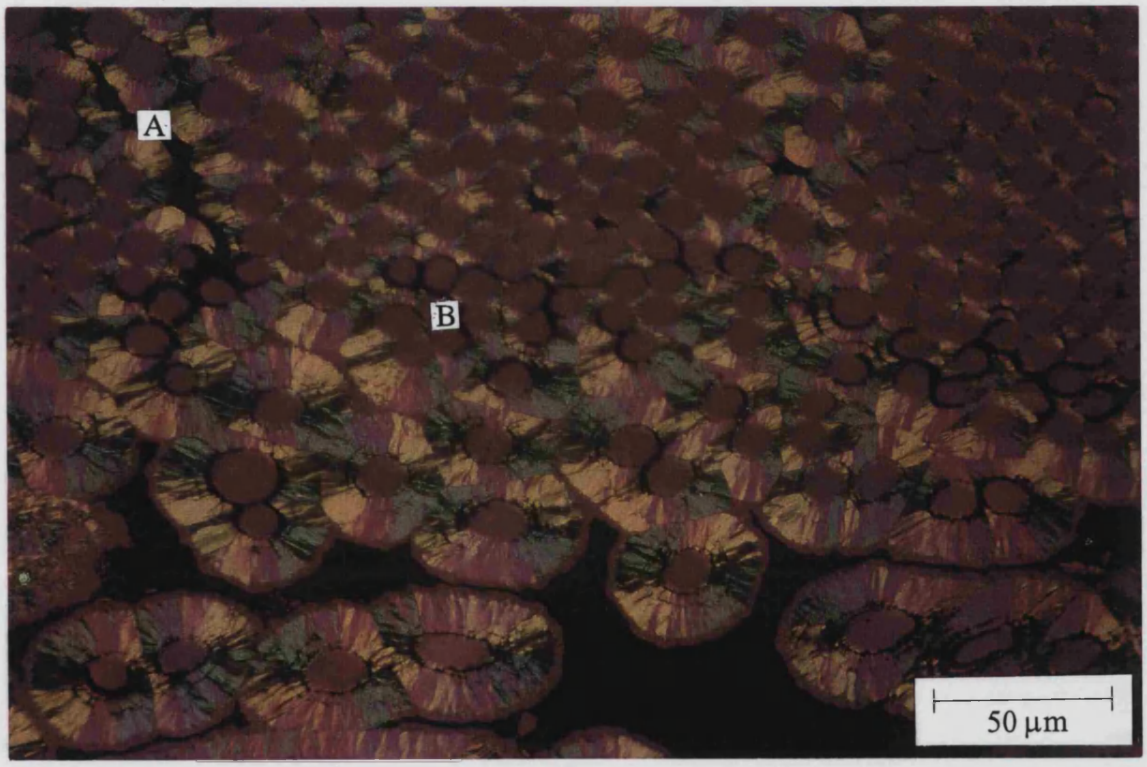

Figure 39. Optical micrograph of sample D10c showing both types of extra porosity.

observed in new material although some of the features suggested that this porosity was slightly different in nature. The second type was much more common and consisted of pores of crescent section located at the interface between fibres and matrix material (B). The incidence of this type of porosity was highest in those

samples which exhibited particularly low densities and compressive strengths. These samples were from the failed discs and particularly from the inner circumference. There is significant evidence that this crescent shaped porosity is associated with low density and strength of failed discs. However it is not clear whether its occurrence is a cause, or simply an artefact of the failure of the disc. It is also possible that this porosity is in fact a result of shrinkage during manufacture, and hence the cause of the failure of the disc.

It is known that in general oxidative attack of carbon-carbon composites occurs preferentially at the interface between the fibre and the matrix, and that this is extremely detrimental to the properties of the material. Coincidentally this is where the extra porosity in weak samples occurs and so it is proposed that Figure 39 shows the effect of oxidation on the microstructure, and that this was a probable cause of the failure.

7.4.2. Observed crack paths

Initial examination of the samples by the naked eye after testing revealed that they all failed in a similar manner. Generally the sample cracked along a diagonal line across the plies as shown in Figure 40. Shear along this line allowed accommodation of the compression by a lateral expansion. Clearly the cracks were not linear but tended to zigzag as shown. The zigzag was made up of a series of cracks of two types; along the boundary between layers (delamination), and across layers. Delamination often continued beyond the position where the crack passed through the layer and near the surface of the specimen plies occasionally became completely detached.

Varying degrees of delamination were observed but no pattern to its extent could be established. Microscopic examination revealed that these cracks generally occurred close to the boundary between continuous fibre and felt layers as shown in Figure 41. Cross-layer cracking mostly occurred in regions of low density such as stitches and this is not unexpected as these are natural weak points in the material (Figure 42). An example of cross-layer cracking by compressive shear failure (Figure 43) was observed in a few samples and is due to good alignment of the fibres with the axis of the load. Some tensile failure of continuous fibre layers, probably as a result of buckling, was also seen.

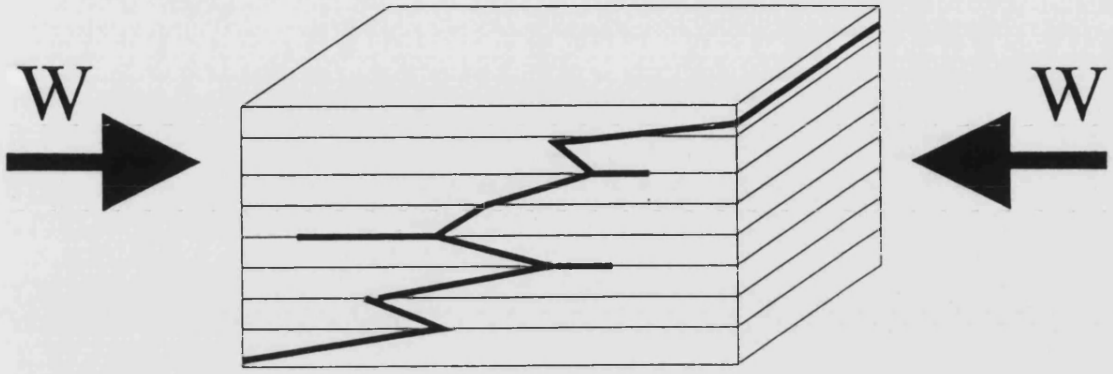

Figure 40. Schematic diagram of the crack path in a compression test specimen.

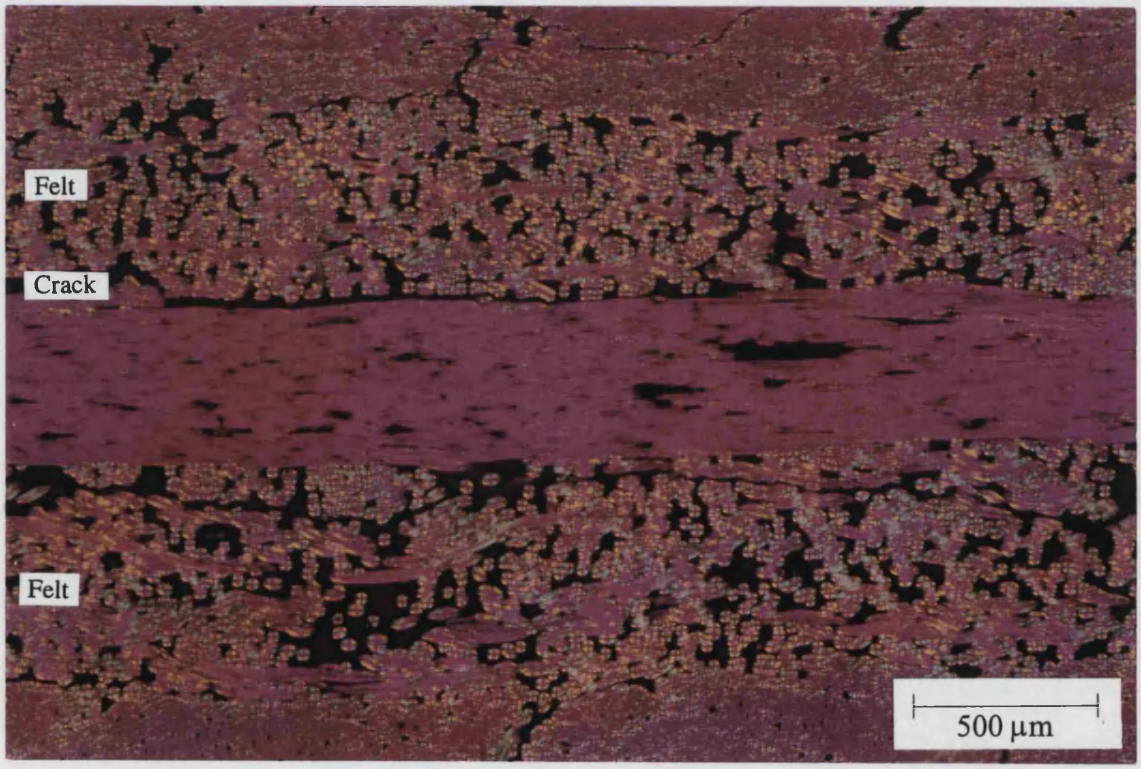

Figure 41. Typical material failure under compressive loading.

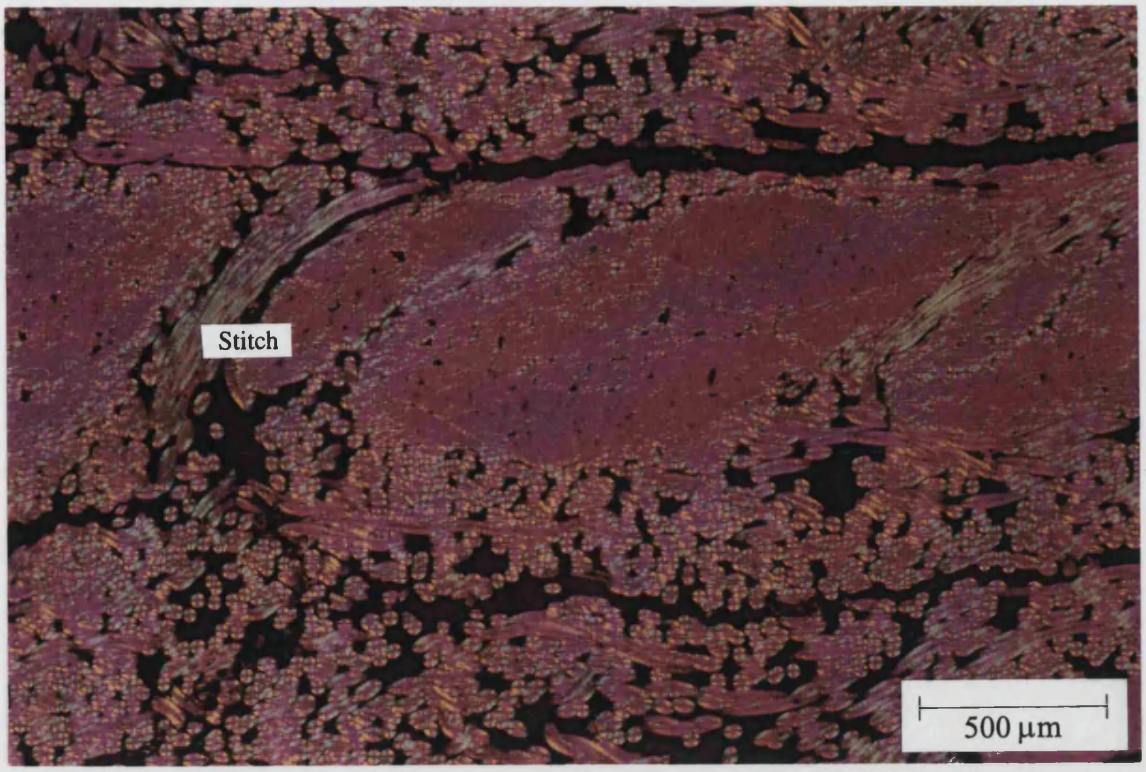

Figure 42. Cross-layer cracking occurs through natural points of weakness such as stitches.

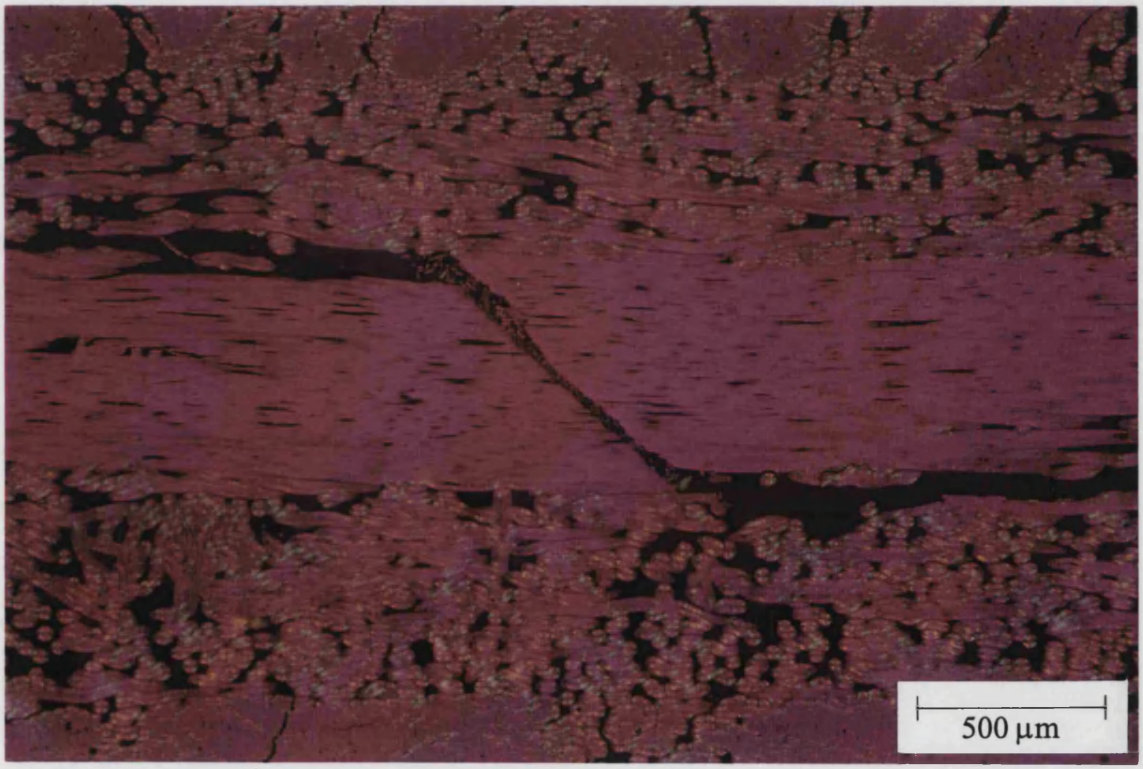

Figure 43. Compressive shear failure of continuous fibre layer.

8. FAILURE MECHANISMS OF AIRCRAFT BRAKE DISCS

The aim of this project is to investigate the causes of premature failure of carbon-carbon composite aircraft brake discs. However, before the causes of failure can be determined the mechanism of the failure process must be understood. Therefore in this chapter possible failure mechanisms are discussed after first describing the loading conditions on a disc in service.

8.1. Loading conditions in service

In service, the forces on a brake disc are complex with many of the individual forces being intimately related to many others. This makes accurate modelling of the service conditions impossible. However the main mechanical forces on the disc can be relatively easily understood and it is these which will be described below.

There are two large forces which act on a brake disc and these both arise from the application of the brakes. During a braking operation, the kinetic energy of the aircraft is dissipated by conversion to another form in the brakes. All of the braking force arises from friction caused by sliding contact between the turning rotor and the static stator. The friction can only be caused over the area of contact, and this is commonly called the swept area. Figure 44 shows the way the braking forces are transmitted through the brake assembly. There are two very important steps which are the transmission of the torsional loads in the discs (stators and rotors) to the supporting structures (wheel and torque tube). These are critical steps due to the relatively small areas across which the loads can be transmitted.

The loading condition can be more easily understood if it is abstracted and a single tenon is considered. Figure 45 shows a schematic diagram of the loading condition on a single tenon using a stator tenon as an example. Here the two main forces are obvious. The first is compressive and occurs at the contact face of the tenon and the second is shear and occurs in the disc at some point between the tenon contact area and the swept area. Consequently it is expected that if failure of a disc should occur in service, it should be concentrated in the region of the tenon since this is where the highest loads are experienced.

Many other loads can arise during service although all of them are of much less significance than those already discussed. These include thermo-mechanical stresses

resulting from heating and cooling of the brakes, vibrational fatigue and cyclic loading during rotation of the discs arising from variations in the thickness of the discs.

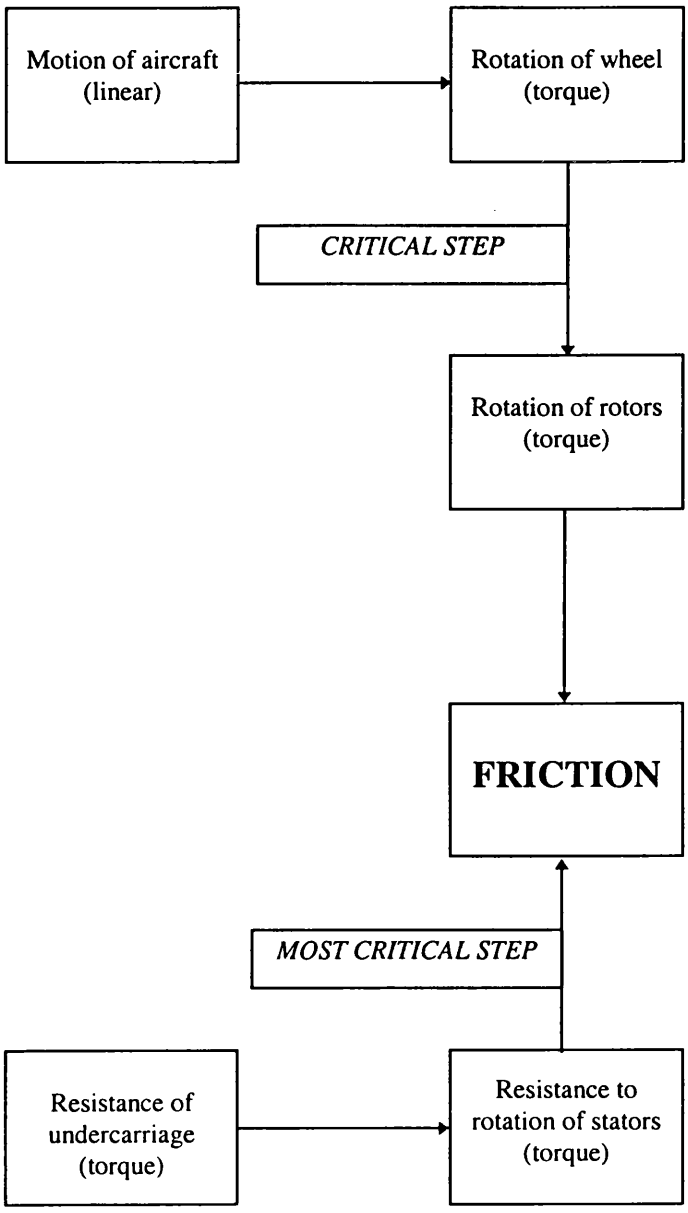

Figure 44. Schematic flow diagram showing the way in which forces are transmitted through the brake assembly.

8.2. Analysis of failed discs

During normal service brake discs are put under the highest stresses during the landing of the aircraft. The exception to this is the rejected take-off condition where higher stresses are developed, however the brakes are routinely replaced after an RTO. After landing and braking to taxiing speeds there is a series of further applications of the brakes as the aircraft manoeuvres on the ground. These are known as taxi snubs. If it is assumed that brake discs fail while they are under their peak loading condition, then clearly further damage to the discs will occur during taxi snubs. In addition, if only one disc fails in a heatpack, frequently it is not noticed for several flights, or until another fails. Hence failed ex-service discs tend to exhibit gross secondary damage.

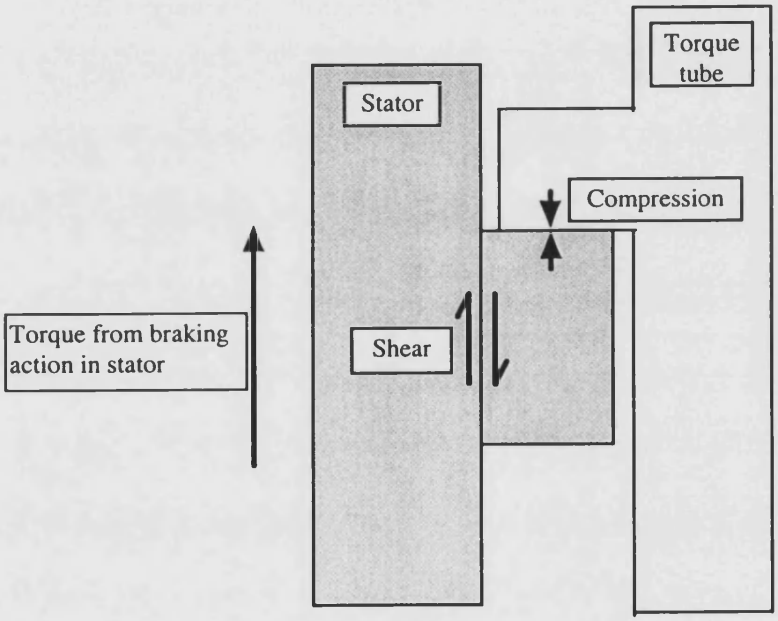

Figure 45. Schematic loading condition for a single stator tenon.

The vast majority of discs which fail in service are double stators. In a heatpack there is an even number of rotors (usually 4) and an odd number of stators (usually 5). All the discs are connected to the surrounding structure by tenons which are made by machining wide slots in the circumference of the disc. In stators the tenons are on the inner circumference whereas in rotors they are on the outer circumference. A simple consideration of lever balances shows that the moment on the stator tenons is greater than that on the rotor tenons and therefore stators are more likely to fail. The stators

on the ends of the heatpack are called single stators since they only have one friction face, whereas the others have two and are called double stators. Despite the fact that single stators are thinner, the additional loading from twice the friction area in double stators means that the tenons of these are discs the most highly loaded.

Failed double stators generally show a typical pattern of damage. All the material in the region of the tenons is absent and the inner circumference is very rough indicating a high degree of damage. Also, there is damage, albeit less extensive, to the outer circumference. It is likely that this is secondary damage which is caused by the disc rattling round inside the wheel after the tenons have failed. Figure 46 show the inner circumference of a double stator from a Boeing 757 which had failed in service.

Figure 46. Photograph of the damage caused to the inner circumference of a double stator by failure in service.

Clearly there is much evidence of damage and this implies that the failure of the disc involves a great deal of energy. The shape of the fracture surface suggests that the failure mechanism is one of shear along a line between the tenon root and the inner edge of the swept area. Persuasive though the evidence is, caution must be exercised when drawing such conclusions. After tenon failure the stator is clamped between two

rotors and hence rotates with the wheel. Hence any post-failure damage is likely to be annular in pattern and therefore the fracture surface could be a result of either failure itself, or post-failure damage.

Sections of a failed disc were mounted, polished and examined using optical microscopy to find out if there were any microstructural features which would indicate the failure mechanism. Figure 47 is an optical micrograph of a section of the failed disc close to the inner circumference which is just to the right of the picture. What is immediately clear is that there is a great deal of porosity at the fibre-matrix interface, and that the amount of this porosity increases from left to right (i.e. closer to the inner edge). This confirms that the porosity of this type seen in the compression samples was not a result of the test, however it does not confirm whether it is a cause or the result of the failure of the disc.

Figure 47. Optical micrograph of a section of a failed disc showing significant quantities of fibre-matrix interface porosity (the inner circumference of the disc is just out of shot to the right).

8.3. Failure criteria

The only way in which a component can mechanically fail in service is if it is subject to a stress in excess of its strength, and there are only three mechanisms by which this can occur.

i. Service stresses exceed designed stresses
ii. Dimensional change of critical component
iii. Property change of critical component

The first of these mechanisms is extremely unlikely, as the components are designed with safety factors, unless one disc fails in which case the rest of the discs in the heatpack are subject to higher loads than anticipated. Dimensional change of the critical component (tenon), raises the stress in the component even under normal loads and is possible by three mechanisms.

i. Oxidative surface burn-off
ii. Tenon delamination
iii. Slot widening

Oxidative surface burn-off is self explanatory and would cause a reduction in the cross-sectional area of the tenon which bears the compressive load arising from the braking torque. A similar effect could be achieved by delamination of the composite material of the tenon. This is possible as similar effects have been observed during the compressive testing programme. There is no evidence for either of these, although even if there were, it would be destroyed by the processes of failure. To gather evidence for tenon delamination ex-service discs are required which are on the point of failure and these are very rare. There is practical evidence however, for slot widening. In this process the load bearing face of the tenon wears during the service life of the disc. While this does not reduce the area bearing the compressive loads, it does reduce the area bearing the shear forces between the tenons and the swept area. Slot widening is discussed in detail in Section 8.5., and evidence for the delamination theory collected from structural torque tests is presented in Section 8.4.

The advantage of failure by dimensional change is that it is possible to detect imminent failure during routing brake maintenance by visual inspection. By contrast, changes of the properties of the material are more insidious as these are frequently difficult to detect before the advanced stages are reached. Because of this, much of the research on which this thesis is based is directed towards the investigation of this

topic. There are many mechanisms by which the properties of a component may change during its service life. Fatigue, corrosion, stress-corrosion cracking and thermal fatigue are just a few examples of such mechanisms. Under the conditions of service of carbon-carbon composite aircraft brake discs, the most likely mechanism for degradation is oxidative attack. This is due to the high temperatures experienced in oxidising atmospheres. Hence the emphasis of this thesis is on the effects of oxidation on the mechanical properties of carbon-carbon composites.

8.4. Structural torque testing

Structural torque testing is an experimental technique which is designed to simulate the loading conditions experienced by a disc in service. It is routinely used by Dunlop Ltd. to verify the properties of the discs which they produce on a commercial scale, and it can also be used to proof test new designs.

8.4.1. Experimental technique

The technique consists of loading a single disc in torsion using parts of a real brake assembly. Usually stators are tested although the technique can be simply adapted to test rotors. A single disc has fifteen holes drilled in it along the centre-line of the swept area. These are used to bolt the disc to two steel bearing plates through which a controlled torque can be applied. This assembly is positioned on a section of torque tube, and the engagement between this and the tenons of the disc resists the applied torque. The torque is applied using a hydraulic ram in controlled steps until the disc fails. A continuous record is made of the applied torque.

The objective of this testing programme was to develop a more detailed understanding of the failure mechanism of the composite material, when it is loaded in a manner similar to the conditions experienced in service. The loading condition is mainly shear similar to that which would be experienced in a short span edgewise bend test, with an element of compression at the contact between tenon and the torque tube. It was hoped that microstructural examination of tenons which have experienced loads of varying levels below the expected failure level, would reveal the mechanism of damage accumulation.

The experimental programme required that tenons were loaded to increasing percentages of the expected failure stress. There are two ways of doing this using whole discs. The first involves preparing a number of similar discs by removing all

but one drive tenon. By stressing the discs to different loads it is possible to obtain tenons which have experienced these loads. The advantage of this method is that since only one tenon is involved in each test, the tenon tested must have taken all of the applied load. The major disadvantage is that the method is extremely uneconomic in its use of material, and, since more than one disc is used, inherent variability is introduced. The other method involves taking a disc with all its fifteen drive tenons and loading it to a load below failure. Here the fifteen tenons have experienced a percentage of their failure load. One of these tenons can be removed and examined. The disc can then be reloaded to the same torque level. However, since one of the tenons has been removed, the load experienced by each will be higher. Again, another tenon can be removed and examined and should show more damage than the previous one, since it has experienced a higher load. By repeating this cycle of events one disc could in theory yield up to fifteen tenons each showing damage as a result of different loads. The major advantage of this method is that at uses a lot less material. However its validity relies on one major assumption, that all the tenons share the applied load equally. If this is not the case, then remaining tenons will not necessarily experience increasing load as more are removed. Indeed, no absolute conclusions about the load carried by each tenon can be drawn. As a direct result if this, the order in which the tenons are removed may bear little relation to the amount of observed damage.

Four discs were selected for testing using the modified structural torque test method and the details of these are given in Table 15.

Disc Number	Service History	Target Peak Torque (Nm)
E055039S	Ex-Service	5423
E086800S	New Condition	8135
E052577S	Ex-Service	10847
E085662S	New Condition	10847

Table 15. Origin of the discs used in modified structural torque tests. The testing machine used was calibrated in lb ft and target torque values were selected to be round numbers in these units. This is the origin of the somewhat abstract nature of the target torques in Nm.

8.4.2. Results

Table 16 shows typical results from the modified structural torque test and Table 17 shows a summary of the results of modified structural torque testing on all four discs.

No of remaining tenons	Index of removed tenons	Peak applied torque (Nm)	Torque per tenon (Nm)
15		8288	553
14	15	8302	593
13	15, 5	8102	623
12	15, 5, 10	8288	691
11	15, 5, 10, 8	8208	746
10	15, 5, 10, 8, 3	8235	824
9	15, 5, 10, 8, 3, 13	8208	912
8	15, 5, 10, 8, 3, 13, 1	8261	1033
7	15, 5, 10, 8, 3, 13, 1, 11	8288	1184
6	15, 5, 10, 8, 3, 13, 1, 11, 6	6143 (F)	1024 (F)

Table 16. Results of modified structural torque testing on disc E086800S. (F) denotes failure during the loading cycle before the target torque was achieved.

Disc ID	Service history	Target torque (Nm)	Torque at failure (Nm)	No of tenons at failure	Failure torque per tenon (Nm)
E055039S	Ex-Service	5423	4846	4	1212
E086800S	New Condition	8135	6143	6	1024
E052577S	Ex-Service	10847	9877	15	659
E085662S	New Condition	10847	10724	12	907

Table 17. Summary of results from modified structural torque testing.

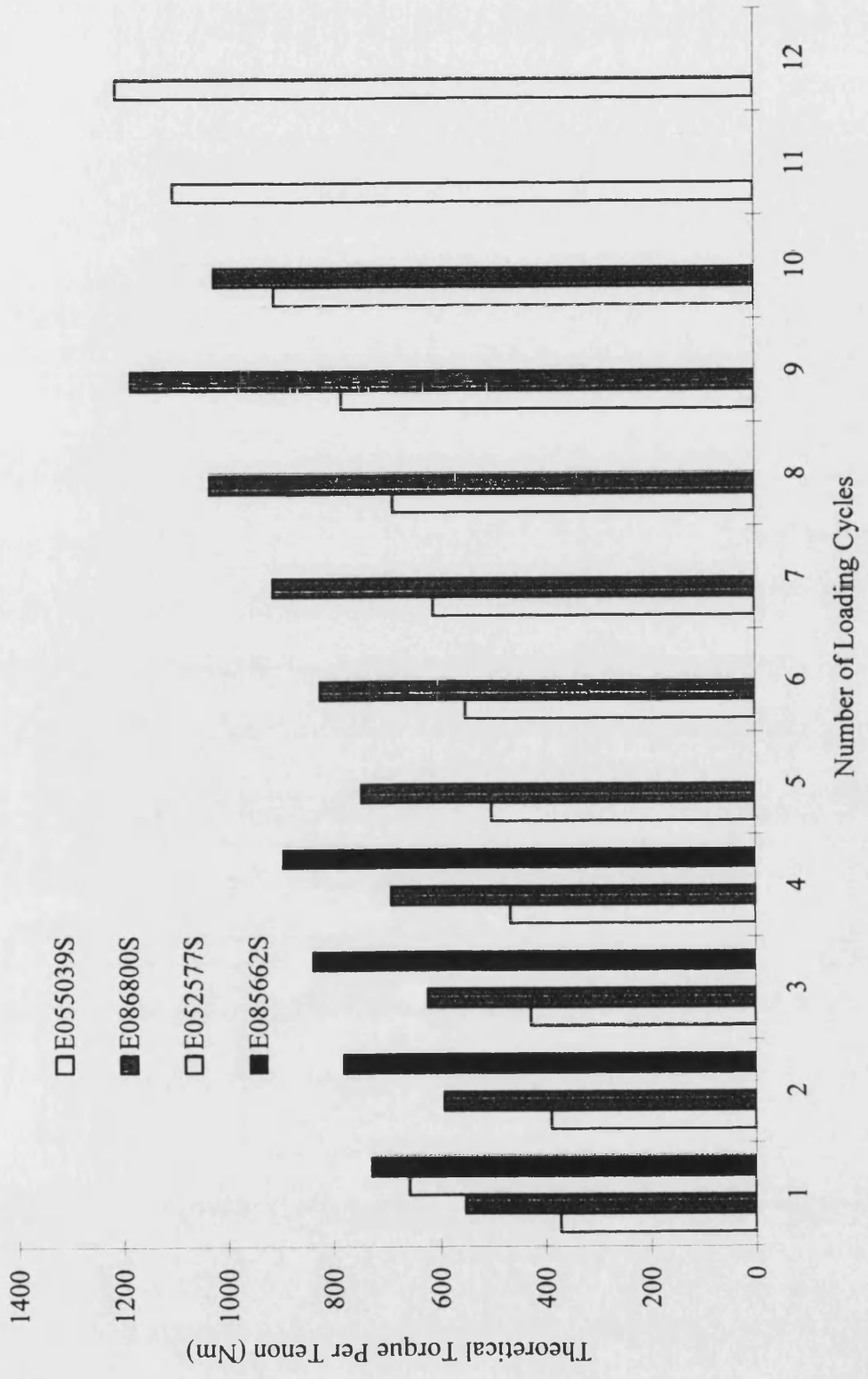

Figure 48. Graph showing the theoretically calculated torque per tenon for each cycle of the modified structural torque tests.

Comparing the two discs subject to testing at a peak torque of 10846 Nm it can be seen that the only difference between them is that one is new and the other is ex-service. However the results of the tests show two marked differences. Firstly, the failure torque for the new disc is 10724 Nm, whereas the ex-service disc exhibited a failure torque of 9877 Nm. Secondly, the new disc survived three loading cycles at 10846 Nm, but the ex-service disc failed on its first loading cycle before the target torque was reached. This produced a torque per tenon at failure of 907 Nm and 659 Nm for the new and ex-service discs respectively. Clearly then, the ex-service material appears to be weaker.

From the results (Table 17 and Figure 48) it can be seen that an increase in the target peak torque causes a reduction in the failure torque per tenon. It must be noted that the value of torque per tenon is purely mathematically derived. It is not measured in any way but is calculated by dividing the applied torque by the number of remaining tenons. The reasons for the relationship between target torque and failure torque per tenon are unclear, but it could be due to the load being more evenly distributed between the tenons of discs loaded to lower torques as a result of there being fewer of them at failure.

Finally it can be seen from Figure 48 that disc E086800S shows a rather unusual failure. In all other cases the data shows that the torque per tenon (TPT) increases with each successive loading cycle, up to the point of failure. This is exactly as is expected since the applied torque is the same but it is applied to one less tenon each time. It seems logical to suggest that for all loading cycles except the last one the TPT is below the failure TPT value since the disc does not fail. However Figure 48 clearly shows that for disc E086800S the failure TPT is *lower* than that borne by the disc on the previous two loading cycles. Therefore either the disc has been damaged between loading cycles or the load distribution model is inaccurate. The damage theory seems unlikely, but the inaccuracy of the model is very plausible since it is assumed that the tenons all bear equal shares of the applied torque.

The unevenness in loading of tenons of a given disc is caused, at least in part, by inaccuracies in machining. Unless all the contact faces of the tenons and the torque tube are machined perfectly, so that all fifteen tenons contact with the torque tube at zero load, some tenons will be loaded more than others. Machining to this level of precision is very difficult and, as a result, is also very expensive. The high level of

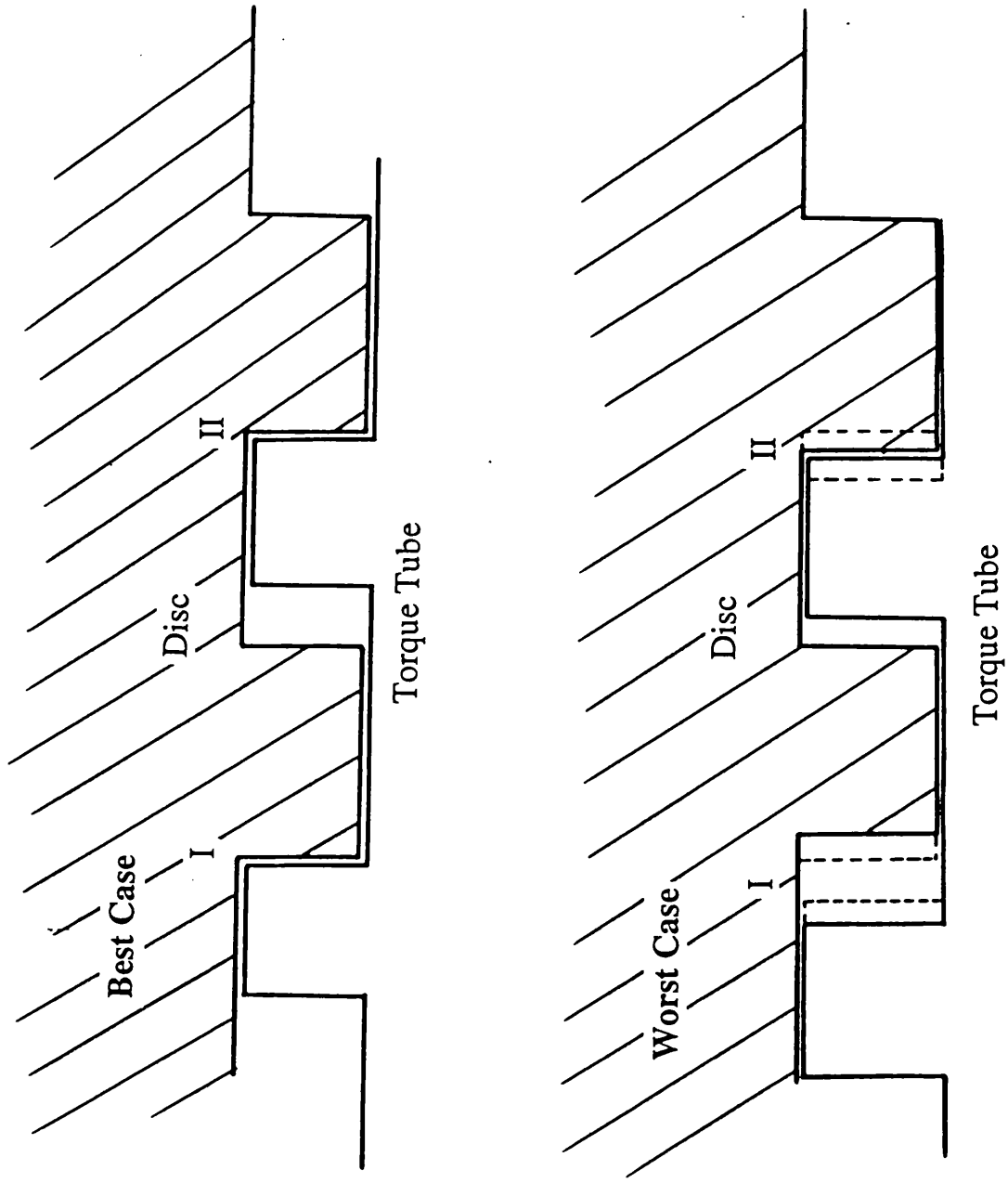

Figure 49. The effect of machining tolerances on contact faces of tenons and torque tube illustrating best and worst case scenarios. The diagrams also demonstrate that relatively large gaps can arise even if the machining of the components is highly accurate.

precision required is partially a result of the high modulus and low strain to failure of the material. If this was not the case the material would be able to deform to some extent to absorb the machining inaccuracies. Edgewise compression tests have shown that the strain to failure of the material is around 1.5 %.

A simple thought experiment demonstrates that in the worst case the possible gap between contact faces is four times the machining tolerance. Figure 49 shows two adjacent tenons and their corresponding contact fins on the torque tube. For clarity the geometry has been reduced to an analogous linear situation, however the arguments are still valid. The figure shows two contacts (I and II) and therefore four contact faces are involved. In the case of all four surfaces being machined perfectly both contacts are made. However, if both the faces at contact I are recessed by the machining tolerance (x) a gap is produced which is 2x wide. Similarly if the faces at contact II are proud by the machining tolerance (x) a gap is produced (at contact I) which is 2x wide. If both these conditions occur simultaneously contact is maintained at contact II but a gap occurs at contact I which is 4x wide. This leads to the obvious question, in this case could the tenon at contact II fail before that at contact I bears any of the load? If the assumption is made that the tenons fail in a purely compressive manner, which is clearly untrue since there is at least an element of shear to the loading, then the mathematics become relatively simple.

Strain to failure $\approx$ 1.5 %

Length of tenon $\approx$ 32 mm

$\Rightarrow$ Displacement to failure $= 32 \times 0.015$

$\approx$ 0.5 mm

$\therefore$ if $4x > 0.5$ mm then failure of a tenon is possible before other tenons have made contact (where x is the machining tolerance).

i.e. if $x > 0.125$ mm

So if the machining tolerance is 0.125 mm (or greater) and one of the tenons is machined proud while the other fourteen are machined recessed (and the torque tube was coincidentally inaccurate), the proud tenon would have enough slack to fail in a purely compressive mode before the other tenons contributed to bearing the load. Since in the initial loading condition of this scenario only the single proud tenon bears any load it will be subject to fifteen times the normally expected load. This would certainly be enough to cause failure. However in this scenario the other fourteen tenons are required to be recessed to the limit of the machining tolerance. Therefore upon failure of the single tenon the other fourteen tenons would bear the load and share it equally. This would only result in a load on each tenon 7 % above normal and would be unlikely to cause failure of these tenons, and hence the disc. In a case where

eight of the tenons are machined proud and seven are machined recessed, the eight tenons which initially bear the load are subject to 188 % of the normal load. This may not be enough to cause failure of the eight tenons, but if it did there would be sufficient free movement to do so, and more importantly the load would then be carried by the remaining seven tenons. Since the load had been too great for eight tenons to carry, it would seem logical to suggest that the remaining seven would also fail. So in the case with eight proud tenons and a machining tolerance of 0.0125 mm a disc could fail at 53 % of the expected torque purely as a result of geometric considerations.

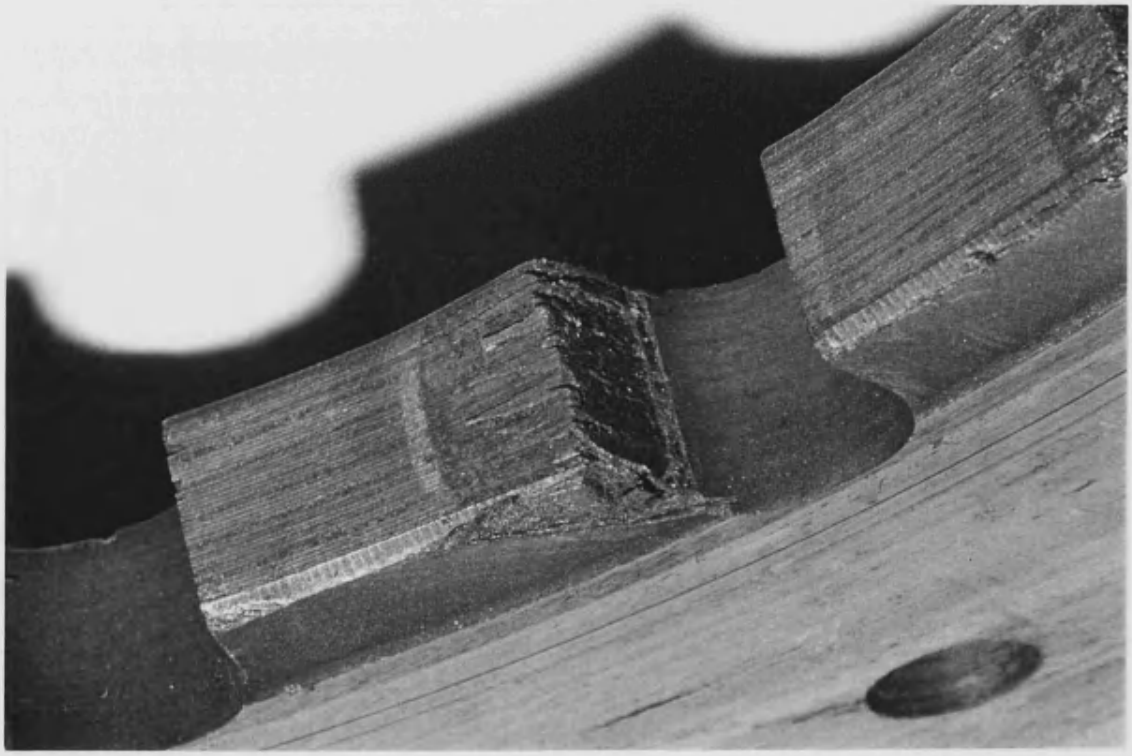

Figure 50. Photograph of a tenon after failure during a structural torque test. The "broomstick" type failure can clearly be seen.

8.4.3. Macroscopic failure mechanism

As previously detailed, tenons were removed during the testing of each disc in an effort to observe the build up of damage in the material as failure is approached. Examination of the tenons removed on cycles where failure did not occur revealed that

most did not show any damage. However, after failure all the remaining tenons showed the same pattern of damage. A series of short cracks run from the contact face into the tenon between plies giving the tenon the appearance of a "broomstick". This is shown in Figure 50. This allows the accommodation of the compression of the tenon by a lateral expansion in a manner analogous to that observed under compressive test conditions. Figure 50 also shows that some material has been lost from the side of the tenon through delamination. This reduces the strength of the tenon by reducing the area of material bearing the load as discussed earlier.

It is possible that the failure mechanism observed during these tests is that which occurs under service conditions, however observation of this phenomenon is only possible as a result of abruptly removing the applied torque at the onset of failure. As this is not possible during the service of the discs there is no practical evidence to either support or disprove this theory.

8.4.4. Microscopic failure mechanism

Each of the tenons removed during the course of the modified structural torque testing programme was mounted and polished using the methods detailed in Section 6.2.1. Unfortunately, the optical analysis of these tenons did not reveal a systematic increase in damage as a result of increasing theoretical load, as was hoped. This is due to two reasons. First, the tenons have not necessarily experienced increasing load since the load is not evenly distributed, and second the material fails by rapid crack propagation and therefore there is very little damage accumulation prior to failure.

However, during routine analysis of the post-test tenons an interesting effect was noticed. It appeared that the load bearing faces (LBF) of the tenons, particularly those which had experienced high loads, were covered by a thin film of finely textured material. This is shown in Figure 51. The micrographs suggest that this film is a mixture of fibre derived and CVI derived material. Some intact fibres can clearly be seen in the film in Figure 51, along with material of indeterminate structure. It is proposed that the film forms as a result of the redistribution and compaction of material removed from the substrate during compressive loading. As the LBF is microscopically rough, point loading must occur and subsequent fracture processes can result in fine debris which can be compressed into a film. Also basal plane shear

Figure 51. Load bearing face of a tenon after a structural torque test showing the film which is formed.

of the carbonaceous material can result in the formation of a film on the surface. As the resulting surface of the film is much flatter than that of the substrate, it appears more shiny to the naked eye and hence the phenomenon is known as contact area polishing. This effect has been observed on the compression faces of the carbon-carbon composite samples used in compression testing and also with nuclear graphites.

The formation of films on the surface of carbon-carbon composites is a well known effect, although in previous work the films form on the friction faces of the material. Here, there is a large degree of shear loading, sliding contact and a great deal of energy available for the transformation of the structure of the material. However in the case of compression and structural torque testing none of these conditions are present. Nevertheless films can clearly still form although this has not been studied in any depth. As will be discussed in the next section, this effect could be of great industrial significance in the field of aircraft brakes since it could be one of the mechanisms by which premature disc failure could occur.

8.5. Slot widening

Slot widening is the name given to the result of a loss of material from the LBF of tenons of ex-service discs. This manifests itself by the reduction in length of the tenons and hence a lengthening of the gaps between them. The effect is not uncommon and a reasonable degree of slot widening can be tolerated without causing failure of the disc. Evidence for this is provided by ex-service discs which have not failed but exhibit slot widening. Figure 52 shows a tenon from an ex-service disc which exhibits a large amount of slot widening. Indeed it may be that some slot widening is a good thing since it may allow all the tenons on a disc to "bed in" and share the load more evenly. The effect of uneven load distribution between the tenons has been discussed in Section 8.4.

Since material is removed the process must be one of wear, but the micromechanism by which it occurs is as yet unclear. The loading condition on the tenon face is fairly complex. The main load is compressive, however it can be demonstrated that flexure of the tenon and the corresponding drive spline on the torque tube can induce shear. The tenons are also subject to combined fatigue and impact loading. Fatigue occurs as a result of taxi snubs where the load is cyclic but always positive in a compressive

sense as the aircraft brakes are applied. Impact occurs whenever the load on the tenons rises from zero. When the load is zero i.e. when the wheel is not spinning or when the brakes are completely off, the loaded faces of the tenon and the torque tube may drift apart. Consequently when the brakes are applied the faces are brought together at speed, causing impact loading. The final possible cause for the wear of tenons is the sliding of the discs along the torque tube.

8.5.1. Ex-service evidence

Tenons from the disc shown in Figure 52 which showed roughly 5 mm of slot widening were removed using a saw and mounted and polished in preparation for optical analysis. The LBF of other tenons were prepared and examined using scanning electron microscopy.

Figure 53 shows a section of a tenon from a disc showing slot widening. The polishing process has produced a surface for analysis within a layer of staple fibre. The LBF of the tenon is at the top of the frame. It can be seen that the LBF shows cracking in the composite between 10 and 40μm below the surface. The material in the layer bounded by the crack and the surface (A) appears to be made up of small fragments of the base composite. To the right of the photograph a small depression approximately 10μm deep can be seen (B). This would indicate local weakness in the composite or an indentation left by an asperity on the torque tube or debris between the torque tube and the tenon.

Figure 54 shows a section of another tenon. In this case the polishing process has produced a surface within a layer of continuous fibre which is oriented at approximately 75° to the LBF. There are several interesting features in this photograph. Firstly the tenon shows subsurface cracking similar to that shown in Figure 53, however in this case it occurs at depths of between 20 and 100μm. It can also be seen that this layer is in two parts. The lower layer (A) consists of material which has become partially detached from the rest by propagation cracks roughly parallel to the LBF. This material is made up of large pieces and is relatively ordered in that it bears a strong resemblance to the material which is still attached and is adjacent to it . The top layer (B) is much thinner, up to 10μm thick, and is also much more disordered. The individual pieces which make up this film are much smaller than that in the lower layer although some of the larger pieces can be seen to resemble

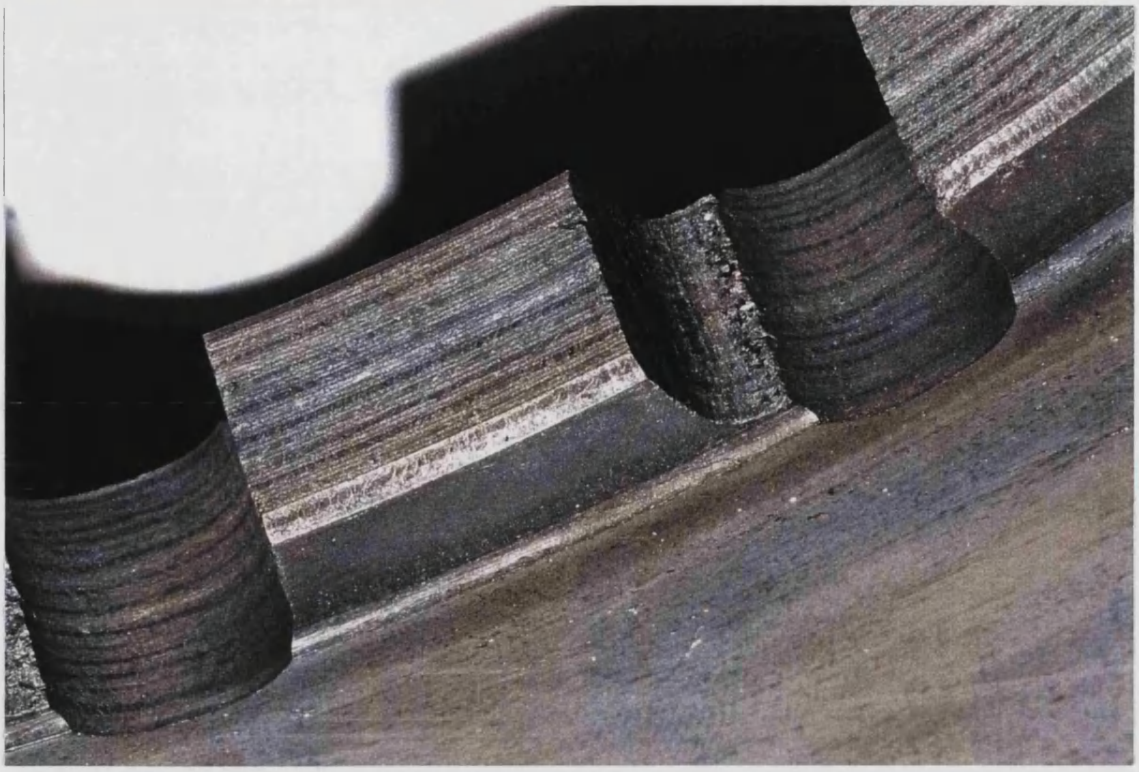

Figure 52. Load bearing face of a tenon showing a large degree of slot widening.

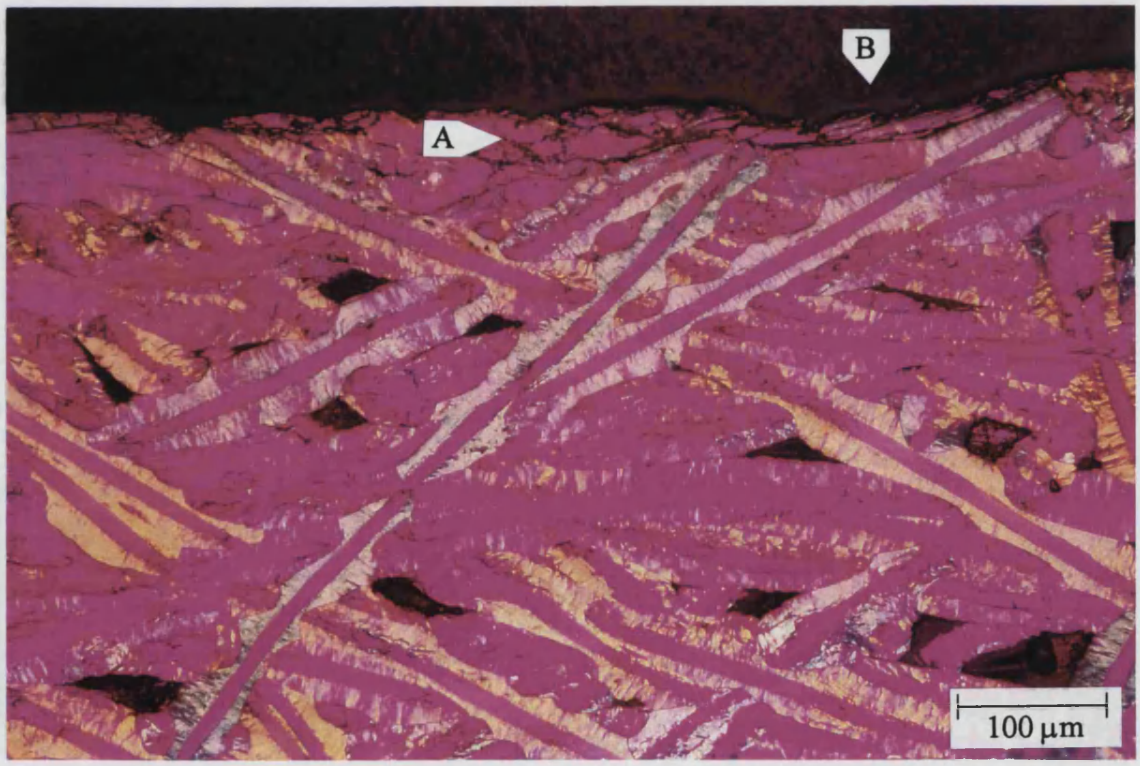

Figure 53. Load bearing face of a tenon from a disc exhibiting significant slot widening.

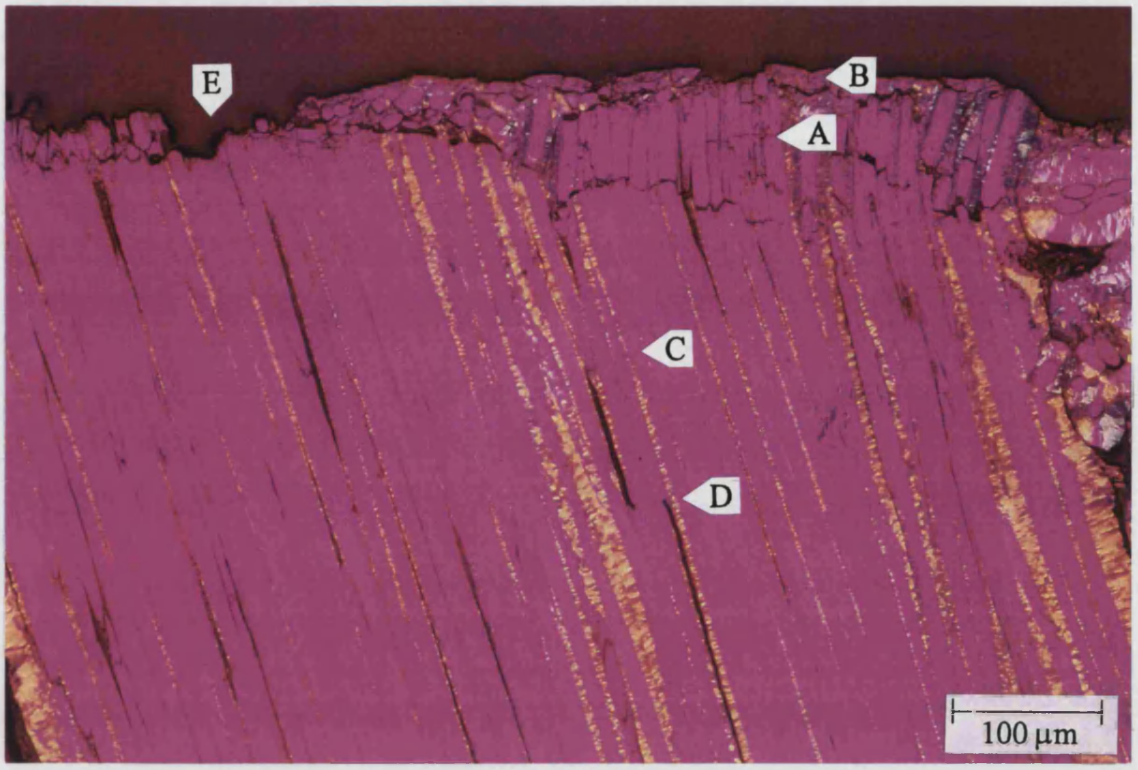

Figure 54. Load bearing face of another tenon from a disc exhibiting significant slot widening.

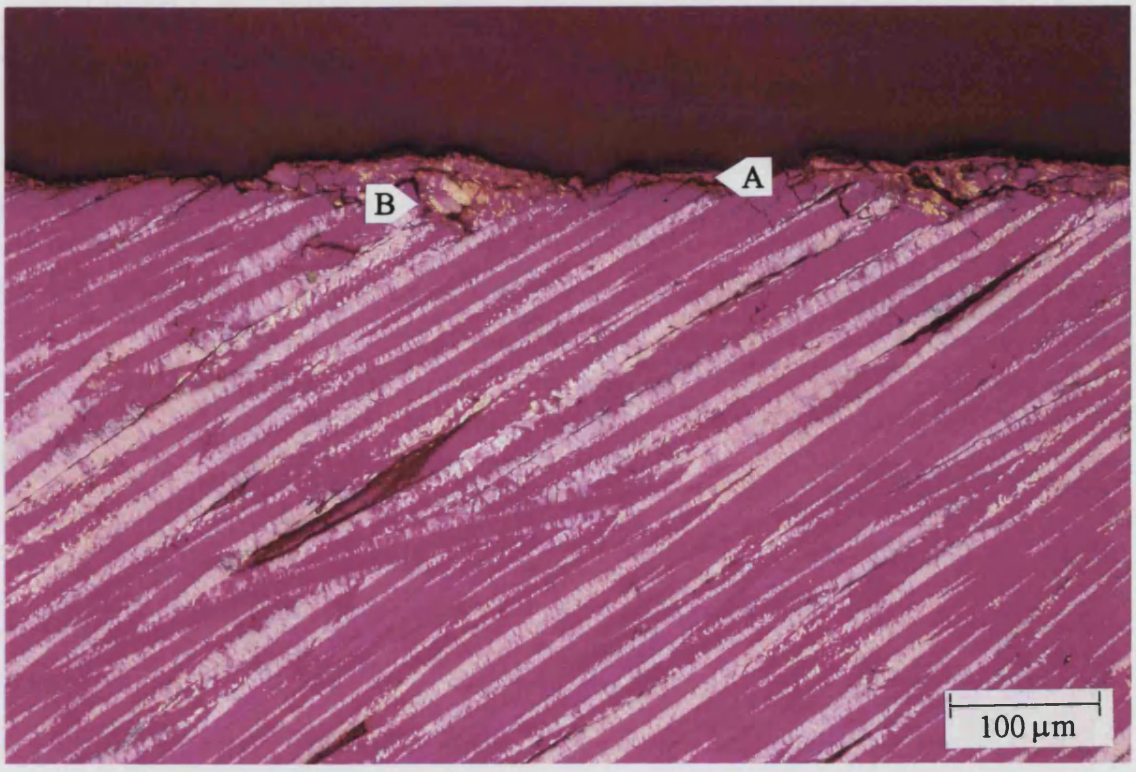

Figure 55. Load bearing face of a slot widened tenon showing the smoothing of the surface by filling of depressions with a thin film.

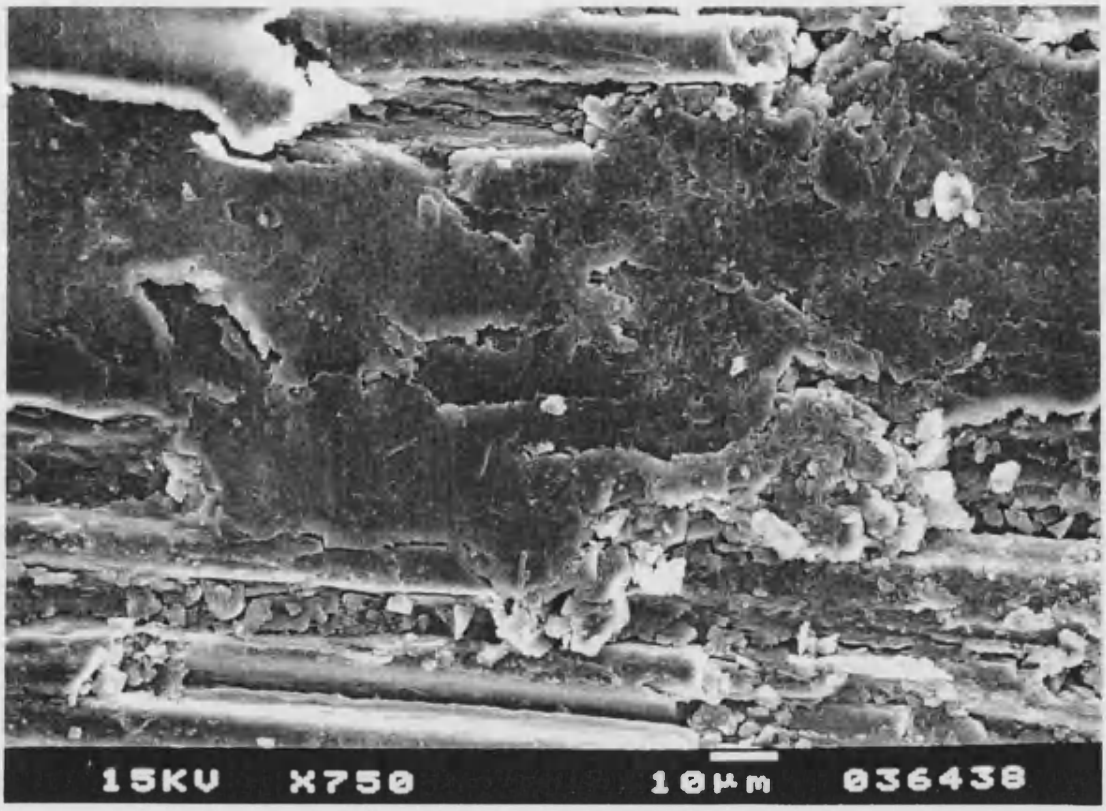

Figure 56. Scanning electron micrograph of the surface of the load bearing face of a worn tenon.

fibres. This sample also shows some deep cracking (C) across fibres and a compressive shear failure (D) similar to that observed in compression tests.

Secondly an area where the lower layer has spalled can be seen to the left of the photograph (E). If this process were to continue across the whole of the LBF a layer of material would have been removed and this could be the mechanism by which wear occurs.

The final observation to be made from this figure is that the fibres in the lower layer appear to have been displaced in a clockwise rotating manner. This would be consistent with a shear force at the surface similar to a sliding contact in a left to right direction. The only way in which a shear force could be applied to the LBF across the surface in the figure is by deformation of the tenon and the torque tube. However in the case of Figure 54 this would produce a shear force acting in the opposite sense.

Figure 55 shows another part of the LBF of the same tenon as is shown in Figure 54 but closer to the inside radius. A thin top film can be seen (A) in the absence of

significant quantities of subsurface cracking. It can be seen that the film fills depressions in the surface of the tenon (B) to produce a smoother surface.

Scanning electron microscopy was used to further elucidate the nature of the surface film. Figure 56 shows the surface of the LBF of one of the tenons. An area of the thin top film can be seen in the centre of the micrograph. In the bottom quarter of the picture a gap in the film is present allowing the fibre structure underneath to be seen. The very fine debris mentioned earlier can be seen at the edge of the film. The size of the particles that make up this debris is of the order of 10μm across. Where the film is continuous it is relatively featureless and smooth. Its appearance suggests either that the particles at the surface are so fine that they are beyond the resolution of the photograph, or that the particles have in some way been deformed. The thickness of the film in this micrograph is of the order of 10μm. This is consistent with the results of the optical microscopy. However, it was noted that the film was irregular in its occurrence and highly discontinuous.

8.5.2. Blunt indentation

The formation of films on the surface of carbon-carbon composite samples when not subject to sliding contact was of interest and so the phenomenon was deemed worthy of further investigation. The evidence for film formation presented thus far had been gathered in a somewhat ad-hoc manner, and a more systematic approach was required. Since the loading condition of a tenon in service is one of compression with a small element of shear, the test method was designed to simulate these conditions. Blunt indentation is a convenient and simple test method which induces compression and shear at the surface of the sample, and so this technique was employed.

The method consists of pressing a hard sphere onto the prepared surface of a specimen. The test used an Instron 1195 testing machine to drive a 6 mm diameter tungsten carbide sphere into the surface of the sample while making a continuous record of both the applied load and the crosshead displacement. This is a technique which has been use to study fracture in polycrystalline nuclear graphite[91,92], where the formation of surface films is attributed to basal plane shear. The effect of increasing peak load and increasing the number of loading cycles has been investigated.

It was important that the films formed during this investigation could be solely attributed to the effect of the blunt indentation. It is well known that carbon-carbon

composites form surface films under sliding contact conditions such as those which occur over the swept area of brake discs. However, when test samples are produced they are routinely machined using milling or grinding. Both of these are sliding contact wear processes and as such are likely to produce a surface film of their own. This is frequently evidenced by a lustrous surface and the presence of such a film would cast doubt over the origin of any film observed after testing. Thence a method of removing the surface film formed by machining was needed. Murdie *et al*[93] report a method of stripping the surface film from the substrate by the application of an adhesive tape. Upon removal the tape pulls the film from the substrate leaving a "clean" surface. This method was found to work well although several applications of tape were often required to remove all of the film. Examination by SEM of stripped and as machined surfaces showed that a film was produced by machining and also confirmed that it was subsequently removed by the tape stripping method. All blunt indentation testing was therefore carried out on surfaces which had had any pre-existing surface film stripped.

Figure 57 shows the effect of a single loading cycle to a peak load of 0.5 kN. Typically the composite failed a about 2.5 kN by interlaminar cracking allowing a transverse expansion to accommodate the indenter. In this photograph a circular region can clearly be seen which appears brighter than the rest of the surface. This is the result of contact area polishing and is evidence of film formation. When the peak load was increased it was found that the film which was formed tended to be more reflective, implying that the film was flatter and more complete[94]. This is a logical finding since an increase in the applied load means that there is more energy available during the test for structural change in the material. Also, under increased load the depth of the indent which was formed on the surface of the sample increased. Another interesting effect can be seen in Figure 57 which is that the film does not form evenly over the entire surface of the material. In the picture the prepared surface shows the edges of the plies of cloth which make up the composite. The ply which lies just to the left of the centre of the indent appears much darker than the others and it seems that a film has not been formed in this region. This ply is made up of continuous fibre running perpendicular to the surface . A film can be seen on the other layers in the indent which are either staple layers or continuous fibre aligned parallel to the surface.

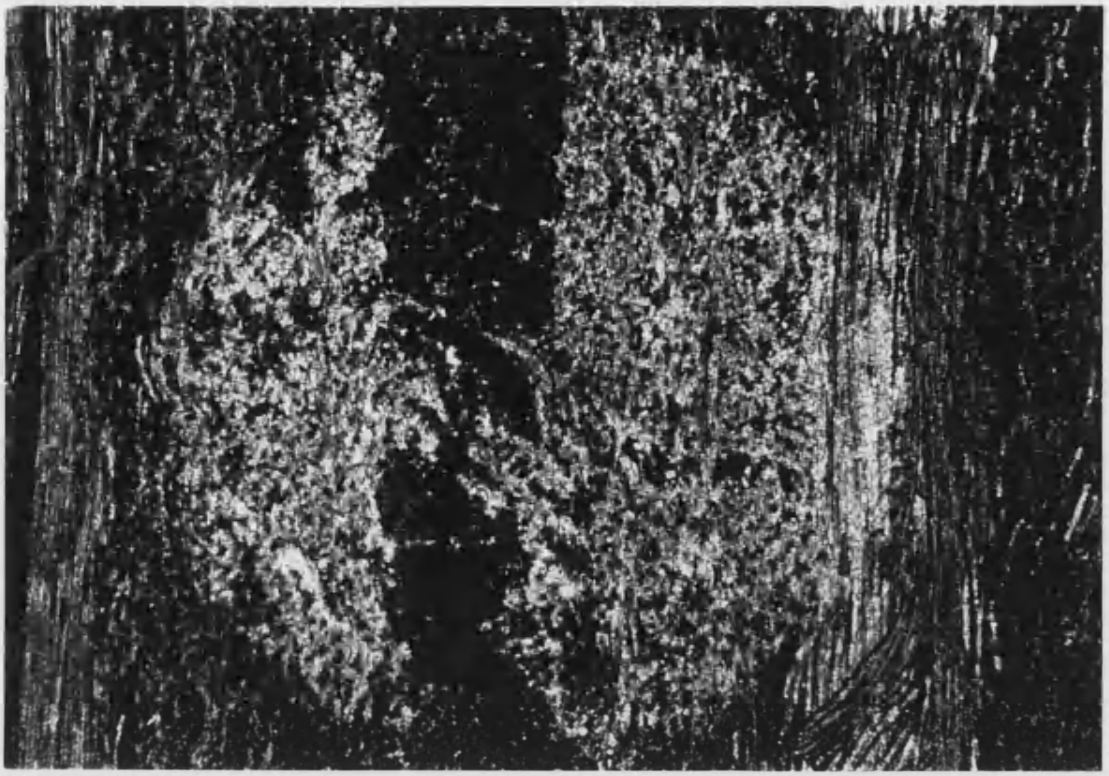

Figure 57. Photograph of a typical blunt indentation showing evidence of contact area polishing.

It can be concluded then, that the film forms at low loads under blunt indentation conditions and that increasing the load improves the quality (reflectivity and coherency) of the film. Also the film forms preferentially on layers in the composite which have low fibre volume fraction or fibres aligned parallel to the surface of the sample.

The other part of the blunt indentation testing programme was an investigation into the effect of repeated indentation. To this end samples were loaded to 1 kN and then the load was removed. This constituted one loading cycle. Load versus displacement traces were produced for samples subject to up to ten loading cycles. Also the films formed were examined using SEM.

A typical load versus displacement trace is shown in Figure 58. For clarity only the first, third and fifth cycles are shown and the curves have been smoothed using an eleven point rolling average method. From the traces it is clear that the composite

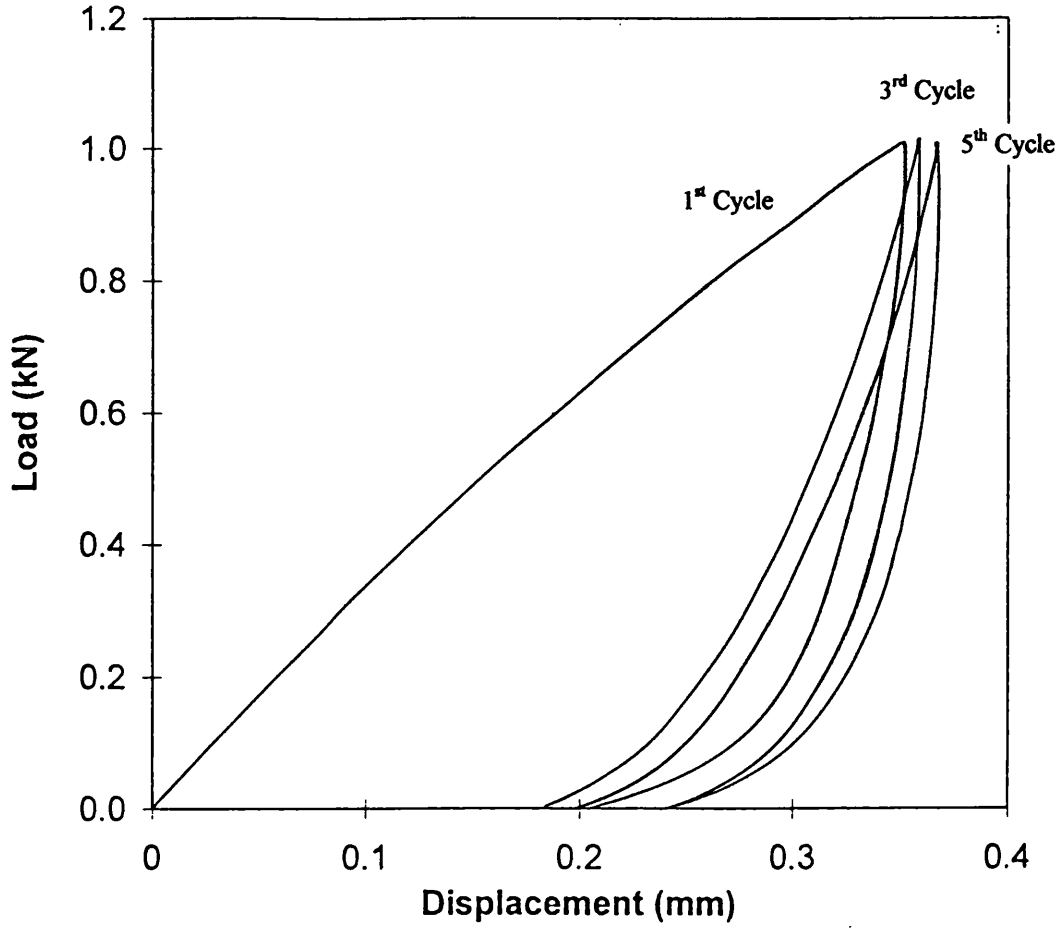

Figure 58. Load versus displacement trace for cyclic blunt indentation. Curves have been smoothed using an eleven point rolling average method and for clarity only the first, third and fifth cycles are shown.

responds in a largely pseudo-plastic manner, particularly on the first cycle, and that the depth of the indentation does not increase significantly with increasing number of cycles. This is in contrast to the effect of increasing the peak load where the depth of the indentation is increased. The elastic response of the material was calculated using Equation 27 and the results are given in Table 18.

$$R = \left(1 - \frac{A}{B}\right) \times 100 \qquad \textit{Equation 27}$$

Where R = % elastic recovery

A = area within the hysteresis loop

B = area under the loading curve

	Cycle 1	Cycle 3	Cycle 5
Loading curve area (Nm)	0.177	0.052	0.075
Hysteresis loop area (Nm)	0.085	0.030	0.028
% Elastic recovery	27	42	63

Table 18. Results of analysis of load versus dispalcement traces for cyclic blunt indentation shown in Figure 58.

The figures presented in Table 18 show that as the number of indentation cycles increases so the response of the material becomes more elastic, and it seems likely that near perfect elasticity will eventually be achieved.

SEM analysis of the indentations showed that the quality of the film produced improved with increasing number of indentation cycles. Figure 59 shows the surface of the carbon-carbon composite sample in three states. The first photograph shows the as stripped surface and the ends of fibre which are perpendicular to the surface of the sample are clearly visible. In the second picture, which shows the surface after two indentation cycles, the structure of the underlying composite cannot be determined. This is due to the presence of a film on the surface. It is evident from this photograph, that the film is made up of small angular particles which are pressed together to for a coherent surface. In the final picture (after 5 loading cycles), the film has spread to cover more of the surface and it appears to be smoother. However it can be seen that it does not cover all of the surface and it contains many cracks and defects.

8.5.3. Proposed wear mechanism

The industrial significance of the formation of surface films on carbon-carbon composites under non-sliding contact conditions, is that it may explain why wear occurs where there is no obvious cause. Examination of Figure 51 shows that while the surface of the film may appear coherent, it is only bound very loosely to the substrate. Apart from this obvious pictorial evidence more support is supplied from the fact that adhesive tape stripping is effective at removing the film. This implies that the bonding between the tape and the film is stronger than that between the film and the substrate. Since the adhesives used in adhesive tape are not particularly strong it can be concluded that the substrate/film bonding is weak. It is this fact which leads to the suggestion of a wear mechanism which does not involve a sliding contact.

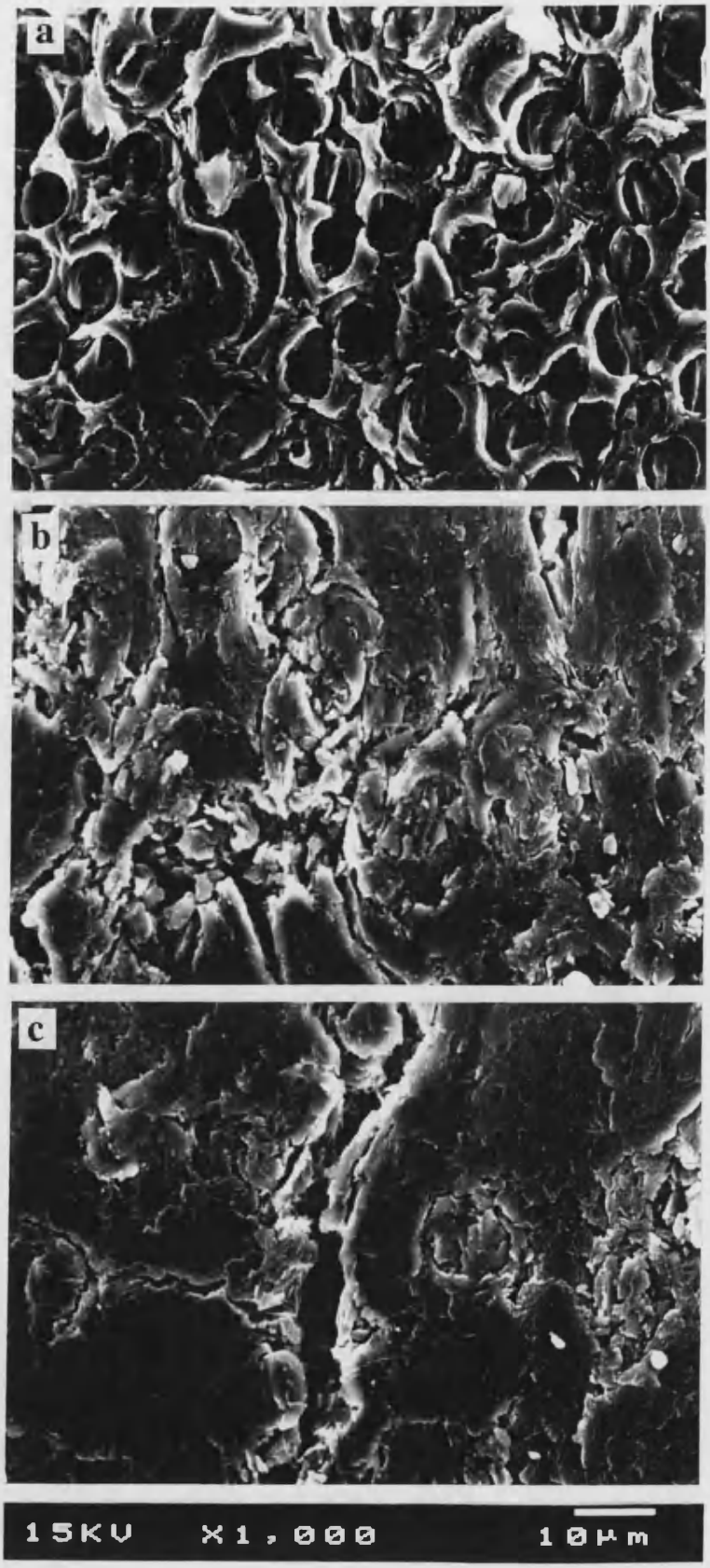

Figure 59. Three SEM micrographs showing the surface of the composite after a) zero, b) two and c) five indentation cycles.

If a component is put into service and the loading conditions are suitable a surface film will form. Because this film is only loosely bound to the substrate it is conceivable that the film could become detached. This is very likely in aircraft brakes where there is a lot of vibration and light impact loading. Having lost its surface film the substrate is exposed and so a new film can form. This cyclic process can continue indefinitely and, since material is lost at each stage it represents a wear process, however it is not known how quickly the film forms under service conditions and since the film is only of the order of 10 μm thick the process would be slow. By this mechanism the tenons of brake discs could wear to a point where the remaining tenon cannot support the loads involved in braking and the disc could fail.

8.6. Causes of changes in material properties

8.6.1. Physical mechanisms

There are in fact very few physical mechanisms by which the properties of a material can be altered. Of course the changes to material properties can be positive or negative. Since this chapter is concerned with the reasons for failure of carbon-carbon composite brake discs, only negative changes will be considered here.

The reduction of mechanical properties of carbon-carbon composite materials by physical methods is caused by the accumulation of damage in the structure. In carbon-carbon composites this means the formation of cracks or porosity as a result of the applied stresses. Under conventional test conditions the stress in a sample of carbon-carbon composite is gradually increased until failure occurs. In this case the damage is built up in the structure of the material only close to the point of failure. While this kind of damage accumulation is of scientific interest, it is not so significant from an industrial point of view since components are designed such that the stresses in them should never approach the failure stress of the material. What is of commercial interest is the build up of damage in response to loads which should be benign. Many materials are known to fail under cyclic loading to well below their static strength i.e. they have a finite fatigue life. In aircraft brakes there are obviously many components to the stress state placed on the discs, however some of these will be fatigue-like in nature. Surprisingly there is very little information in the open literature on the subject of fatigue in carbon-carbon composites. What information there is suggests that the

fatigue response of carbon-carbon composites is dependent on nano-scale defects[95], and the amplitude of the mean stress[96]. However in general it is thought that carbon-carbon composites exhibit extremely good fatigue properties with infinite fatigue lives being predicted at around 50 % of the static strength[97]. Therefore it can be concluded that fatigue is unlikely to be the cause of failure of carbon-carbon composite aircraft brake discs.

It is possible that local damage could be caused if high stresses were produced in limited regions of the component. For example, if a piece of debris were to be introduced between the torque tube and the LBF of a tenon this could cause point loading and very high stresses. However it has already been shown that the material copes well with blunt indentation, which is an analogous loading situation, and therefore this seems unlikely to occur in the practical application.

8.6.2. Chemical mechanisms

Carbon can undergo chemical reaction with all known elements and some of these reactions have extreme effects on the mechanical properties of the carbon material. Some of the most deleterious reactions are those which involve consumption of carbon and the formation of gaseous products. These gasification reactions have been discussed in detail in Section 4.3. They are of particular significance in the field of aircraft brakes where high temperatures are routinely achieved during service. Also since aircraft brakes are open to the atmosphere, which contains oxygen, oxidation is of particular pertinence. Unfortunately the oxidation reactions of carbon are among those having the most severe effect on mechanical properties. For carbon-carbon composites a general rule of thumb is that for 10 % oxidative weight loss the tensile strength is reduced to about 50 % of its unoxidised value.

Oxidation and general structure disruption of nuclear graphite can also occur as a result of the radiation which is present in nuclear reactors. This is commonly referred to as radiolytic oxidation and its effects can be as severe as the more conventional thermal oxidation. Fortunately, aircraft brake discs are not subject to high doses of radiation and so this effect can be ruled out.

9. CHARACTERISATION OF MODEL COMPOSITES

Thus far all the results presented in this study have arisen from tests conducted on, and observations of, commercial disc material. There are a number of difficulties associated with this approach. Firstly, the fibre architecture of the material is very complex. This means that two samples machined from positions adjacent to each other in a disc, might actually contain different quantities of fibrous reinforcement in different orientations. Obviously this introduces a random factor into the results and hence increases the scatter. Also, it makes the interpretation of micrographs more difficult and this is of particular importance when the failure modes are being characterised.

The second major drawback of using disc material is that for ex-service material the exact nature of the conditions of service are not known. As was discussed earlier, this means that the "age" of the material can never be truly assessed.

Finally, there is the problem of physically obtaining material which exhibits significant changes in material properties. The problem of material degradation in service is fairly rare and so ex-service material exhibiting the effect is also scarce. There is ex-service material available from failed discs, but the problem here is that often the observed changes in the structure of such material could be as equally attributed to events occurring before and after failure.

Clearly a method of eliminating some of these variables is required if the results of a testing programme are to be significant. One way of doing this is to reduce the variation in a group of samples, and hence results, by testing a very large number. This is expensive in terms of both time and money and so was impractical for the purposes of this project. Therefore another method of simplifying the problem was used. This involved manufacturing a number of model materials which represented parts of the structure of the commercial disc material. A number of model fibre architectures were designed which represented intermediate stages between the simplest case and the commercial material. It was hoped that by interpretation of the results from tests on these materials, inferences about the performance of the commercial material could be drawn.

9.1. Fibre lay-up and composite production

Possibly the simplest composite material which can be imagined is that which contains unidirectional fibrous reinforcement in a homogeneous matrix. To construct a unidirectional composite the fibre pre-form must have enough strength to hold the fibres in position while the matrix is added. Obviously in the case of a carbon-carbon composite where the matrix is deposited by CVI, the fibrous pre-form has no transverse strength at all. This means that the unidirectional cloth is almost impossible to handle, and hence a unidirectional composite is very difficult to make. Therefore the simplest fibre architecture which is practically possible is an orthogonal, non-woven laminated structure. This was achieved by laying a unidirectional continuous fibre cloth on top of and perpendicular to another layer of similar cloth, and mechanically linking the two using a needling technique. This resulted in a two layer cloth which was structurally sound before CVI and hence could be easily handled. This cloth was denoted TGAM which stands for textile grade aligned mat.

Another cloth used in the manufacture of some of the model composites was that also used as the basic cloth for the manufacture of the commercial material. This cloth also consisted of two layers, a continuous fibre layer and a layer of staple. The staple layer consists of short, stretch broken fibres which are carded such that they have an approximate alignment. These fibres are loosely entangled and the fibre volume fraction is very low so that the cloth has the appearance of a felt. This is the other name for this type of fabric and the term is widely used in industry. The two layer cloth was made up of a continuous fibre layer and a felt layer positioned so that the axes of the fibres in the two layers were orthogonal. These layers were needled together to aid handling as with the TGAM cloth. This cloth was denoted DAM for Dunlop aligned mat.

The final cloth used was made entirely of the staple material and hence was denoted as STA (for staple).

In order to model the role played by these layers in the commercial material as accurately as possible, it had to be ensured that they resembled the commercial cloths as closely as possible. In addition to selecting the correct fibre architecture, this involved measuring and modelling the fibre volume fraction in each of the layer types. The fibre volume fraction in the cloths prior to densification by CVI is generally lower than that found in the corresponding layer in the composite. Therefore it was possible

to increase the fibre volume fraction by compressing the cloths before the deposition of the matrix carbon. It was found that in the commercial material the continuous fibre layers contained around 30 % by volume of fibre, and the staple layers contained around 5 % of fibre. The correct number of layers of cloth to be used for each of the model materials was calculated from the weight of the cloth, the density of the fibres, the volume of the piece of material which was being made, and the required fibre volume fraction. For example to make a simulation of the staple layer in the commercial composite a fibre volume fraction of 5 % is required. Therefore to make 100 cm^3 of the model material, 5 cm^3 of fibre is required. With a density of 1.86 gcm^{-3} this means that 9.3 g of fibre is required.

All the cloths for the model materials were cut into 10 cm by 10 cm squares and then laid up by hand in the required sequence and to the required mass. Four stacking sequences were used. The first consisted of all STA cloth stacked such that the fibre axes in all the layers were parallel. The material resulting from this lay-up was denoted STAZZ, standing for STA zero zero. Schematic representations of this and all the other lay-ups used are shown in Figure 60. The other basic material which was manufactured had a fibre architecture made up entirely of the TGAM cloth. This was stacked such that the fibre direction in adjacent layers was perpendicular. This material was simply known as TGAM.

Two materials of intermediate complexity were designed using the DAM cloth. In both, each piece of cloth was laid the same way up in the stack such that the continuous fibre occupied alternate layers. In the first material, known as DAMZZ (DAM zero zero), all of the continuous fibre layers were parallel. In the second the continuous fibre layers alternated direction between 0° and 90°. Since each of these continuous fibre layers was attached to a staple layer these also alternated between 0° and 90°. This material was denoted DAMZN which stands for DAM zero ninety.

These fibre architectures are quite simple, but are reasonable representations of parts of the structure of the commercial material. Figure 60 shows the fibre lay-ups in schematic form. Obviously, the actual material consists of more cloth layers than are shown but for clarity the diagram shows only the repeat unit.

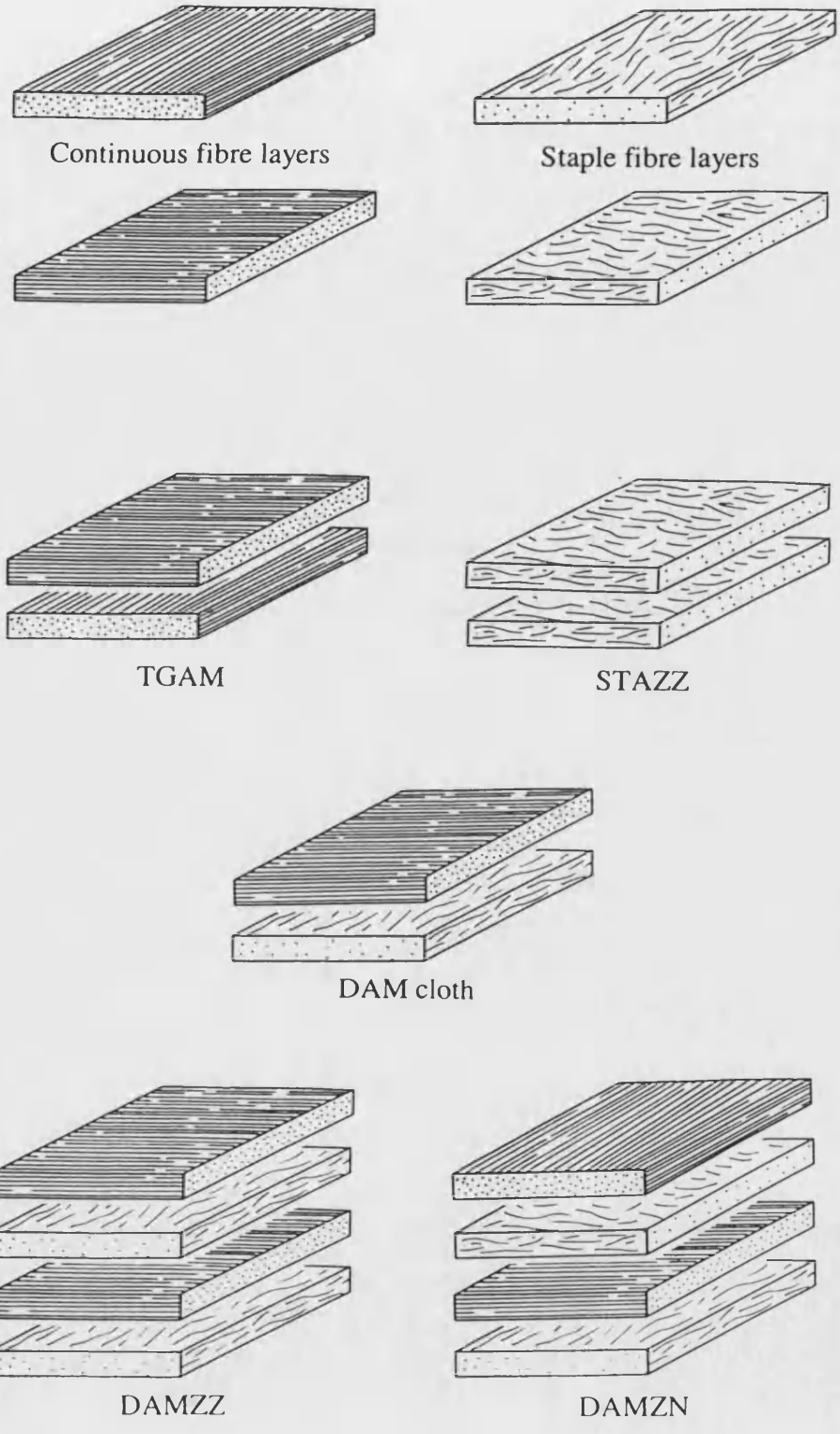

Figure 60. Schematic representation of the fibre architectures used in the manufacture of the model carbon-carbon composites.

9.2. Optical microscopy

Optical microscopy was used to characterise the structure of the model composites. The sample preparation and polishing routines used were the same as those used for the commercial disc material. As was expected, many of the same features were again seen.

Figure 61 shows an optical micrograph of a section of the TGAM model material. The majority of the figure shows the array of continuous fibres which in this case are close to perpendicular to the polished surface. The exposed ends of the fibres appear elliptical because they are not quite normal to the surface. The diameter of the fibres is approximately 8 μm and it can be seen that each is coated in a sheath of CVI carbon which exhibits the characteristic Maltese Cross pattern. It is also evident that the distribution of fibres is not completely uniform. A region of low fibre density can be seen in the bottom centre of the figure. Clearly the composite is not completely dense, and it is interesting to note that the remaining porosity tends to be large in scale. Three such pores can be seen in the top right of the picture. It is well known that CVI tends to be good at filling small pores and poor at filling large ones, an the evidence from this picture reinforces this fact.

Figure 62 shows a section of the DAMZN model material. The figure shows the distinct junction between the continuous fibre region in the bottom half of the picture, and the staple layer in the top half. The features of the continuous fibre region are identical to those of the TGAM material and this is unsurprising since the structures are analogous. The staple region, however, shows some interesting additional features. Firstly it can be seen that the fibre volume fraction is very much lower and that as a result there is more space available in which CVI carbon can be deposited. While the diameter of the fibre in these regions is still 8 μm, the surrounding matrix material forms a cylindrical structure with a diameter of about 30 μm. The much higher porosity content is also evident.

Image analysis was used in order to asses the approximate volume fractions of the various constituents of the model materials. The system used a Zeiss reflected light microscope with a video camera attached. This camera fed live images to a computer running Optimas 6.1 image analysis software. It was hoped that macros could be written for this software which would enable the measurement of the volume fraction

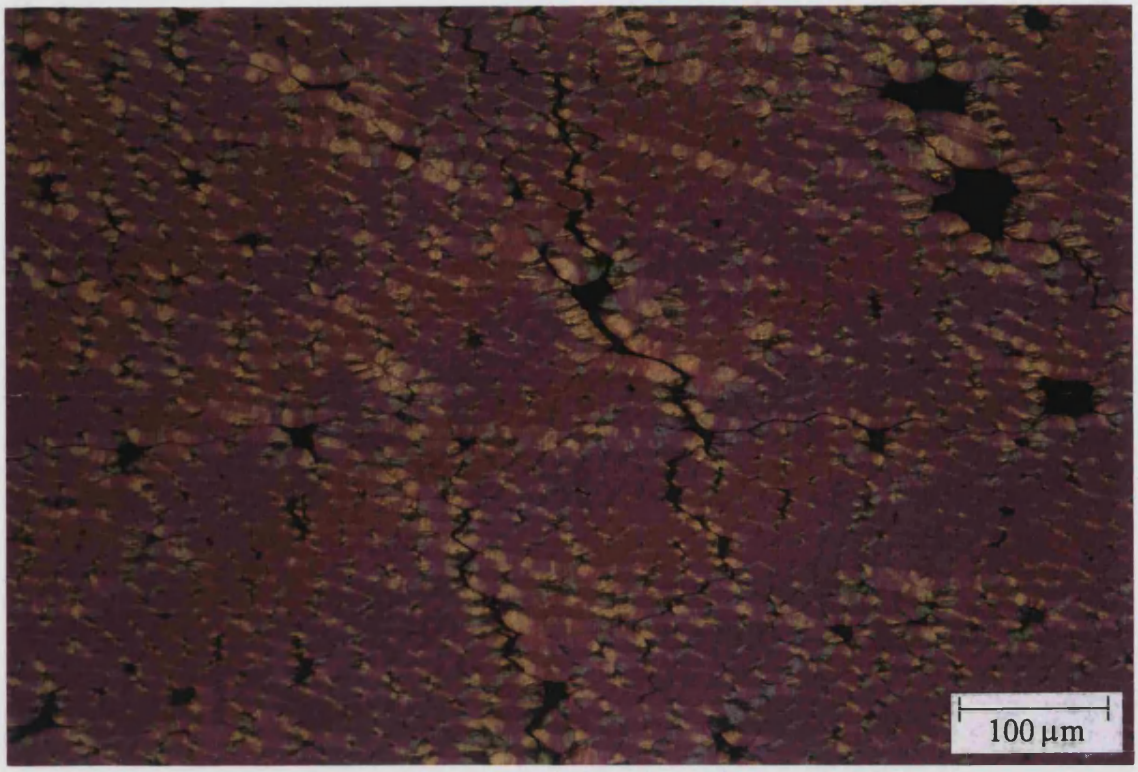

Figure 61. Optical micrograph of a section of the TGAM model showing the array of continuous fibres perpendicular to the polished surface.

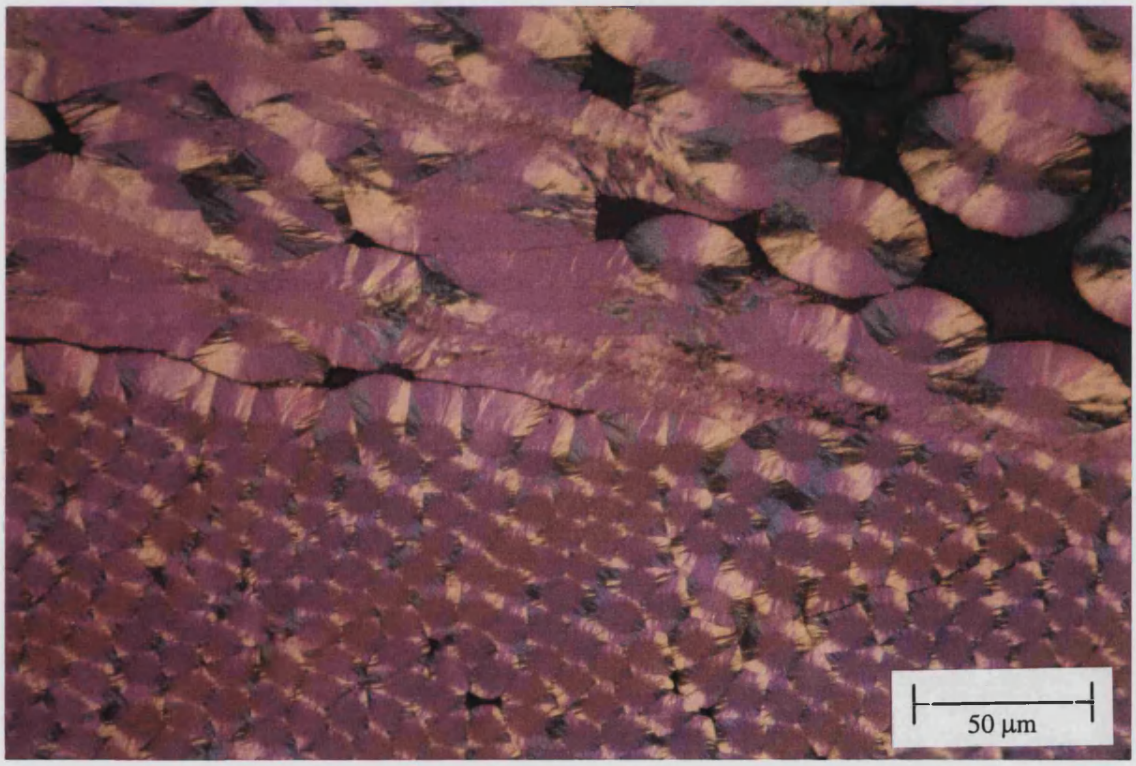

Figure 62. Micrograph of DAMZN model material showing both continuous fibre and staple layers.

of fibre, matrix and porosity in the model materials. Unfortunately, the software was only able to utilise greyscale images. This meant that in practice it was impossible to write an algorithm which could distinguish between the fibre and its surrounding sheath of CVI carbon. However it was possible to measure the porosity content.

Two methods were used and both were found to work equally well. The first involved mounting the sample in fluorescing resin and illuminating it under the microscope using ultraviolet light. In this case the porosity (now resin filled) appeared brighter than the carbon. The second involved using either fluorescing or non-fluorescing resin and illuminating the sample with white light. Because of the relatively low reflectivity of the resin it appeared dark while the reflective carbon appeared bright. Having acquired the image of the polished sample, a greyscale histogram was produced. This showed two peaks and a trough in between. The peak at the light grey end represented all the carbon material, and the dark grey peak was representative of the porosity. A greyscale value between the two peaks was determined and the image was split into two regions. Then the area fraction of the darker regions was calculated. This percentage was equal to the percentage porosity in the picture. Figure 63 shows the first and last stages of this process. At the top is a captured image of a mostly staple region, and at the bottom is the manipulated image with the porosity highlighted in white.

Material / Layer	Porosity content %
Staple layer	19
Continuous fibre layer	8
STA	20
TGAM	11
DAMZZ	15
DAMZN	15

Table 19. Results of porosity content determination by image analysis on model materials.

Table 19 shows the results of the image analysis and gives the approximate porosity content of each of the layers and model materials. Two things should be borne in

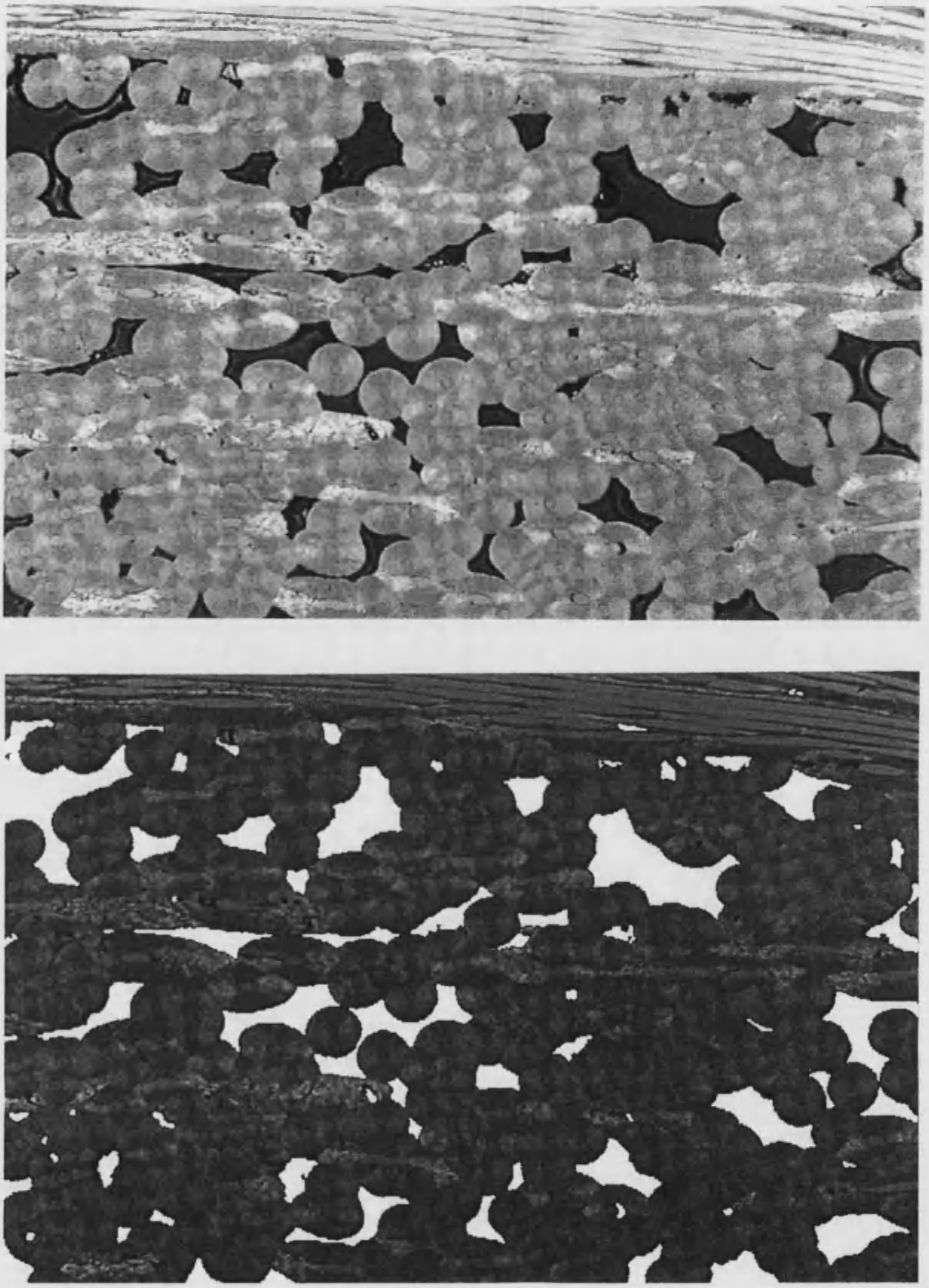

Figure 63. Two images of the DAMZN model material. At the top is the as captured image, and in the image below the porosity has been automatically selected and highlighted in white.

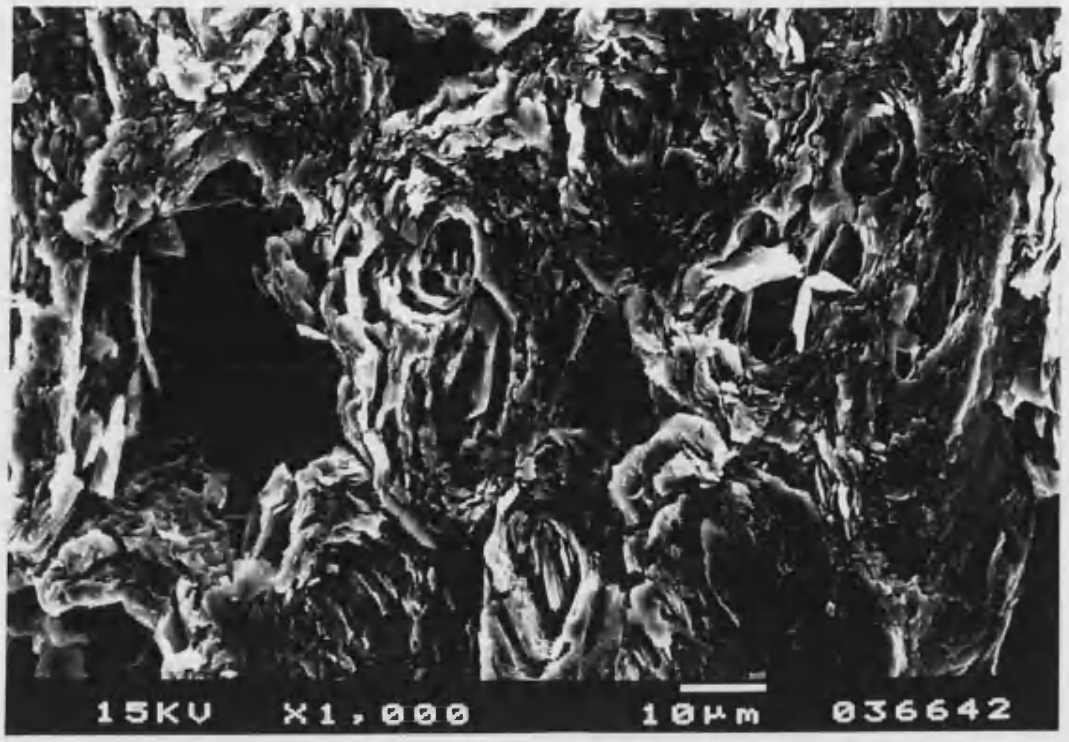

Figure 64. Scanning electron micrograph of a section through a layer of staple in one of the model materials.

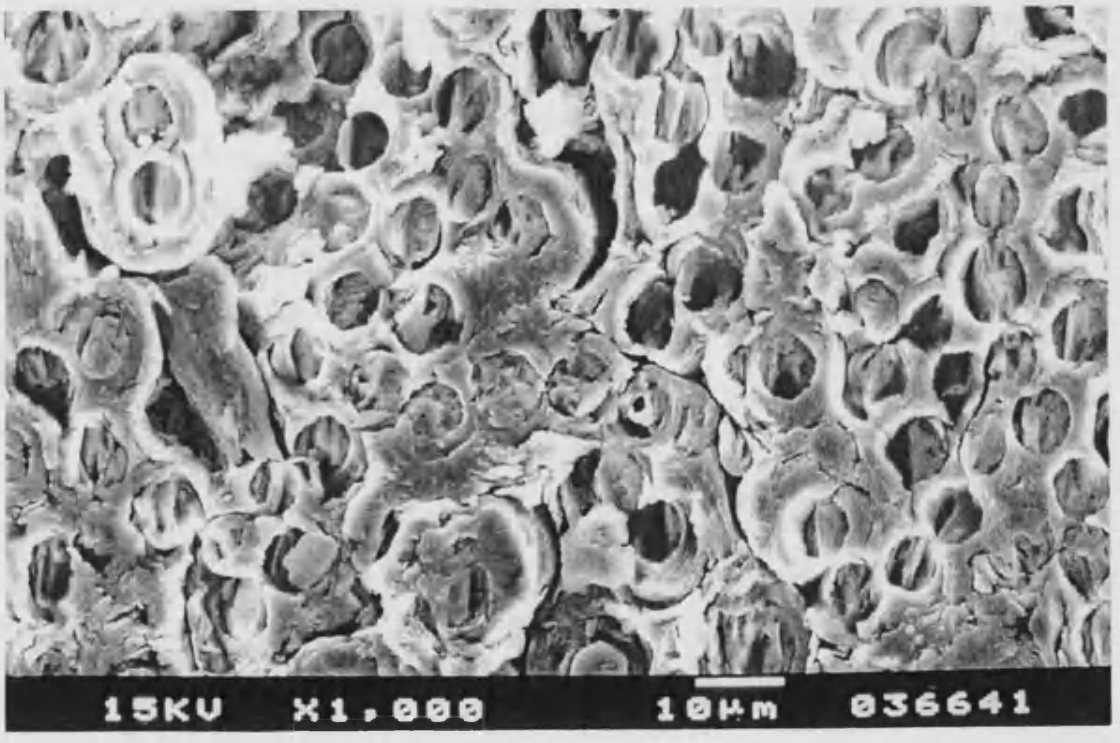

Figure 65. Scanning electron micrograph of a continuous fibre region in one of the model materials.

mind when considering these data. The number of samples analysed was small and obviously the porosity content of the material varies from point to point and block to block. Also, the image analysis system assesses the greyscale cut-off value between porosity and carbon automatically. By over illuminating the sample the computer can underestimate the porosity content by up to 10 %. Finally, the computer system has a finite resolution. Therefore, these figures should be regarded as approximate only.

9.3. Electron optical analysis

SEM was also used to investigate the structure of the model materials. As expected there were no fundamental differences between the materials except for those caused by the different fibre architectures. The samples were prepared for SEM examination by milling and stripping in an identical manner to the surfaces used in the blunt indentation investigation.

An SEM image of a section through a staple layer is shown in Figure 64. As with the optical micrographs the low volume fraction and uneven distribution of fibres can be seen along with significant porosity. In the centre of the picture two fibres can be seen, and the sheaths of matrix appears to have been wrapped around them in layers in a manner identical to that seen in the commercial material. This feature is not so evident in the continuous fibre regions (Figure 65). However the absence of this feature is probably due to the low volume fraction of matrix which is a direct result of the closer packing of the fibres.

10. FOUR POINT FLATWISE FLEXURAL TESTING

10.1. Introduction

In order to measure the mechanical properties of a material a suitable test method has to be found. In the case of long fibre reinforced carbon-carbon composites this is a difficult task as a result of the unique properties of these materials.

Direct compression testing, as has already been shown, is fraught with difficulties. In essence most of these are concerned with the premature failure of the material by non-compressive modes. This is caused by elastic spreading of the platens, non-axial loading, and buckling instability[98]. Although the method is satisfactory for carbon fibre-SiC matrix composites, the low interlaminar shear strength of laminated carbon-carbon composites means that the principal failure mode is vertical splitting of the test piece, with individual plies then free to buckle[99]. The likelihood of this type of failure can be minimised by reducing the length to lateral dimension ratio of the specimen, and hence the results of these tests are geometry dependent. Indirect compression test methods similar to those used for polymer matrix composites such as that utilising the Celanese jig[100,101], have been successfully used for carbon-carbon composites and interestingly the strengths reported tend to be significantly higher than those for direct compression tests.

Tensile testing is a simple test method, particularly for "forgiving" materials. However in the case of brittle materials, carbon-carbon composites and indeed ceramic matrix composites (CMC) in general, it suffers from the difficulties of applying the load to the specimen and in the alignment of that load. Perfect alignment of the loading axis and the specimen axis is required so as to reduce the bending stresses in the sample to as near zero as possible[102]. Gripping the sample is difficult as it is a requirement of the test that the failure is not associated with the gripped part of the specimen. Wedge grips are commonly employed, however with these grips the gripping force is not controlled and so they are often used with a compliant inter-layer in order to spread the load. This means that end tabs, commonly of aluminium, have to be attached to the specimen, and hence the test loses its simplicity. Alternatively a dog bone shaped specimen can be used, and gripped by pairs of rods acting on the shoulders of the sample. This geometry causes a lateral compressive load at the grips

sufficient to avoid delamination of the sample. However, this method requires considerable precision in the machining of the specimens and is known to be unsuitable for materials with poor shear or compression properties.

The measurement of the shear properties of CMC materials can be achieved by any one of a number of methods, many of which work well. These include short-span three point bending, double punch shear, plate shear and Iosipescu. These tests can give good information on the shear strength, and in some cases modulus, of materials.

Usually brittle materials are conveniently tested in flexure because the test piece can be loaded without a mechanical means of attaching it to the test machine. The load is applied by compressive contact at three or four rollers which apply a bending moment to the sample. This allows the use of simple rectilinear specimens, and the use of articulated rollers can even tolerate reasonable machining inaccuracies. Of course there are some difficulties with flexure testing and these include high point stresses at the loading rollers, measurement of strain, calculation of true stress, and induction of the desired failure mode. All of these require careful consideration if the result of the test is to be valid and correct. Some of the more significant problems of flexure testing are addressed in Section 10.2. with the particular problem of strain measurement discussed in Section 10.2.4.

10.2. Selection of appropriate sample and test geometry

10.2.1. Representative structure sampling

It an obvious requirement of any testing that the measured results represent, as closely as possible, the true property of interest. In the case of mechanical testing it extremely important that the samples which are prepared resemble the bulk material. It is all too easy to discard samples which contain obvious defects on the grounds that they are made from poor material. However this defeats the object of the testing and therefore in this testing programme all samples were tested irrespective of how poor the material appeared. The exception to this was samples which contained defects which were clearly an artefact of their preparation.

The model materials used in this investigation were manufactured in blocks measuring 100 mm by 100 mm, with a thickness of approximately 20 mm. This allowed a little scrap in the length dimension of the specimens and a great deal of scrap in both the width and depth directions. In order to reduce the sample to sample variation as much

as possible, as many samples as was possible were machined from as few blocks as possible. This reduces the potential for scatter in the results but unfortunately also increases the chance that the particular blocks used are not representative of the batch as a whole. To reduce any bias as a result of selection of the blocks they were chosen at random. In general the specimens were machined from the middle of the blocks to reduce the effects of any property gradients within the blocks. Also, the specimens cut from an individual block were tested both face up and face down at random to reduce the effect of any advantageous sampling of the fibre layers.

10.2.2. Three and four point flexure

Flexure was chosen as the best test method for reasons of simplicity, and also because if performed correctly it will yield a value of tensile strength. However it remained to decide between three and four point flexure. Figure 66 shows schematic diagrams of the loading conditions in idealised three and four point loading.

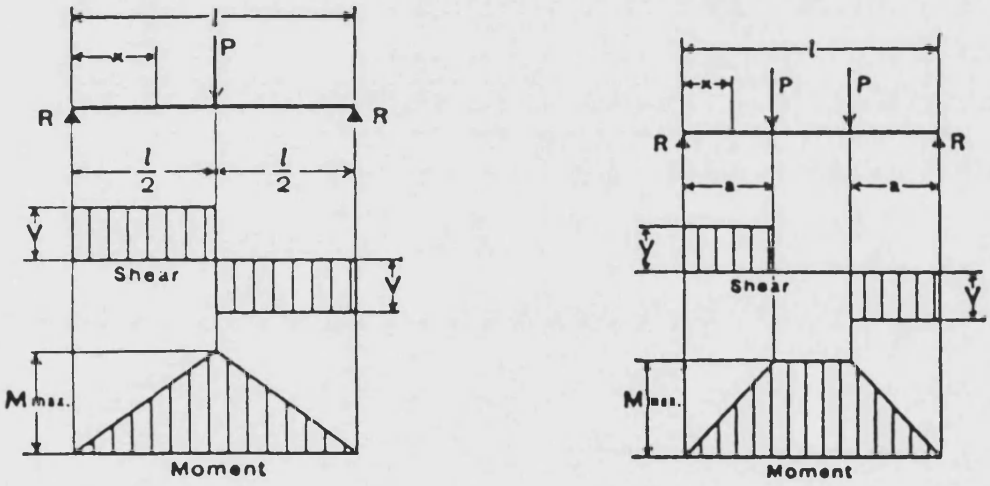

Figure 66. Schematic diagrams of the loading conditions in three and four point flexure[103].

These loading conditions are discussed in detail in many basic mechanics books[104,105,106], but there are two significant differences between the conditions. Firstly, the sample in three point bending is subject to shear stresses for its entire length, whereas the sample in four point bending experiences zero shear between the

inner rollers. This is important since it is known that carbon-carbon composites favour failure by interlaminar shear mechanisms and this type of failure renders the calculation of strength invalid. Secondly, in three point flexure only the plane of material below the loading roller is subject to the peak stress. By contrast in four point flexure, the entire volume of material between the loading rollers is subject to the peak stress. Therefore four point flexure effectively tests a larger amount of material[107]. Hence it could be expected that the results of four point flexural testing would be more consistent and more representative of the true strength and so four point flexure was chosen as the most desirable test method.

10.2.3. Induction of desired failure mode

It is most important for the valid calculation of the strength from a flexure test, that the failure mode be valid, i.e. either tensile of compressive. However it is well known that the use of short spans can induce failure of the specimen by a shear mechanism. Usually the mode of failure for a given material can be controlled by altering the span to depth ration (SDR) of the specimen. Altering the SDR has the effect of changing the ratio of the peak tensile and shear stresses. High SDR values increase the ratio of tensile to shear stress and hence favour failure by a tensile mechanism. For glass fibre reinforced plastics an SDR greater than 20:1 is commonly sufficient to induce tensile failure. However laminated carbon-carbon composites suffer from very low interlaminar shear strengths while achieving high tensile strengths. Theoretically this means that much higher SDR values are required to cause tensile failure. Unfortunately in practice, interlaminar shear failure is almost impossible to avoid even at SDR greater than 50:1[64]. It is not entirely clear why this is although it has been suggested that the point loading effects beneath the loading rollers and overlap of the associated stress fields might be sufficient to induce failure[108]. Finite element analysis has been used to model this condition and it has been found that failure can be initiated by the high stresses associated with the loading rollers[109]. An indication of the magnitude of these stresses is shown in Figure 67. This is a photoelastic diagram of a beam in four point flexure and shows that the upper and lower surfaces in the centre section are subject to 6 units of stress, the four corners are subject to zero stress and under the load points the stress is greater than 10 units[110].

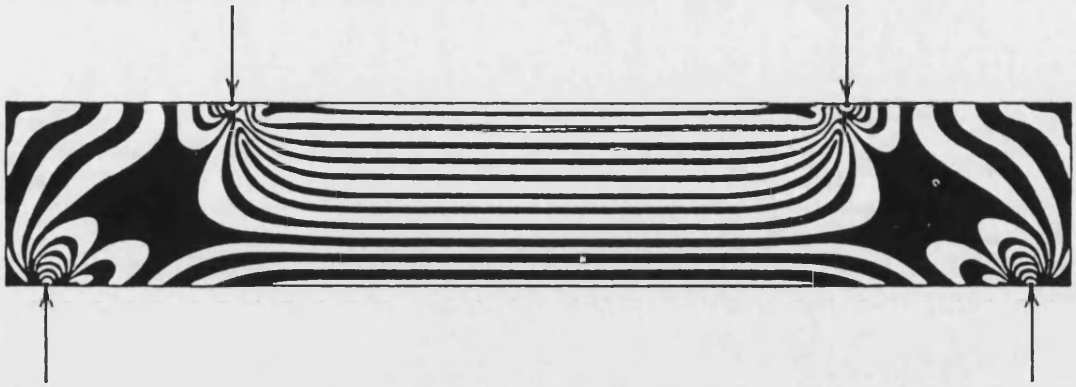

Figure 67. Photoelastic diagram of a beam in four point bending[110].

So in choosing the dimensions of the specimens it was realised that the SDR should be as high as possible. However the total size of the specimen was restricted by the size of the manufactured blocks. This meant that the length of the sample was restricted to a maximum of 90 mm. For a SDR of 20:1 this implied a depth of 4.5 mm. However there is a conflicting requirement which is to stress as representative a sample of the structure as possible. A depth of 4.5 mm will include around 6 reinforcement layers, and it was considered that this did not constitute a good representation of the whole structure. It was determined that a depth of 7 mm would sample enough of the structure to be representative and that the SDR of 10.7:1, while far from ideal, would be sufficient.

Hence the dimensions of the specimens that were used were 90 mm long, 10 mm wide and 7 mm deep. The testing rig used a loading span of 25 mm and a support span of 75 mm.

10.2.4. Sources of error in flexure testing

As with all other test methods, there are many potential sources of error in flexural testing. It is impossible to completely avoid all of these, but it is important that they are understood so that they can be minimised as much as is practically possible. Broadly, the sources of error can be divided into internal sources, or those arising from mathematical assumptions and interpretations, and external sources, caused by practical inaccuracies.

Internal errors can arise from four main assumptions which are made in simple beam theory;

i. Transverse planes perpendicular to the longditudinal axis of the beam remain plane after the beam is bent.
ii. The modulus of elasticity in tension is equal to the modulus of elasticity in compression and the beam material is isotropic and homogeneous.
iii. The maximum deflection must be small compared to the beam depth.
iv. The beam must deflect normally under elastic bending stresses but not through any local collapse or twisting[111].

The first two of these assumptions imply that the stress and strain are proportional to the distance from the neutral axis and that the stress does not exceed the limit of proportionality of the material. They disregard the effect of any shearing resistance. Also, the stress is only proportional to the distance from the neutral axis if the loading is achieved without the application of local stresses to the beam. This is not practically possible and so, inevitably, there are local departures from linearity in bending stress around the loading points[112]. These loading point effects are known as wedging stresses. It has been mentioned previously that these stresses may well be the cause of premature failure of carbon-carbon composite beams tested in flexure even at high values of SDR.

Some error arises from the assumption that the material of the beam is isotropic and homogeneous. Clearly this is not the case for composite materials. However the solutions for materials which do not satisfy these criteria are extremely complex. In short, non-homogeneity of the beam can cause the applied bending stress to be resolved non-symmetrically which in turn can cause twisting and non-circular bending to occur. Some of the error is due to the erroneous assumption that the neutral axis of the beam is at the mid-depth. It is known that the accumulation of damage will cause the neutral axis to shift towards the undamaged side. This implies that the neutral axis is at mid-depth only before the onset of damage in the sample. Carbon-carbon composites are pre-cracked bodies and so it may well be the case that the neutral axis is not at mid-depth even before the application of any load. However if it is assumed

that the distribution of cracks (damage) in the unstressed state is uniform then this effect can be ignored.

It is also usually assumed that the tensile and compressive moduli of the material are the same. Chamlis[113] has derived in closed form the solution for the bending stress when this condition is not met. The effect of the ratio of moduli on the calculation of bending stress is given in Table 20.

E_T/E_C	Percentage error	E_T/E_C	Percentage error
1.000	0	1.025	- 0.6
0.975	+ 0.6	1.050	- 1.2
0.950	+ 1.3	1.075	- 1.8
0.925	+ 1.9	1.100	- 2.4
0.900	+ 2.6	1.150	- 3.5
0.800	+ 5.6	1.200	- 4.6

Table 20. Errors in calculated bending stress when the tensile modulus (E_T) is not equal to the compressive modulus (E_C). After Baratta[111].

The validity of the assumption that the strain in a beam is proportional to the distance from the neutral axis can also be questioned, and is dependent upon the ratio of the width and depth of the beam. At intermediate values of this ratio, the beam can flex in an anticlastic manner and render incorrect the use of simple beam formulae. Again these errors have been assessed, this time by Ashwell[114]. Using a model material with a Poisson's ratio of 0.35, and a Young's modulus to fracture stress ratio of 1000:1 it was shown that at ratios of breadth to depth of up to 20:1 the error in the calculated stress was less than 0.1 %.

External error sources, those arising from the practicality of the test, can be caused by a number of phenomena;

i. Load mislocation.
ii. Beam twisting.
iii. Friction.
iv. Local stresses.

v. Contact point tangency shift

vi. Surface preparation.

It is usual to assume that, for the four point bending condition, the moment within the centre span is constant. However, if the loading contacts are not perfectly symmetrical about the loading axis this is not the case. This condition can also be caused if the loading rollers are displaced with respect to each other in the direction of the load. Here the loads applied by the rollers will be different and hence the loading condition as a whole becomes asymmetric. Torsional loading of the beam can be caused inadvertently by non-uniformity or non-parallelism of the loading lines. It can also arise if the sample itself is twisted along its length. Both of these effects can be significant, but they can be reduced by judicious use of articulations in the loading rig and by taking care when conducting the test.

Simple beam theory assumes that the loading point contacts are frictionless. However this is not the case and friction at the loading point can also induce couples at the contact and axial forces at the neutral axis. The axial forces are small but failure to account for the couple in the calculation of the flexure stress will result in error. Newnham[115] and Weil[116] report errors as high as 13 % between failure stresses calculated from test results using roller type contacts, and rigid knife edges.

Local stresses are of two main types, contact stresses, and wedging stresses. In both cases they can be practically controlled by the dimensions of the loading points. Wide knife edges or large diameter rollers must be used to reduce the chance of crushing at the loading points. Another local stress factor which cannot be ignored is the influence of the ends of the beam. There must be sufficient overhang beyond the support points such that the ends of the beam do not amplify the local stresses at the loading points. It has been determined[110] that the contact stresses are minimal at a distance from the loading point equal to the depth of the beam and therefore the beam should overhang the support points by at least one beam depth.

Significant changes in span can occur during flexure if the dimensions of the load and support points are large with respect to the depth of the beam. The effect is known as tangency shift and is shown schematically in Figure 68. Thus the requirement to minimise tangency shift is for the diameter of the loading points to be small. This is in direct conflict with the local stress considerations.

The final external error source is that of poor or careless surface finishing or sample preparation. This can cause the inclusion of significant defects which reduce the ultimate stress bearing capability of the sample. Although care is required in the machining of carbon-carbon composites, this effect is of extreme importance in the testing of truly brittle materials such as monolithic ceramics.

Interestingly, some of the effects mentioned in this discussion cause negative errors in the calculated bending stress, while others cause positive errors. Hence it is possible that in some cases an approximately correct stress is calculated by chance due to the errors cancelling each other out.

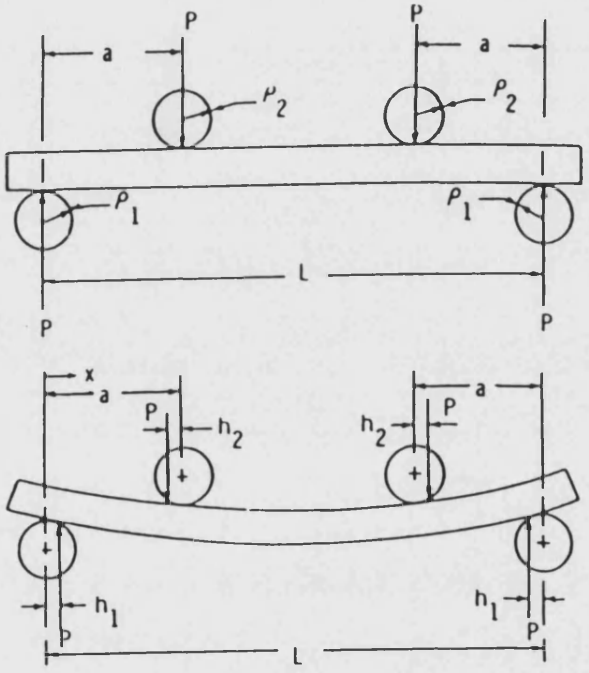

Figure 68. Schematic diagram showing tangency shift in four point bending as a result of sample flexure[111].

10.3. Strain measurement

As has been shown, the successful employment of the four point flexure test is not as simple as it might at first have seemed. Most of the considerations discussed so far concern errors in the calculation of the bending stress. However in order to gain the most from each test it is essential to determine both the stress and the strain. This

allows the calculation of strain to failure, the modulus and the work of fracture. Unfortunately the correct measurement of strain is not simple either.

Conventionally the flexural strain is calculated from the measurement of displacement of the centre of the beam. These calculations make use of the geometrical fact that the radius of curvature of an arc can be calculated if the position of three points on that arc are known. Figure 69 illustrates one of the most common mistakes which is made when using four point flexural testing. In the first, and incorrect case, the three points whose position is known are the centre of the beam and the two support points. If it is assumed that the radius of curvature of the beam at any point is related to the applied moment, then it is clear that the radius of curvature of the beam varies along its length. Since the radius of curvature of the line varies it is not an arc, and hence the circular geometry on which the strain calculation is based is not valid.

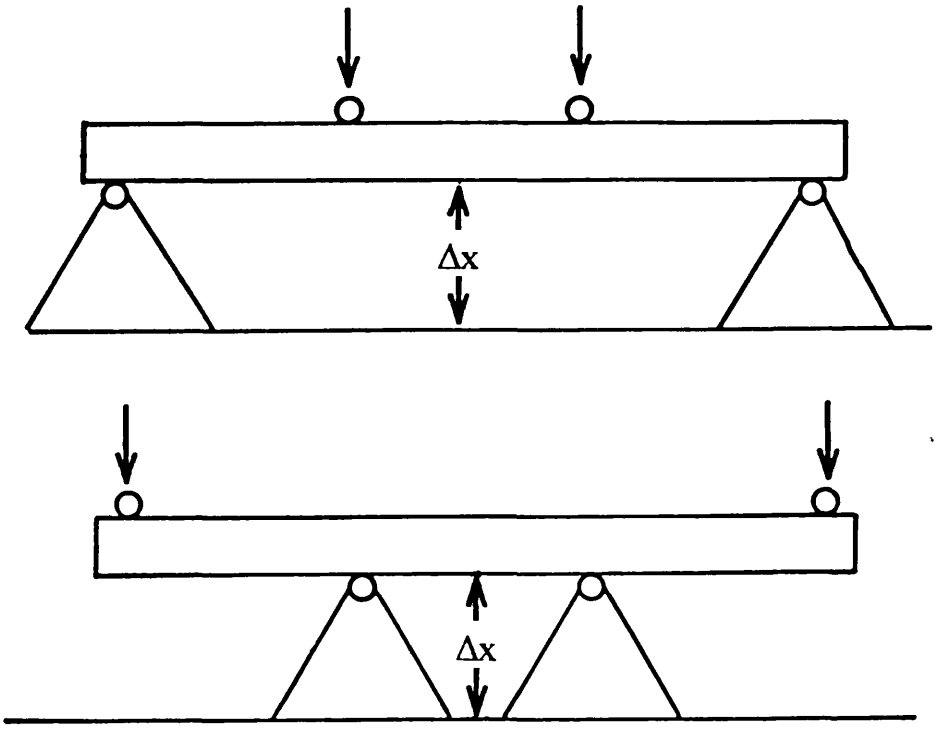

Figure 69. Incorrect and correct measurement of centre point deflection in four point flexure.

In the second case, the three points are the centre of the beam and the two loading points. Since in theory this central portion of the beam is subject to a constant moment, it seems logical to assume that in this region the radius of curvature is also

constant, and hence the three points do lie on an arc. Thence the calculation of strain by circular geometry is valid. It is this displacement measured by the second method which is the true centre point displacement which is referred to in the standard testing methods.

This does cause a practical difficulty since it is obvious that, for a given sample size and loading rig dimensions, the correct centre point displacement is very much smaller than the total beam deflection. Consequently for moderate sample sizes it is often the case that the true deflection is very small. Indeed for the sample dimensions used in this study, it was impossible to confidently determine the strain by a displacement measurement method. It should also be noted that the determination of strain by this method also assumes the validity of the beam equations which is not the case once matrix cracking or delamination occurs.

It has been suggested that the strain can be calculated from the relative displacement of the support and loading points[117]. However, despite the fact that this method fixes the position of all four loading points, no three of them lie on an arc and hence the strain cannot be calculated from circular geometry.

The other method of determining the surface strain of a sample is by the use of strain gauges. Strain gauges are small electronic devices which make use of the direct relationship between the resistance and the strain in a conducting element. They consist of a thin conducting element, usually copper, which is doubled back on itself several times, and attached to a polymeric sheet. When connected using lead wires to a resistance monitoring device the gauge gives a direct measurement of the strain to which it is subject. This device is attached to the sample using a suitable adhesive, typically a cyanoacrylate, and hence the strain in the surface of the sample can be continuously recorded. Since the gauge is thin it is assumed that it does not significantly contribute to the stiffness of the sample. There is some doubt, however, over the influence of the adhesive. For non-porous solids the effect is likely to be negligible, but the carbon-carbon composites tested here are porous. During attachment of the gauges it was apparent that some of the adhesive was soaking into the specimen. When cured, this adhesive is likely to have the effect of strengthening and stiffening the sample. Notwithstanding this, strain gauges were found to be the only practical and reliable method of measuring strain for samples of the type and size tested here.

10.4. Sample preparation

The materials were supplied in blocks measuring approximately 100 mm by 100 mm by 20 mm thick. Due to some misalignment of the cloth layers the edges of the block were not suitable for the manufacture of samples and so these were cut off using a water-lubricated diamond saw. During this operation care was taken to maintain the parallelism of the faces of the block and the registry with the original axes of the cloth layers. Also as little material as was possible was removed. At this point the centre thickness of the block was marked on each face using a silver pen. Then the large faces of the block were trimmed using a mill with a tungsten carbide tool. During milling of the first face the pattern of emergent fibre was noted and if required, adjustments were made to the positioning of the block so that the machined face and the fibre layers were parallel. In practice very little adjustment of the blocks was necessary since the parallelism of the as manufactured blocks in this plane was usually good. However in some cases the cloth layers were not perfectly flat and so layers emerged across the surface of the block.

Having trued the first large face of the block it was repositioned and the opposing face was milled so that it was parallel to the first. This resulted in a block measuring approximately 95 mm square with a thickness of around 15 mm. The thickness of the block corresponded to the depth dimension of the samples and so the block was milled to the required thickness, which in this case was 7 mm. During this lengthy process care was taken to remove material equally from the two sides using the silver marks as a reference. Also, as the final dimension was approached, the depth of the cut which was taken was reduced in an effort to minimise the damage done to the material. Initially cuts of up to 1.5 mm were taken but this was reduced so that the final cut was around 0.1 mm. Optical microscopy of sections of the material after cuts of various depth had been taken showed that the extent of damage was slight after large cuts, and was insignificant after shallow cuts.

Having assessed the correct orientation with respect to the fibre layers, the thin plate was then cut, using a diamond saw, into a number of oversized specimens. These were machined to the final dimensions using the milling technique described above. Each sample was marked with a unique identifier and checked for parallelism and correct dimensions.

10.5. Test method

The three dimensions of each sample were measured and recorded and the samples were also weighed. This allowed the calculation of a bulk density by the simple division of the mass by the volume.

If used, the strain gauge was then attached to the centre of the tensile face of the specimen. The gauges used were supplied by Measurements Group UK Ltd. and were of the general purpose copper foil type. The gauges used (CEA 06-250UW 350) were selected so that the gauge area and the solder tabs were large. Large tabs allowed direct connection of the leadwires, and a large gauge area reduced the effects of variation in strain across the area. The gauges were attached to the sample using M Bond 200 cyanoacrylate adhesive in accordance with the manufacturers instructions[118,119]. Care was take to align the axis of the gauge with the axis of the sample, and to position it at the centre. Figure 70 shows two installed strain gauges, the one on the right with the leadwires attached.

All testing was conducted on an Instron 1195 testing machine as shown in Figure 71. This produced a continuous analogue trace of time versus load. Of course, multiplication by the known crosshead speed easily converts the time axis to displacement. In addition to this the machine was connected to a computer based data logger which allowed the recording of load at given time intervals. This computer also had the facility to record the outputs from a number of LVDT and strain gauge devices simultaneously. The logged data were compatible with standard analysis software such as Microsoft Excel.

The loading rig used was of the standard adjustable, four point bend type but with a lever arrangement which allowed the measurement of the deflection of the centre of the beam. The rig is shown in Figure 72. Here the rig is exactly as it was used during the tests, with a 75 mm support span and a 25 mm load span. The contact rollers were stainless steel and were 6.35 mm in diameter. They were free rolling but not articulated. There was provision, however, for adjustment and alignment of the rollers by movement of the supporting bearings. This was done before beginning the test and further adjustment was impossible after commencement of the test. Also, due to the small amount of slack, the loading fixture was free to pivot about its point of attachment to the load cell. This allowed a degree of self levelling of the upper rollers

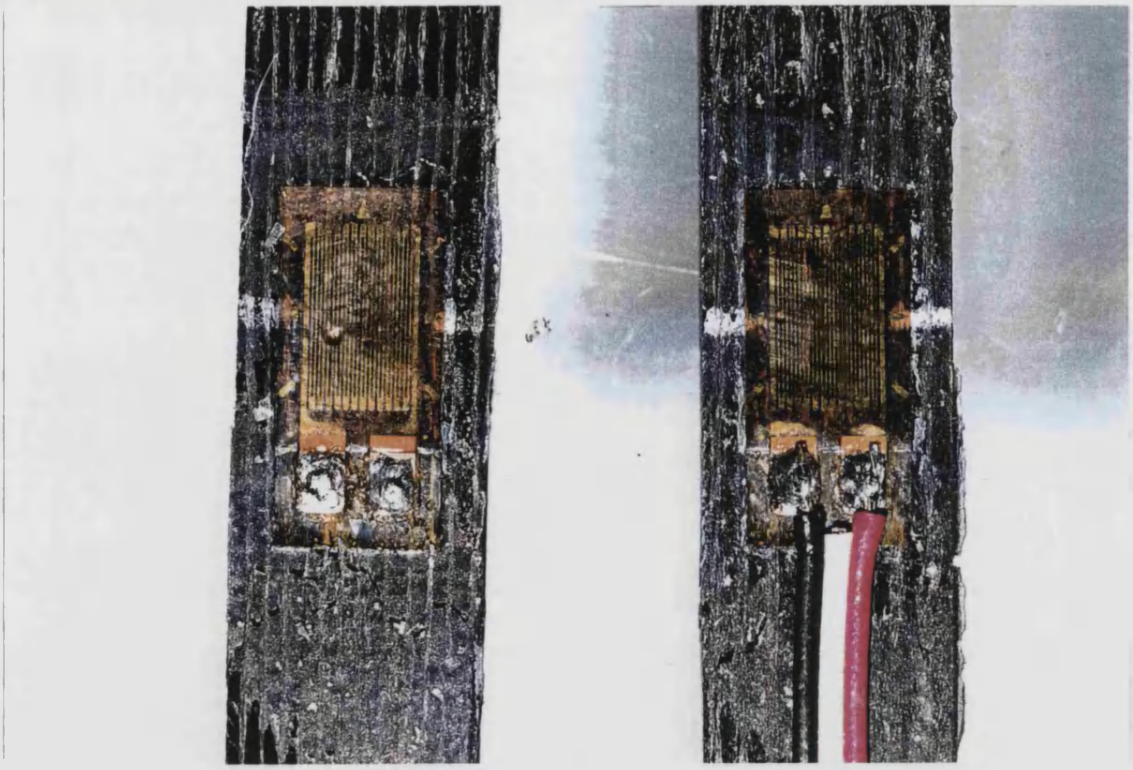

Figure 70. Photograph showing two strain gauges installed on the tensile face of flexure samples. The gauge on the right shows the attached leadwires.

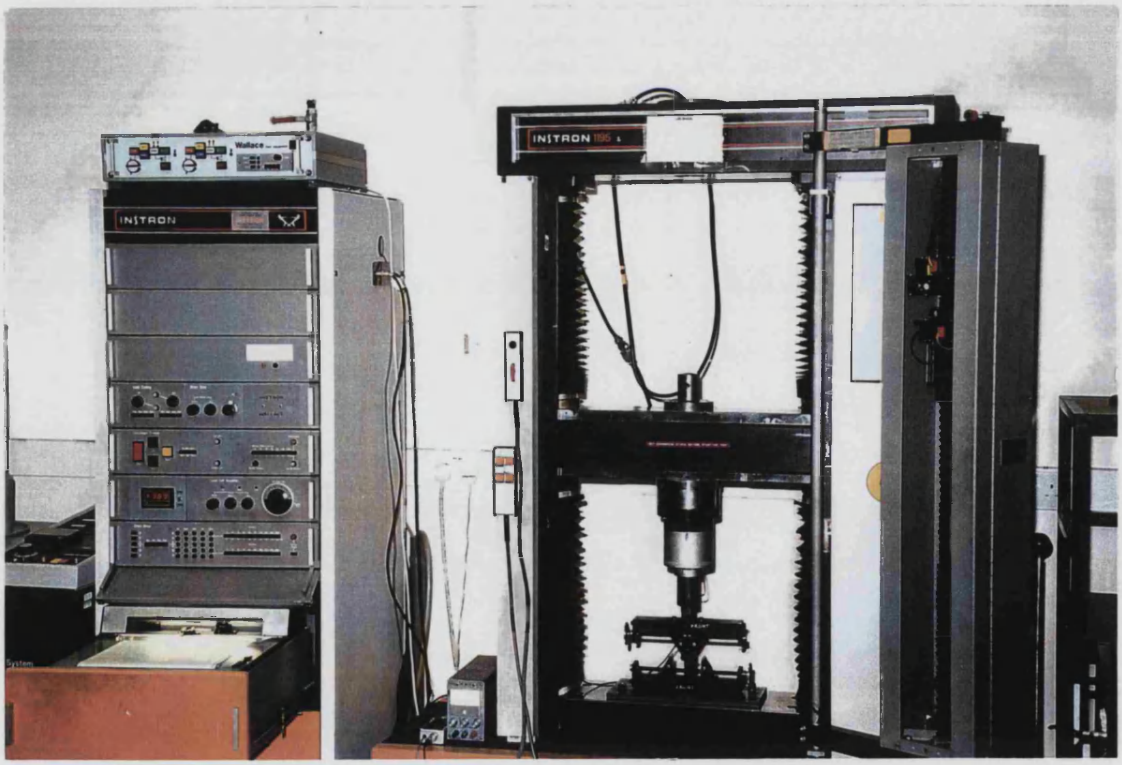

Figure 71. Instron 1195 testing machine showing test apparatus on the right and the control and recording unit on the left.

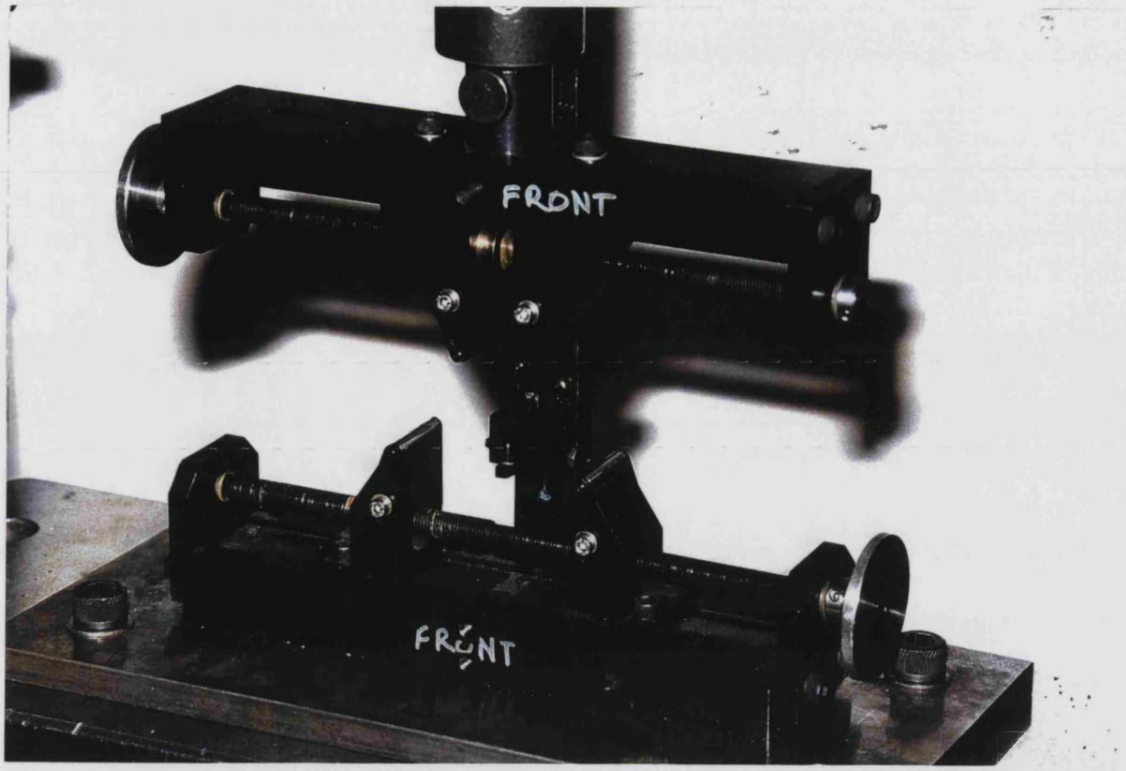

Figure 72. Four point bending rig used for flexural testing.

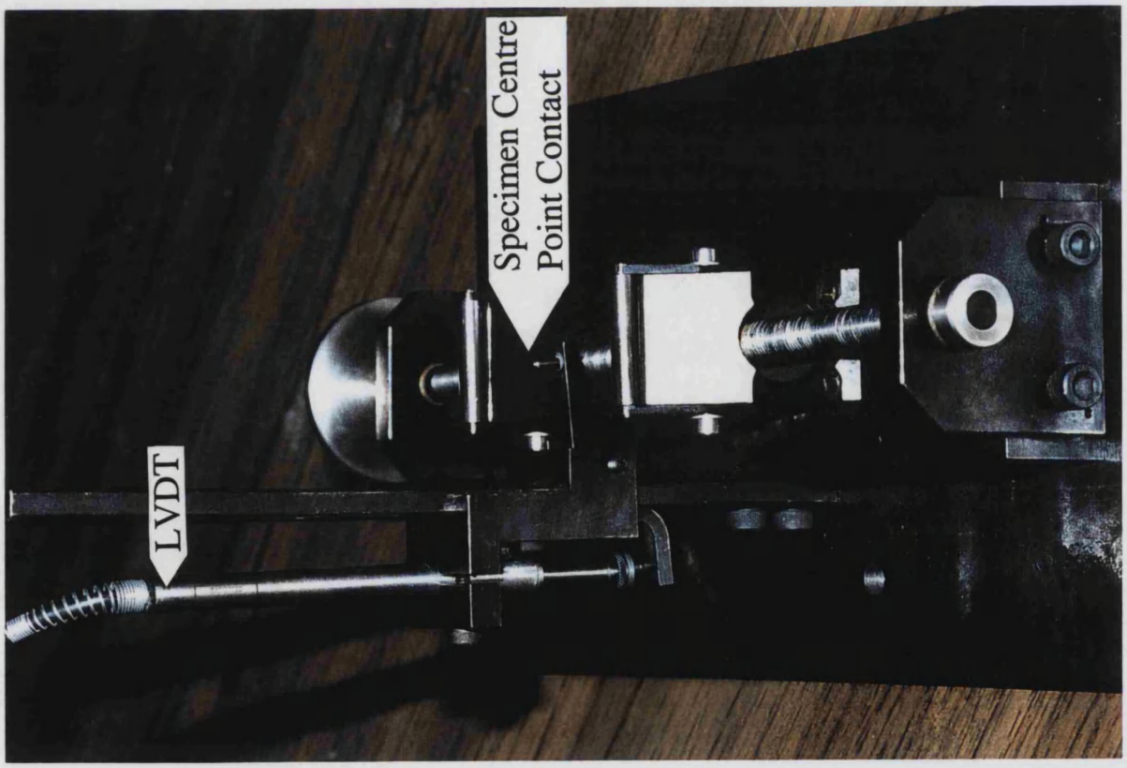

Figure 73. Lever arrangement allowing the measurement of centre point displacement by an LVDT out of the loading axis.

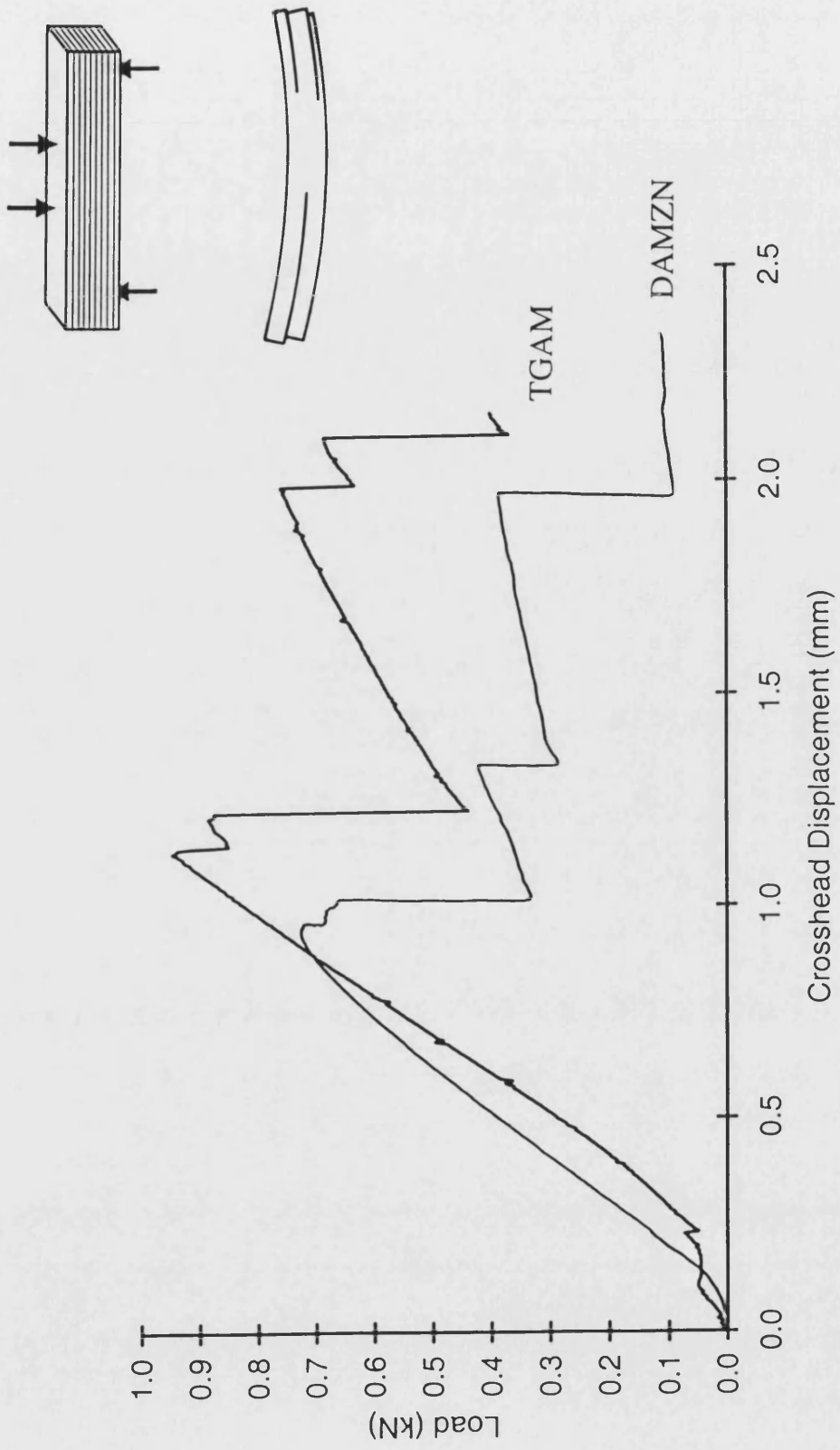

Figure 74. Typical load versus displacement traces for flatwise flexural testing of model materials.

and although this is associated with a lateral translation, it was assumed that the translation was small, and that the consequent eccentricity of load was insignificant.

In order to measure the centre point deflection of a sample in a four point flexure test an LVDT is usually employed. Since this must be positioned at the loading axis, the rig is consequently bulky. The rig used here utilised a lever to translate the centre point displacement to a plane parallel to the loading axis. This meant that the LVDT could be attached alongside the rig and hence the rig could be more compact. Figure 73 shows the lever arrangement and the LVDT and the specimen contact can clearly be seen. It was verified that the displacement at the two ends of the lever were equivalent.

Tests were conducted on samples of TGAM and DAMZN model materials. All testing was carried out using a crosshead speed of 0.5 mm per minute.

10.6. Results and discussion

10.6.1. Analysis of load versus displacement traces

Figure 74 shows an example of the load versus displacement traces for samples of TGAM and DAMZN tested in flatwise flexure. In this case the displacement axis represents the crosshead displacement which, for a rigid testing machine, is considered equivalent to the displacement of the loading points with respect to the support points. Although there was inevitable variation between the results for individual samples, the form of the traces was similar in all cases.

There are a number of significant features of the curves which should be noted. Firstly the peak load for the TGAM material is significantly higher than that for the DAMZN material. Since the samples are of similar dimensions this implies that the peak bending stress is higher in the TGAM than in the DAMZN. The peak stress was calculated from the traces for each of the samples tested using simple beam formula shown in Equation 28.

The results of this analysis on the traces is given in Table 21 along with other data gathered during the testing programme.

$$\sigma = \frac{3W(L - L_i)}{2bd^2}$$ *Equation 28*

Where σ = Stress

W = Applied load

L = Outer span

L_i = Inner span

b = Specimen breadth

d = Specimen depth

	TGAM		DAMZN	
	Mean	St Dev	Mean	St Dev
Failure Stress (MPa)	146	25	103	11
Flexural Modulus (GPa)	48	4	-	-
Shear Stress at Failure (MPa)	3.4	0.6	2.4	0.3
Strain at Peak Load (%)	0.31	0.05	-	-

Table 21. Results of flatwise flexural testing programme.

The flexural modulus was calculated from the slope of the first linear loading portion of a stress versus strain graph, the strain having been recorded directly from the strain gauge output, and the stress having been calculated from the load via the simple beam formula. Unfortunately the DAMZN material was not tested with the use of strain gauges and therefore strictly the modulus and strain at failure cannot be reported.

The failure stress as derived from the simple beam formula is significantly higher for the TGAM material. This must be due to the two structural differences between the materials, i.e. the higher continuous fibre content in TGAM and the absence of staple fibre layers. Therefore it can be concluded that the inclusion of continuous fibre and the exclusion of staple material increases the failure stress. There are two points which should be noted however. Firstly, the increase in failure stress as a function of the difference in fibre structure is not solely due to the fibre architecture but also to the associated matrix structure. Remember that the structure of the matrix is highly dependent of the fibre orientation. Secondly, the figures are reported here as failure

stresses, and not as the flexural strength. In order for the flexural strength to be reported the sample must fail in either a compressive or else a tensile mode. In every case in flatwise flexure the samples failed by interlaminar shear[120]. This was as expected and precludes the strict use of the term strength. Instead the figure must be reported as a failure stress or less commonly a modulus of rupture.

Although the strain was not measured for the samples of the DAMZN material it is possible to infer the values of modulus and strain at peak load if it is assumed that the crosshead displacement is an indication of the strain. The curves in Figure 74 clearly show that the linear part of the loading curves are of approximately the same slope. Since all elements of the testing geometry are very similar this implies that the moduli are also similar. However if there is any difference, it appears that the modulus of the TGAM material is a little higher. A similar argument can be applied to the data for the strain at peak load and here it also seems that the values are similar for the two materials although perhaps slightly higher for TGAM. Both these findings should, however, be treated with some caution arising from the way in which they were derived.

Again one has to be careful with the use of nomenclature. Here, strain at peak load has been used to remove any uncertainty from its meaning. Often this value would have been reported as a failure strain since at this point a failure does occur. Clearly though, the load traces show that during continuation of the test beyond this point, the sample can often support loads approaching the value at the first failure point. Although cracked this sample could be considered to be performing most of its required function and therefore it could be considered that it has not failed. Hence the value of the failure strain depends upon the point which is taken as representing failure. Therefore the use of the term failure strain should always be coupled with a definition of failure.

The general form of the load versus displacement curves gives some insight into the failure mechanism. All the curves for both materials were of the same form, i.e. a series of loading regions terminated by a sharp reduction in load. The relatively linear nature of the loading parts of the curve imply that there is little damage accumulation, and that what damage is caused is sub-critical. The sharp reductions in load indicate the rapid propagation of a crack through the sample in such a way as to reduce the stress in the sample. That the supported load does not decrease to zero and that it

increases again after these reductions implies that the crack does not pass completely through the sample. In practice the first major reduction in load corresponds with the rapid propagation of a crack in a plane perpendicular to the loading axis from one end of the sample, at mid-depth. This is obviously an interlaminar shear crack. Since only the outer thirds of the sample are loaded in shear, it might be expected that the crack would grow from the end of the specimen to under the loading roller closest to that end. However, frequently the crack grows to the centre of the beam or even beyond, i.e. through material which is in theory not subject to shear stress. It seems likely that this is a dynamic effect associated with the rapid release of a great deal of stored strain energy.

Since at this point the beam has not been broken in the vertical plane it can still support load and so upon continuation of the test the load rises once again. This is shown clearly in Figure 74. Interestingly the slope of the second loading curve is somewhat shallower than that of the first. This is a result of the damage (the shear crack) sustained by the beam during the first failure, and is to be expected. The two slopes before and after the first failure can be approximately explained by simple calculations.

The modulus of a beam can be expressed as a function of the test geometry and the slope of the load versus centre point displacement curve by Equation *29*.

$$E = \frac{\Delta W}{6I\Delta D}\left(l_1^2\left(l_1 + 3l_2\right)\right) \qquad \textit{Equation 29}$$

Where E = Flexural modulus (of material)

ΔW = Change in load

ΔD = Change in displacement

I = Second moment if area of the sample

l_1 = Distance between a loading point and an adjacent support point

l_2 = Distance from the centre line to a loading point

For a rectangular beam,

$$I = \frac{bd^3}{12} \qquad \textit{Equation 30}$$

If it assumed that the crosshead displacement is related to the centre point displacement by a simple factor, which is at least approximately true at small displacements, then the slope of a load versus crosshead displacement curve is analogous to a load versus centre point displacement curve for the purposes of comparison. If the test rig geometry is considered constant then;

$$E \propto \frac{\Delta W}{6I\Delta D} \qquad \textit{Equation 31}$$

i.e. the slope of the loading curve is;

$$\frac{\Delta W}{\Delta D} = 6EI = \frac{Ebd^3}{2} \qquad \textit{Equation 32}$$

So for a beam of 1 unit square cross section (b=1 and d=1) the slope is equal to;

$$\frac{E}{2} \qquad \textit{Equation 33}$$

For a beam which is half as deep i.e. b=1 and d=0.5 the slope is equal to;

$$\frac{E}{16} \qquad \textit{Equation 34}$$

Assuming the stiffness of a beam consisting of two beams stacked one on top of another is equal to double that of a single beam then the slope of the loading curve for a stack of two beams with b=1 and d=0.5 is;

$$2\frac{E}{16} = \frac{E}{8} \qquad \textit{Equation 35}$$

Now this beam has the same overall dimensions as that for which the slope is given by Equation 33. Thence the ratio of the loading slopes for a beam before and after a horizontal shear crack grows from one end to the other is 4:1. This is an analogous

situation to that observed in flatwise flexural testing of these model carbon-carbon composites.

This simplistic analysis has failed to take account of two major departures from the practical situation. First it is assumed that the crack occurs through the whole sample at exactly the mid-depth. Secondly it is assumed that there is no friction between the two halves of the beam. Both of these assumptions would tend to underestimate the stiffness of the fractured beam and hence reduce the ratio of the slopes before and after the first failure.

Analysis of the experimental loading curves in Figure 74 yields a ratio of slopes of approximately 3:1. This agrees quite well with the remarkably simple mathematical argument presented here.

During mechanical testing it is important to interpret the data in a thorough manner. In these tests it was found that the samples failed by interlaminar shear and (the mode of failure is discussed in detail in Section 10.6.2.) this means that the stress at failure cannot be quoted as a value of strength. In this test the sample is subject to both tensile and compressive stresses and shear stresses. The mode of failure is dictated by which stress exceeds the respective strength first. Therefore a failure by shear indicates that the shear stress applied exceeded the shear strength before the tensile stress applied exceeded the tensile strength. This argument allows two statements to be made. First, the tensile strength of the materials is *higher* than the failure stress reported, and second the shear strength of the material can be calculated from these data. The shear stress is calculated using Equation 36:

$$\tau = \frac{W}{2bl} \qquad \textit{Equation 36}$$

Where	τ	=	Shear stress
	W	=	Applied load
	b	=	Specimen breadth
	l	=	Specimen length

Since in these tests the failure mode was shear, the shear stress at failure could legitimately be reported as a shear strength, but since the measurement of shear

strength was not the aim of the test it is reported as the shear stress at failure. Values of the shear stress at failure for the TGAM and DAMZN model materials are given in Table 21.

It is interesting to note that shear stress at failure is higher for TGAM than for DAMZN. This is arguably more significant than the apparent difference in the tensile stress at failure for the reasons stated in the previous paragraph. The data suggest that the bonding between the layers in the TGAM material is stronger than that in DAMZN. The simple explanation for this is that there is less porosity in the TGAM material, or in other words, there is more material in the interlaminar regions in TGAM than in DAMZN.

10.6.2. Comparison of failure mode of TGAM and DAMZN

The similar shapes of the loading curves indicate that the basic failure mode is similar for both of the materials. Figure 75 and Figure 76 show typical fracture modes for TGAM and DAMZN respectively. In these photographs small wedges have been inserted into the cracks to make them more obvious. Without the wedges the cracks are almost completely closed. In all cases the samples are shown such that the compressive face is at the top and the view is of one side of the specimen.

Some differences can be detected between the fracture paths in the two materials. The most obvious of these is that the fracture path in TGAM is much more linear than in the DAMZN material. In both materials the cracks run along the boundary between adjacent cloth layers, but it appears that the inclusion of the staple layers in the DAMZN material makes it easier for the crack to cross through layers. This is due to the relatively open and disordered nature of these layers. It seems logical that this subtle change in fracture mode is related to the lower failure stress of the DAMZN material. One possible explanation is that the DAMZN material is "weaker" because the growth of the crack is possible in all three dimensions. This allows the crack more freedom to link all the pre-existing defects within the structure, of which there are many. By contrast, in the case of TGAM the crack seems to be restricted to propagation in the horizontal plane and is not able to easily cross layers. Since the crack is now only able to link all the pre-existing defects within a given plane, it would be expected that this material would be able to support a higher stress. This of course assumes that the statistical distribution of defects is the same in both materials.

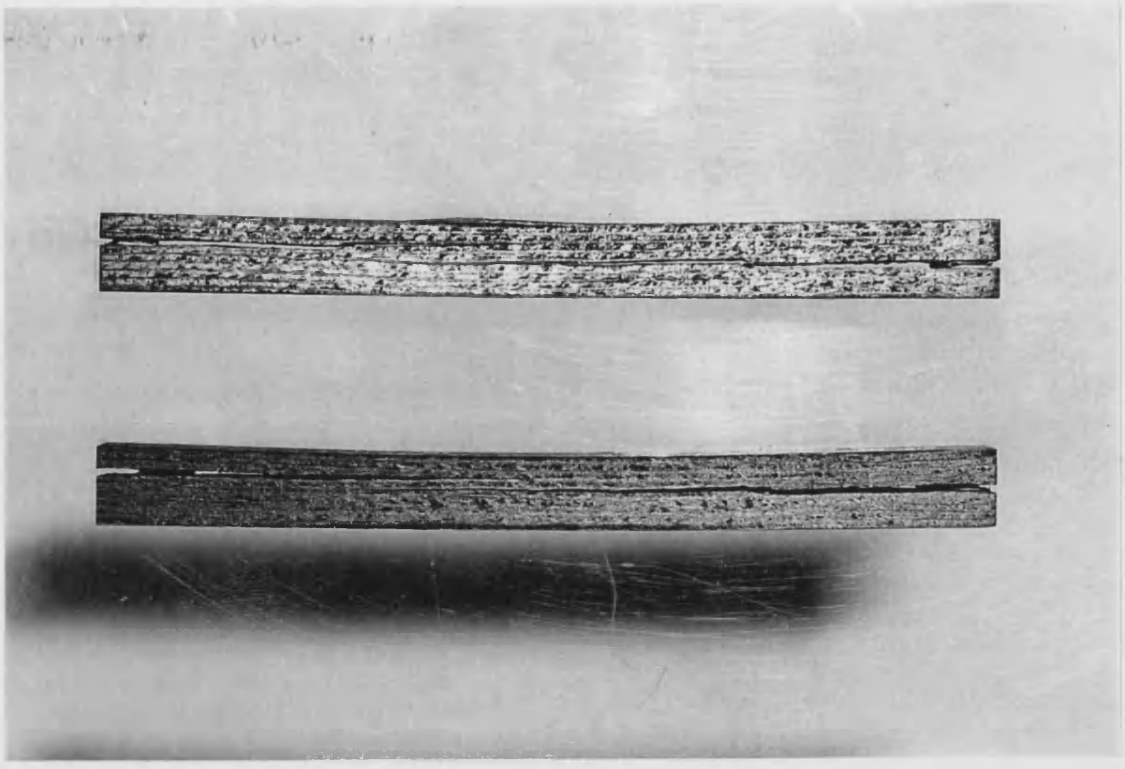

Figure 75. Fracture mode of two samples of the TGAM model material in flatwise flexure.

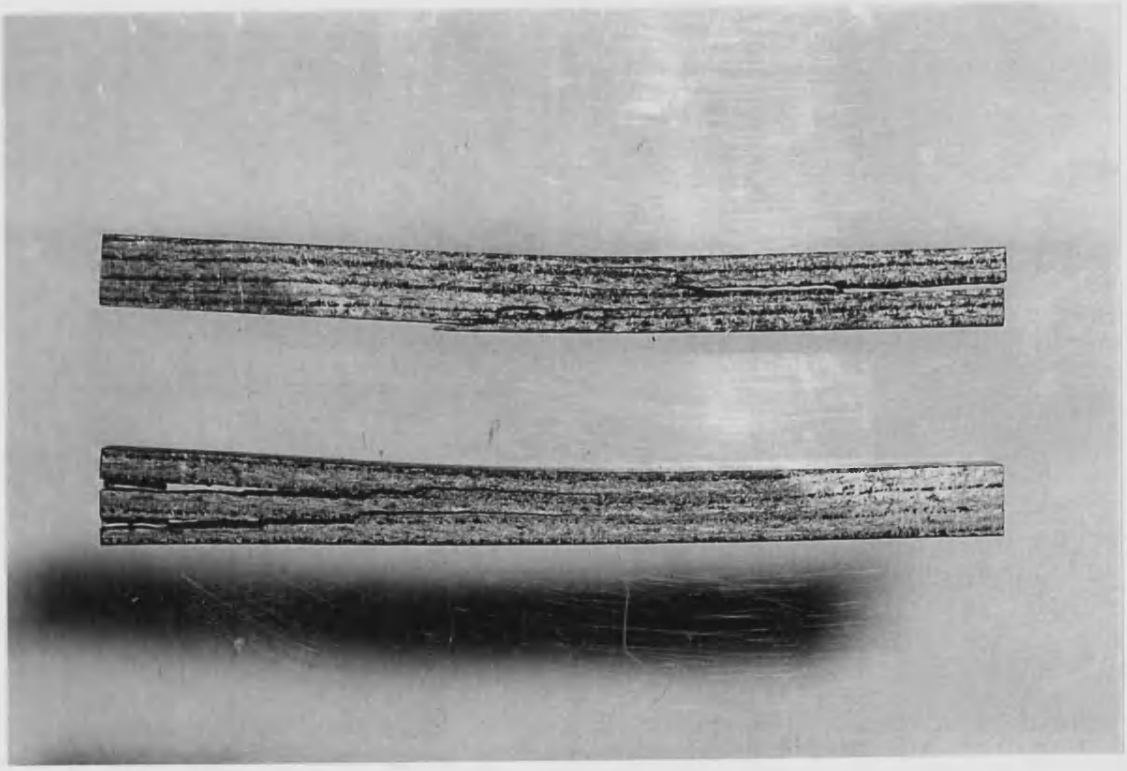

Figure 76. Fracture mode of two samples of the DAMZN material in flatwise flexure.

Perhaps of more significance is the fact that the disordered nature of the staple layers introduces many more significant defects to the structure as a whole.

Another point worthy of note is the unusual failure of the top sample in each of Figure 75 and Figure 76. In the TGAM material it can be seen that a small piece of material has delaminated from the compressive face of the sample, presumably by some kind of compressive buckling mechanism. Whereas there is some evidence of tensile failure on the tensile face of the DAMZN sample.

10.7. Conclusions and summary

There are several conclusions which can be drawn from this work. Firstly it is clear that the testing geometry which was used was unsuitable for the determination of the strength of the materials. This was a direct result of being unable to induce failure by compressive or tensile fracture. Instead the samples of both materials failed by an interlaminar shear mechanism. It must be stated when reporting the results of such tests that this was the failure mode, and a strength should not be reported but rather a bending stress at failure or something analogous to this. Also the definition of failure should be reported in these cases.

Without the use of strain gauges (or other direct strain measuring devices) or the correct measurement of the true centre point displacement, it is impossible to accurately measure the modulus of the material. The modulus of the TGAM material has been measured and by comparison of the slopes of the loading curves it has been deduced that the modulus of the DAMZN material is similar but slightly lower.

The peak bending stress has been determined for the two materials and has been found to be significantly higher for the TGAM material. However, since the failure mode for both materials was by interlaminar shear, this does not imply that the TGAM material has a higher tensile strength, but only that it has a higher interlaminar shear strength.

Calculation of the bending stress and shear stress at failure highlights the vast difference in the magnitude of these properties for these materials. Since failure is by shear, this value is a reasonable approximation to the interlaminar shear strength, whereas the peak bending stress must be somewhat lower than the true tensile strength.

The form of the load versus displacement curves is similar for all the samples of both materials, and the main features have been ascribed to the various failure mechanisms

which occur. The first large reduction in load is associated with the fast propagation of a crack at mid depth, inwards from on end of the beam. It is postulated that the turn over of the curve just before this point could indicate the build up of small, sub critical shear cracks in the material and that the mid depth crack simply links some of the more significant of these cracks together.

The fracture paths were similar for both the materials tested, however there appeared to be a greater extent of cross-layer cracking in the DAMZN material and this is due to the inclusion of the relatively disordered staple layers. It is possible that the lower failure stress of the DAMZN material was a result of the ease with which the crack could join the small shear cracks by a cross-layer cracking mechanism. Since the TGAM inhibits cross-layer cracking, the large shear crack is less able to join all the significant small shear cracks and so the material can bear higher stresses.

11. FOUR POINT EDGEWISE FLEXURAL TESTING OF UNOXIDISED MODEL MATERIALS

11.1. Introduction

The previous chapter has served to highlight some of the difficulties of testing carbon-carbon composites. Many standard mechanical test methods prove difficult, mainly as a result of the high tensile strength and very low interlaminar shear strength of these materials. This study, and many others, have shown that in conventional (flatwise) flexure it is difficult to avoid failure by interlaminar shear. While it may be important for designers to know that the material fails in this manner when stressed this way, the intention of the test method is to test indirectly in tension. A valid failure, by tensile or compressive mechanisms, allows the calculation of the tensile strength of the material which is another property that is important for the designer to know. Hence it is pertinent that a method of inducing tensile failure during a flexural test is found. For most materials it is sufficient to increase the SDR to a point where the increased ratio of tensile and shear stress causes failure by the desired mechanism. However, for carbon-carbon composites this method is ineffective, possibly because coalescence of the small shear cracks formed in the localised stress fields under the loading rollers is the primary cause of shear failure.

Fortunately the failure mechanism is *interlaminar* shear and so it is possible to avoid failure by this mechanism if the coincidence of interlaminar planes and shear stresses can be avoided. In the flexure test, the principal shear stresses are the vertical and horizontal ones associated with the bending moment (Figure 77) and so the weak planes in the material must be positioned such that these stresses do not act upon them. For the materials tested here this can be achieved by simply turning the sample such that it lays on its side. In this case the cloth plies are parallel to the side of the sample and thus avoid stressing in shear. This test will be called edgewise flexure for obvious reasons. It should be noted that this technique is suitable only for carbon-carbon composites with laminated reinforcement. In the case 3-D of carbon-carbon composites shear failure should not represent a problem due to the absence of weak planes. However, with unidirectional carbon-carbon composites it is impossible to

avoid the coincidence of shear stresses and weak planes since there are effectively two orthogonal sets of weak planes.

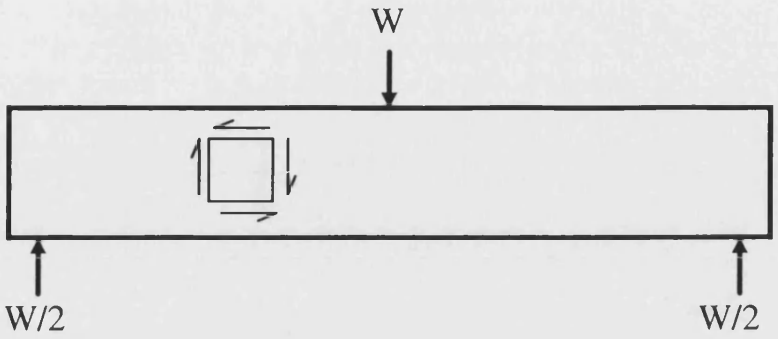

Figure 77. Principal shear forces associated with the application of the bending moment in a flexure test.

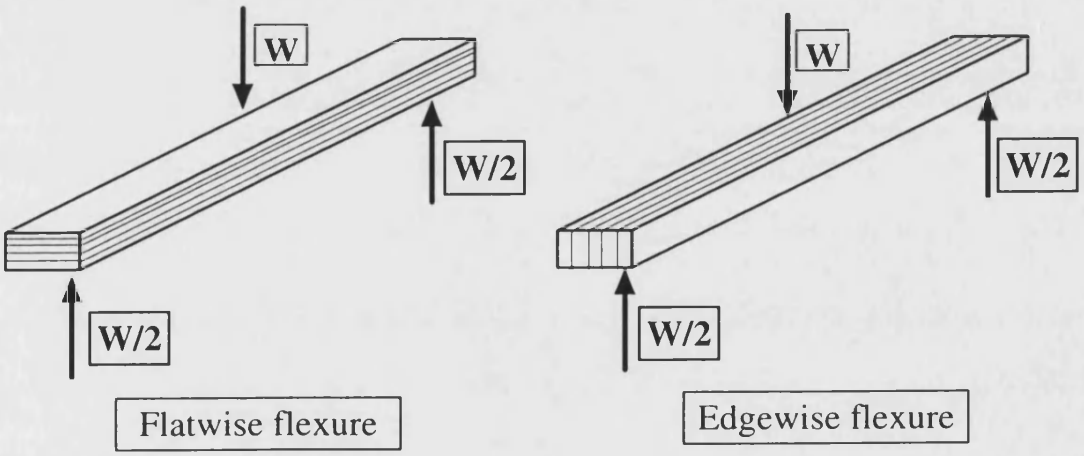

Figure 78. Flatwise and edgewise flexural testing arrangements showing laminate orientation.

A schematic diagram of both flatwise and edgewise flexure is shown in Figure 78. Although the use of the edgewise flexure technique negates the chance of failure by interlaminar shear, it does not guarantee a valid failure mechanism. The sample could still fail by a non-interlaminar shear mechanism and this would be the expected failure mechanism for a laminated unidirectional carbon-carbon composite tested in edgewise

flexure. However, the edgewise test method has been successfully used with materials very similar to those used here by Dunlop Ltd. for many years. Dunlop use the test for quality control purposes and hence there is no reference to their use of it in the open literature. Indeed there appears to be no published literature on the subject of edgewise flexural testing of carbon-carbon composites.

However, the edgewise flexural test is not entirely new. It has been used extensively by the timber industry for many years. The annular cellular structure of wood can cause samples to appear to have a laminated structure if they are cut from large logs, and like laminated composites wood is known to have highly anisotropic properties. Hence there are some similarities between sawn timber and laminated composites[121]. However, the similarities are even more marked in the case of laminated timber products. Laminated veneer lumber (LVL) is made by gluing veneers a few millimetres thick together to form large pieces of timber. This has the advantages of being able to use smaller trees, and to manufacture very large pieces. LVL is becoming more widespread in its use in the construction of large buildings, and where it is stressed in flexure it is almost exclusively used in the edgewise configuration. In response to this, grading tests also use the edgewise method[122,123,124,125]. These tests also use large specimens typically more than a metre in length and so the control of testing geometry is somewhat easier. However many of the practical difficulties are similar to those experienced when testing carbon-carbon composites.

11.2. Test method

The four point edgewise flexural test method was identical to the flatwise method except for the orientation of the layers within the materials with respect to the sample and loading direction. Given the difficulties associated with the determination of the modulus of the materials, a small investigation was made into the use of the sonic resonance method and this is reported in Section 11.2.2.

11.2.1. Edgewise flexure

The samples for edgewise flexure were prepared in a manner identical to those tested in flatwise flexure except that the dimensions were different. Although the depth, width and length of the specimens was 7 mm, 10 mm and 90 mm respectively as with the other specimens, the orientation of these dimensions with respect to those of the blocks of supplied material was different. As before, each block was milled on its

large faces such that they were flat and parallel. However, whereas before the thickness of the remaining plate was 7 mm, for edgewise samples it was 10 mm. This plate was cut into oversize sample shapes and these were then milled to the final dimensions.

The three dimensions of each sample were measured and recorded along with the weight of each. They were also checked for parallelism and marked with unique identifiers. Strain gauges were attached to half of each group of specimens using the cyanoacrylate adhesive as described previously.

The same testing machine (Instron 1195) and loading rig as was used for flatwise testing was used. The normal load and support spans were 25 mm and 75 mm respectively and a crosshead speed of 0.5 mm per minute was used in all cases. The load and strain gauge outputs were recorded on a computer along with that from an LVDT which measured the displacement of the centre of the beam with respect to the support points. This is not the true centre point deflection and hence cannot be used for strain calculations but it is the only measurement which it is practically possible to measure for samples of this size. A trace of load versus time was automatically made by the testing machine.

11.2.2. Sonic resonance for modulus determination

Sonic resonance is, in theory, a simple practical method by which the modulus of elasticity of a material can be determined. In essence it involves measuring the resonant frequency of a sample and from this, and various other physical measurements, the modulus can be calculated.

The method used here consisted of vibrating the beam shaped specimens used in the flexural testing programme in flexure. The specimen was supported on two knife edges at its nodal points and a vibrational impulse was applied at one end of the sample by a stylus from a record player. This was driven by a variable frequency generator, and a second stylus was employed at the opposite end of the specimen as a pickup. The sinusoidal input frequency was displayed on an oscilloscope as was an amplified version of the output frequency. The amplitude of the output frequency was monitored as the driving frequency was slowly scanned through the range from about 100 Hz to 100 kHz. When the driven frequency equalled the resonant frequency of the

specimen the amplitude of the output was a maximum. The resonant frequency is related to the modulus by a simple formula[126];

$$E = CMf^2 \qquad \textit{Equation 37}$$

Where	E	=	Modulus
	C	=	Geometrically derived constant
	M	=	Mass
	f	=	Resonant frequency

In practice it was extremely difficult to detect the maximum amplitude of the output signal. This was due to the fact that the signal amplitude gradually increased and decreased either side of the maximum. Also the output signal included significant noise which obscured the true signal. It was found that this was due to both electromagnetic interference from other sources, and vibration of the sample on the supports. It was found that the detected resonant frequency was dependent on the positioning of the pickups and the supports and even of the material from which the supports were made. Even if all these factors were carefully controlled the test did not produce repeatable results. This is probably for three main reasons. Firstly, it is very difficult to be sure which mode of vibration is being induced. Second, the measured property is the dynamic elastic modulus, as distinct from the Young's modulus, and it is possible that these properties are different. Finally the test method is intended for "the room temperature determination of the dynamic moduli of elasticity and rigidity of slender rods or bars composed of homogeneously distributed carbon or graphite particles"[126]. The carbon-carbon composites tested are obviously far from homogeneous and hence the method might be expected to be approximate at best.
Given the poor results from this technique it was abandoned and the moduli were measured solely from the flexure tests.

11.3. Effect of altering the test geometry

Much has been made of the effect of the testing geometry, principally the SDR, on the failure mode of flexural specimens and other physically measured properties. A short testing programme was undertaken to assess the effect of the SDR on properties

measured and calculated from the flexural test. In these tests the DAMZN model material was used in the edgewise orientation and the SDR was altered by adjusting the position of the support and loading rollers of the loading rig. The standard geometry, i.e. beam depth of 7 mm and support and loading spans of 75 and 25 mm respectively, yielded an SDR of approximately 10.7:1. Here the loading condition is known as $^1/_3$ point four point loading since the support span is 3 times the loading span. It was decided to keep this constant and vary only the SDR. Spans were chosen to give alternative values of SDR of 6:1 and 9:1.

The tests were conducted in a manner identical to that for all the other tests in all other respects. The modulus was calculated from the displacement of the loading rollers with respect to the support rollers in accordance with the method described by Hammant[117] using Equation 38.

$$E = \frac{\Delta W}{6I\Delta D} l_1^2 \left(l_1 = 3l_2\right) \qquad \textit{Equation 38}$$

Where

E	=	Flexural modulus
ΔW	=	Change in load over linear region
l_1	=	Distance between loading and adjacent support points
l_2	=	Distance from centre line to a loading point
I	=	Second moment of area of the specimen
ΔD	=	Change in displacement over linear region

11.3.1. Results and discussion

Table 22 shows the results of the testing programme on DAMZN material at various SDR values. It is clear that the strength of the material as measured by this method is fairly constant over the range of geometry tested and this is reassuring as it validated the use of the standard geometry for the rest of the testing programme. However the modulus shows a distinct trend, i.e. that the modulus decreases with decreasing SDR. This is a direct result of erroneous assumptions made during the derivation of Equation 38. These assumptions include that the flexure of the beam is of constant radius and that there is no deformation at the loading point of either the specimen or the loading rig. The first of these is likely to be significant and so given that the

bending of the beam is closer to circular at higher SDR values, the calculated modulus is also likely to be more accurate. Clearly though, even at high SDR values the calculated modulus will be incorrect.

Sample (SDR= 10.7)	Stren-gth (MPa)	Modu-lus (GPa)	Sample (SDR= 9.0)	Stren-gth (MPa)	Modu-lus (GPa)	Sample (SDR= 6.0)	Stren-gth (MPa)	Modu-lus (GPa)
01s	127	24.0	*41*	154	28.2	*31*	165	17.7
02s	145	27.5	*42*	159	35.9	*32*	157	15.2
03s	145	27.3	*43*	187	24.6	*33*	148	15.9
04s	144	28.6	*44*	150	31.3	*34*	184	20.9
05s	166	31.9	*45*	114	19.7	*35*	141	14.2
06s	173	38.6	*46*	148	22.8	*36*	158	16.7
07s	150	34.0	*47*	169	32.2	*37*	177	21.0
08s	154	32.5	*48*	147	20.7	*38*	157	15.4
09s	170	36.4	*49*	147	23.1	*39*	148	16.2
			50	141	30.3	*40*	179	19.6
Mean	**153**	**31.2**		**152**	**26.9**		**161**	**17.3**
Stdev	**15**	**4.7**		**19**	**5.5**		**15**	**2.4**

Table 22. Results of edgewise tests on DAMZN model material at various SDR values.

A further test programme was undertaken to assess the importance of span to depth ratio on "beam stiffness". This used the measurement of total centre point deflection as a means of assessing the beam stiffness. The X - Y plots of load versus total centre point deflection were analysed and the slope of the linear loading section measured. The values of slope were than normalised so that for each test a value of "Standard Deflection at 1 kN load" was produced. In order to conserve specimens the samples were only loaded to just below their estimated elastic limit, and then unloaded. This allowed the same specimens to be tested at each of three span to depth ratios. The span to depth ratios used were chosen to be the same as those used for the previous investigation. As before, samples of unoxidised DAMZN material were used.

Table 23 shows the results of this investigation. The standard deflection of the sample reduces with reducing span to depth ratio, which is not surprising since effectively a shorter sample is under test. It should be remembered that the standard deflection is inversely related to the modulus by a non-linear function. However, due to the non-circular nature of the bending, the derivation of the numerical value of modulus is impossible.

Sample No	Standardised Deflection at 1 kN (/mm)		
	SDR = 10.7	SDR = 9	SDR = 6
DAMZN51	0.70	0.43	0.14
DAMZN52	0.57	0.36	0.12
DAMZN53	0.46	0.29	0.10
DAMZN54	0.76	0.46	0.15
DAMZN55	0.50	0.30	0.11
DAMZN56	0.70	0.41	0.21
DAMZN57	0.69	0.54	0.24
DAMZN58	0.87	0.49	0.25
DAMZN59	0.77	0.47	0.25
DAMZN60	0.53	0.30	0.15
Mean	**0.66**	**0.41**	**0.17**
Standard Deviation	**0.13**	**0.09**	**0.06**

Table 23. Effect of SDR on beam stiffness of DAMZN material.

$$SD@1kN = 0.0279e^{(0.2941SDR)} \qquad \textit{Equation 39}$$

Where SD@1kN = Standard deflection at 1 kN load

SDR = Span to depth ratio

If the standard deflections in Table 23 are plotted against span to depth ratio (Figure 79), it is possible to quantify the non-bending elastic deformation which occurs at the support points. The intercept of an arbitrarily chosen exponential best fit line where

SDR = 0 gives the standard deformation at 1 kN load using this test rig. The result of the regression is given in Equation 39.

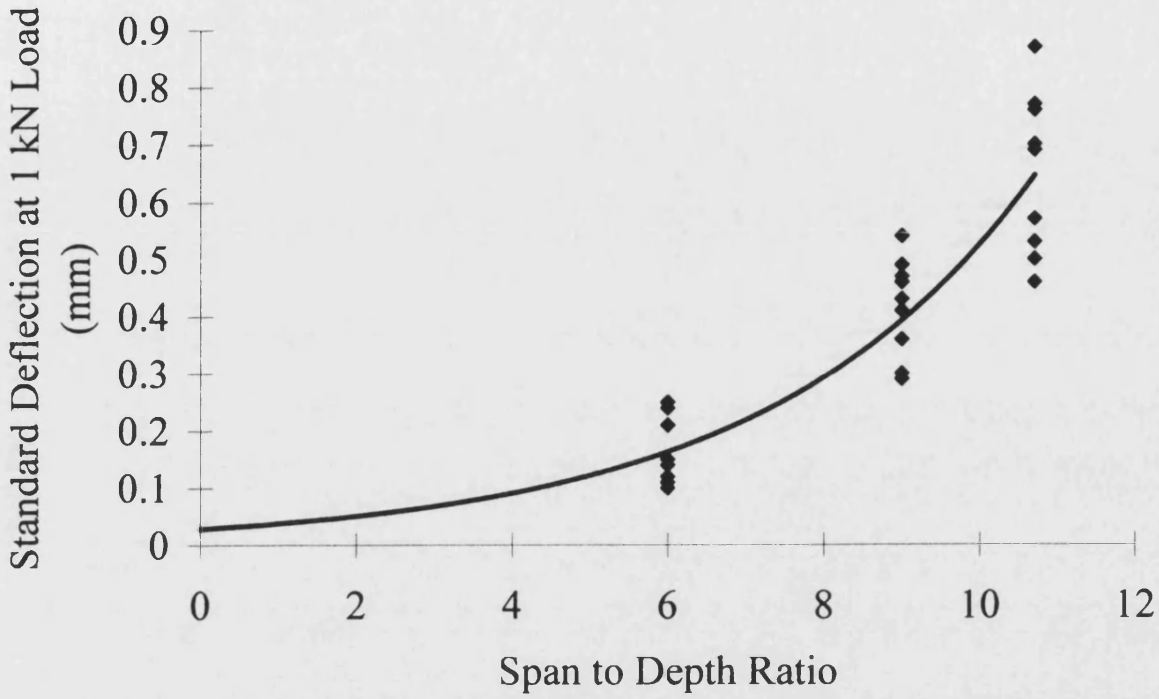

Figure 79. Graph of SDR versus standard deflection at 1 kN load for DAMZN material in edgewise flexure.

Equation 39 predicts that for a sample tested such that the span to depth ratio equals zero, a deflection of 0.0279 mm would be expected under a load of 1 kN, i.e. under 1 kN the rig and sample deforms by 0.0279 mm. An attempt was made to verify this result experimentally. This was achieved using the same samples as for the previous investigation and a modified testing geometry. The samples had to be tested using the same bending rig as before but with a span to depth ratio of zero. Therefore the rig was altered so that the support and load spans were the same. Also, in order to spread the load evenly over the top surface of the sample, a thick steel backing plate was used. The experiment yielded a mean standard deflection at 1 kN load of 0.0203 mm with a standard deviation of 0.0026 mm. This is in good agreement with the best fit prediction, especially when it is borne in mind that the best fit line has been extrapolated well beyond the range of available data.

When the steel backing plate was tested in a similar manner, the test revealed a standard deflection of 0.0308 mm. This result seems to suggest that the majority of the measured deflection is accounted for by flexure of the test rig as opposed to deformation of the sample.

All of this work serves to highlight the inaccuracies which can arise as a result of calculating the strain, and hence modulus, while making geometrical assumptions, and reinforces the case for the use of strain gauges.

11.4. Results of testing model materials

The results from tests where strain gauges and data logging was used, proved to be very reliable and clear. An example of typical raw recorded voltage data is shown in Figure 80.

Here the voltage outputs from three sources are recorded. The load voltage is obtained directly from the testing machine and is relative to a 10 V full scale. The full scale was selected on the machine prior to the test and was usually 1, 2, or 5 kN. The

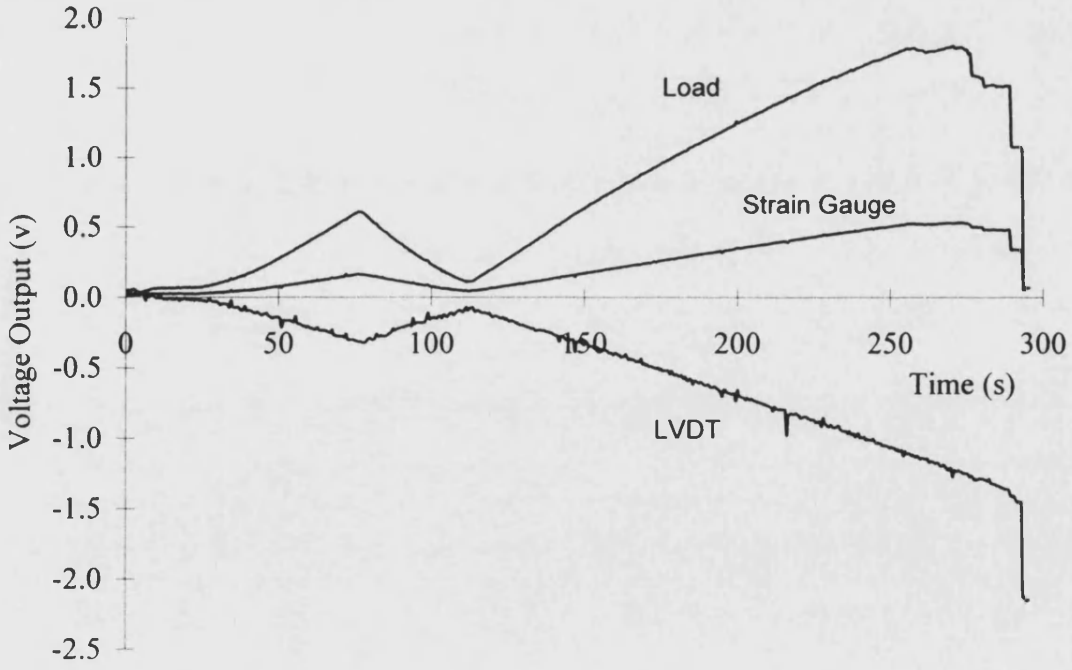

Figure 80. Plot of typical raw voltage data from flexural test on sample DAMZZ049.

LVDT output was a measure of the deflection of the centre of the specimen with respect to the support points. The voltage output was related by a simple linear equation to the displacement although the nature of this equation had to be measured before each testing session using a calibration rig. This allowed the output to be measured for given displacements and hence a graph to be plotted of one versus the other. Linear regression identified the equation of the best fit and this was used to calculate the displacement in the experiments. The R^2 value for the best fit lines was greater than 0.99 indicating that the output from the LVDT was linear. The voltage output from the strain gauge (SG) was converted to true strain using Equation 40.

$$\varepsilon = \frac{2V_{out}}{G(500 - V_{out})} \qquad \textit{Equation 40}$$

Where ε = Strain

V_{out} = Output voltage

G = Gauge factor

The form of this equation is dependent upon the electronics in the measuring equipment, and specifically the resistances in the Wheatstone bridge. G is the gauge factor and is dependent upon the materials, construction and design of the strain gauge which is used. In this investigation the gauges used were CES-06-250UW-350 supplied by Measurements Group, and the gauge factor was 2.080.

The raw data were converted into stress and true strain and the results re-plotted. An example is shown in Figure 81. For interest the total centre point deflection was also plotted against stress and an example is shown in Figure 82.

Figure 80 shows that during the early stages of loading there is a distinct departure from normal behaviour consisting of a period of crosshead movement with no increase in load or strain. This usually occurred at a load of about 0.1 kN and is evidenced by the horizontal region of the graph. During this period the loading rig was seen to swivel about its upper attachment point until both loading rollers contacted the specimen. In order to ensure that this would not occur during an important phase of the test it was deliberately induced by loading the specimen to a proportion of the failure stress and then unloading to a low, but non-zero load. This cycle is the origin

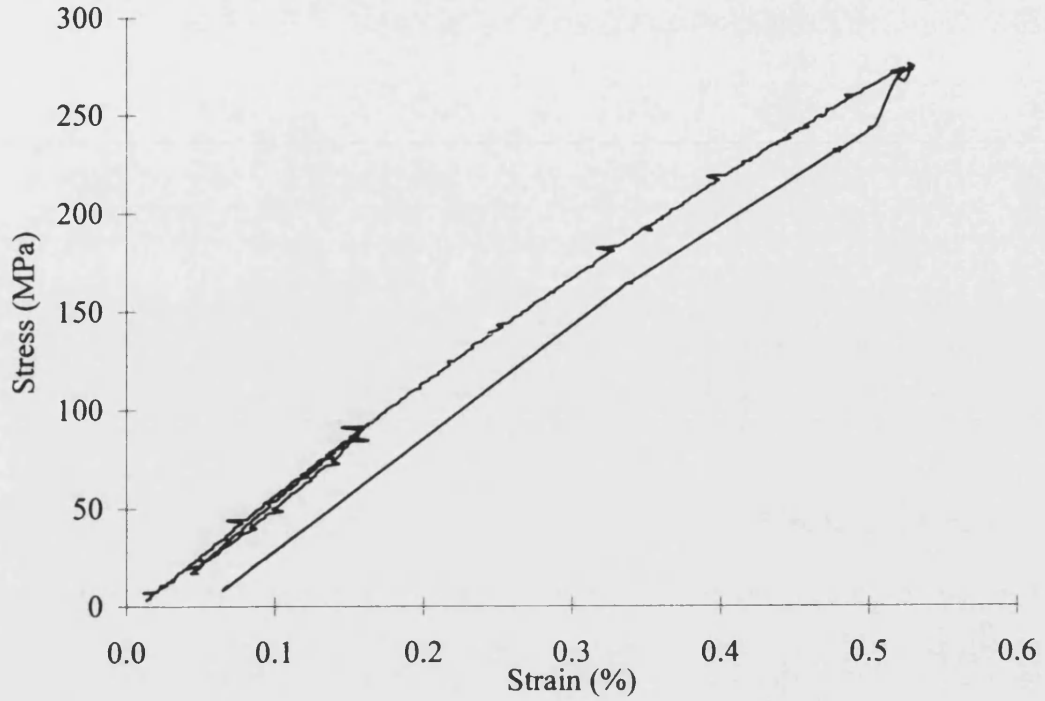

Figure 81. Typical graph of stress versus strain calculated from raw SG data (sample DAMZZ049).

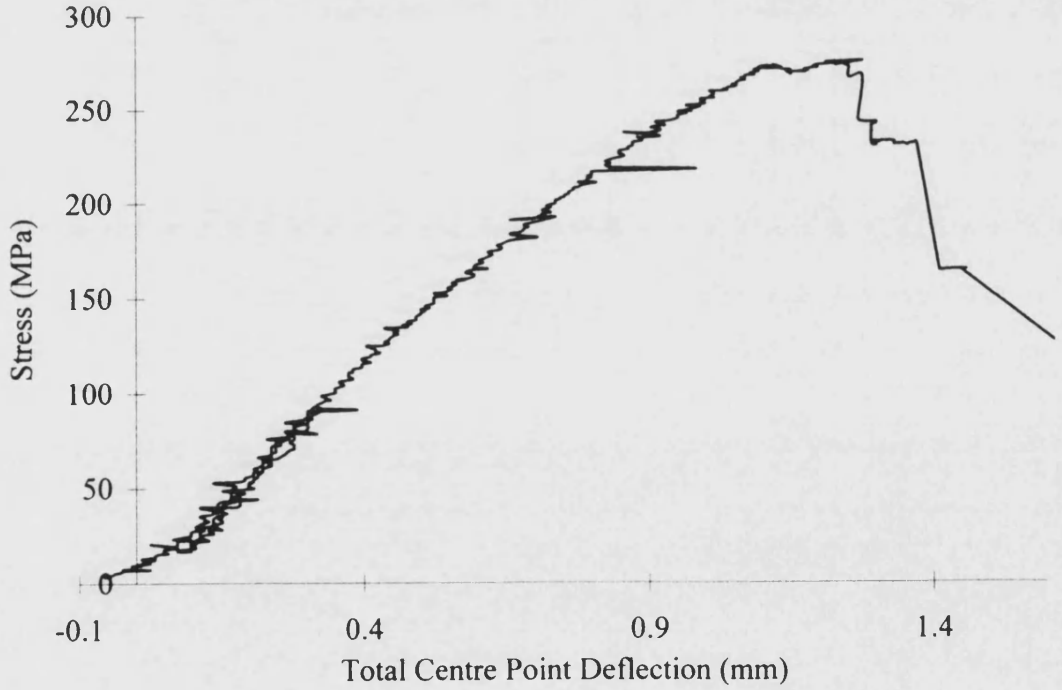

Figure 82. Graph of stress versus total centre point displacement as measured by an LVDT (sample DAMZZ049).

of the first peak in Figure 80, and also the hysteresis loops in Figure 81and Figure 82. The hysteresis loop in Figure 82 is clearly much larger than that in Figure 81 and this suggests that the loop is indeed a result of the bedding-in of the vertical position of the sample, and not a stabilisation of the flexure of the sample.

Material	Strength /MPa	Modulus /GPa	Strain to failure /%	Stored strain energy /kJm^{-3}
TGAM Mean	246	49	0.54	707
TGAM Stdev	*12*	*3*	*0.05*	*93*
DAMZZ Mean	313	65	0.53	877
DAMZZ Stdev	*42*	*4*	*0.02*	*147*
DAMNN Mean	48	11	0.65	182
DAMNN Stdev	*2*	*1*	*0.02*	*5*
DAMZN Mean	133	45	0.35	251
DAMZN Stdev	*10*	*13*	*0.07*	*64*
STANN Mean	43	12	0.45	108
STANN Stdev	*13*	*3*	*0.03*	*37*
STAZZ Mean	83	23	0.49	231
STAZZ Stdev	*4*	*1*	*0.04*	*33*

Table 24. Results of edgewise flexural testing of model materials.

The results of the analysis of all the traces from the edgewise flexural testing of the model materials are given in Table 24. In this table the strength was calculated from the peak load using the standard beam formula, and the modulus from the linear loading portion of the stress versus strain plot using the strain gauge as the source of strain data. The strain to failure represents the value of strain at the point of failure, i.e. maximum strain since most failure was by fast fracture as in Figure 81. The stored strain energy was calculated from the total area under the loading curve.

11.4.1. Explanation of material designation

For the materials with 90° rotational symmetry, i.e. TGAM and DAMZN, the sample designation is simply the name of the cloth used in their manufacture (see Figure 60 on page 127). However, in the case of the materials with 180° rotational symmetry clearly two types of specimen can be made, with the main fibre axis either parallel or perpendicular to the long axis of the sample. Where the long axis of the sample is parallel to the principal fibre direction, the sample name consists of the cloth name with the added suffix ZZ to denote zero zero. Conversely, where the long axis of the sample is perpendicular to the principal fibre direction, the sample name is the cloth name with the suffix NN for ninety ninety. In the DAM cloth the principal fibre axis is taken as parallel to the fibres in the continuous fibre layer. Hence a DAMZZ sample is made up of alternate layers of staple and continuous fibre where all the continuous fibre is parallel with the long axis of the specimen and hence from the definition of the structure of the DAM cloth, all the staple runs across the sample.
There is a lot if information contained in Table 24 and so the effect of the fibre architecture on each of the physical properties measured are discussed in turn in the following sections.

11.4.2. Influence of fibre lay-up on strength

Possibly the easiest comparison to draw from the data in Table 24 is that between the strength of the STAZZ and STANN model materials. Both materials consist of staple layers oriented parallel to each other. In the STAZZ material the short fibres have a preferred orientation which is parallel to the length of the specimen whereas in STANN the preferred orientation is perpendicular to the length of the specimen. This variation in orientation has a marked effect on the strength values of 83 and 43 MPa for STAZZ and STANN respectively. So staple material is twice as strong parallel to the fibre axis as it is perpendicular to the fibre axis. This is unsurprising since in the stronger material the fibre bridges the crack path and hence is a more effective reinforcement. However, this is not purely an effect of the fibre orientation, but rather a combination of the fibre reinforcement and the alignment of the matrix material. It should also be remembered that the fibre in these layers is short and non-continuous.
In the TGAM material the fibre is all-continuous but it is divided equally between parallel (0°) and perpendicular (90°) directions. It seems logical to suggest that an all-

staple material with such an orientation (STAZN) would have a strength intermediate between that of STAZZ and STANN, i.e. around 63 MPa. That the strength of TGAM is 246 MPa implies that between short and continuous fibre there is a four fold difference in strength. This is logical since comparing continuous and staple fibre cloths, there is an increase in orientation and a reduction in the "defect" density. Both of these factors will hinder the propagation of cracks across the fibre layers and hence increase the strength of the material. It should also be borne in mind that the fibre and matrix volume fractions are different in the two materials. Typically TGAM contains 30 % fibre whereas staple-based materials are about 5 % fibre. It could therefore be argued that the increase in strength between TGAM and the calculated value for STAZN is due to an increased fibre content. However, if this were the sole explanation, a six fold increase might be expected and hence the differences in fibre volume fraction must represent only part of the reason for the differences in observed strength.

The problem of accounting for materials with different fibre contents is absent in the comparison between DAMZZ and DAMNN materials since they are both made from the same cloth. The results in Table 24 clearly show that the DAMZZ material is much stronger than the DAMNN material. In both the materials half the layers are parallel (0°) and half are perpendicular (90°) to the sample length. In the DAMZZ material all the continuous fibre is parallel and all staple is perpendicular to the sample length, whereas in DAMNN it is the opposite way around. It is already known that parallel staple is stronger than perpendicular staple and so if the continuous fibre layer has equal strength in the parallel and perpendicular directions, it might be expected that DAMNN would be stronger than DAMZZ. Since this is not the case, the continuous fibre must be stronger when in the 0° direction than the 90° direction. Also since the ratio of strength of STAZZ and STANN is 2:1 and the ratio of strength of DAMZZ and DAMNN is approximately 6:1 the influence of the continuous fibre must be greater than that of the staple. Indeed, since the ratio of strengths of the staple in the two directions would work in the opposite sense to that of the continuous fibre it can be postulated that the ratio of the strengths of continuous fibre layers in the two directions would be much greater than 6:1.

Interesting information can be drawn from the comparison of the strengths of the TGAM and DAMZZ materials. Both of these materials have half the layers as

continuous fibre in the 0° direction. In both the other layers are in the 90° direction but in TGAM these layers are continuous fibre whereas in DAMZZ they are staple. Interestingly DAMZZ exhibits a higher strength than TGAM implying that inclusion of 90° staple contributes more to the strength of the material than the inclusion of 90° continuous fibre. This is a direct result of the less ordered structure of the staple layers. In the same way that 0° continuous fibre was stronger than 0° staple by virtue of the lower defect density, so 90° continuous fibre is weaker than 90° staple because the defects (inter fibre areas) run parallel to the preferred crack propagation direction. In other words, the small percentage of poorly oriented fibres in the staple layers serve to bridge the crack direction thus reinforcing the material more effectively. This effect is absent in 90° continuous fibre layers.

The strength of the DAMZN material, which is the most complex of the model materials and the closest to the commercial disc material, is intermediate as might be expected. The structure is a combination of that of TGAM and STAZN, and STAZN is a mixture of STAZZ and STANN. The strength of TGAM is 246 MPa and the strength of STAZN is estimated at about 63 MPa. The strength of DAMZN (133 MPa) lies neatly between these values. It has been shown that good orientation of the continuous fibre with the applied stress is the most influential factor on strength. Since in the commercial material the fibre lay-up is even more complex than in DAMZN, resulting in less good orientation with the applied stress, it would be expected that the strength of the commercial material would be lower than the DAMZN material.

A simple method of analysing the results from a group of related materials such as those tested here is to use the rule of mixtures. In essence the rule states that the property of a material is equal to the sum of the contributions from each of its component parts. Clearly this is dubious since the rule takes no account of the nature of the interfaces between the components, and its use is especially questionable for strength data since the strength is dependent upon defect concentrations. Nevertheless an attempt was made to rationalise the results using the rule.

The following abbreviations are used;

C_0 = Strength of 0° continuous fibre material

C_{90} = Strength of 90° continuous fibre material

S_0 = Strength of 0° staple material

S_{90} = Strength of 90° staple material

Testing six materials provides six simultaneous equations with four unknowns (Equation 41 to Equation 46).

Equation 41 and Equation 42 are solved directly from the experimental results which can be used to derive the strengths of all continuous fibre material in the two orientations via Equation 43 and Equation 44. This analysis yields strengths for the all unidirectional continuous fibre composites which could not be made and hence allows the assessment of the influence of each of the four fibre layer types used in this investigation. The results are shown in Table 25.

Strength STAZZ	=	S_0	*Equation 41*
Strength STANN	=	S_{90}	*Equation 42*
Strength DAMZZ	=	$½(C_0+S_{90})$	*Equation 43*
Strength DAMNN	=	$½(C_{90}+S_0)$	*Equation 44*
Strength TGAM	=	$½(C_0+C_{90})$	*Equation 45*
Strength DAMZN	=	$¼(C_0+C_{90}+S_0+S_{90})$	*Equation 46*

Fibre layer type	Strength (MPa)	
	Mean	St Dev
0° continuous	583	71
90° continuous	13	0
0° staple	83	4
90° staple	43	12

Table 25. Solution of simultaneous equations in strength for the four fibre layer types investigated.

In an attempt to validate this analysis, Equation 45 and Equation 46 were used to calculate theoretical strengths for the TGAM and DAMZN model materials. These equations produce values of 298 and 180 MPa for TGAM and DAMZN respectively compared with experimental values of 246 ± 12 and 133 ± 10 MPa respectively (Table

24). Clearly in both cases the strength has been overestimated by this method. However, if the standard deviations are taken into account it could be argued that the values are reasonable. For example for the TGAM material, adding one standard deviation to the measured strength gives 258 MPa, while subtracting one standard deviation from the calculated strength gives 263 MPa. These figures are in reasonable agreement. However, the rule of mixtures is not a sufficiently subtle technique to model the strengths of these materials, for the reasons mentioned earlier.

The results in Table 25 allow the rank order of the fibre layers to be assessed with a fair degree of confidence. Clearly the inclusion of 90° fibre is detrimental to the strength of the composite with continuous fibre having the greatest deleterious effect. This is primarily due to the relative ease with which crack can propagate through the material as a result of the coincidence of the fibre direction and the preferred crack growth direction. By far the most influential fibre layer is 0° continuous fibre as evidenced by the very high strength of this layer in Table 25. This is a result of the fact that a propagating crack is forced to break fibres in order to grow, causing its path to become more convoluted in order to exploit structural weaknesses. This is the principle behind all fibre reinforced materials.

11.4.3. Influence of fibre lay-up on modulus

The modulus data gathered from the testing programme can be analysed is a similar manner to the strength data.

Comparison of the moduli of STAZZ and STANN shows that the STAZZ material has a significantly higher modulus. It can therefore be deduced that even for short fibre materials, the alignment of the fibre with the applied stress is highly influential on the modulus. Once again though, it must be stressed that any observed effects of fibre orientation are actually a combination of the effects of fibre orientation and the consequential matrix orientation.

It seems logical to suggest that the modulus of a material made half of 0° staple and half 90° staple would be between the moduli of STAZZ and STANN, i.e. approximately 18 GPa. This material, if it had been made, would have been called STAZN and would be directly comparable with TGAM with the main difference between them being that the fibre in STAZN is short, while in TGAM it is continuous. The fact that the modulus of TGAM is 49 GPa, i.e. two and a half times greater than

that calculated for STAZN, suggests that the effect of replacing short fibre with continuous fibre is to significantly increase the modulus. However, as with the arguments for strength, it should be remembered that the fibre volume fractions are different in the two materials. Hence it could equally be argued that the higher modulus of TGAM is due to the higher fibre content.

The comparison of the moduli of DAMZZ and DAMZN shows that DAMZZ has a modulus nearly six times greater than DAMNN. This implies that the modulus of 0° continuous fibre layers is higher than 90° continuous fibre layers. Also, since the ratio of moduli of STAZZ and STANN is 2:1 and the ratio of the moduli of DAMZZ and DAMNN is 6:1, the influence of the continuous fibre layers must outweigh that of the staple fibre layers. As with the strength data the implied ratio of the moduli of continuous fibre layers in the two orientations is much greater than 6:1.

The trend of strength is mirrored by the trends in modulus, and the difference between the values for TGAM and DAMZZ is no exception. The modulus of DAMZZ is significantly higher than that of TGAM which suggests that the 90° staple fibre layers contribute more to the modulus of the composite than an equivalent quantity of 90° continuous fibre layers. Also the DAMZN material exhibits an intermediate value of modulus which is expected as it also shows an intermediate strength.

Rule of mixtures analysis has been carried out on the modulus data as it was with the strength data, and the results are given in Table 26.

	Modulus (GPa)	
Fibre layer type	Mean	St Dev
0° continuous	118	5
90° continuous	-1	1
0° staple	23	1
90° staple	12	3

Table 26. Results of rule of mixtures analysis of modulus data.

Once again Equation 45 and Equation 46 can be used to calculate theoretical moduli for TGAM and DAMZN materials. The equations produce moduli of 59 and 38 GPa for TGAM and DAMZN respectively, which are reasonable approximations to the

experimental values of 49 ± 3 and 45 ± 13 GPa respectively (Table 24). One of the most surprising results of this analysis is the calculated modulus for 90° continuous fibre which it can be seen from Table 26 is negative. Clearly this is nonsense, but it does imply that the contribution of perpendicular continuous fibre to the modulus of a composite is close to zero. The rank order of the other fibre layer types is the same as for strength with 0° continuous fibre being by far the most beneficial.

11.4.4. Influence of fibre lay-up on failure strain and stored strain energy at failure

The strains to failure of all the materials are similar, lying in the range 0.35 to 0.65 % (Table 24) and hence do not show as clear trends as the strength and modulus results. The highest strain to failure is observed in the DAMNN material implying that the inclusion of 0° staple and 90° continuous fibre increases the strain to failure. One confusing result arises from the testing of all the DAM based materials. The strains to failure of DAMZZ and DAMNN are 0.53 % and 0.65 % respectively. The structure of DAMZN is effectively a mixture of these two materials and so it might be expected that the properties of DAMZN would be intermediate between those of DAMZZ and DAMNN. However, the strain to failure of DAMZN is 0.35 %, i.e. some way outside the range covered by the other two materials. Clearly then, combining the two structures has a large negative effect on the strain to failure (but interestingly not on any of the other physical properties measured). The reasons for this are not understood. The only trend, albeit vague, it was possible to identify was that the three materials with the lowest strain to failure (DAMZN, STAZZ and STANN) were the only ones with adjacent fibre layers with parallel orientations. The physical meaning of this result is unclear, but it may be that the interaction between parallel fibre layers and the resulting stress distributions cause composite failure at lower strains than in those materials where this parallel fibre layer interaction is absent. By implication then, the interaction between orthogonal fibre layers has a positive (or at least a smaller negative) effect on the strain to failure.

The results for the stored strain energy at failure (Table 24) show much greater differences between the materials. The figures represent the energy density in the material at the point of failure and are calculated by integrating the total area under the stress versus strain curve for each sample. They effectively measure a combination of the other three physical measurements made. The most obvious trend in the data is

that the values for DAMZZ and TGAM are very much higher than for the other materials. These are the two materials which contain a large amount of continuous fibre in the 0° direction. The only other material which contains this type of fibre is DAMZN and it can be seen that, of the other four materials, this has the highest stored strain energy. So it seems that the inclusion of 0° continuous fibre causes a significant increase in the value of the stored strain energy at failure for the material. Comparison of the values for TGAM and DAMZZ suggests that the contribution of 90° staple is greater than that of 90° continuous fibre. However, caution must be exercised in drawing this conclusion since if the standard deviations are considered it can be said that although the mean values are very different, the sample groups are not statistically that dissimilar. The mean stored strain energy value for TGAM is 707 kJm^{-3} which if two standard deviations are added becomes 893 kJm^{-3}. Similarly the mean stored strain energy minus two standard deviations for DAMZZ is 583 kJm^{-3}, and it is the large overlap between these values that suggests that the difference between them is not that significant.

11.4.5. Influence of fibre lay-up on failure mode

There are three main ways in which information about the failure mode may be gathered; acoustic emission studies, examination of loading curves and examination of the fracture surfaces. Acoustic emission techniques essentially involve measuring acoustic activity in the sample during the test. Acoustic emissions are generally associated with sub-critical failure events and so can give information particularly about the point during the test at which damage begins. This technique was attempted with the carbon-carbon composites used in this study but ,sadly, it did not provide any information further to that which could be gleaned from the load versus displacement traces.

The failure of acoustic emission meant that all information about the failure processes had to be gathered by examination of the load versus displacement curves and by observation and microscopy of the fracture surfaces. Both optical and electron optical microscopy were used.

Figure 83 shows six plots of stress versus strain, one example for each of the model materials tested in this study. There are several features which should be noted. The first of these is that the data gathered after the point at which damage initiates is

somewhat dubious since the stress is calculated from the applied load using the beam equations which are not valid once damage occurs, and the true stress state becomes indeterminate. Also the nature of the unloading curve (during failure) is of little or no relevance since the output from the strain gauge and load cell are suspect under these conditions and may well be responding to dynamic loading effects. It is clear that the equipment used suffers to a certain extent from signal interference particularly on the small strain gauge signal. The evidence for this is in the form of the horizontal spikes on the loading curves. Noise on the load cell signal is less likely since the signal is larger and indeed very little is observed. This is inferred from the absence of vertical spikes of any significance. The reason that one can be sure that the observed spikes are indeed interference and not a result of fracture events is that a fracture event would effect both the measured stress and strain. In other words, fracture event would cause diagonal spikes. This is due to the fact that the testing machine is under displacement control and not load control. This means that the testing machine cannot react to a failure event in order to maintain a load level and hence both stress and strain are relieved.

Four of the traces (DAMNZ, DAMZZ, TGAM and STANN) show hysteresis loops during the loading phase of the test. This is a result of the loading and unloading of the specimen and the rig so as to allow the rig to conform to the exact shape of the individual sample. This was performed in cases where severe non-linearity was observed in the time versus load curve during the early stages of the test. This effect was observed in the majority of tests. However in those tests where it was absent, the pre-loading cycle was omitted as in the case of the traces for DAMNN and STAZZ shown in Figure 83.

Traces of this type allow the measurement of strength and strain to failure as well as the calculation of modulus, however they do not provide much information about the failure mode itself. The type of failure is shown much more clearly in plots of load versus crosshead displacement. Plots of this type have been prepared for the same six samples as used in Figure 83, and these are shown in Figure 84.

The graphs in Figure 84 show some marked differences in the way the six materials fail. Where it is present, the initial peak should be ignored as it is purely an artefact of the pre-loading cycle. The form of the load versus displacement curve for the STAZZ

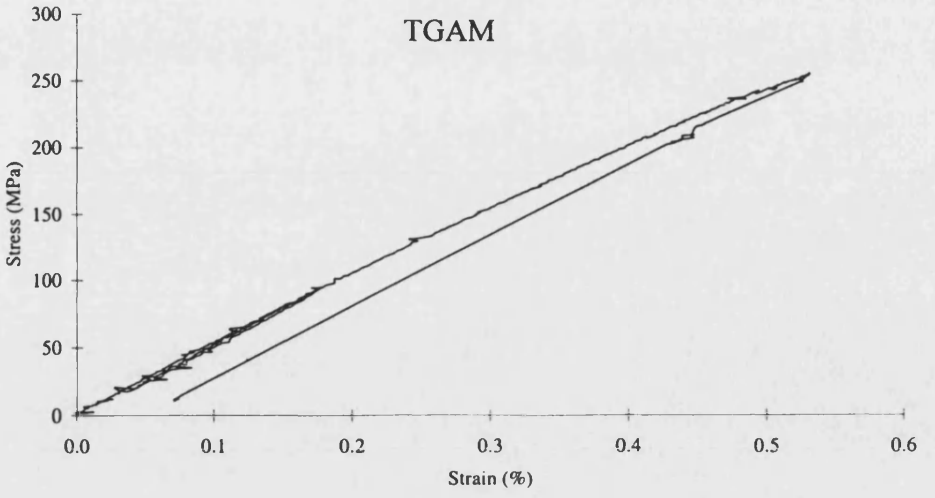

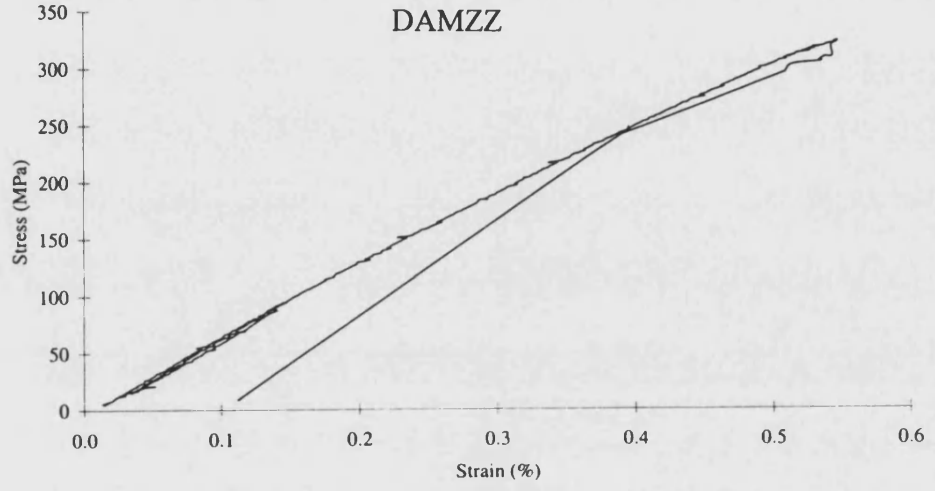

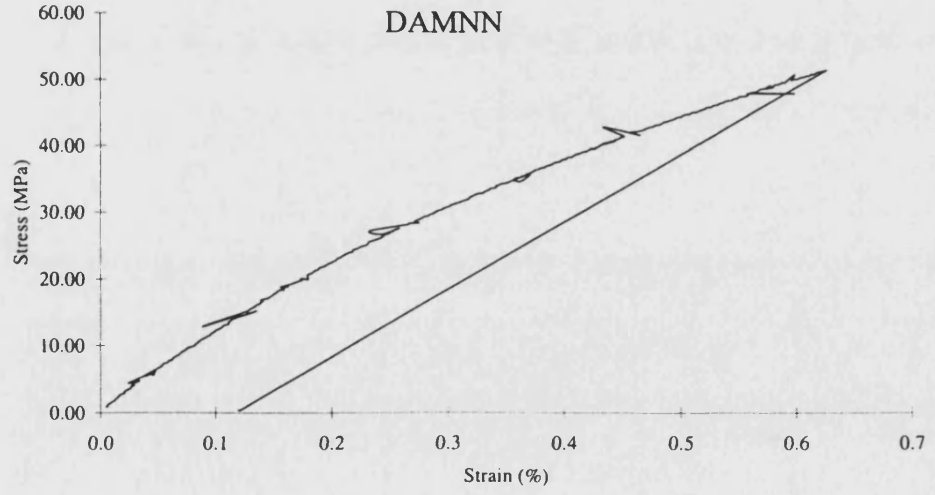

Figure 83a. Examples of stress versus strain plots typical of samples of three of the six model materials tested.

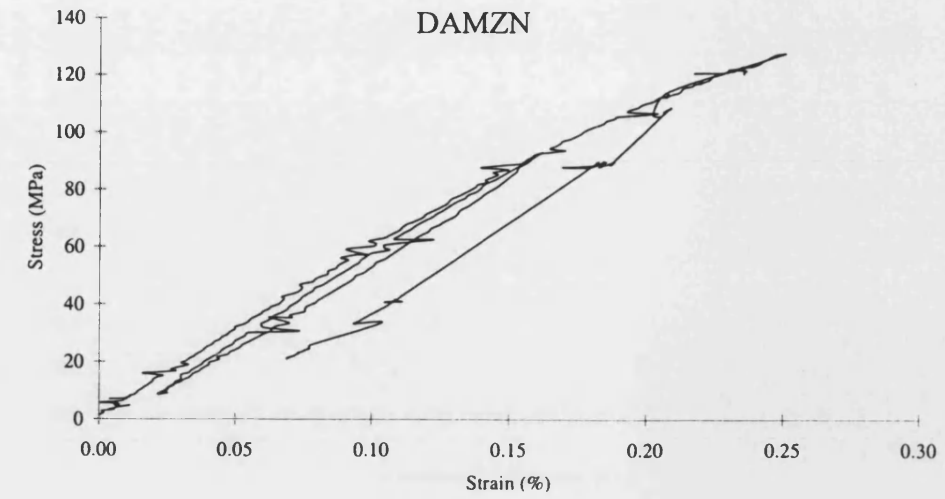

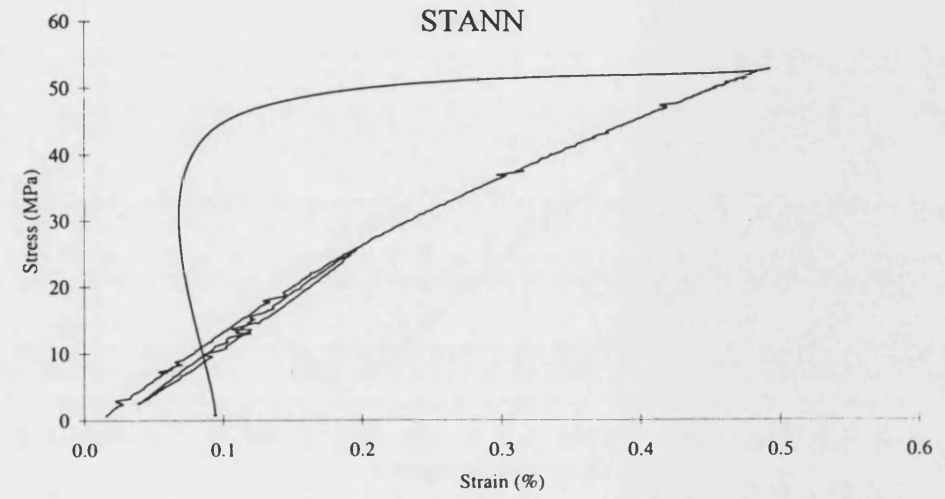

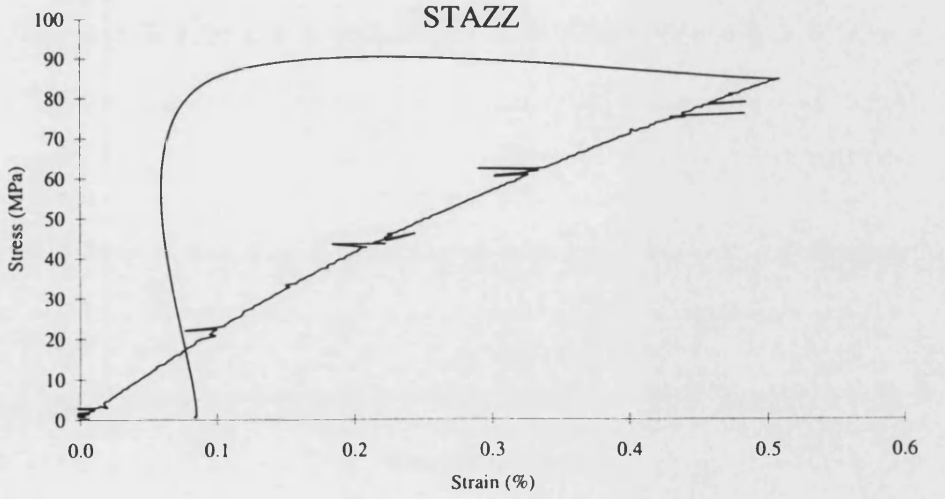

Figure 83b. Examples of stress versus strain plots typical of samples of three of the six model materials tested.

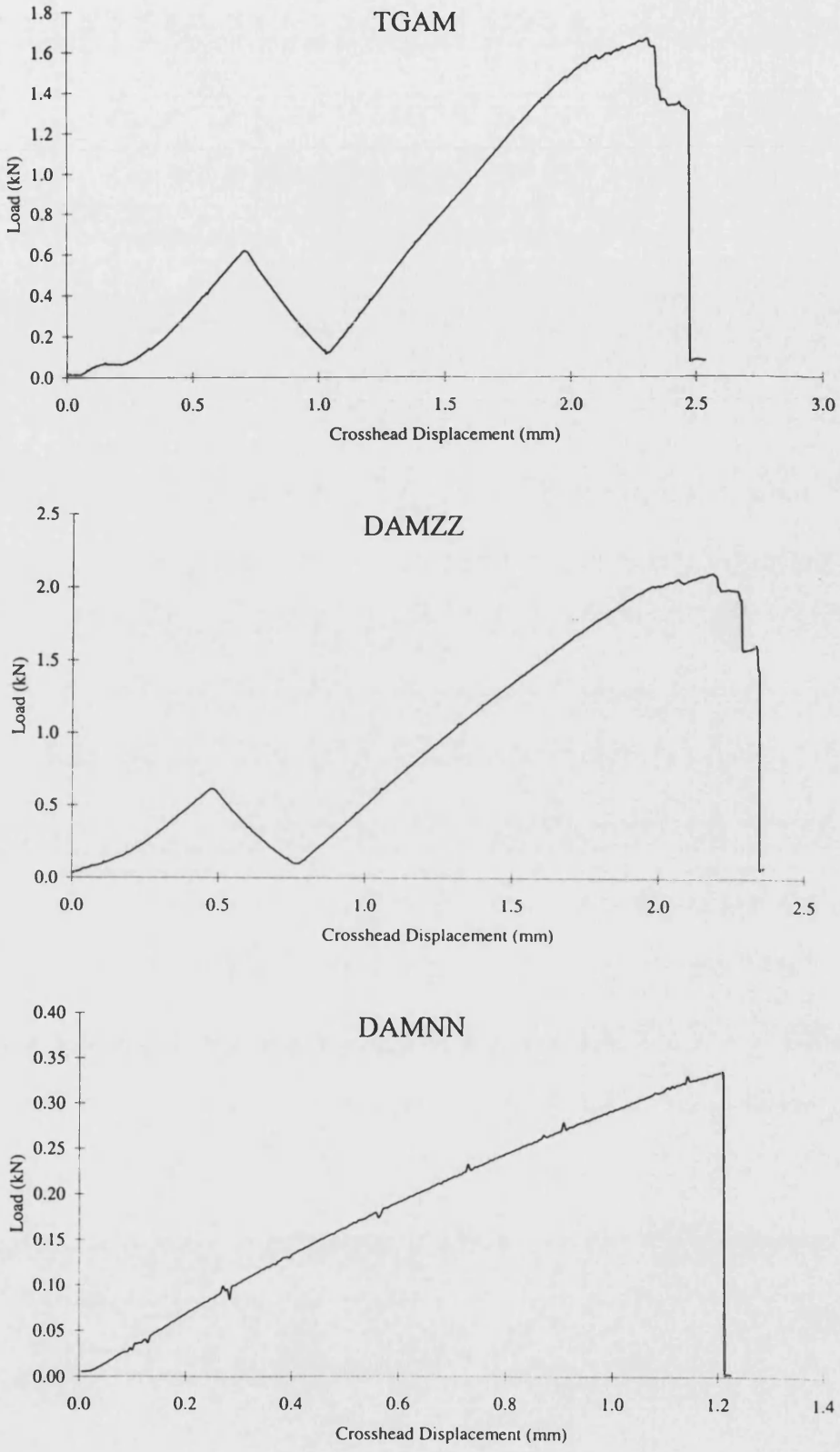

Figure 84a. Typical examples of load versus crosshead displacement plot for three of the six model materials tested.

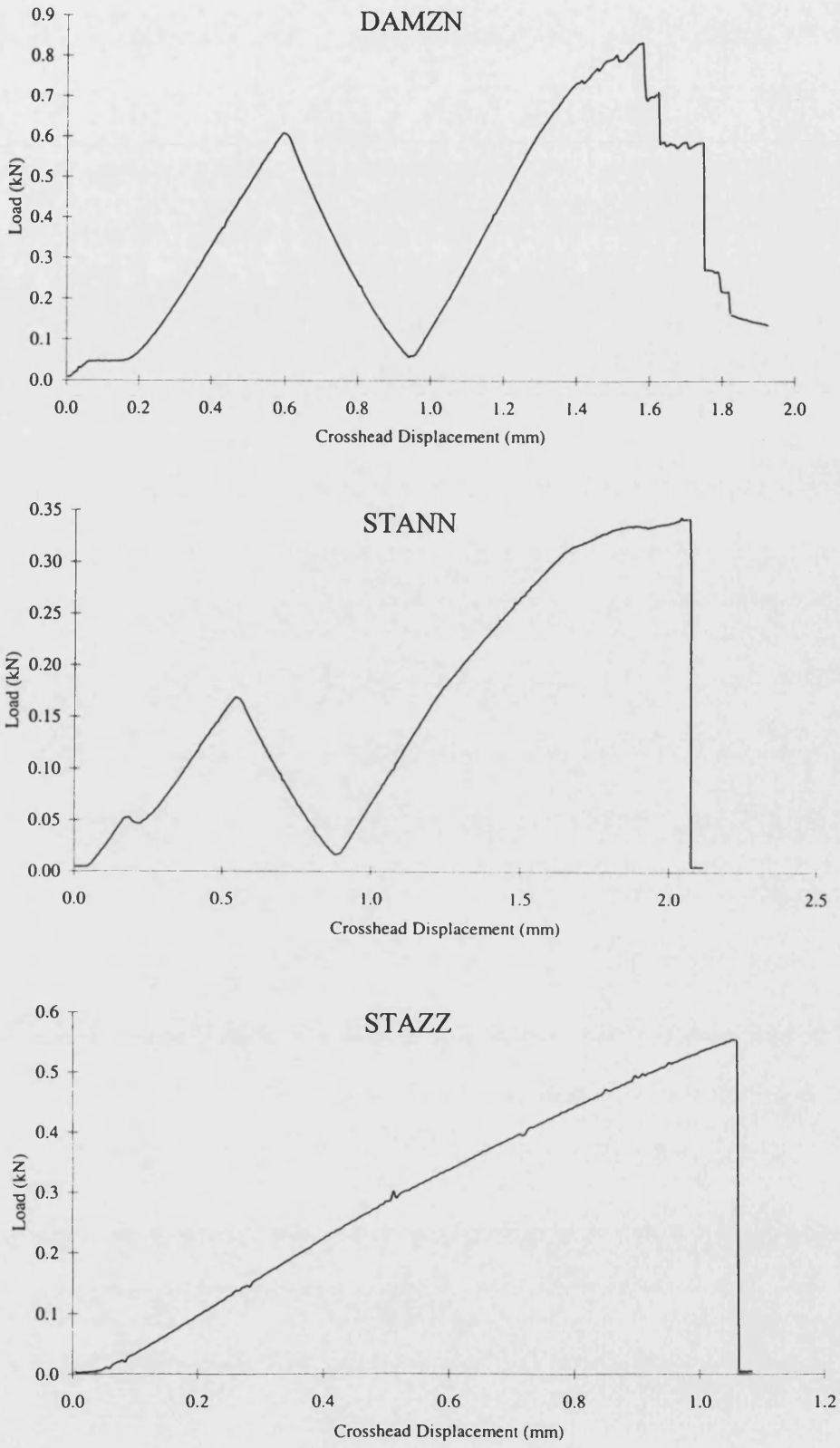

Figure 84b. Typical examples of load versus crosshead displacement plot for three of the six model materials tested.

and DAMNN materials reveals that the failure of these materials is by rapid crack propagation. Here the materials fail in a brittle manner. This indicates that the composite is not behaving as a composite should. The reinforcement in a composite is generally included to toughen it, i.e. alter its fracture behaviour from a brittle to a more graceful mode. This is achieved by energy absorbing mechanisms. The occurrence of brittle behaviour in a composite material implies that these energy absorbing mechanism are inactive. This can be caused either by the absence of crack bridging fibres, or by excessively strong bonding between the fibre and the matrix which causes it to act like a monolithic material. In these two materials the only fibre in crack bridging orientations (0°) is in the staple layers where the fibre volume fraction is low. Therefore it can be concluded that the use of 0° staple fibre layers as a toughening mechanism is ineffective.

The failure mechanism for the other four materials is, by comparison with the other two, relatively graceful. The traces for TGAM, DAMZZ and DAMZN show appreciable amounts of damage accumulation after the peak in load, and this is attributed to the inclusion of continuous fibre in the 0° direction which bridges the crack, and in the case of DAMZN, to the deflection of the crack by the differing structure of the layers. The trace for STANN shows that the failure is rapid and occurs at the peak load, but only after significant damage accumulation has occurred as evidenced by the marked turn over of the curve. At first glance it is puzzling why STANN exhibits relatively graceful failure when it contains no fibre in the crack bridging direction. Indeed this seems even more anomalous when it is considered that STAZZ, which does contain 0° fibre, is more brittle. The brittleness of STAZZ implies that the fibre to matrix bond is strong and so the crack propagates through both with impunity. Given that this bond is strong, the advancing crack in STANN is forced to break the bonding between adjacent sheaths of matrix material. In circumnavigating each fibre the crack is deflected, and the crack path is lengthened, both of which are recognised as toughening mechanisms. The cost in terms of performance, of this advantage is a significant reduction in strength since the strength of the fibre is only utilised to a very limited degree.

Examination of the fracture paths in the materials was first conducted by visually assessing the crack path where possible. In most samples fracture did not cause the sample to break into two pieces. Hence the crack path could only be examined where

it emerged from the sample, i.e. at its edges. Subsequent to this visual examination, the sample was broken into two pieces so that the whole of the fracture surface could be examined. In all cases this could be achieved by hand, indicating that although not fully fractured, the residual strength of the samples was very low. The whole of the fracture surfaces were then examined by eye. Some representative samples were then selected for microscopic analysis. For optical microscopy half of the sample was trimmed to about 10 mm from the fracture surface and then this piece was mounted in resin, polished and examined using a Zeiss microscope, as detailed in Section 6.2. The samples were mounted such that all of the constituent fibre layers could be examined. This allowed the examination of a plane close to either the tensile face or the compressive face of the sample. Most of the samples were mounted such that the tensile side was examined since this is where failure occurred, however to check if compressive failure had occurred, some were mounted the other way around.

Electron optical analysis is a more flexible technique for examining fracture surfaces, since for carbon-carbon composites, it does not require any mounting and polishing. Hence the whole of the fracture surface can be studied as opposed to the single plane which is available in optical microscopy. As with optical microscopy, typical samples were selected for examination, and one half of each of these specimens was trimmed at about 10 mm from the fracture surface. This piece was glued by its freshly cut face to a planchette using an epoxy adhesive, and when this had dried, a conducting path between the sample and the planchette was created using a conductive paint. Thus the fracture surfaces were examined in plan, i.e. the microscope acted along the long axis of the sample. Conveniently, the stage of the microscope could be translated, tilted and rotated allowing almost total freedom to examine the fracture surface from any angle.

Figure 85 shows examples of fracture surfaces for each of the six model materials which were tested in edgewise flexure. Although the amount of information which can be gathered by visual examination is relatively limited, some trends can be noticed which seem to complement the conclusions which were drawn from the examination of the load versus displacement traces.

Broadly speaking, there are two classes of fracture surface which can be seen. First there is the relatively flat and featureless surface exhibited by the DAMNN, STAZZ and STANN materials. The flatness of the fracture surface suggests that the crack has

not been deflected by the reinforcement to any great extent and this in turn implies that the failure is brittle in nature. This agrees well with the evidence from the load versus displacement traces where STAZZ and DAMNN were considered to have failed by a brittle, fast fracture mechanism. There was some doubt over the failure mechanism of STANN from these traces although significantly they show a single rapid reduction in load at failure, albeit after some damage accumulation. Hence, even in this case there is some agreement between the evidence from the two examination methods.

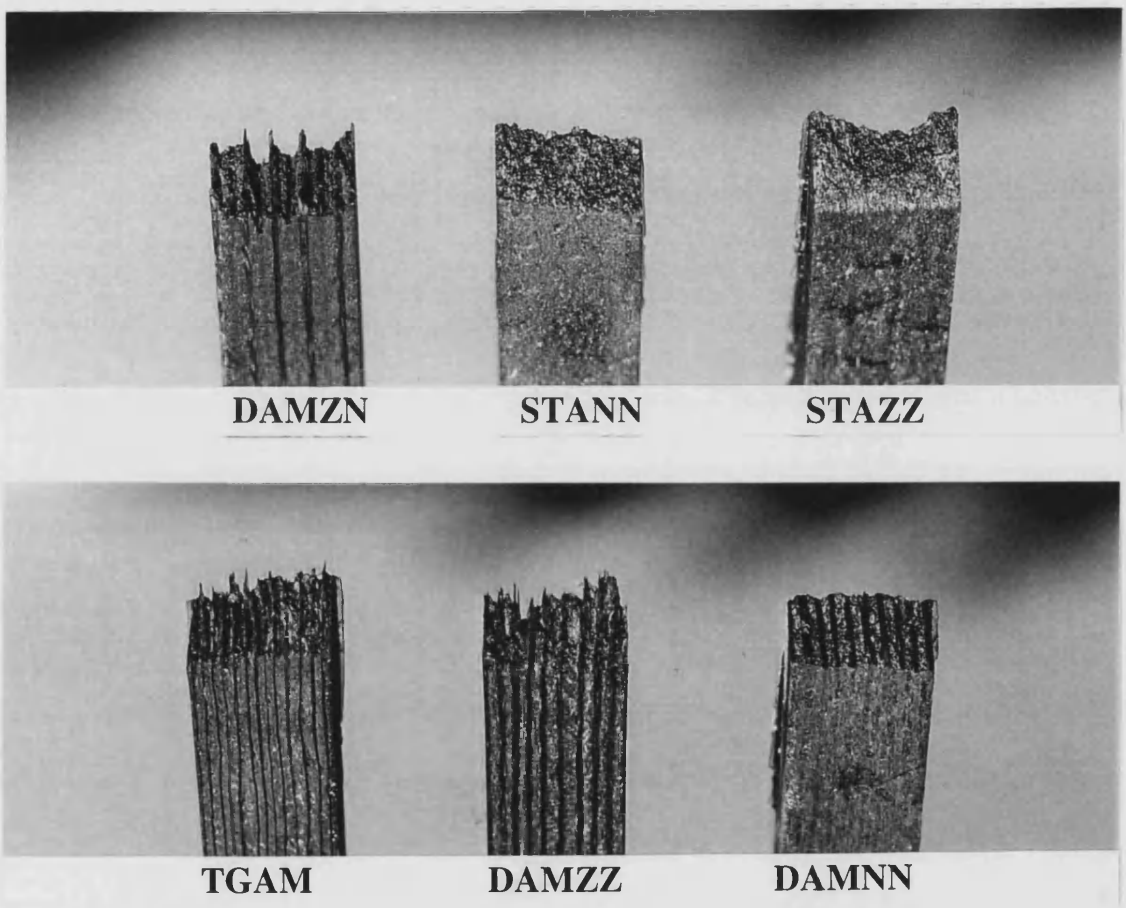

Figure 85. Typical fracture surfaces for each of the six model materials tested in edgewise flexure.

By contrast, the fracture surfaces of the other three materials (DAMZZ, DAMZN and TGAM) show significant roughness. Fracture surface roughness implies crack deflection and hence a more graceful failure mechanism. The roughness is a result of the protrusion of 0° continuous fibre layers implying that it is these layers which have deflected the crack the most and hence have provided the most effective toughening

mechanism. A slight difference can be seen in the form of the fracture surface between that of DAMZN and those of TGAM and DAMZZ. The fracture surface of DAMZN seems to have a coarser texture than those of the other materials. This is caused by the greater spacing of the protruding areas which are made up of 0° continuous fibre regions. In the TGAM and DAMZZ materials alternate layers are of fibre of this type, whereas in DAMZN every fourth layer is this type. This is the explanation of the difference in fracture surface texture. These differences seem to suggest that the DAMZN material should be more brittle in character than the other two materials since the crack path is deflected by 0° continuous fibre layers half as often. However examination of the load versus displacement traces shows that the opposite is true and in fact that DAMZN shows the most graceful failure of all the materials. An indication as to the likely explanation for this is given by the stored strain energy figures shown in Table 24. Primarily as a result of greater strength, the stored strain energy at failure for TGAM and DAMZZ is much greater than for DAMZN and hence there is more energy available to drive a fracture process. Therefore it is much more difficult to arrest or deflect an advancing crack in the TGAM and DAMZZ materials than in DAMZN. Hence there is a trade off between strength and fracture behaviour, with the disadvantage of high strength being an association with more brittle failure. This though, only applies to those materials with significant reinforcement from 0° continuous fibre layers since the materials without these layers are both weak and brittle.

Closer examination of the fracture surfaces showed that the four types of fibre layer (continuous fibre and staple in 0° and 90° orientations) exhibit very similar fracture characteristics regardless of the material in which they are included. So the fracture surface of the 90° staple layers in DAMZN were identical to the fracture surface of the STANN material. Therefore the fracture surfaces can be simplified into four types which correspond to the four fibre layer types.

Figure 86 is an optical micrograph of a section of the fracture surface of a sample of DAMZN material and shows fracture paths typical of those in 0° continuous fibre and 90° staple fibre. There are a number of clear features which reinforce the interpretations made from visual examination of the fracture surfaces. The first of these is that the fracture paths in the two regions are different. In the 0° continuous fibre the crack has obviously been deflected around the fibres to a certain extent. This

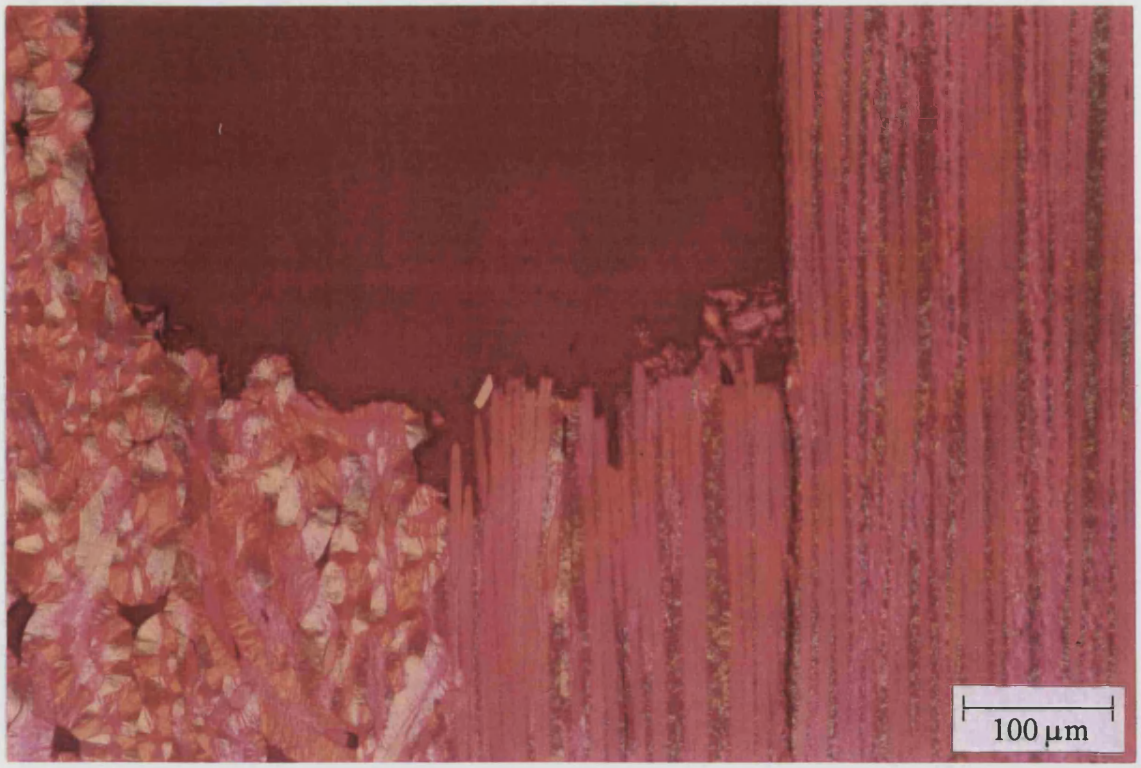

Figure 86. Fracture surface of a sample after edgewise flexural testing. The picture shows 0° continuous fibre and 90° staple fibre regions from close to the tensile face.

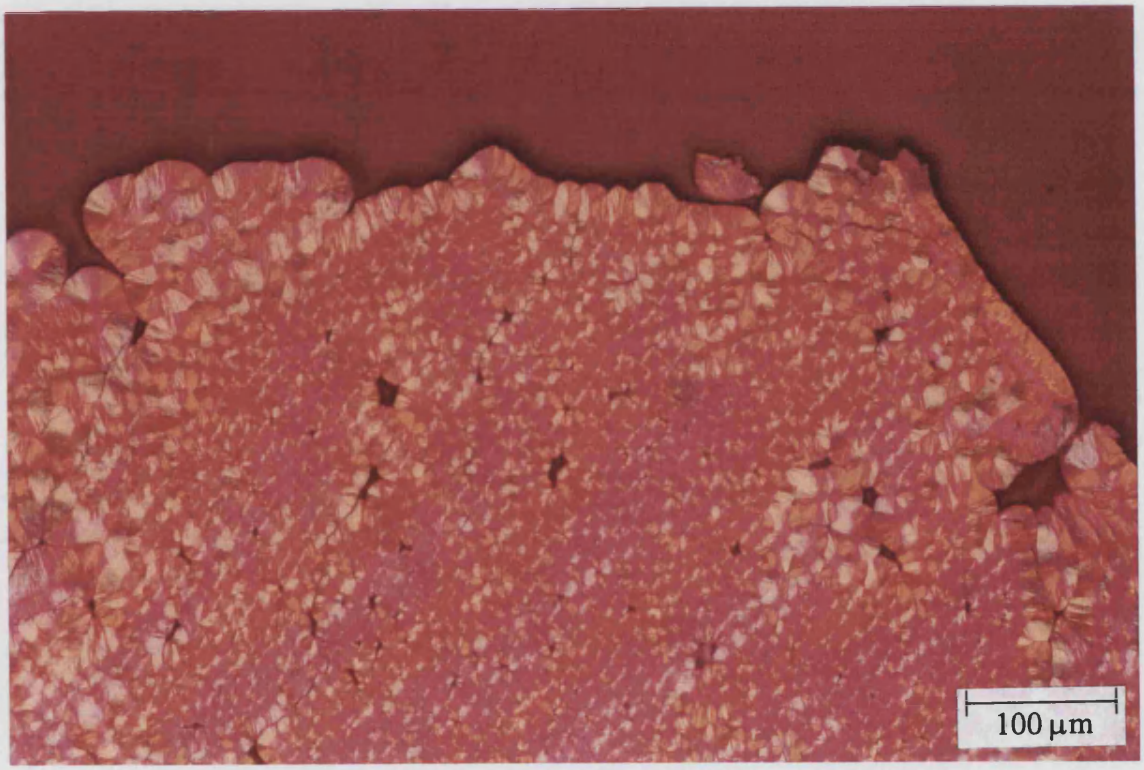

Figure 87. Optical micrograph of a typical fracture surface in a 90° continuous fibre layer.

is a classical toughening mechanism. However, it can be seen that the length of fibre which protrudes (up to roughly 50 μm) is relatively short and hence the whole layer has acted together. This protrusion of fibres above the underlying level of the fracture surface is known as fibre pull-out, and is generally acknowledged as being indicative of toughening of the material by energy absorbing crack deflection mechanisms. The short fibre pull-out in these layers implies that these layers are responsible for some toughening of the material and hence more graceful failure. Another feature visible in the continuous fibre region of this photograph which is indicative of toughening by crack deflection is that the fibre layer has split along the fibre direction and acted in two distinct parts. The fracture surface of the right hand half is beyond the top of the frame. Therefore it can be concluded that the 0° continuous fibre layers deflect the crack and hence toughen the material but that the deflection is caused by the layer either as a whole or as large parts, and not by significant individual fibre pull-out.

The left half of Figure 86 shows a 90° staple fibre region, and it can be seen, particularly in the extreme top left hand corner, that the fracture path is between the matrix sheaths which surround the fibres. Hence the contribution to the strength of the material from these layers is dependent on the bonding between adjacent matrix sheaths and also by physical interlocking of these sheaths. That the failure occurs entirely in the matrix, and significantly not at the fibre-matrix interface, is an indication that the fibre-matrix bond is stronger than the matrix-matrix bond at the interface between sheaths. This is further evidence that the material is not toughened by individual fibre pull-out.

Visual examination of the fracture surfaces revealed that the roughness of the surface was due to the protrusion of 0° continuous fibre layers. However it was unclear how the crack advanced along the plane of the cloth layers in order to produce this roughness. Figure 86 shows two ways by which this can be achieved. The first is the longditudinal splitting of a 0° continuous fibre layer and the second is by crack diversion in 90° staple layers. Of these mechanisms the second was observed much more frequently. So it appears that the inclusion of the 90° staple fibre layers allows the crack to change path relatively easily to take advantage of natural weaknesses in the reinforcing 0° continuous fibre layers. Figure 86 shows evidence of this having occurred in the middle of a 90° staple fibre layer, however it was more commonly seen closer to the boundary between the staple layer and the adjacent layer.

Interestingly, the location of the fracture path was found to be primarily dependent on the fibre orientation and not on the fibre type, i.e. the fracture path in 0° and 90°staple was very similar to that in 0° and 90° continuous fibre respectively. This is due to the similar nature of the structure of the material in these layers. Figure 87 shows a typical fracture path in 90° continuous fibre and it is clear that as with 90° staple, the fracture path is between matrix sheaths. Also evident is the fact that the crack has propagated through a low fibre density region formed at the boundary between adjacent fibre bundles. In these regions the structure of the material strongly resembles that of a 90° staple fibre region. Again then, it would appear that the crack has chosen the path of least resistance. This implies that the strength of 90° continuous fibre is higher than that of 90° staple since if this were reversed the crack should avoid the staple-like regions of the continuous fibre layers. This is a direct contradiction of the findings of the analysis of the strength data and solution of the simultaneous equations in strength which imply that 90° continuous fibre is less strong than 90° staple. It must therefore be concluded that the fracture surface shown in Figure 87 was not formed in a staple-like region. The likely explanation is that the region through which the crack propagated was of unusually low density and hence was inherently weak.

In the true staple layers, the adjacent sheaths of matrix material impinge on each other as they are formed and so if a cross-section of one is analysed in isolation its circumference is seen to be far from circular. Usually there are several reasonably linear sections where the growth of the sheath has been impeded. Many of the matrix sheaths at the fracture surface shown in Figure 87 are very rounded and this implies that their growth was not impeded by proximity to other growing matrix sheaths. All this evidence points to the existence of porosity at the fracture site prior to testing which supports the theory that the cause of the failure at this point was not due to the resemblance of the region to staple regions but rather to a pre-existing inherent weakness.

Clearly then, the structure of the fibrous reinforcement has a significant influence on the location of the crack path. Any coalescence of porosity at a given location offers a relatively low resistance path for the crack. These are of most significance when they offer a crack path across a fibre layer. An obvious point of cross-layer weakness in the structure of all the materials are the stitches which are used to hold the cloth layers

together. Figure 88 shows the fracture surface (at the top of the photograph) in a 90° continuous fibre layer after edgewise flexural testing. The undisrupted 90° continuous fibre structure can be seen in the bottom of the photograph and is in stark contrast to the structure of the material close to the fracture surface. Here, the fibre orientation and density is different as a result of stitching. It is a feature of stitches that in any fibre layer the fibre orientation in the stitch is across the layer. The fibre structure in the immediate vicinity of the stitch also tends to be disrupted. The orientation of fibres across the layer forms a low resistance path across the layer for crack propagation and so it is extremely common to see stitches close to, or at, the fracture surface. It is clear that the inclusion of stitches aids cross-layer cracking and so it would seem logical to suggest that they be omitted from the fibre structure. However, it is essential to include some stitches so that the DAM cloth may be handled during fabrication of the composite material. Perhaps more importantly though, they do lend some sort of tri-directionality to the structure of the composites. Although the cloth layers are only linked in pairs, this reduces the number of non-linked planes in the material by a factor of two. Hence stitches increase the interlaminar strength of the material and serve to reduce the anisotropy in the in-plane and cross-plane properties.

When the stress versus strain traces for the materials were examined it was noticed that all the model materials tested showed some degree of departure from linear elastic behaviour. True linear elasticity implies direct proportionality of stress and strain and so traces of stress versus strain are of the form of a straight line. Any departure from a straight line is evidence of non-linear elasticity and is caused by plastic deformation or damage accumulation. Figure 83 shows examples of stress strain behaviour for the model materials and these all show curved loading portions. In each case there is a change in slope of the curve at between 40 % and 60 % of the peak stress. If the load versus displacement traces are examined (Figure 84) this change of slope is also apparent. Evidence of pseudo-plastic behaviour has been found during the optical analysis of tested samples and an example is shown in Figure 89. In this figure the fracture surface is on the extreme right hand side of the photograph and the picture shows a region of 90° staple fibre. There is a clear band of material, approximately 400 μm wide, in which multiple cracking and general gross deformation has occurred. The picture gives the distinct impression that this is the effect of a plastic deformation process. This effect was observed exclusively in 90° staple fibre regions, although not

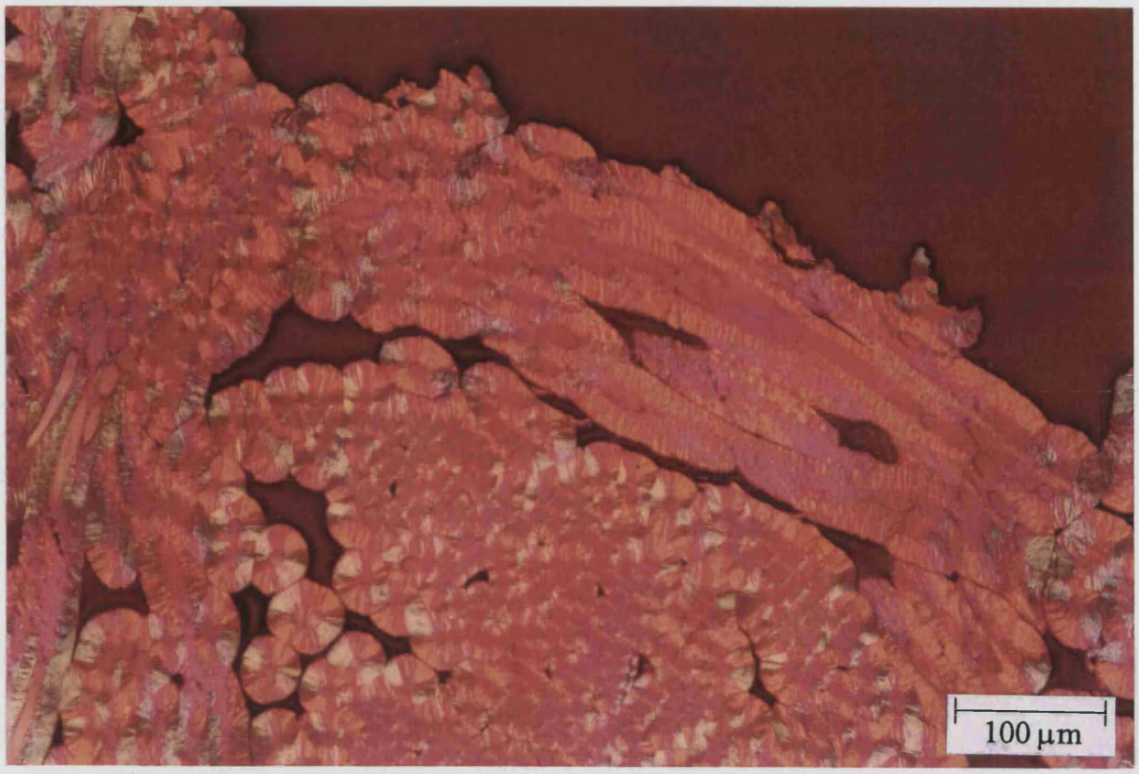

Figure 88. Fracture surface in a 90° continuous fibre layer showing the influence of a stitch on the fracture path.

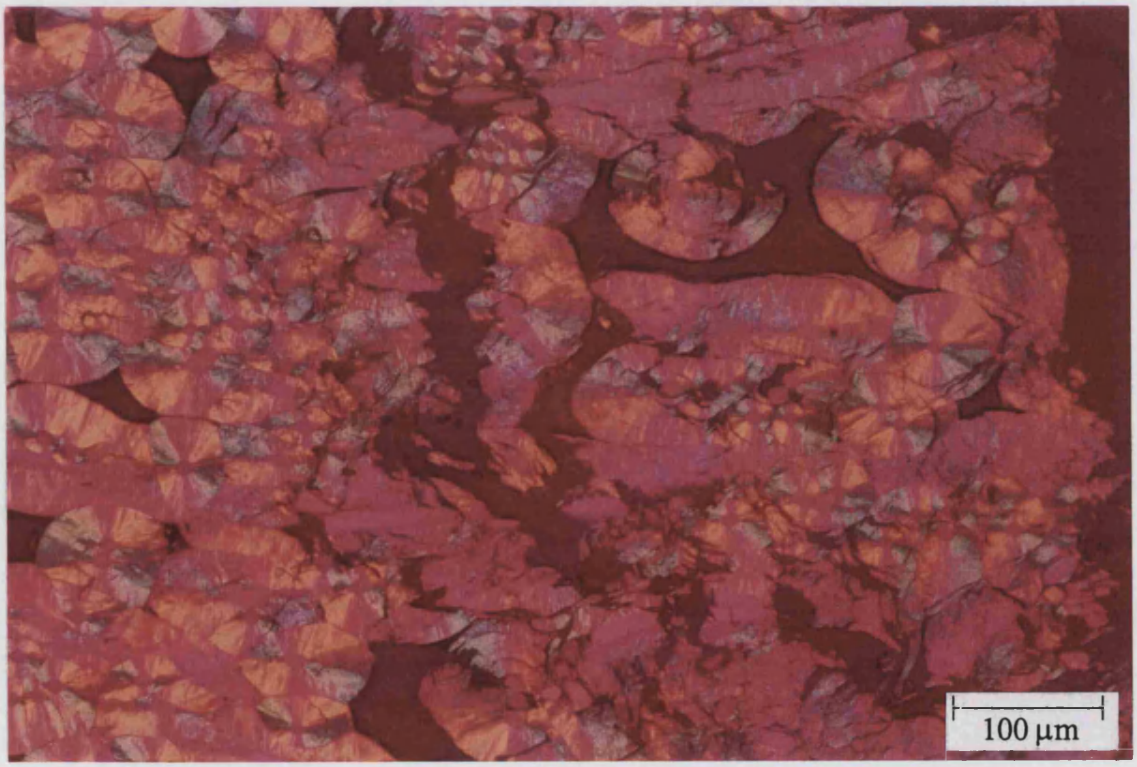

Figure 89. Evidence of possible pseudo-plastic behaviour in 90° staple fibre layers.

all of these regions exhibited the effect. Close examination reveals that it is the matrix material which has deformed leaving the fibres relatively unaffected. Whereas most of the optical micrographs of fracture surfaces give the impression of a rapid, energetic and brittle failure, this picture suggests a slower, less energetic and more plastic failure. The STANN material consists entirely of this fibre layer type and examination of the load versus displacement trace for this material shows that as the peak load is approached a very smooth turn over is exhibited. Comparison with the curves for the other materials (none of which are exclusively 90° staple) shows that they all have a degree of undulation of the curve during the turn over. This undulation takes the form of a saw-tooth like wave and is the result of short but rapid propagation of the crack, or cracks, within the material. That the effect is absent in the case of STANN implies that the fracture processes are more continuous and less stepwise in their nature.

It is postulated that the deformation of the sheaths of matrix material in 90° staple material allows the sheaths to slide past one and other in a controlled fashion after cracking has initiated between them, in order to relieve the applied stress. This produces the smooth turn over of the load versus displacement curve and the optical evidence for plastic deformation. Effectively the structure is detangled during the fracture process as the mechanical interlocking of the fibres and their sheaths is destroyed. It would seem logical to suggest that such an effect might be observed in 90° continuous fibre layers, however it has not been seen. It could be that the samples examined do not exhibit the effect, but that it does occur, but it is more likely that the effect is absent or at least less significant. This is probably for two reasons. Firstly, the fibres in 90° continuous fibre layers are more close to parallel and so there is less mechanical interlocking. Secondly, the volume fraction of matrix material in the 90° continuous fibre layers is very much lower than in the 90° staple layers. Since the micrographs suggest that the plastic deformation occurs in the matrix, plastic deformation in continuous fibre layers is therefore less likely.

Examination of the fracture surfaces by SEM helped to clarify the location and mode of the failure. Optical microscopy is a useful technique which reveals the structure of the material in section and this is complemented well by SEM which is able to examine the whole fracture surface. However, without sectioning the sample, SEM is unable to probe into the material.

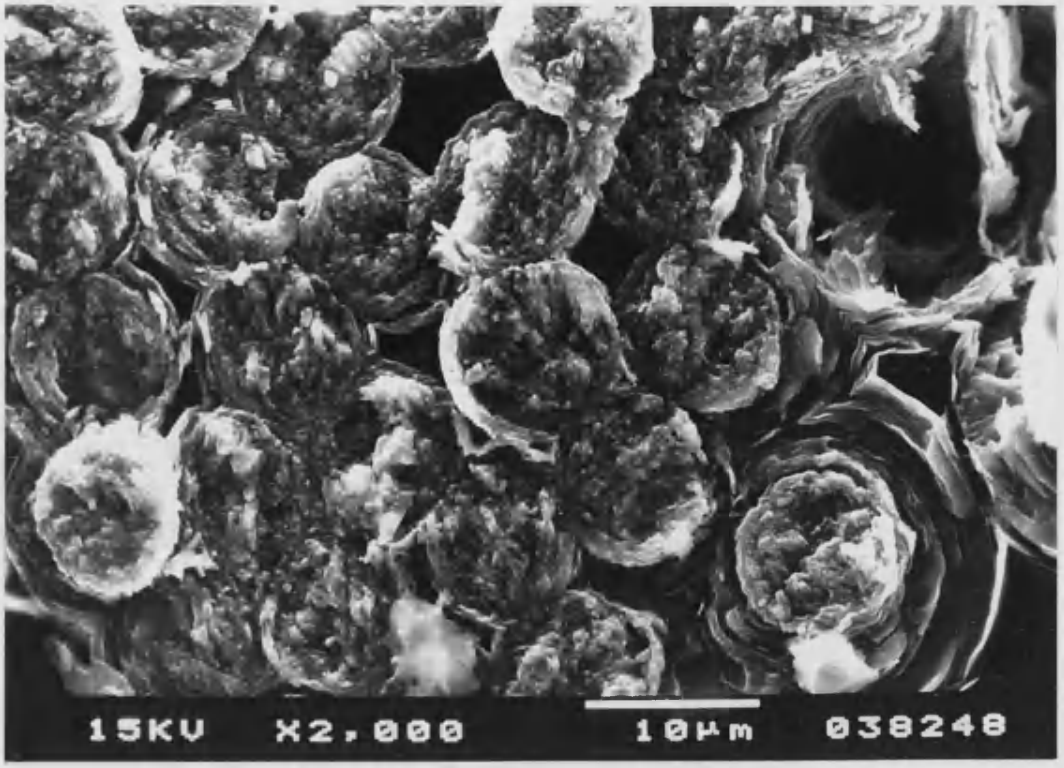

Figure 90. SEM micrograph of the fracture surface of material in a 0° continuous fibre layer.

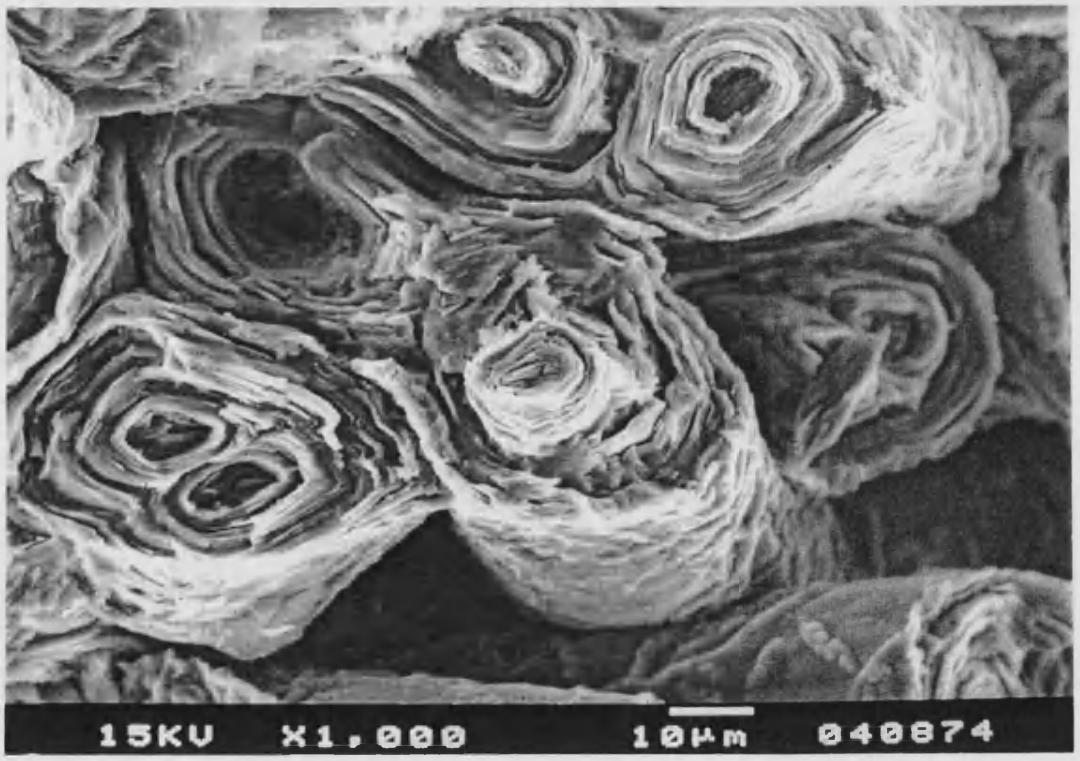

Figure 91. SEM micrograph of the typical fracture surface in 0° staple fibre layers.

Figure 90 shows part of the fracture surface in a 0° continuous fibre layer. The structure of the material is clearly visible with an array of fibres about 8 μm in diameter each coated in matrix material of varying thickness. In the bottom right hand corner of the picture a single fibre is surrounded by matrix material roughly 5 μm thick whereas in the main part the fibres are only coated to a thickness of around 1 μm. Also visible are many pores most of which have sharp corners which are significant stress concentrators and would provide ideal points for the initiation of through-matrix cracks. Perhaps the most striking feature of this photograph is the relative flatness of the fracture surface and the absence of any appreciable fibre pull-out. In the top right corner an empty sheath of matrix material can be seen which indicates some pull-out, but this is the only evidence. This agrees well with the optical microscopy where little fibre pull-out was observed.

Optical microscopy of the fracture surfaces of 0° continuous fibre and 0° staple fibre layers indicated that the main features were similar in both, hence it is expected that the appearance of both should also be similar under SEM. Figure 91 shows a section of the fracture surface of a 0° staple fibre layer and clear similarities with Figure 90 can be seen. The most important of these is that the fracture surface is relatively flat and that there is no appreciable fibre pull-out. Again this agrees with the interpretation of the optical micrographs. The open nature of the structure in staple fibre layers is very apparent from this photograph, indeed the impression is given that the porosity volume fraction is higher than the 20 % measured by image analysis (Section 9.2.). It is also clear that the orientation of fibres in staple layers is much less perfect than in the continuous fibre layers and also that the fibre volume fraction is very low. This causes there to be much more matrix material in these regions with each fibre being coated to a thickness of about 10 μm. In these greater thickness the concentric tube-like structure of the matrix material is clearly visible. In this photograph the some of matrix seems to be cracked along the boundary between layers of matrix material around some of the fibres. These fine cracks have been observed using optical microscopy in both tested and un-tested material. It is concluded that their occurrence is an artefact of manufacture and is not caused by testing or subsequent failure. It is likely that they are caused by thermal shrinkage stresses set up in the material as it is cooled after completion of a CVI run.

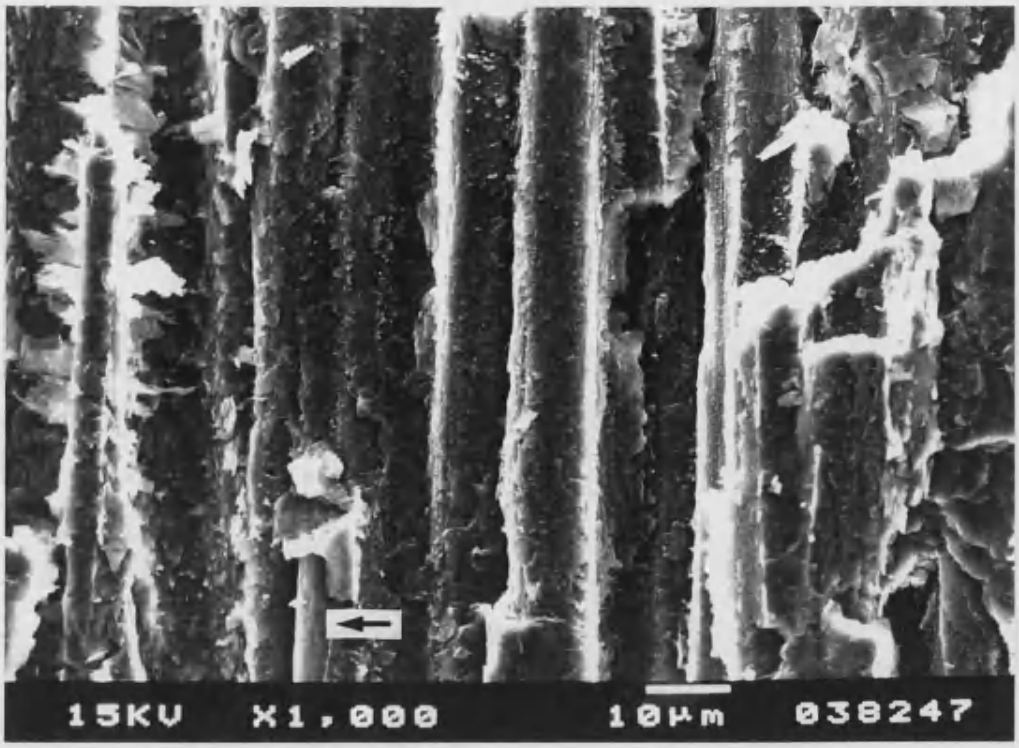

Figure 92. SEM micrograph of the fracture surface in a 90° continuous fibre layer.

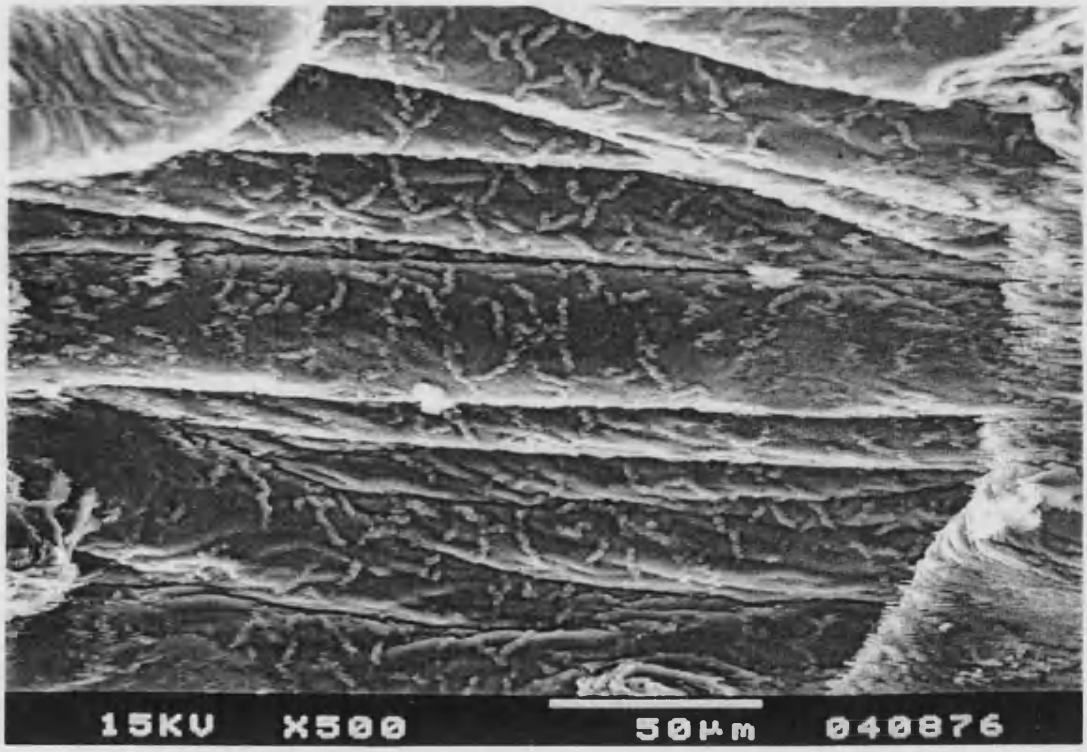

Figure 93. SEM micrograph of a typical area of the fracture surface within a 90° staple fibre layer.

The nature of the fracture surfaces in 90° fibre layers of both types showed marked differences from the equivalent layers in the 0° orientation. Figure 92 shows a typical part of a fracture surface in a 90° continuous fibre layer. Multiple parallel cylindrical structures can be seen and at first glance it is difficult to tell if these are fibres or matrix sheaths. Optical microscopy leads to the conclusion that cracking is through-matrix and so it would be expected that the structures in the photograph are matrix sheaths. Three things confirm this speculation. Firstly the structures are about 10 μm in diameter and this is too large for fibres which are typically about 8 μm in diameter. Secondly the structures have the scaly appearance characteristic of the matrix material, and finally the shallow, longditudinal grooves typical of the surface of the fibres are absent. The SEM pictures confirm that the preferred crack path in these fibre layers is through-matrix. As with the optical microscopy there was evidence from SEM investigation of occasional fibre-matrix debonding, however this was observed in single fibres rather than whole bundles or layers. In these cases the crack passes through the matrix to the fibre-matrix interface, around part of the circumference of the fibre, and continues through the matrix at the other side. In SEM photographs the evidence for this is sections of fibre which have been stripped of their matrix sheath. An example of this is arrowed in Figure 92 where the exposed fibre surface can be clearly seen. It should be emphasised that this type of cracking was unusual.

The fracture surface of 90° staple fibre layers showed significant similarities with that of 90° continuous fibre layers. Figure 93 shows a typical section of the fracture surface of a 90° staple fibre layer. The scaly appearance and diameter of the cylindrical features (roughly 30 μm) indicates that they are matrix sheaths and not fibre surfaces. Hence, as with 90° continuous fibre layers, the crack propagates through the matrix between adjacent sheaths. Again the relative lack of alignment of the fibres is apparent, although in this photograph the degree of alignment is relatively high. Interestingly, there is much more particulate debris on the fracture surface of 90° continuous fibre than on that of 90° staple and also the surface of the matrix sheaths is much smoother. The reasons for this are unclear, but it is possible that it is a function of the relative thicknesses of the matrix sheaths in the two layer types.

11.4.6. Introduction of k, the correction factor

It has been shown that the best way to measure the true strain is to use a strain gauge. However, strain gauges are expensive and cannot be re-used and therefore, despite the difficulties associated with the calculation of true strain, there are economic advantages to the other methods of strain measurement. One of the easiest of the other methods is the total centre point displacement method and so an attempt was made to obtain an empirical correlation between the output from a centre point LVDT and a strain gauge.

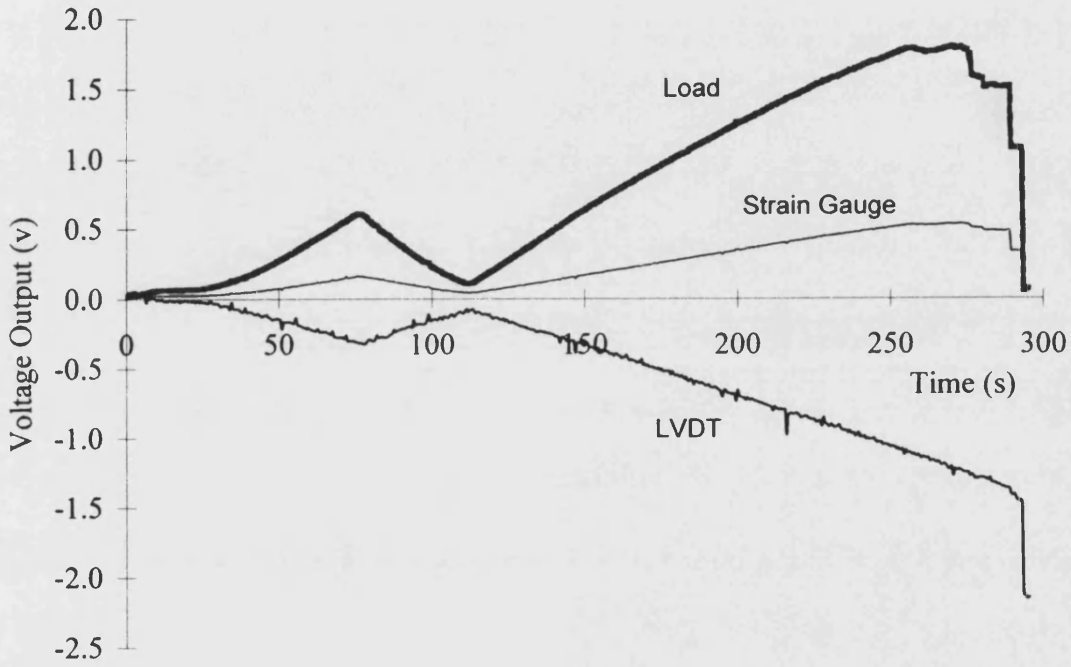

Figure 94. Typical plot of the raw voltage data from the load cell (load), the strain gauge (SG) and the total centre point displacement LVDT (LVDT) from an edgewise flexural test.

The raw data were compiled in four columns; time, load (0-10 volt scale), strain gauge output (mV) and LVDT output (mV). To check that the experiment had produced reliable data, the three outputs were plotted on the same axis against time (Figure 94). If the raw data looked reliable they were converted into time, true load (kN), true strain (%), and centre point displacement (mm). Then two plots were made of load

versus strain, and load versus centre point displacement. Best fits to the data in the linear loading region were plotted to correct for any zero offset error. The data from the strain gauge invariably gave zero strain at zero load, but the LVDT data were not so consistent. This was because the voltage output corresponding to zero displacement, although constant for a given test, varied from test to test. Therefore a constant was added to the LVDT data such that the straight line best fit for the loading curve passed through the origin.

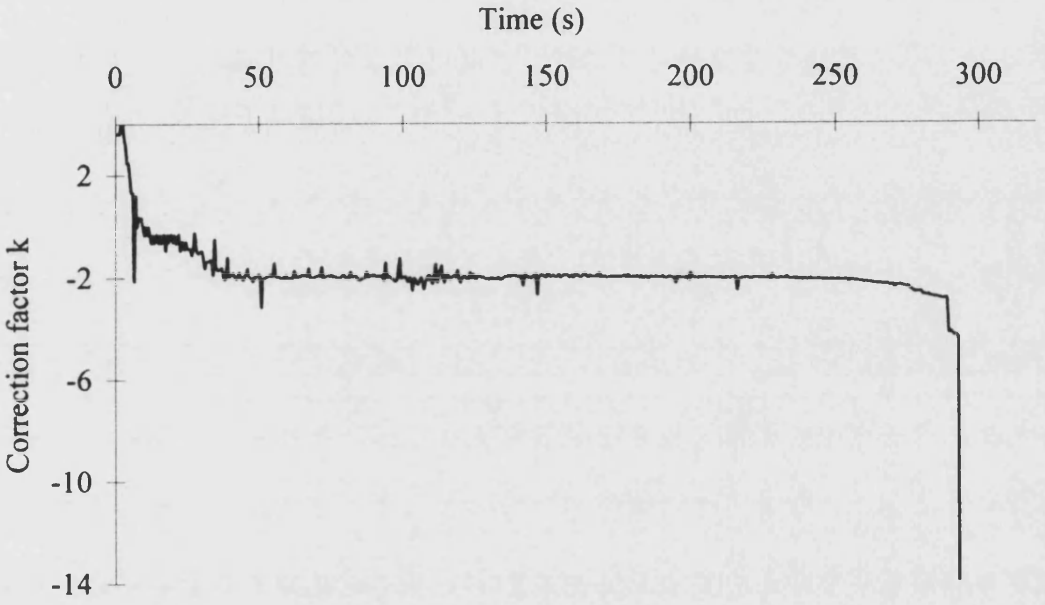

Figure 95. Plot of the correction factor (k) against time show its stability for most of the test except initial settling and during the fracture process.

To find the correction factor, each of the LVDT displacement data values (mm) was divided by its corresponding true strain value (%), to give a column of ≈ 500 correction factors. It was necessary to chose a single correction factor for the curve which transformed as many to the data points as accurately as possible. Taking a simple average of the correction factors is not the best way of finding the best fit, since at low loads the correction factor is different to that during the majority of the test, and this has an adverse affect on the average. It was found that the best way to select the

data range was by eye. A graph of time versus correction factor was plotted, and the result was typically of the form shown in Figure 95, which clearly shows the varying proportionality at low loads. The time invariant correction factor was extracted from this plot by taking the best horizontal line fit to the linear regions of the plot.

Having found the correction factor the LVDT displacement data (mm) was divided by the correction factor to produce a column of calculated strain (%) data. Finally, the true strain and calculated strain data were plotted on the same axis versus load. An example of this type of plot is shown in Figure 96. There is clearly an extremely good correlation between the true and calculated strain values.

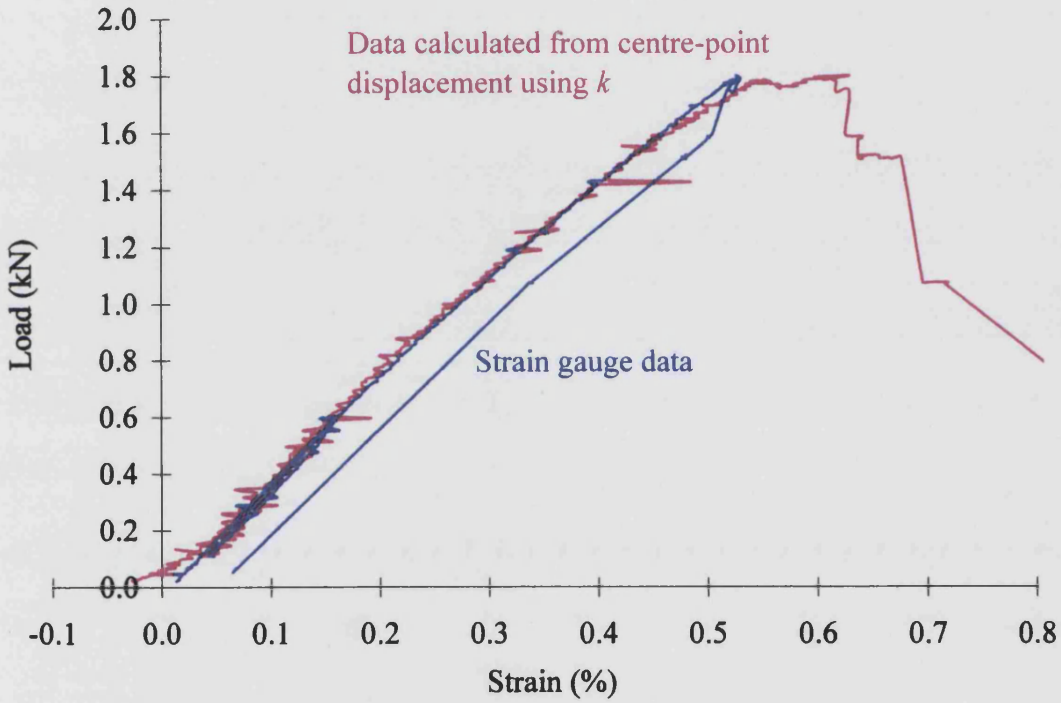

Figure 96. Plot of measured strain (SG) and strain calculated from the total centre point displacement data using the correction factor. The plot shows the good agreement between the two excluding the beginning and end of the test.

This procedure was carried out on the data from all the strain gauge tests and the correlation was found to be very good in all cases. The implication from this result is that the true strain can be calculated from the total centre point displacement, provided the correction factor is known. A list of the correction factors for each of the samples

is given in Table 27. It should be noted that all the correction factors are negative because the centre point displacement is measured in the negative sense.

Sample	Correction Factor (k)	Sample	Correction Factor (k)
TGAM Mean	-1.94751	DAMZN Mean	-2.15639
TGAM Stdev	0.04071	DAMZN Stdev	0.09513
DAMNN Mean	-2.17139	STAZZ Mean	-2.12919
DAMNN Stdev	0.10050	STAZZ Stdev	0.15327

Table 27. Calculated correction factors using the true strain calculated from the measured total centre point displacement for some of the model materials tested in four point edgewise flexure.

The results in Table 27 show that the range of correction factor (k) for any given material is small, i.e. the value of k is relatively constant. This means that there can be a high degree of confidence in values of strain worked out by this method using data from tests where only the total centre point displacement was recorded. In other words the strain at any load, and hence modulus, of the materials can be calculated from tests by measuring only the total centre point displacement and the load, provided the correction factor is known with confidence in advance.

The results show that k is very similar for all the materials with the exception of TGAM. This can be explained if the physical meaning of k is considered. The relationship of total centre point displacement, true strain and k is described formally by Equation 47.

$$\varepsilon_w = \frac{D_w}{k} \qquad \textit{Equation 47}$$

Where ε_w = True strain at load W

D_w = Total centre point displacement at load W

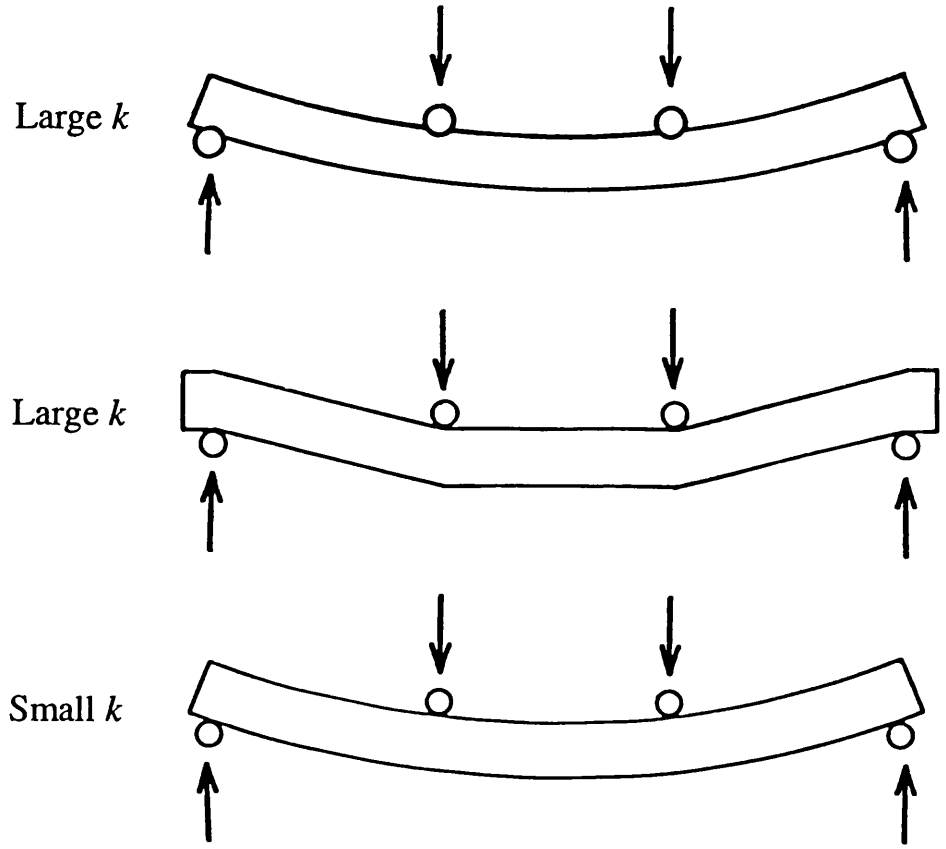

Figure 97. Schematic diagram illustrating the physical meaning of the magnitude of the correction factor, *k*.

Hence a large value of *k* means that for a given strain the total centre point displacement is larger than that for a sample with a small value of *k*. This implies that either more shear deformation or more loading point indentation occurs in tests which yield a large *k* values. This is illustrated schematically by Figure 97. Effectively the magnitude of *k* reveals the combination of these two effects since in practice both probably occur to some extent. Therefore the lower *k* value for TGAM implies that this material deforms less by shear (i.e. it conforms more closely to perfect bending) than the other materials, and/or TGAM is more resistant to indentation at the loading points. TAGM has one of the higher moduli of the materials tested and therefore it can be assumed that the indentation at the loading points would be small relative to the other materials. Therefore, the low value of *k* can be attributed in the main part, to this effect. However the modulus of DAMZZ is greater than that of TGAM and so even

less indentation might be expected. If this is so the reason for the large k value for DAMZZ must be mainly due to greater shear deformation in this material. It must be remembered that the modulus used in these assumptions is the in-plane tensile modulus as measured in flexure and not the cross-plane compressive modulus which is of importance in calculating the significance of load point indentation.

12. FOUR POINT EDGEWISE FLEXURAL TESTING OF OXIDISED MODEL MATERIALS

12.1. Introduction

The previous chapter has dealt with the influence of the fibre architecture on the mechanical properties of the PAN-CVI system analogous to the material produced commercially by Dunlop Ltd. Of course, these properties are important, however they represent only part of the information required by a designer who is to use the materials. Of particular significance is the way in which the material will respond when it is put into service in practical conditions. Possibly the most important consideration is the way in which the properties of the component might change and result in component failure. It has already been explained that the main ways in which this can occur are component dimensional change and intrinsic material property change. In materials which can suffer from fatigue failure, another consideration is the accumulation of fatigue damage. In this case the component can be considered as having failed from the moment damage is initiated, and hence it may spend much of its life in the failure process. However it is believed that carbon-carbon composites have very high fatigue tolerance, and so the two mechanisms of interest are dimensional change and material property change. Of these, the change of material properties is by far the most insidious. Dimensional change can be easily monitored during service and the appropriate action taken if a problem arises, however material property changes can frequently occur without accompanying changes of appearance. Therefore it is important to know the way in which property changes might occur.

In the case of carbon-carbon composites used in aircraft brake discs, the most likely cause of material change is oxidation. This is due to the exposure of the discs to oxidising atmospheres at elevated temperatures in which carbon-carbon composites are known to have a propensity to undergo oxidising reactions. It is also well known that oxidation has extremely deleterious effects on the mechanical properties of carbon-carbon composites, and, since this is the main limitation on their use, much work has been done in this area. Of particular interest has been methods by which oxidation can be inhibited in order to prolong the useful life of carbon-carbon composite products[78]. However this work is proceeding without the full

understanding of the effects of oxidation on microstructures, and equally importantly the effect of microstructure on the oxidation behaviour. It seems that to the industrial community which funds much of the research in this area, the knowledge that oxidation is bad news and should be avoided is sufficient. There is little work available which suggests that a full study has been conducted which encompasses the interdependence of microstructure and oxidation behaviour, and the effects of oxidation on mechanical properties, fracture behaviour and microstructure. It is important that the effects of oxidation are understood more fully, and so an investigation was initiated with the aim of elucidating the relationship between microstructure and oxidation behaviour for the model PAN-CVI carbon-carbon composites. Also, the dependence of the mechanical properties on the extent of oxidation were to be investigated. The aim of this study was to suggest ways in which the oxidation characteristics of the commercial Dunlop material may be improved without the consideration of chemical or physical inhibition systems.

12.2. Oxidation

In order to assess the effects of oxidation it is an obvious condition that samples must be tested and examined at various levels of oxidation. The examination of all the model materials in all possible states of oxidation is beyond the scope of this study both in terms of time and cost. Therefore it was necessary to narrow the field of investigation. The most obvious way that this could be achieved was by reducing the number of materials used and so four model materials were selected on the basis of their structures being representative of a range of complexities. The materials used were TGAM, STANN, DAMZZ and DAMZN. The fibre architecture and microstructure of these materials has been described in Sections 9.1. and 9.2. respectively. The second method used to reduce the scope of the investigation was to concentrate only on low levels of oxidation. The reasons for choosing the low end of the oxidation range are threefold. First it is known that the first stages of oxidation have the greatest negative effect on the mechanical properties of carbon-carbon composites. Zhao *et al*[65] found that the strength and modulus of a PAN fibre and resin char and CVI matrix carbon-carbon composite were reduced by about 40 % at around 10 % oxidative weight loss (Figure 98 and Figure 99). Secondly, the detection of oxidation by visual examination becomes somewhat easier at higher oxidation

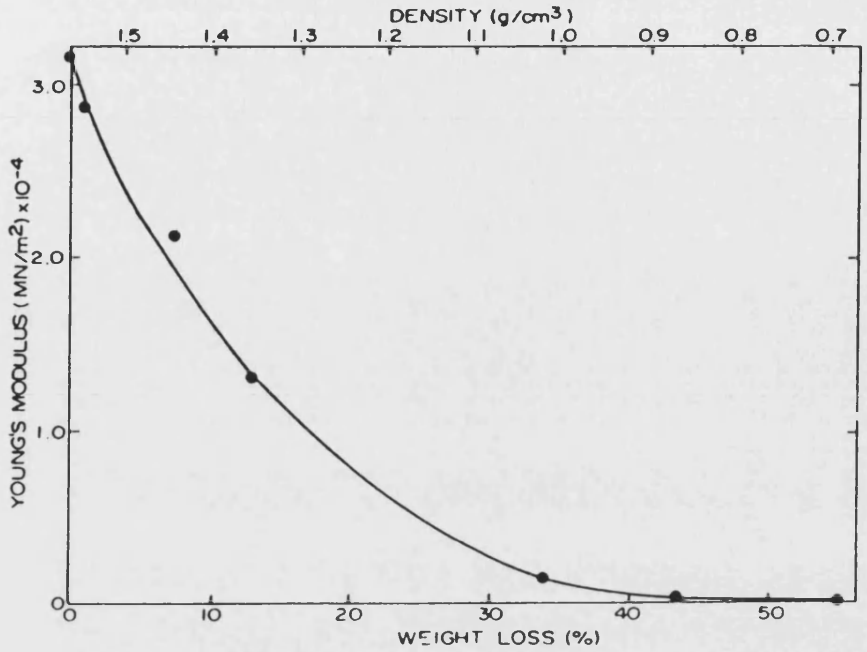

Figure 98. The effect of oxidative weight loss on the modulus of a PAN fibre, resin char and CVI matrix carbon-carbon composite[65].

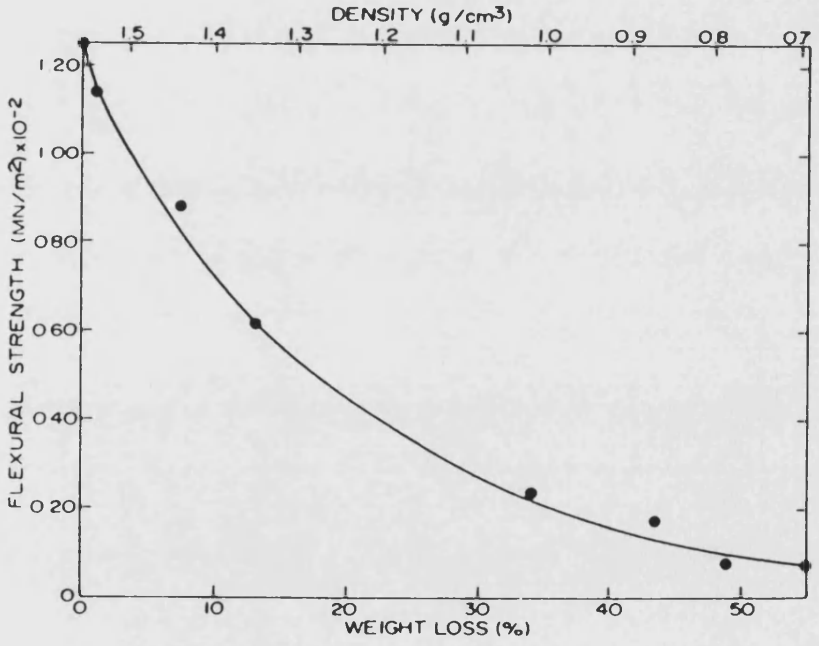

Figure 99. The effect of oxidative weight loss on the flexural strength of a PAN fibre, resin char and CVI matrix carbon-carbon composite[65].

levels. This is of practical importance since during routine maintenance of aircraft brake discs the operative can be relied upon to recognise high levels of oxidation and take remedial action. Hence it is most important to understand the effects of oxidation during the stages where it has deleterious effects whilst remaining relatively undetectable. Finally, investigation of low level oxidation is more appropriate to this study because of the shorter experimental oxidation times required.

The best way to investigate the effects of oxidation on these materials is to take a group of nominally identical samples and subject them to varying degrees of oxidation. Inherent in this is the need for a method by which oxidation of the material can be controlled to produce samples which have experienced various levels of oxidation. Thermal oxidation of carbon materials requires two conditions, elevated temperature and an oxidative atmosphere. The elevated temperature can be easily supplied by conventional furnaces and, provided that the furnace is environmentally sealed, the atmosphere can also be controlled. The choice of appropriate temperature and atmosphere are interlinked and depends upon the rate and type of oxidation which is required. Oxidation occurs in three distinct kinetic zones and the physical effects of oxidation in each of the zones can be very different. These were reviewed in Chapter 4. To summarise, in Zone 1 the oxidation rate is under chemical control, i.e. the rate determining step (RDS) is the chemical reaction between carbon and the oxidative gas. In Zone 3 the RDS is the diffusion of the oxidative gas to external surface of the carbon hence the reaction is under boundary layer diffusion control. Generally Zone 1 occurs at low temperatures whereas Zone 3 occurs at high temperatures. Between these Zone 2 operates where the reaction rate is influenced by the diffusion of the oxidative gas in the pores of the material as well as the chemical reaction rate at the surface.

For a scientific study, oxidation in Zone 1 is generally preferable since this produces the most uniform oxidation. However there are occasions where other zones of oxidation can be successfully used. Accurately modelling the effects of oxidation in service will require the assessment of the Zone which is operating in service. If this is Zone 3, then Zone 3 oxidation should be used to model the effects of service conditions on the material. In the case of aircraft brake discs the thermo-chemical conditions in service are difficult to assess. The temperature of the disc can vary across its diameter by a large amount resulting in one part being in Zone 1 and another

in Zone 3. Of course the atmosphere at various parts of the disc will also alter. At the inside circumference, which is relatively open to atmosphere, the atmosphere will probably be close to that of the ambient air. However, at the centre of the swept area, which is usually in close contact with the adjacent disc, the atmosphere is effectively sealed and therefore will be different. On top of these complications the temperature of the disc is not constant since the disc goes through heating and cooling cycles upon each application of the brakes. Therefore modelling of service conditions is a complex task and it is necessary and sensible to simplify the conditions for the purposes of a scientific investigation.

12.2.1. Reasons for using carbon dioxide

When choosing the conditions under which oxidation will be studied, the main variables are the temperature and the atmosphere. It is usual to choose an appropriate atmosphere first and then decide upon a temperature which is within the oxidation zone of choice. The gases most often used as atmospheres in oxidation experiments are air, carbon dioxide or a mixture of carbon dioxide and carbon monoxide, and in most cases Zone 1 oxidation is desired to ensure uniform oxidation. In order for the effect of oxidation on the properties of the material to be independently studied, all the material must be subject to uniform oxidation. If this is not the case, for example if the oxidation is concentrated at the surface, the sample effectively becomes a mixture of two materials (oxidised and unoxidised). This situation complicates the analysis of the results and makes the effect of the oxidation more difficult to assess. Of course it may be that in service the material does not oxidise uniformly at all and therefore the relevance of uniform oxidation to the practical application of the material can be questioned. However, it has already been discussed that the accurate modelling of service conditions is difficult, and so while the pattern of oxidation in service is important, it is more important to first understand the effects of controlled oxidation under laboratory conditions.

The choice of atmosphere is dictated by the need for control in Zone 1. While this can theoretically be achieved in any atmosphere by accurate temperature control, it is much easier to obtain in carbon dioxide. The reaction between carbon and oxygen (which is in air) is exothermic, and so during the reaction the sample is heated. Since in Zone 1 the rate of reaction is highly dependent on temperature (see Chapter 4),

small rises in temperature cause increases in the reaction rate and hence energy (heat) release rate. Conventional furnaces can raise the temperature of samples relatively quickly but they are extremely poor at dissipating the excess heat produced in the specimen by the reaction. Therefore it is extremely difficult to control the temperature of the specimen if air is used as the oxidative atmosphere. By contrast the reaction between carbon and carbon dioxide is endothermic which means that no specimen heating occurs as a result of the reaction itself. Indeed, the reaction will actually cause cooling of the sample. Hence it is much easier to accurately control the temperature, and therefore the oxidation, of samples if carbon dioxide is used as the oxidative gas. Occasionally an oxidative gas consisting of a mixture of carbon dioxide and a low concentration of carbon monoxide is used to further control the reaction. The addition of carbon monoxide to carbon dioxide has the effect of inhibiting the reaction between carbon dioxide and the carbon sample because carbon monoxide is a product of this reaction. However the use of carbon monoxide, which is highly poisonous, presents practical safety difficulties. Although not insurmountable these problems added extra complexity to the experimental method. Therefore nominally pure carbon dioxide was chosen as the most suitable oxidising gas.

Having chosen to use carbon dioxide, the most appropriate temperature had to be decided upon. Obviously it had to be within Zone 1 and so this limited the available range. In general, reactions follow the rule of thumb that states that the more slowly the reaction proceeds the more likely it is that the reaction will occur in a controlled and uniform manner. Therefore lower temperatures are more desirable for producing uniform oxidation. However the slower the reaction rate, the longer it takes to produce a given level of oxidation, and so there is a trade-off between achieving uniform oxidation and achieving the desired oxidation levels in a reasonable time. The rate of reaction between carbon and carbon dioxide is known to be very low below around 900 °C except in the presence of a catalyst. However the exact rate at which a given carbon body will oxidise is dependent on many variables, and so the only way to correctly assess the rate of oxidation of a carbon material under specific conditions is to measure it experimentally. So the determination of a suitable oxidation regime for this work was by an iterative experimental trial and error method. To this end many dummy runs were performed using scrap material until a reasonably

high oxidation rate which still produced even oxidation was found. This regime is described fully in the following section.

12.2.2. Practical oxidation method

There are two methods of producing samples of oxidised material. The first consists of oxidising a large piece of material and subsequently machining samples from it, and the second consists of machining the samples and then oxidising them. The first method has one major drawback. It is well known that oxidation is commonly concentrated in the surface regions of a material, and with the first method this region is machined off leaving the core of the original block. Of course, once machined the densities of the samples can be measured, but since there can be no record of their pre-oxidation densities the true oxidation level in any one sample cannon be accurately determined. Another practical difficulty with this method is that it requires the oxidation of a large block of material and this requires a furnace with a large volumetric capacity. As no such furnace was available for this study the second method was chosen as the most appropriate. In addition to the practical advantages, this method also allows the measurement of the dimensional change of the specimens caused by oxidation and this can give an indication of the extent of surface burn off.

Due to time constraints it was not possible to oxidise the samples one at a time, and so oxidation was performed on batches of ten samples. Having weighed and measured these samples the batch of ten was stacked, in a known arrangement, in an open ended alumina tube of dimensions which would allow it to fit in the furnace. The use of an alumina tube was an attempt, which proved reasonably successful, to reduce temperature gradients within the stack of samples. It is difficult, if not impossible, to eliminate temperature gradients within a sample and since in Zone 1 the reaction rate is temperature dependent, it is difficult to avoid differential oxidation rates within the samples and the sample stack. Clearly, the surfaces of the stack will heat up first and this generally results in greater oxidation at the surface. Therefore it was important to reduce temperature gradients as much as possible.

The alumina tube containing the batch of samples was then loaded into a Pyrotherm tube furnace and carefully positioned in the centre of the hot zone. The furnace tube was sealed at both ends with stainless steel end caps, and whilst still cold the entire tube was purged with CO_2 to remove any residual air. The intake of the furnace,

situated at one end, was connected to a cylinder of compressed CO_2 and the exhaust, at the other end, sealed by a water filled airlock. The flow of CO_2 to the furnace was controlled by a two stage regulator attached to the gas cylinder and a needle valve attached to a rotameter used to measure the gas flow rate. The flow rate is required to be high enough to provide excess CO_2 in order that the oxidation be in Zone 1, but it must not be so high as to cause any aerodynamic cooling effects within the furnace. The fine adjustment of the gas flow proved difficult, although in general an approximate flow rate of 40 ml per minute was used.

The furnace used was fitted with a digital controller into which the temperature programme for each run was entered. The maximum temperature ramp rate of 150 °C per minute was used during both ramping up to, and down from, the oxidation temperature which was 900 °C. In order to vary the extent of oxidation the dwell time at 900 °C was varied. Even with every effort to control the oxidation conditions it was found that the exact extent of oxidation was not constant from one run to another. As a general rule however, a dwell time at 900 °C of 72 hours produced an approximate oxidative weight loss of 3 %.

After oxidation each sample was re-weighed and the percentage weight loss calculated by comparison of the change in mass with the original mass. The dimensions of the samples were also measured to check for significant external surface burn-off. If it was found that the samples had not achieved the desired weight loss after an oxidation run they were returned to the furnace for additional oxidative treatment.

It was found that there was some inherent variation in the extent of oxidation between samples in the same batch. Although it might be thought a problem, this scatter in oxidation level was in fact useful in that it caused the spread of weight losses to be more continuous across the range of investigation. After sufficient oxidation the samples were prepared for testing in the same way as unoxidised samples.

12.2.3. Microstructural effects of oxidation

The effect of oxidation on the samples and their microstructure was assessed by visual examination and by using optical microscopy. Samples were prepared for optical microscopy in exactly the same way as was the unoxidised material. A full description of the preparation method is given in Section 6.2.1.

Initial visual examination of early oxidised samples revealed that the end of the sample closest to the gas inflow was oxidised more severely, as evidenced by a significant dimensional change at the end of the sample. This could be produced by temperature gradients along the sample, but it seems more likely that it is the result of changing gas composition along the length of the sample Carbon monoxide is known to inhibit the oxidation of carbon and this gas is also a product of the reaction between carbon and carbon dioxide. The up-stream end of the sample is in pure carbon dioxide and so oxidised relatively rapidly. By contrast the down-stream end of the sample is in a mixture of carbon dioxide and the carbon monoxide produced by the oxidation of the up-stream end, and consequently oxidises more slowly. In later oxidation runs care was taken to position the samples more carefully and further from the open ends of the tubular alumina crucible to reduce any thermal gradients. Also, a sacrificial piece of scrap carbon was positioned up-stream of the samples in order that carbon monoxide be produced up-stream of the leading edge of the samples. It was found that this reduced the leading edge burn-off effect although it also slowed the rate at which weight loss was achieved.

Visual examination also showed that oxidation reduced the surface reflectivity of the material. It is logical to associate reflectivity with a smooth surface and so the dullness of oxidised surfaces indicated an increase in surface roughness. This effect was most noticeable when layers of continuous fibre were perpendicular to the examined face. Despite this apparent evidence of external surface burn-off, measurement of the samples revealed no significant dimensional change even at high weight losses. This implies that, although the oxidation has an effect on the surface appearance of the samples, the extent of surface burn-off is limited.

Optical microscopy of the material showed that there was a distinctive pattern to the oxidation. The oxidation was found to be more extensive closer to the surface of the sample, although there was also evidence of significant oxidation through the complete thickness. The oxidation gradient was found to be greatest in samples subject to low overall weight losses. This implies that the oxidative gas was not able to penetrate the full thickness of the sample during the early stages of oxidation. However, as oxidation progressed, it is clear that the gas was able to gain access to the interior of the sample. Therefore it can be concluded that much of the porosity present

in the sample prior to oxidation is closed to the oxidising gas, and that oxidation opens up the porosity.

On a finer scale, there was a consistent trend in the location of the oxidation-induced porosity. Optical micrographs showing the typical pattern of oxidation at various percentage weight losses are shown in the sequence from Figure 100 to Figure 105. At first, the early stages of oxidation reveal very little microstructural change. However, close examination of Figure 101 shows that there is a small crescent-shaped pore around one of the fibres (arrowed). This pore is different in character from the cracks caused by thermal stresses and volumetric shrinkage during manufacture which are generally positioned a short distance into the matrix sheath and are more wavy in their character. A typical example of a shrinkage crack induced during manufacture is shown in Figure 104 (bottom arrow). By contrast the pore produced by oxidation is at the fibre-matrix interface and is smooth. The study of microstructural changes at higher weight losses showed that this was early evidence of oxidation.

The sequence of micrographs shows clearly that with increasing oxidation, the crescent shaped pores seen in Figure 101 dilate and become more widespread. The right hand half of Figure 105 shows numerous crescent shaped pores in a staple fibre region. Above about 9 % weight loss the microstructural effects of oxidation are extensive. Careful analysis of a number of sequences of micrographs such as these also suggests the sequence of formation of these pores. The pores are first seen at the interface between the surface of the fibre and the surrounding matrix and this is evidence that the oxidation of the composite initiates in this region. The continuation of the oxidation process is by gradual oxidation of the fibre, i.e. the crescent shaped pores become wider by growing inwards into the fibre. This effect is clearly seen in the staple fibre regions mainly as a result of the thick coating of matrix material surrounding each fibre. In the continuous fibre regions the effect can also be seen, although the micrographs are more difficult to interpret. Measurement of the outer diameter of the pores created by oxidation of staple material reveals that they are of a size consistent with that of the unoxidised fibre. This suggests that while the fibre is oxidised there is little, if any, oxidation of the surrounding matrix sheath.

In the continuous fibre regions the porosity which is developed is crescent shaped at low weight losses, but becomes more rounded as oxidation progresses. Whereas in the staple fibre regions the matrix sheath is apparently undamaged, in the continuous

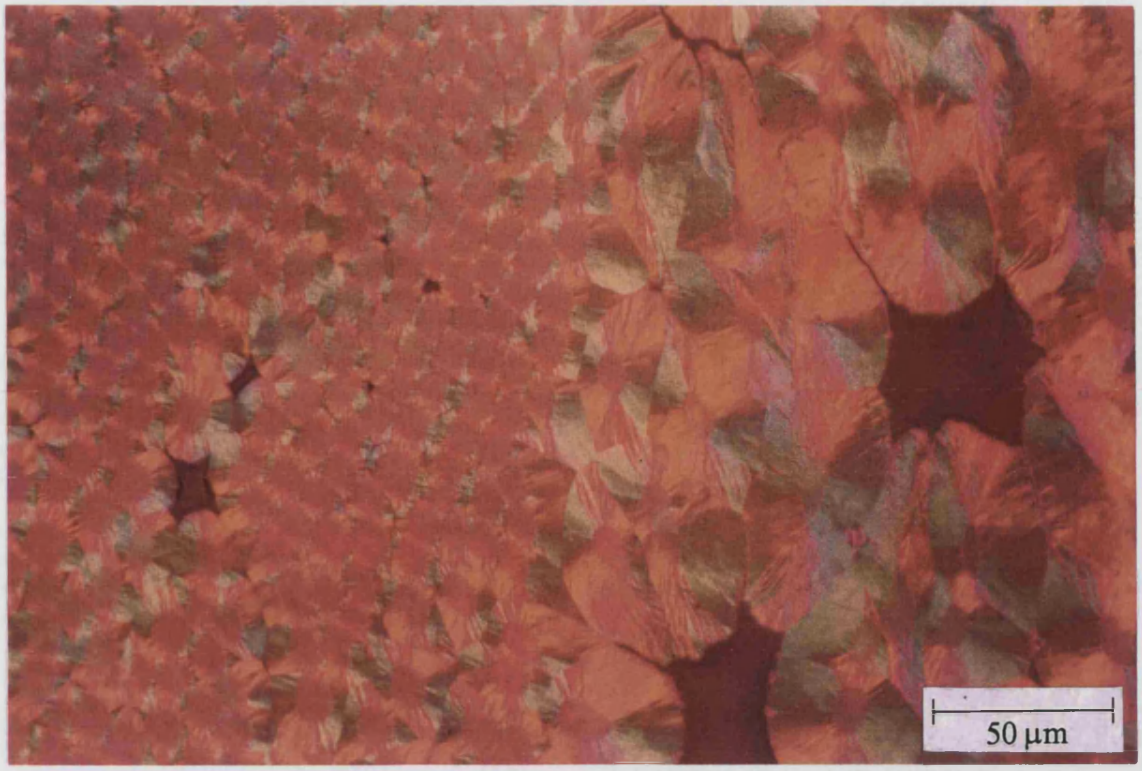

Figure 100. Micrograph of the structure of a continuous fibre layer (left) and a staple region (right) before oxidation, i.e. at 0 % weight loss.

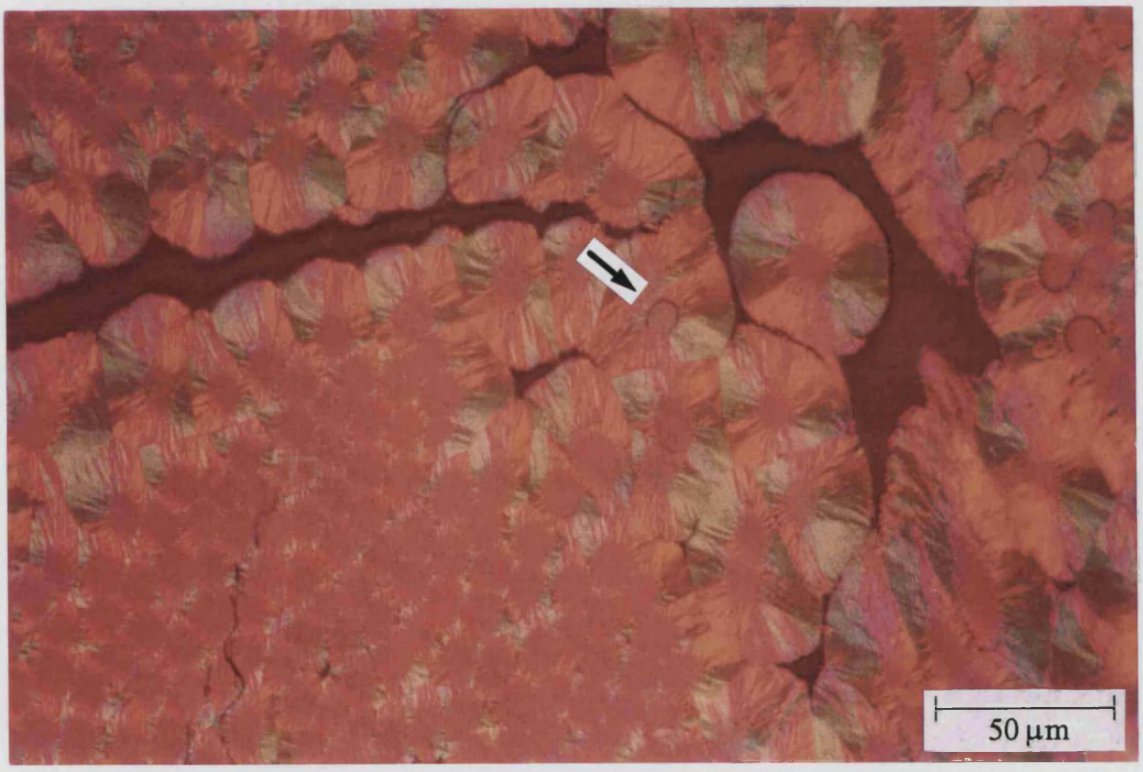

Figure 101. Typical microstructure of the material after oxidation to 0.9 % weight loss showing the early stages of oxidation (arrowed).

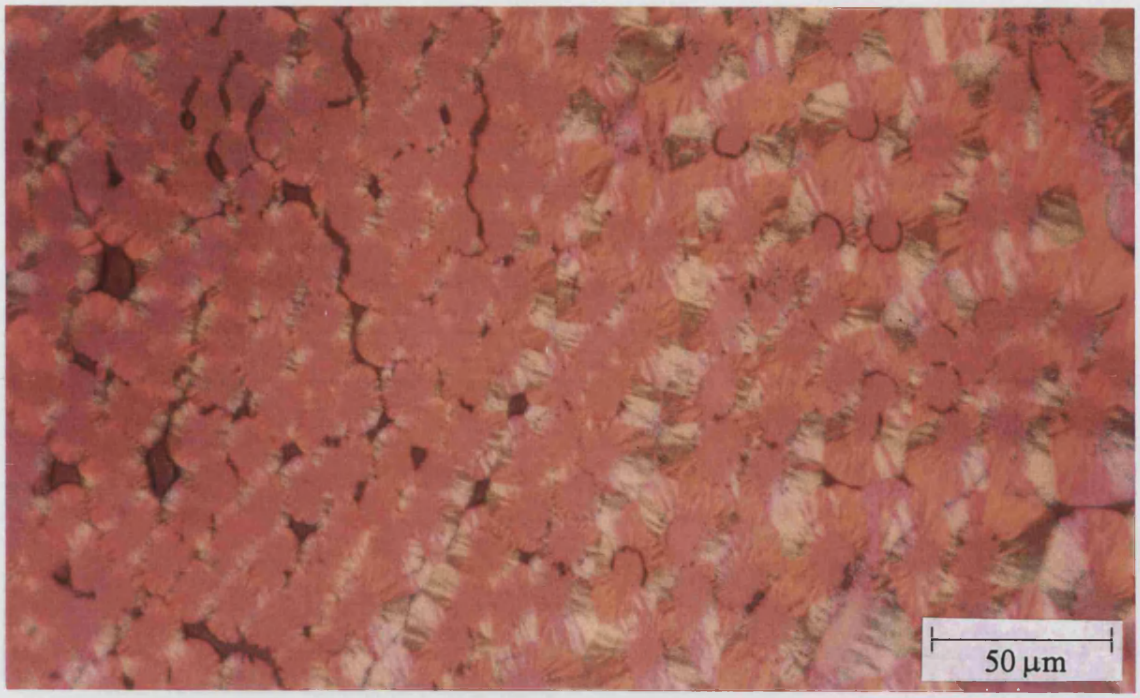

Figure 102. Microstructure of the material after oxidation to 1.3 % weight loss showing more clearly the appearance of crescent shaped porosity typical of oxidative attack of the fibre-matrix interface.

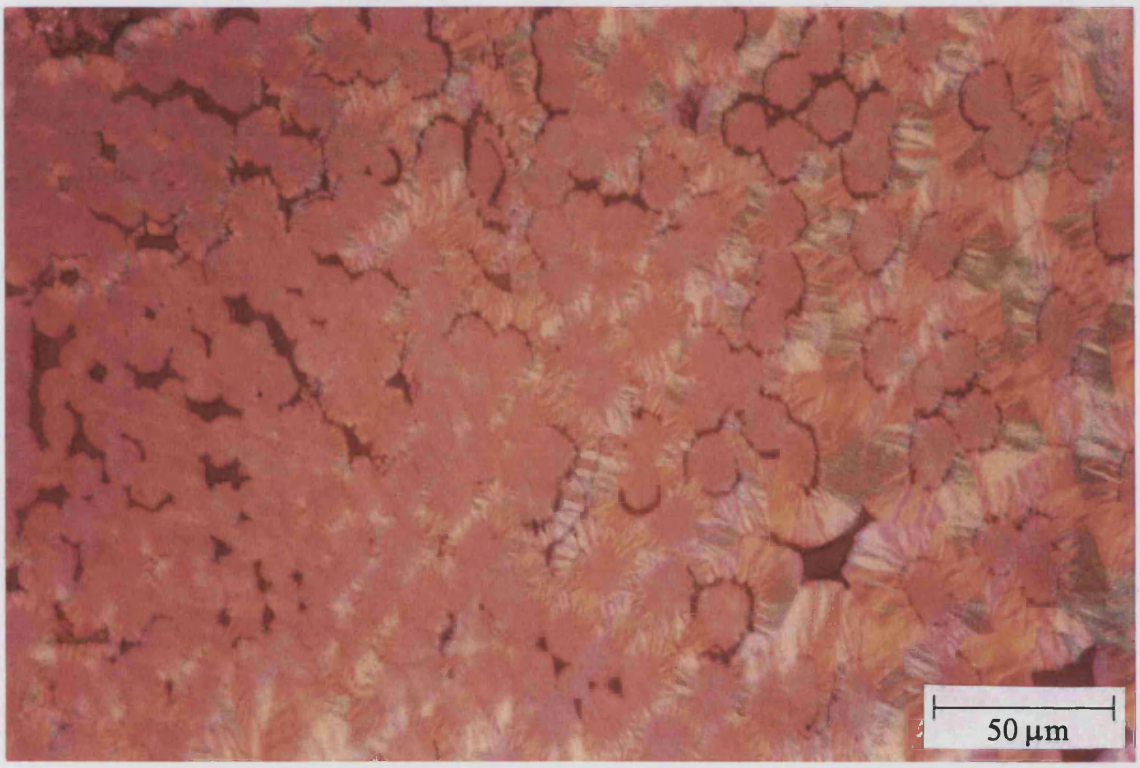

Figure 103. Photomicrograph showing enlargement of the crescent shaped porosity in material after oxidation to 3.9 % weight loss.

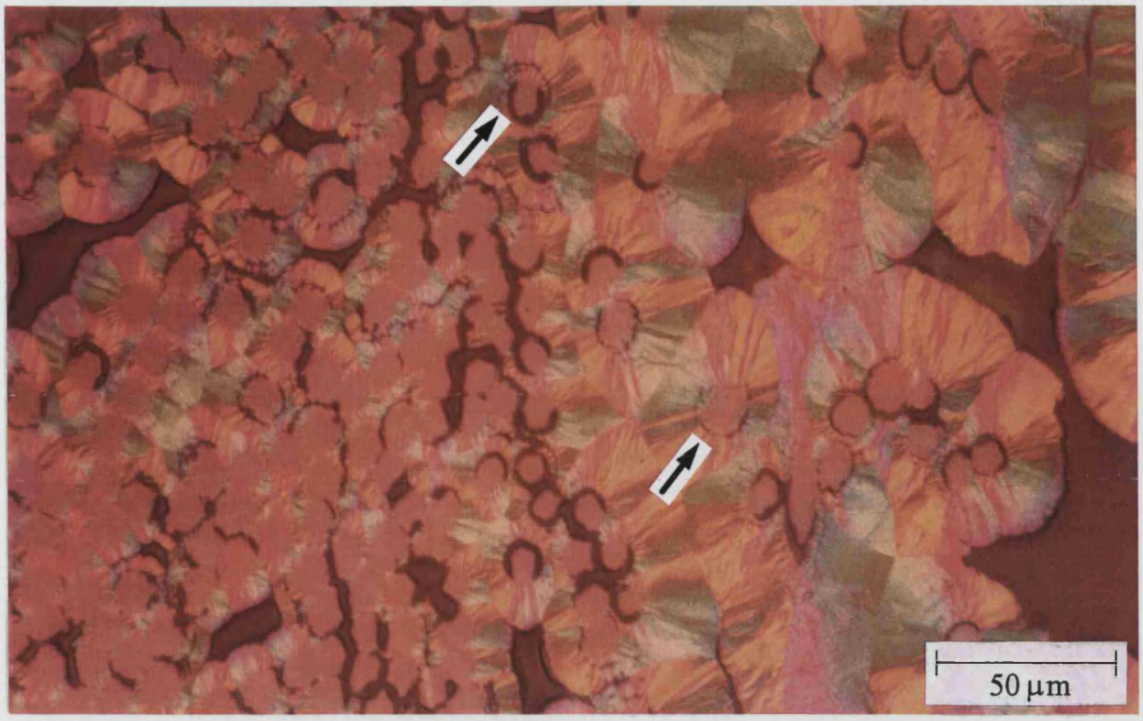

Figure 104. Photograph showing the distinct change to the microstructure in material after oxidation to 6.5 % weight loss. Shrinkage cracks formed during manufacture can be seen around some of the fibres (bottom arrow).

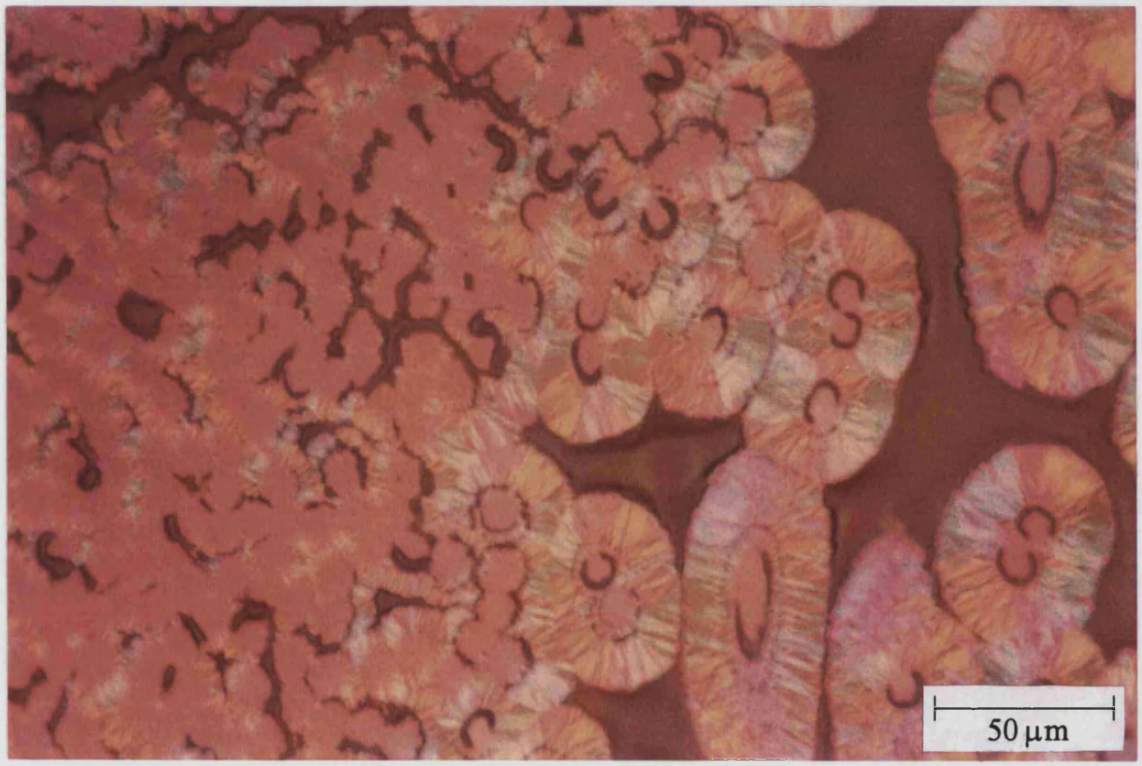

Figure 105. Optical micrograph of the material after oxidation to 8.9 % weight loss showing the advanced degradation of the fibres.

fibre the matrix appears to be oxidised as well as the fibre. One explanation for this is that the oxidation initiates at the fibre-matrix interface and continues into the fibre, and a little way into the matrix sheath. In the staple regions this oxidation of matrix makes little difference to the thickness of the matrix sheath and hence is not easily detected. However, in continuous fibre regions where the matrix sheaths are thin, the effects of oxidation are more obvious.

It was thought that it would be possible to accurately measure the local oxidation level in the composite using image analysis to calculate the area fraction of these crescent shaped pores. A routine was created which allowed manufacture porosity, shrinkage cracks and oxidation pores to be distinguished based on a number of geometrical measurements. Figure 106 shows an example of the result of this analysis. It is clear that the algorithm has accurately identified all of the porosity caused by oxidation.

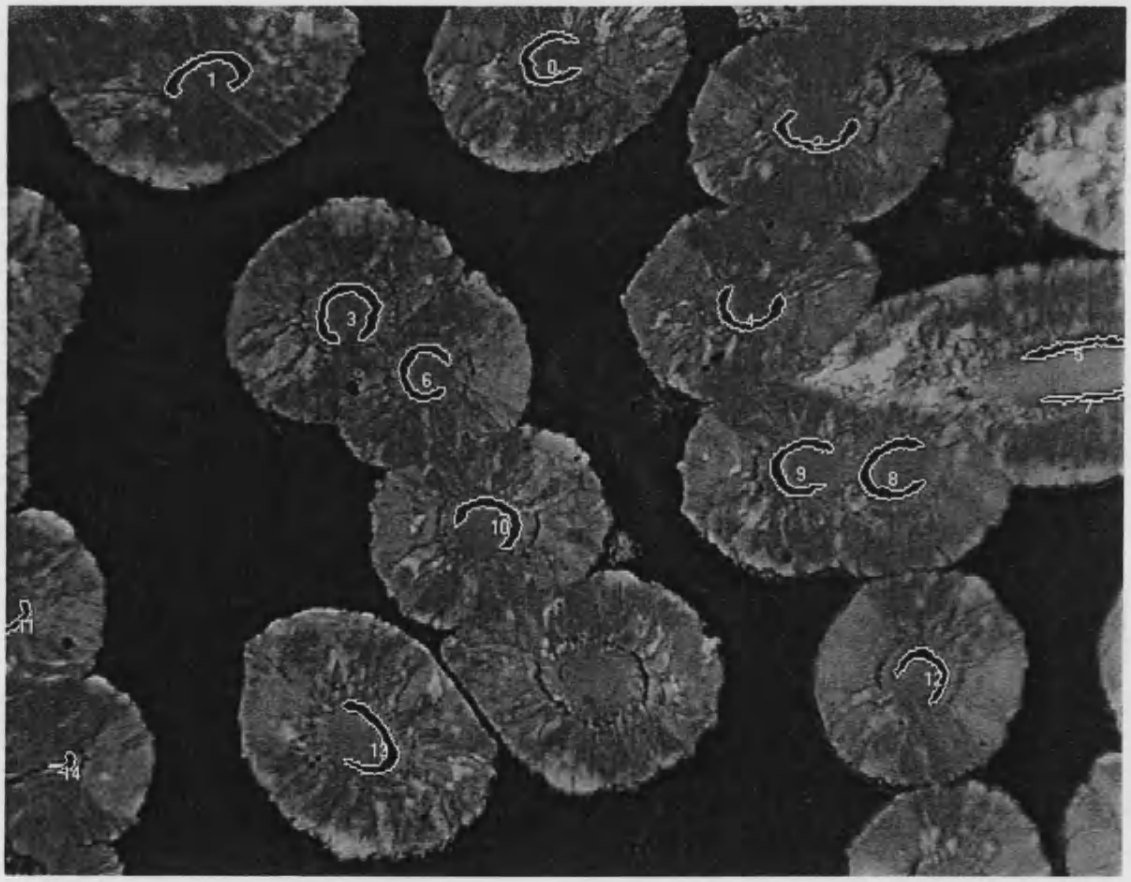

Figure 106. Photomicrograph after image analysis to identify the area fraction of oxidation induced porosity.

However, this image represents a best case, as the porosity is large, clear and distinct. In most cases it was found that image analysis was unable to correctly identify the oxidation induced porosity, particularly where it was of small scale and where pores around adjacent fibres intersected. Even in the cases where the pores were correctly identified, it was found that the measurement of the area of these pores was highly dependent on other factors such as the illumination intensity. Hence the measurement of oxidation induced porosity by this method was found to be unreliable and was consequently abandoned.

The microscopic pattern of oxidation or formation of crescent shaped porosity can be explained as follows. In carbon-carbon composites there are three main factors which influence the pattern and location of oxidation for a given set of physical conditions, namely oxidative gas supply, structure of the components and the presence or otherwise of catalytic impurities. There is evidence for the effect of all of these factors in the pattern of oxidation in the composites studied here. The supply of the oxidative gas, in this case carbon dioxide, to the reaction site is the primary reason that the oxidation was most severe near the surface of the samples. There was also evidence that the oxidation was more severe and progressed deeper into the sample in regions in, or close to, continuous fibre layers. This is a result of easy transport of gas along the porosity created at the fibre-matrix interface. This is most influential where the fibre is emergent at the surface of the sample. Because the fibres in the continuous fibre layers are long, and those in the staple are short, proportionally more of the fibres are emergent in the continuous fibre and so this is where the oxidation is most severe. Also, continuous fibre regions contain a higher volume fraction of fibres and this aids gas transport by providing more pathways. This effect could not be seen close to the surface of the sample because here even the short fibres in the staple layers are emergent. Of course, in all the layers which contain emergent fibre, the presence of shrinkage cracks can also provide an easy route for the ingress of the oxidative gas. If the cracks are close to, or at, the fibre-matrix interface, then the gas gains access to the surface of the fibre and this could result in the pattern of oxidation seen here.

The structure of the material is another factor which can have a large effect on the pattern of oxidation[22, 54, 55, 56, 57, 58, 59]. The oxidation reactions take place at positions on the surface of the material known as active sites. An active site describes a position where it is energetically favourable for a reaction to occur. The activity of a

site is inversely related to the atomic order of the material at the site, i.e. more ordered material tends to be less reactive. In the material studied here the CVI matrix is more ordered than the PAN fibres and so it is expected that the oxidative attack proceeds into the fibre and not the matrix once supply of CO_2 is established by oxidation of the fibre-matrix interface.

Residual stresses are also known to increase the reactivity of a material[127] and there is evidence for the oxidation being influenced by residual stresses in the composites studied. The occurrence of shrinkage cracks in the material indicates that it is likely that there are residual stresses in the matrix sheaths, particularly close to the fibre-matrix interface. It also seems logical to suggest that the formation of a shrinkage crack relieves the stress to a certain extent in the surrounding material. If this is the case then the material surrounding shrinkage cracks should be less susceptible to oxidative attack than other material further from stress relieving shrinkage cracks. Some evidence for this view is in Figure 104. The top arrow in this figure indicates a fibre with significant oxidation at the fibre-matrix interface and into the fibre to form a wide crescent-shaped pore. The significant feature of this particular pore is its spatial relation to the shrinkage crack in the matrix sheath. The shrinkage crack is opposite the widest part of the crescent and adjacent to the only part of the fibre-matrix interface which has not been oxidised. This suggests that the relief of stress in the region around the crack has made the portion of the interface adjacent to it less susceptible to oxidative attack. This opposing alignment of shrinkage cracks and oxidation-induced crescent shaped pores was found to be quite common, although not all shrinkage cracks induced this effect. An alternative explanation for this alignment is that the oxidation-induced pores simply represent a widening of the part of the shrinkage crack which was close to the fibre-matrix interface. From the evidence presented here it is unclear which of these two hypotheses is correct.

It is well known that the most effective method of accelerating the oxidation of carbon materials is by chemical catalysis. This is a particularly insidious problem as the catalyst is not consumed during the reaction. It was thought that catalytic oxidation may affect the shape of the crescent shaped pores as well as accessibility of the oxidising gas and residual stresses. Therefore it was decided that the chemical composition of the critical regions of the composite be assessed. Samples of material were mounted as for SEM analysis and loaded into a JEOL 6310 scanning electron

microscope. This microscope was fitted with an Oxford Instruments AM 10000 energy dispersive x-ray analyser (EDAX) which allowed the identification of all but very light elements. The analyser uses x-rays originating from interactions occurring within a 1 μm diameter sphere in space within the sample. Hence the position if any impurity elements is known to this order of accuracy. Figure 107 shows four EDAX traces originating from matrix (A), bulk fibre (B) and fibre-matrix interface material (C and D). Traces A, C and D were made with the protective beryllium window in position which means that elements of low atomic number cannot be detected, however trace B was made with the window removed and so peaks for carbon and oxygen are present. The most obvious feature of these traces is the high level of background noise which indicates that the impurity elements detected were of very low concentration. The trace from the bulk of the fibre showed small peaks for aluminium, sulphur and chlorine. The aluminium peak is likely to be due to contamination of the signal from the planchette onto which the sample was attached. The origin of the sulphur and the chlorine in the material is not known although it could be from impurities or additives introduced during the processing of the fibres at the polymer stage.

The only impurity present in any significant quantities in the matrix material (trace A) is chlorine and again the origin of this is unclear. However the most significant finding of this investigation was the discovery that impurities known to catalyse the oxidation of carbon, particularly sodium and potassium, were found in the fibre-matrix interface region. Examples of EDAX traces from the surface of fibres in the composite are shown in Figure 107 as traces C and D. These traces show the presence of sodium, silicon, chlorine and potassium. It is possible that these impurities originate from the size which is applied to the fibres in their raw state to protect them from damage and to aid handling. Whatever their origin though their presence is a good indication that the oxidation of the carbon-carbon composite is subject to catalysis in the fibre-matrix interface region.

Hence, catalysis of the oxidation reaction by impurities plays an important part, along with residual stresses and structural disorder, in determining that oxidation initiates at the fibre-matrix interface.

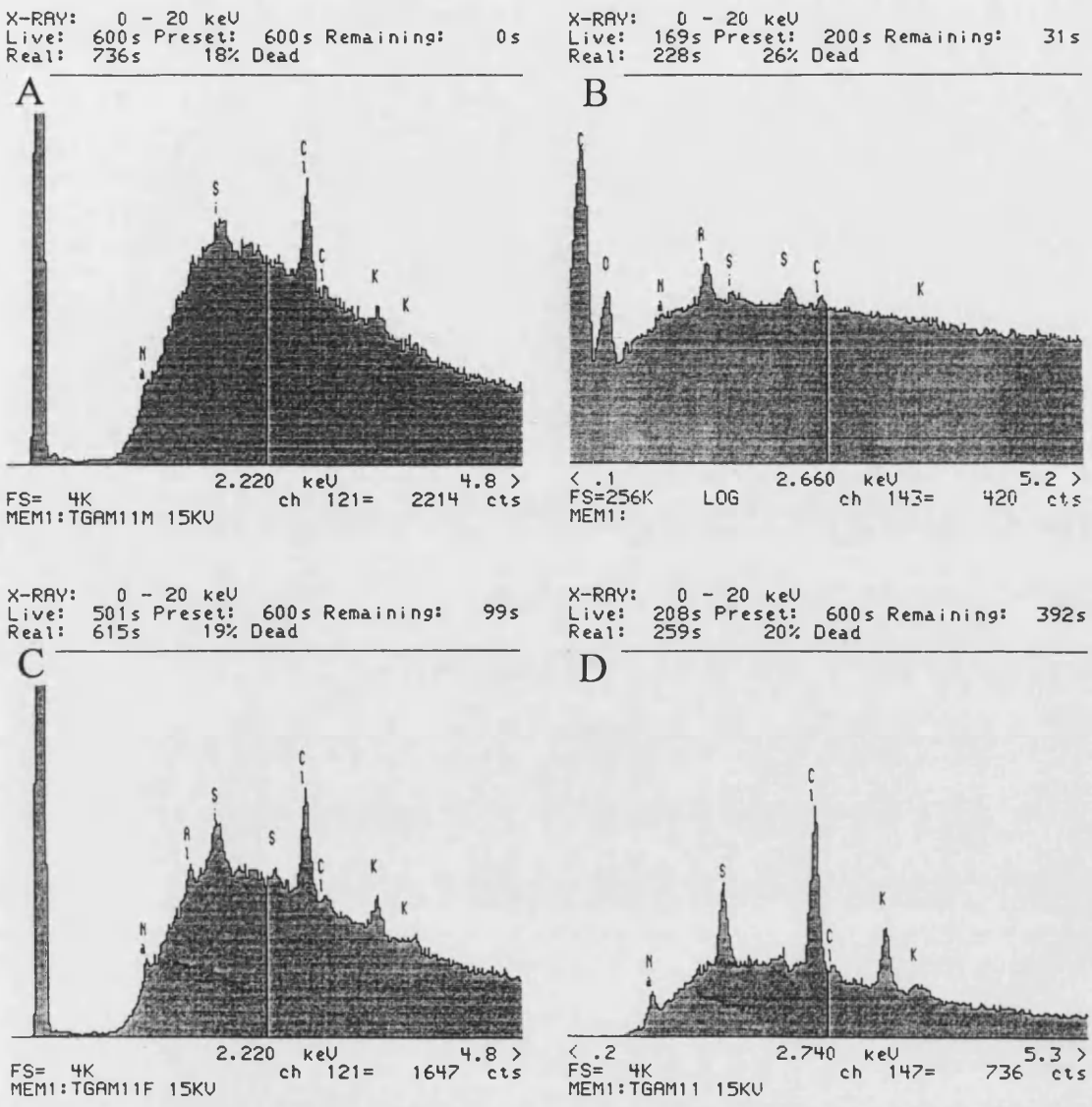

Figure 107. Four EDAX traces from A) Matrix material, B) Fibre bulk, C) and D) Fibre-matrix interface, showing the occurrence of impurities at the fibre-matrix interface.

12.3. Results and discussion

12.3.1. Influence of oxidation on the fracture mode of the model materials

The load versus displacement traces for the tests conducted on the oxidised model materials did not show any conspicuous changes in form as the extent of oxidation increased. In previous work, three main classes of fracture behaviour have been

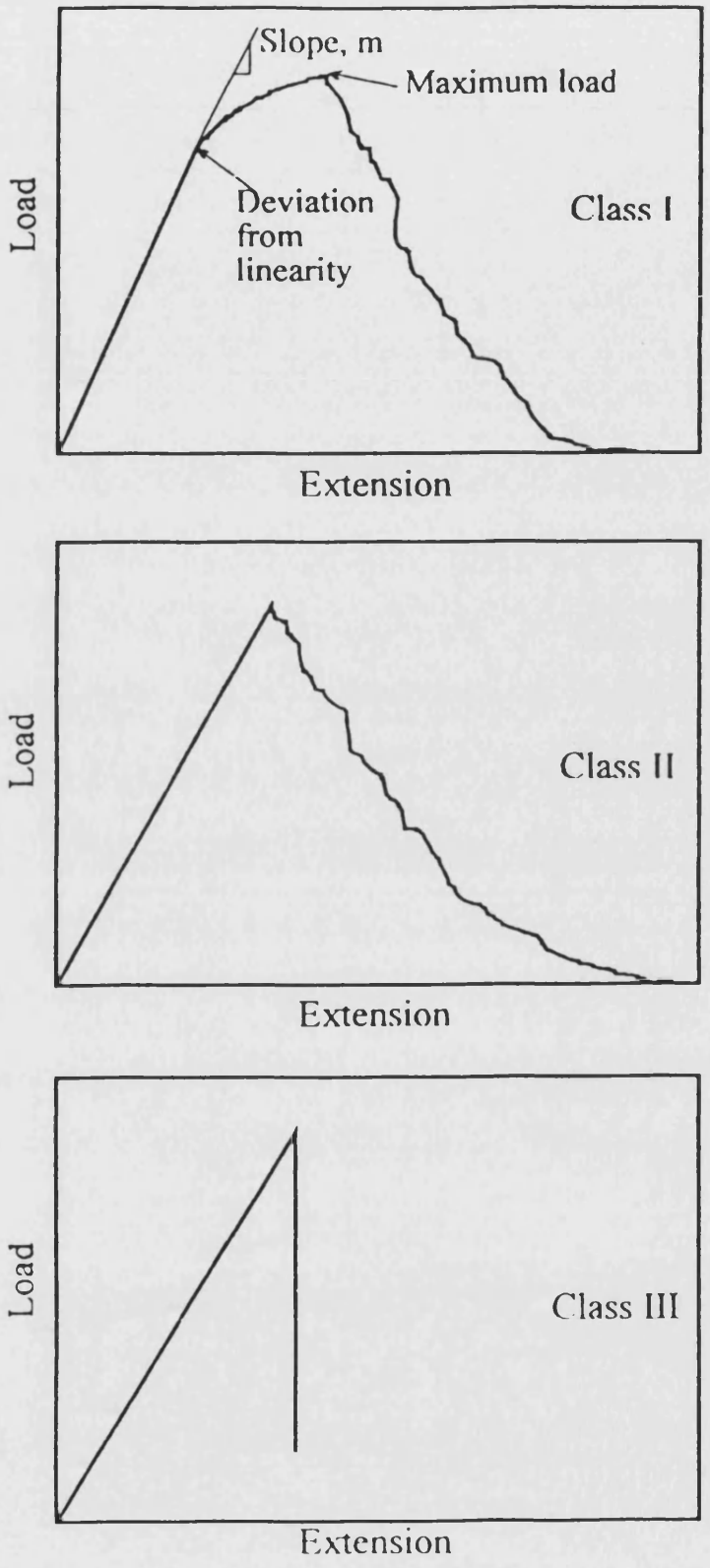

Figure 108. Schematic load versus displacement for the three main classes of fracture behaviour[72] adapted from Evans *et al*[128].

identified. Schematic diagrams showing the load-displacement traces for these three classes are given in Figure 108.

In general terms, the load versus displacement traces for the materials tested here resembled that of Class I fracture behaviour. The exception to this was the STANN material which exhibited elements of both Class I and Class III behaviour. The loading portion of the traces was highly non-linear as in Class I, suggesting a degree of plasticity, but the fracture process was rapid as in that of Class III. The unoxidised TGAM material did show close to linear loading behaviour typical of Class II, but all other materials showed Class I fracture behaviour.

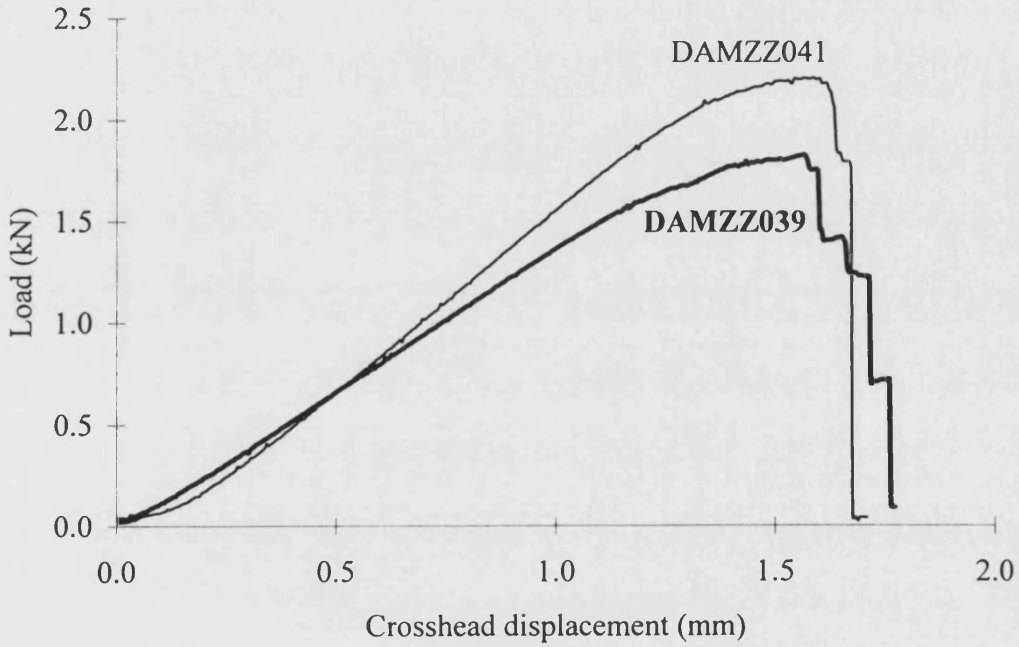

Figure 109. Graph showing load versus displacement traces for two samples of DAMZZ at 0 % weight loss (DAMZZ041) and 5.5 % weight loss (DAMZZ039).

Two slight changes in the form of the load displacement traces were noticed as a result of oxidation, although it should be noted that the assessment of these trends is fairly subjective having been achieved by visual inspection only. The first trend was the extension of the phase of stepwise reduction in load by cracking and possibly a reduction in the height of the steps. Examples of load displacement traces exhibiting

this phenomenon are shown in Figure 109. This effect was seen for all the materials except STANN where the failure process remained generally rapid across the range of weight loss studied.

The second effect was a slight increase in the deviation from linearity during loading. Examples of load displacement traces for oxidised material (STANN034) and unoxidised material (STANN049) showing this effect are shown in Figure 110. Comparison of these two traces is difficult due to their spatial separation. To aid comparison, the trace for the oxidised material has been horizontally and vertically re-scaled (labelled STANN034 scaled) such that the peak load and displacement are coincident with that of the unoxidised material. Comparison of these two traces shows quite clearly that more deviation from linearity is observed with oxidised material. However, these two traces represent extreme examples and were selected to illustrate the effect clearly. Increased deviation from linearity was noticed for all the materials and the effect was clearest in the STANN model material. This indicates an increase in the amount of plasticity of the materials prior to failure, and its prevalence in STANN links nicely with the observation of pseudo-plastic damage in 90° staple fibre layers (Figure 89, page 194).

Microstructural analysis of the fracture surfaces using optical microscopy, elucidated some changes in the response of the material caused by oxidation. In 90° fibre, both in continuous and staple forms, the weakening of the fibre-matrix interface promoted the propagation of cracks through these regions. Figure 111 shows the fracture surface of a sample subject to 4 % weight loss and the effect of oxidation on the microstructure is clear. Also evidence of fibre-matrix debonding can be seen (right arrow) and linking of the oxidation induced porosity to form large scale defects (left arrow). However, the evidence for an explicit change in fracture mode in these layers was not conclusive. The reason for this is that in 90° fibre layers in the unoxidised material, there are large pre-existing defects caused by features such as low fibre volume fraction regions and stitches. These weaken these layers to such an extent that even at 6 % weight loss they are still the most significant defects in the layer. Hence it is through these areas that cracks propagate. It is proposed that if significant linking occurred between oxidation induced porosity around adjacent fibres, this linked porosity might become the most significant defect and hence the cause of failure. Due to the proximity of the fibres, this effect would be most noticeable in continuous fibre

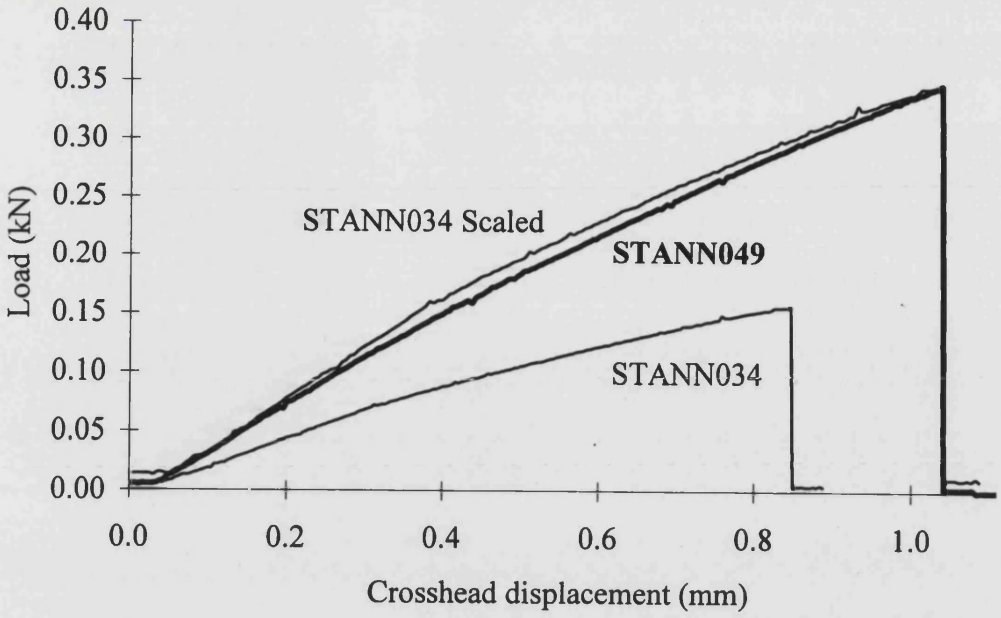

Figure 110. Two load versus displacement traces showing a slight increase in deviation from linearity during the loading phase for two samples of STANN at 0 % weight loss (STANN049) and 5.2 % weight loss (STANN034).

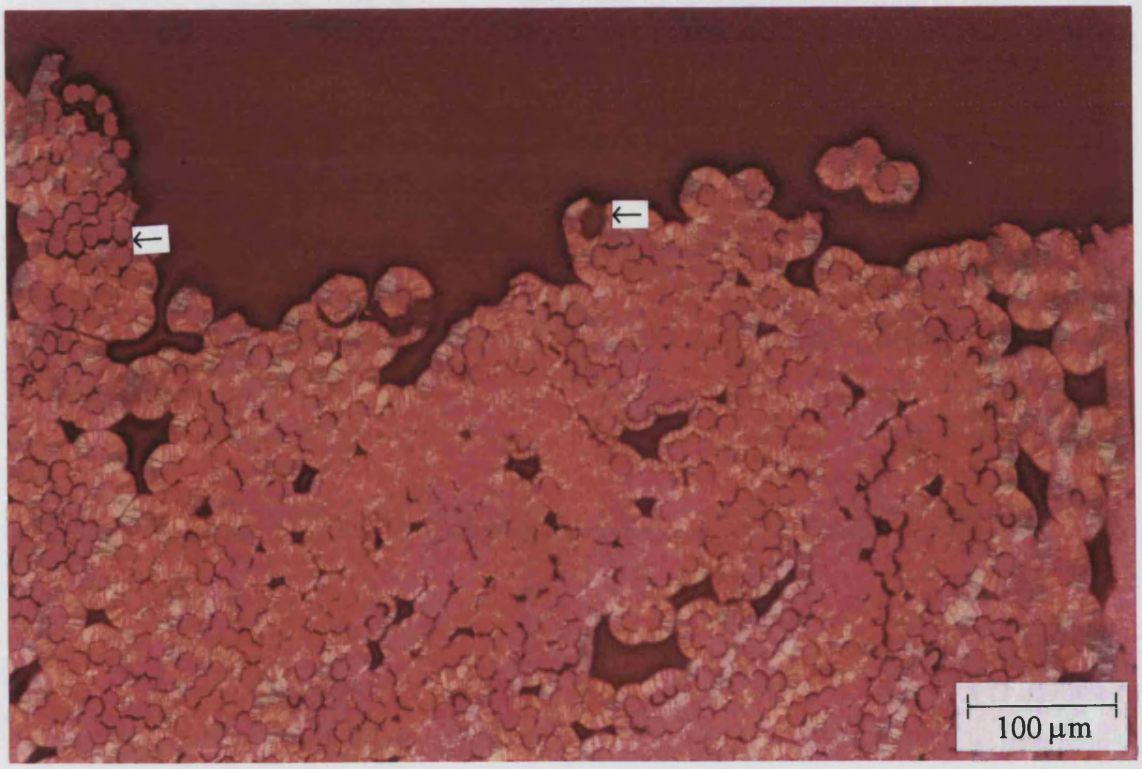

Figure 111. Fracture surface in 90° continuous fibre after approximately 4 % oxidative weight loss. Showing fibre-matrix debonding (left arrow) and linking of oxidation porosity (right arrow).

layers. That the fracture mode does not significantly change in 90° fibre layers as a result of oxidation, suggests that the strength of the material should also be relatively unaffected. This agrees quite well with the data for the strength of STANN (shown in Section 12.3.2.)which was found to only be reduced by a small amount over this oxidation range.

SEM analysis of fracture surfaces in 90° fibre layers confirmed that in general, the fracture path was between matrix sheaths. This was true for both oxidised and unoxidised material. Fracture of this type produced a relatively featureless fracture surface, an example of which is shown in Figure 112. Occasionally fibre-matrix debonding was observed, and although still unusual, this was seen more commonly in oxidised material. In Figure 113 it is clear that most of the fracture surface reveals only the outside of matrix sheaths. However, the surface of the fibre which runs across the picture in the centre, is clearly visible. Either side of the fibre a cross section through the matrix sheath can be seen. This shows that in oxidised material, it is more likely that the crack will cut through the matrix sheath in order to take advantage of the weakness created by oxidation induced porosity. This does not happen so readily in unoxidised material where the fibre-matrix bond is stronger.

In 0° fibre, a more substantial change in fracture mode was observed. As weight loss increased so the amount of fibre pullout increased. Whereas, in the unoxidised material the fracture surface tended to be rather flat and featureless, in oxidised material, the fracture surface of 0° fibre layers was very uneven.

Figure 114 shows the fracture surface of a 0° continuous fibre layer after moderate (≈ 3 %) oxidation. Here it is clear that, rather than propagating straight across the layer, the crack has been diverted by the fibres causing a roughness in the fracture surface. It is also apparent that the fibres have acted in small groups consisting of about three fibres, to divert the crack. By contrast, in Figure 115 the 0° fibres appear to have diverted the crack by acting more as individuals as a result of the higher weight loss of this sample. This transition from the layer acting first as a whole, then as small fibre groups and finally as individuals as weight loss increased, was most obvious in 0° continuous fibre due to the close packing of the fibres. In 0° staple, the effect was not so clear, although a different systematic variation in the form of the fracture surfaces was seen. At higher weight losses, the fibre pullout length increased. This is shown by Figure 116 and Figure 117. In the first figure for material at

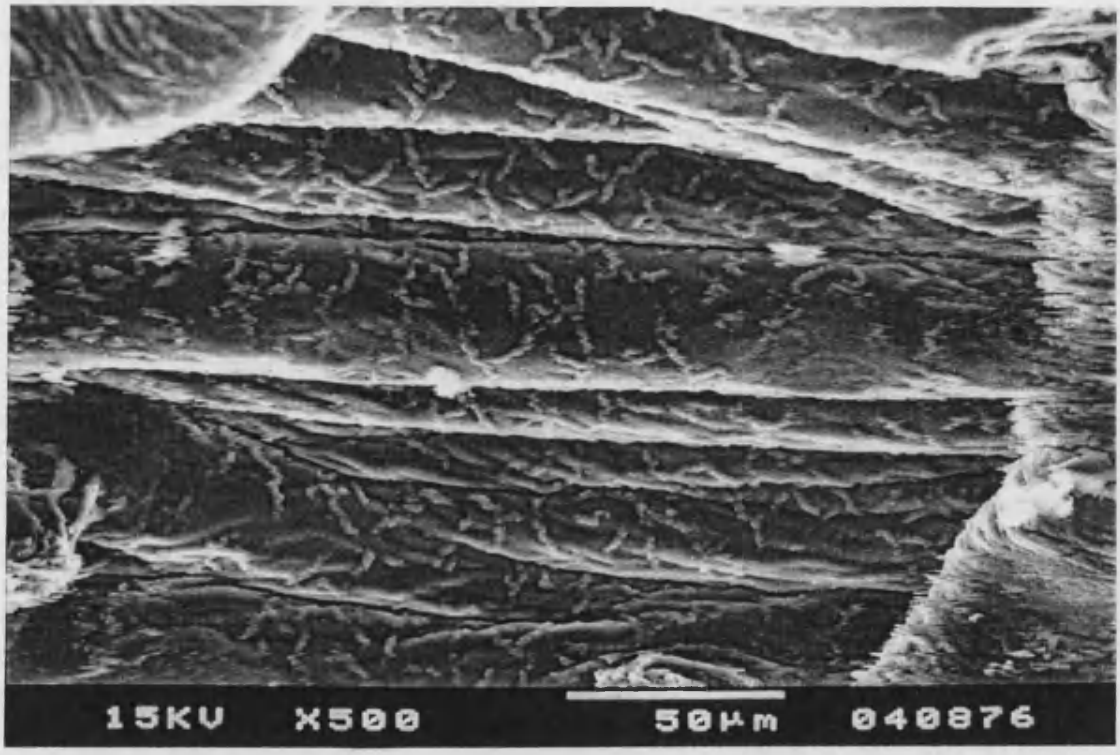

Figure 112. SEM micrograph of the fracture surface typical of that in 90° fibre.

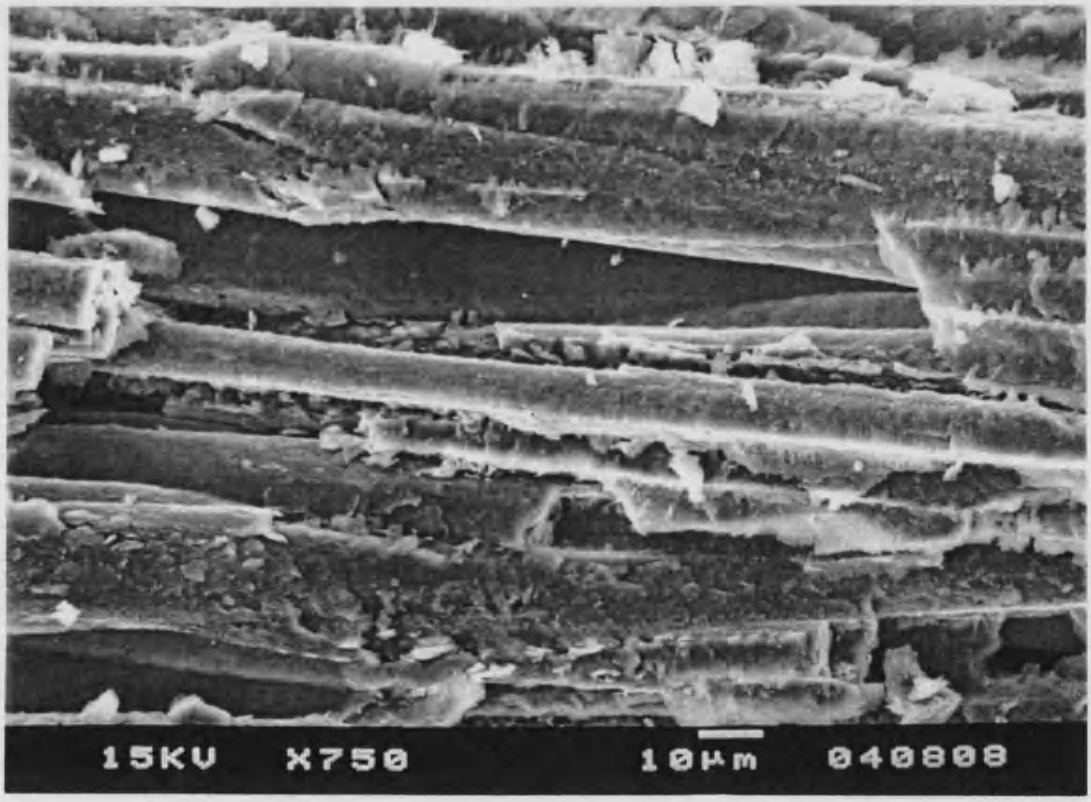

Figure 113. SEM micrograph showing evidence of fibre-matrix debonding (centre of picture) in 90° fibre in oxidised material.

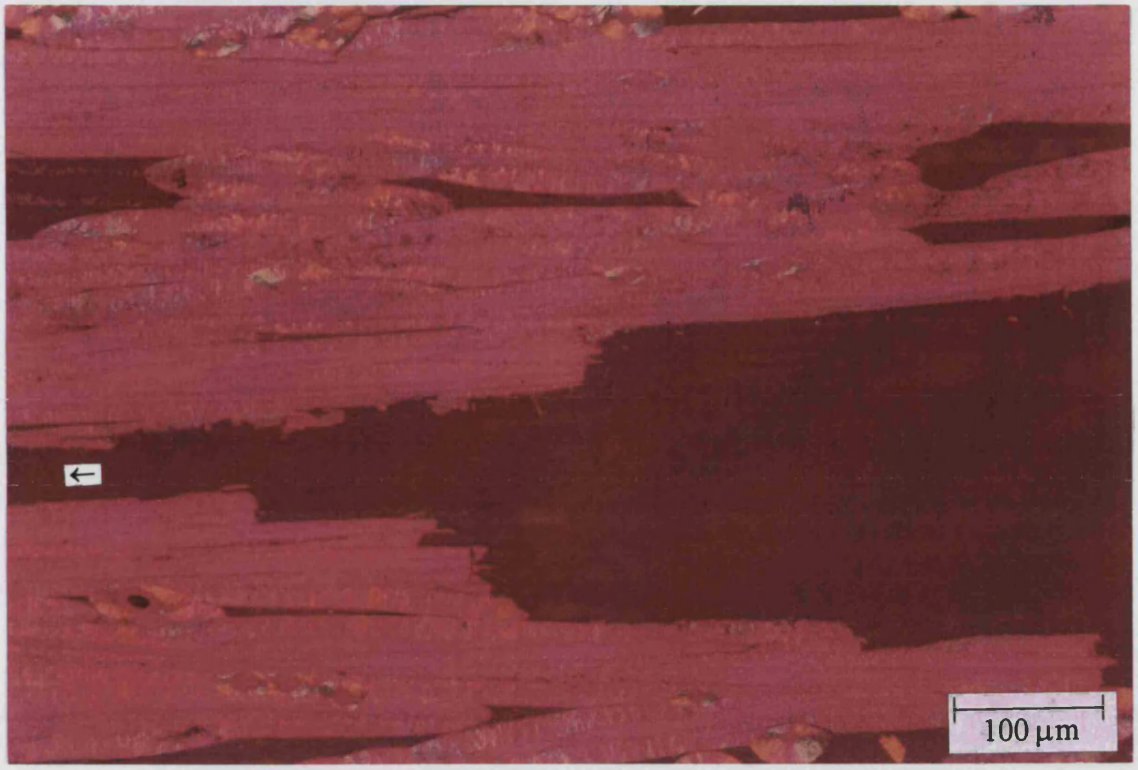

Figure 114. Fracture surface in 0° continuous fibre after oxidation to ≈ 3 % weight loss showing pullout of a group of fibres.

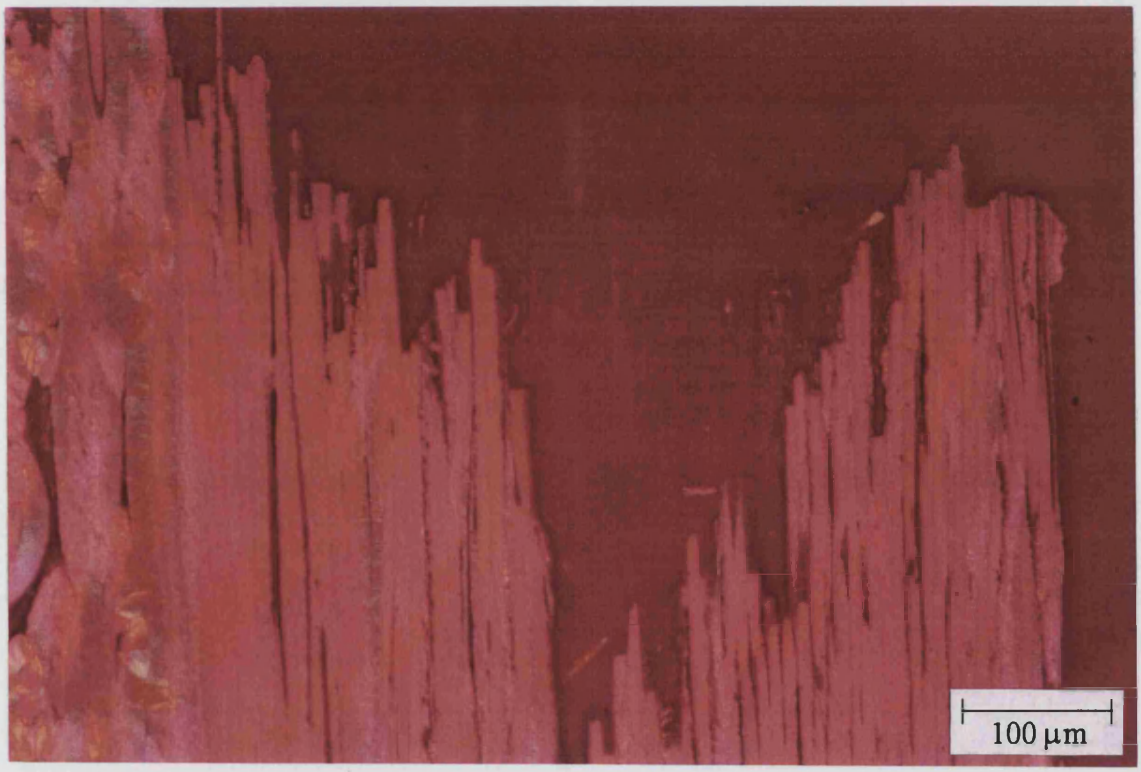

Figure 115. Fracture surface in 0° fibre layer within oxidised material (≈ 9 % weight loss) showing the fibres acting more individually.

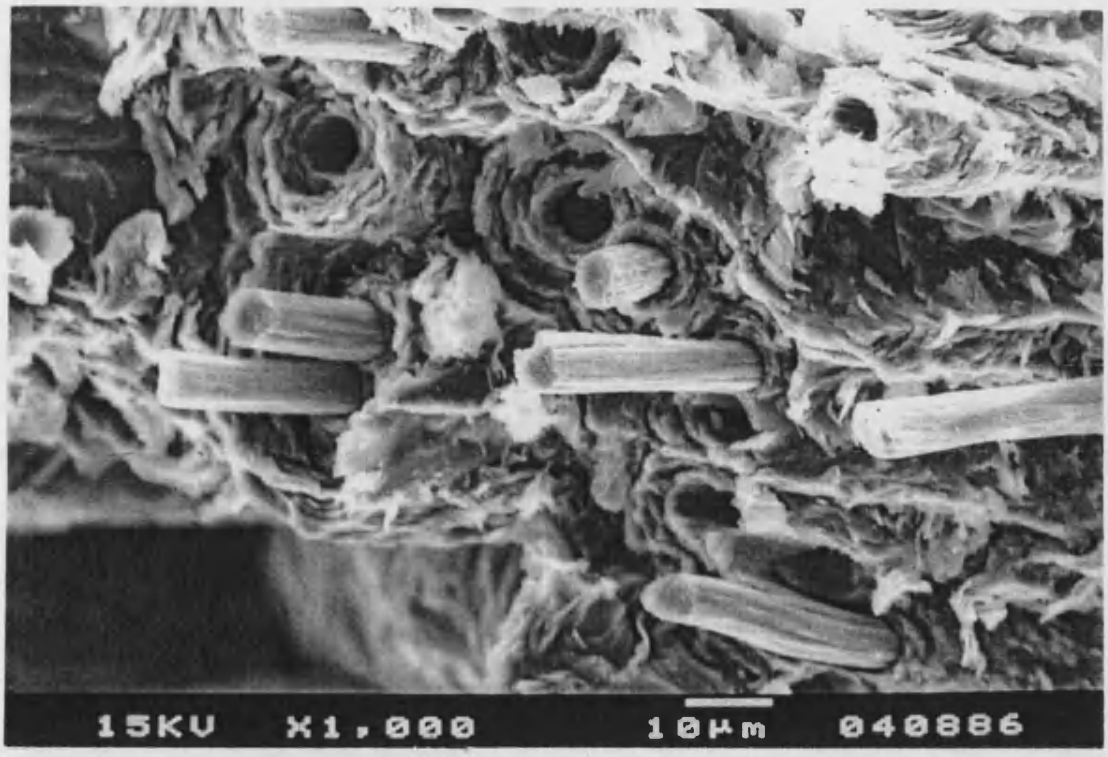

Figure 116. Fracture surface in 0° staple fibre layer after approximately 3 % weight loss, showing short fibre pullout.

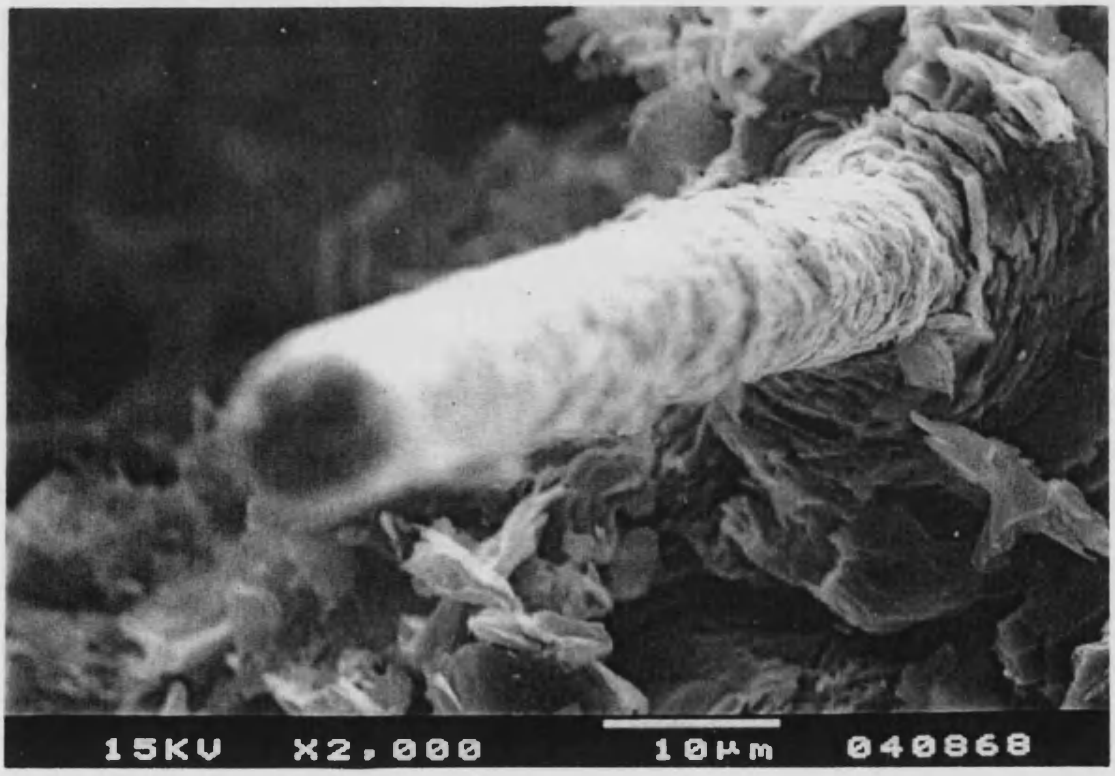

Figure 117. Greater fibre pullout length observed in 0° staple fibre at about 6 % weight loss.

moderate weight loss (≈ 3 %), classic fibre pullout can be seen and the pullout length is around 20 μm. In Figure 117, which shows the fracture surface at higher weight loss (≈ 6 %), the fibre pullout length is estimated at about 40 μm. Both of these effects indicate that oxidation changes the failure mode and fracture path in these materials by weakening the bonding between fibre and matrix.

An interesting effect was noticed near the surface of samples in 90° continuous fibre, Figure 118. It should be stressed that this is not a fracture surface, but rather is a surface which was machined during sample production. The micrograph shows two distinct effects. First, the emergent fibre ends are without their matrix sheaths. At the top of the figure the sheaths of matrix can be seen, and it can be estimated that the length of the exposed fibre is around 50 μm. Secondly, the exposed fibre ends appear pointed, i.e. their diameter decreases towards their end.

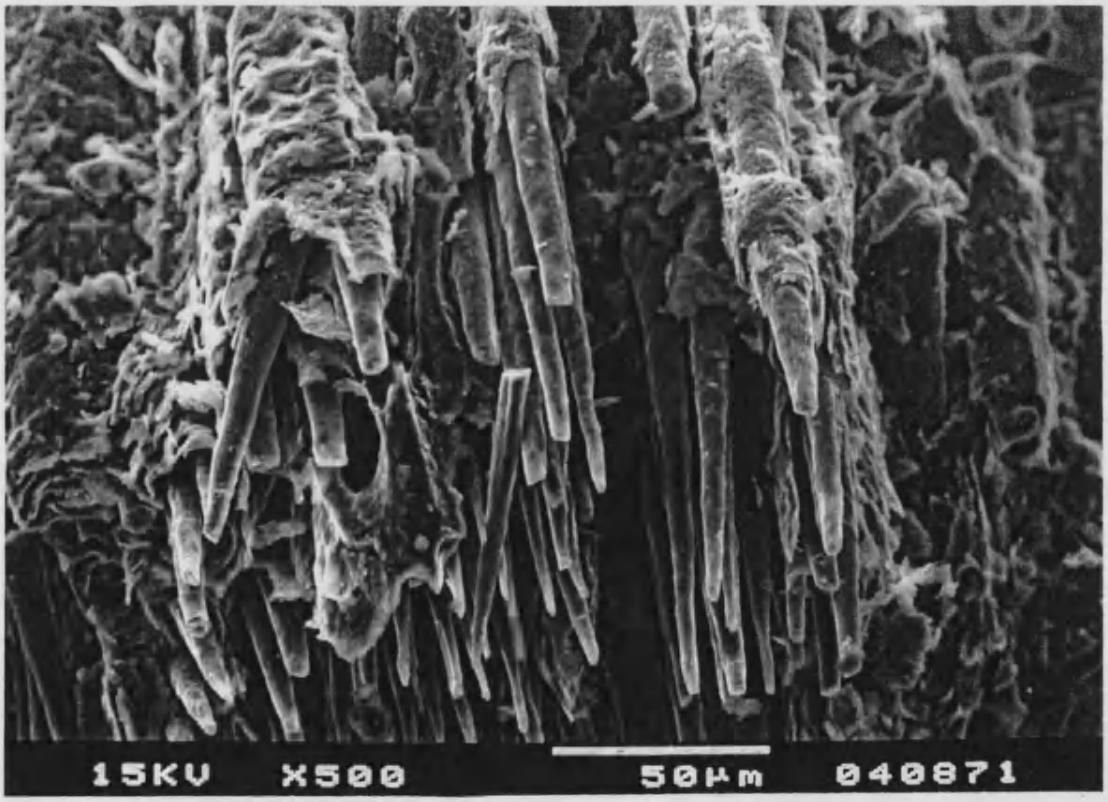

Figure 118. Non-fracture surface of a 90° continuous fibre layer in a post-test sample showing anomalous structure.

This sharpening of the fibres is good evidence that oxidation attacks first the fibre-matrix interface, and then the fibre. The sharpened ends of the fibre were originally at the surface of the sample and hence were exposed to the oxidising atmosphere. Here a

circular section of the fibre-matrix interface would have been present. If oxidation started at the interface and proceeded into the fibre then it would be expected that the fibre diameter would decrease during oxidation. Also, if the oxidative attack originated at the surface of the sample and progressed into the core, then the diameter of the remaining fibre would be least near the surface and greatest in the centre. Exactly this effect can be seen in Figure 118. The relatively shallow chamfer angle of the protruding fibre ends also allows the conclusion to be drawn, that the progression of oxidation is much more rapid along the fibre-matrix interface, than it is into the fibre. Hence a material containing a large amount of continuous fibre might provide easy access for oxidative gases into the bulk at low weight losses, purely as a result of the fibre architecture.

The disappearance of the matrix material in a layer about 50 μm thick is puzzling. One possible explanation is that once most of the fibre-matrix bond is degraded, there is little holding the matrix in place except its attachment to the rest of the matrix sheaths. If subsurface damage was caused during machining, this connection could be broken to a great extent and the matrix might simply fall out. Alternatively, the matrix in this layer might debond from the bulk during the fracture of the specimen during which a large amount of energy is released relatively quickly. This effect is analogous to that of "dusting out" which is commonly observed in composite samples tested to failure in a fatigue loading regime.

12.3.2. Influence of oxidation on the strength of the model materials

The effect of oxidative weight loss on the strength of the model materials has been assessed using four-point edgewise flexure tests. Here the strength is taken as equal to the equivalent tensile surface stress and is calculated from the standard beam equation (Equation 28, page 151). The percentage oxidative weight loss is calculated from the comparison of sample weight before and after oxidation.

Figure 119 shows the results of edgewise flexural testing of oxidised TGAM material. It was possible to calculate the strength results obtained from testing both with and without strain gauges and so both sets of data are presented. It is immediately apparent that there is a large degree of scatter in the data. During testing it was suggested that the adhesive used to affix the strain gauges to the samples might penetrate into the material and reinforce it, thus producing an artificially high strength

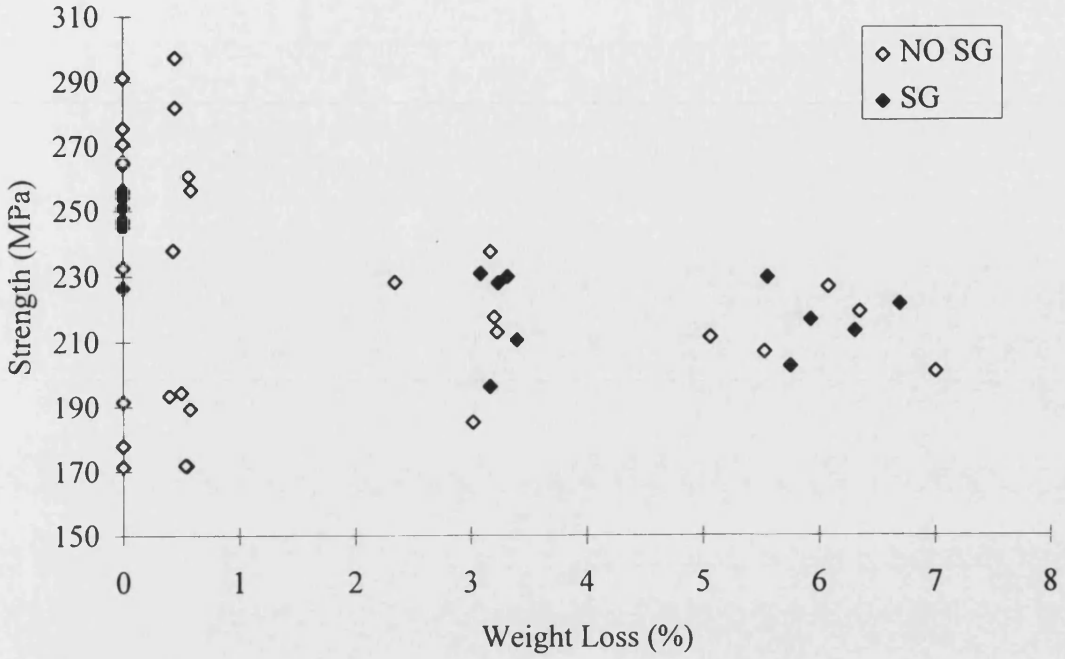

Figure 119. Plot showing the effect of oxidative weight loss on the strength of the TGAM model material for tests both with (SG) and without (NO SG) strain gauges.

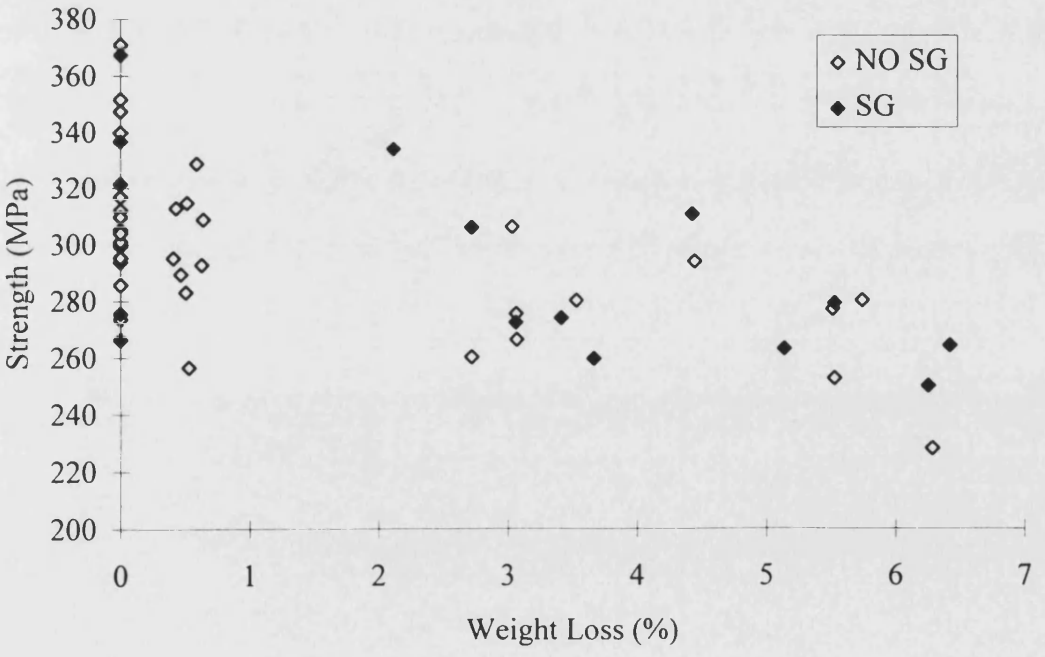

Figure 120. Plot showing the effect of oxidative weight loss on the strength of the DAMZZ model material for tests both with (SG) and without (NO SG) strain gauges.

(Section 10.3.). Reassuringly, the data shown in Figure 119 provide no evidence that there was a systematic difference in the measured strength of samples with and without strain gauges. This allows the conclusion to be drawn that the use of strain gauge adhesive did not affect the measured strength.

Figure 120 and Figure 121 show plots of the data from tests on the DAMZZ and STANN model materials respectively, presented in a similar to the data for TGAM (Figure 119). Neither Figure 120 nor Figure 121 show any systematic effect of the use of strain gauges on the strength of the materials.

That the use of strain gauges does not appear to affect the measured strength of these materials allows all the data for a given material to be analysed as if it belonged to a single distribution. It also allows a valid comparison to be drawn between the data for these materials and DAMZN (where strain gauges were not used). The results of testing on the DAMZN model material are shown in Figure 122.

All four plots of strength as a function of weight loss show broad trends of decreasing strength with increasing weight loss, as would be expected. Due to the large degree of scatter in the data, the precise nature of the relationship between strength and weight loss is not clear. It is widely acknowledged[65, 66] that the form of the relationship is exponential, particularly over a large range of weight loss. However, here the range of weight loss studied is relatively small and as a result the relationship can be approximated to by a straight line. Justification for this approach is given by both theoretical and practical analyses. A relationship of the form;

$$y = y_0 e^{-bx} \qquad \textit{Equation 48}$$

for small x reduces to;

$$y = y_0(1 - bx) \qquad \textit{Equation 49}$$

i.e. a straight line. Also, a comparison of the results of both linear and curvilinear regression analysis performed on the data revealed that the value of R^2 was generally higher for linear regression indicating that a straight line was a better fit to the experimental data than an exponential relationship.

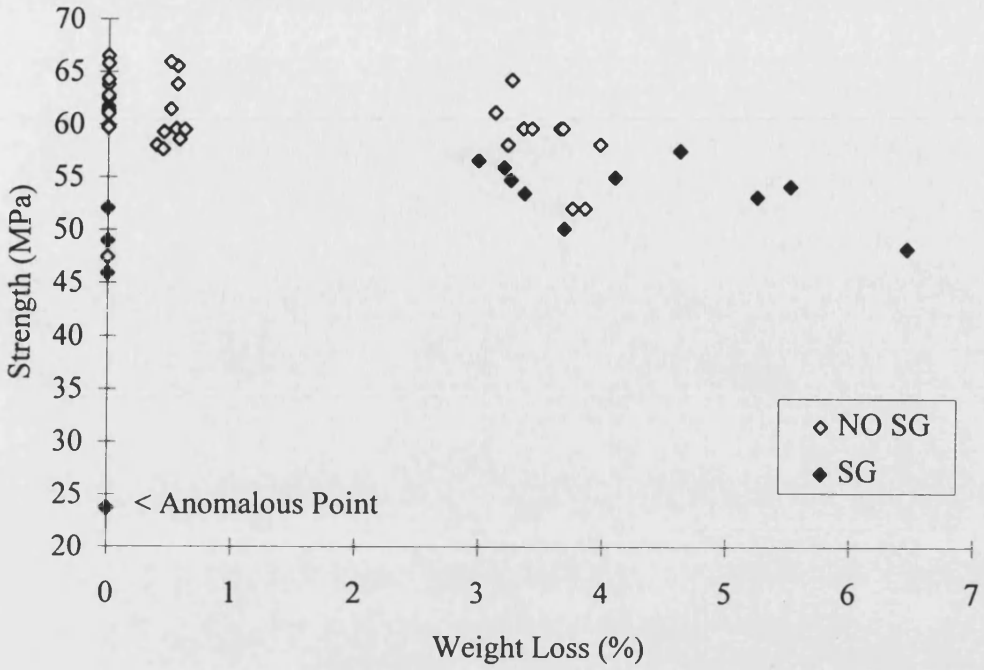

Figure 121. Strength as a function of oxidative weight loss for the STANN model material showing data from tests both with (SG) and without (NO SG) strain gauges.

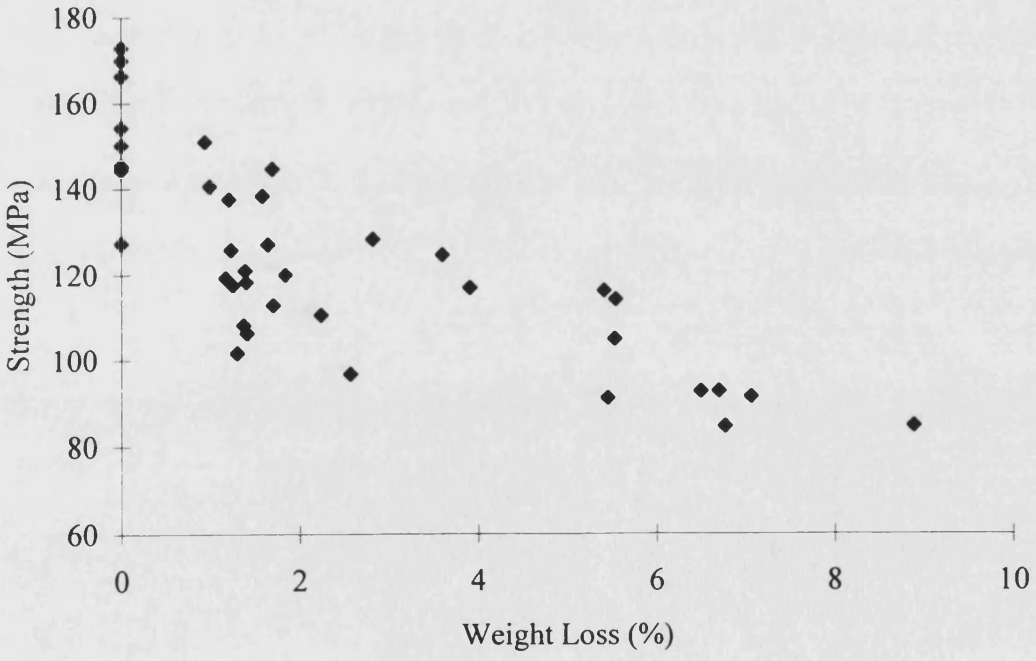

Figure 122. Plot showing the effect of oxidative weight loss on the strength of the DAMZN model material.

Linear regression was performed on the data and the results are shown in Table 28. In this table the equation of best fit line from the linear regression is of the form;

$$\sigma = mx + c \qquad \textit{Equation 50}$$

where c is the intercept, m is the coefficient, and x is the weight loss. For the intercept and coefficient, both a mean value and a standard deviation are presented and together these give some idea of the confidence in the best fit line. It should be stressed that here the means and standard deviations relate specifically to the best fit line. Hence, the mean and standard deviation in the intercept are not the same as the values produced by analysis of the data at zero weight loss. A further measure of confidence in the fit can be gained by comparison of the values of R^2. To simplify the comparison of the performance of the materials, the best fit line has been used to calculate the predicted strength for each at 6 % weight loss. Also, the reduction strength at 6 % weight loss is presented as a percentage of the unoxidised strength.

Material	Intercept *(c)*		Coefficient *(m)*		R^2	Strength at 6% wt loss	Strength reduction at 6% wt loss
	Mean	St Dev	Mean	St Dev		(MPa)	(%)
TGAM	238	40	-4.50	12.9	0.113	211	11.3
DAMZZ	310	33	-8.22	11.4	0.352	261	15.8
STANN	59	9	-0.77	3.7	0.043	54	7.8
DAMZN	142	21	-7.44	6.2	0.604	97	31

Table 28. Table showing the results of linear regression analysis on the strength versus weight loss data for the model materials.

The results of linear regression confirm that there is a large degree of scatter in the data, as evidenced by the standard deviations in intercept and coefficient, and this gives rise to low R^2 values. However, although the fits are relatively poor, the regression equations do allow the comparison of the materials. The materials show

reductions in strength between 7 and 31 % over the weight loss range 0 to 6 %. This compares well with previous studies on this effect. Crocker and McEnaney[66] report 50 % reduction in strength at 10 % weight loss, and Zhao *et al*[65] report approximately 37 % reduction at a similar weight loss. Although of dubious validity, extrapolation of the best fit lines predict strength reductions of 19, 26, 13 and 52 % for TGAM, DAMZZ, STANN, and DAMZN respectively over the range 0 to 10 % weight loss. This suggests that the effect of oxidation on the strength of these model material is generally not as severe as that on the materials tested in other studies. However, both of the investigations by Crocker and McEnaney[66] and Zhao *et al*[65] used different materials and neither used edgewise flexure as a strength measurement technique. Therefore some of the difference in the results can be attributed to the differences between the materials and alternative test methods used.

There is some evidence that oxidation has a greater effect on the strength of DAMZZ than TGAM although the scatter of the data must be borne in mind. Since the only structural difference between these two materials is the inclusion of 90° continuous fibre in TGAM in place of 90° staple in DAMZZ, the difference in behaviour could be attributed to difference in the effect of oxidation on these layers. Hence it could be deduced that oxidation has a more deleterious effect on 90° staple than on 90° continuous fibre. However, this argument considers the layers as separate entities and takes no account of the effect of interactions between them and is perhaps an over simplification.

That STANN shows the smallest reduction in strength as a result of oxidation agrees nicely with the proposal made in Section 12.3.1. This suggested that in 90° fibre layers, pre-existing features such as regions of low fibre density were the most significant defects in the structure, particularly at low weight losses. Perhaps, at higher weight losses than studied here, linking of the oxidation-induced porosity might cause these defects to become the most significant and an increased dependence on weight loss might be observed.

The clearest conclusion which can be drawn from the data in Table 28 is that oxidation has a markedly greater deleterious effect on the strength of DAMZN than on any of the other materials. It seems odd that a material (DAMZN) which is made up of elements from all the other materials, should exhibit the most severe degradation of strength as a result of oxidation. It might be expected that DAMZN should show

intermediate behaviour. That it does not, suggests that the effect of oxidation depends upon the combination of effects from all layers, and that there is a degree of interaction between them. In this case not only do the fibre layer types affect the response of the material, but also the stacking sequence and other physical variables. Unfortunately there is no other experimental evidence to support this hypothesis.

It is expected that, for a given material, high strength is associated with high density. When elucidating relationships between strength and weight loss, no account is taken of the density of individual samples which can vary as a result of the inherent variability of the manufacturing process. This is undoubtedly one factor which contributes to the scatter of experimental results.

A plot of strength as a function of sample density at test for the TGAM model material, Figure 123, shows the expected broad positive correlation between density and strength.

Optical microscopy has revealed that the physical forms of porosity developed during manufacture, and as a result of oxidation are different. It is therefore suggested that the effect of these two types of porosity might have different effects on the mechanical properties of the material. In Figure 123 the results for oxidised and unoxidised samples are plotted separately, allowing this hypothesis to be tested. To further qualify the findings, linear regression (fitting the data to the relationship described by Equation 51) was performed on both data sets, as well as all the data together. The results are presented in Table 29.

$$\sigma = m\rho + c \qquad \textit{Equation 51}$$

Material	Intercept *(c)*	Coefficient *(m)*	R^2	Sig. Diff.
TGAM ox	3.02	127	0.071	
TGAM unox	-88.4	194	0.442	No
TGAM all	-100.4	198	0.146	

Table 29. Results of linear regression analysis on the strength vs density data for TGAM material. Sig. Diff. indicates a lack of overlap between the 95 % confidence intervals in the best fit lines for oxidised and unoxidised material.

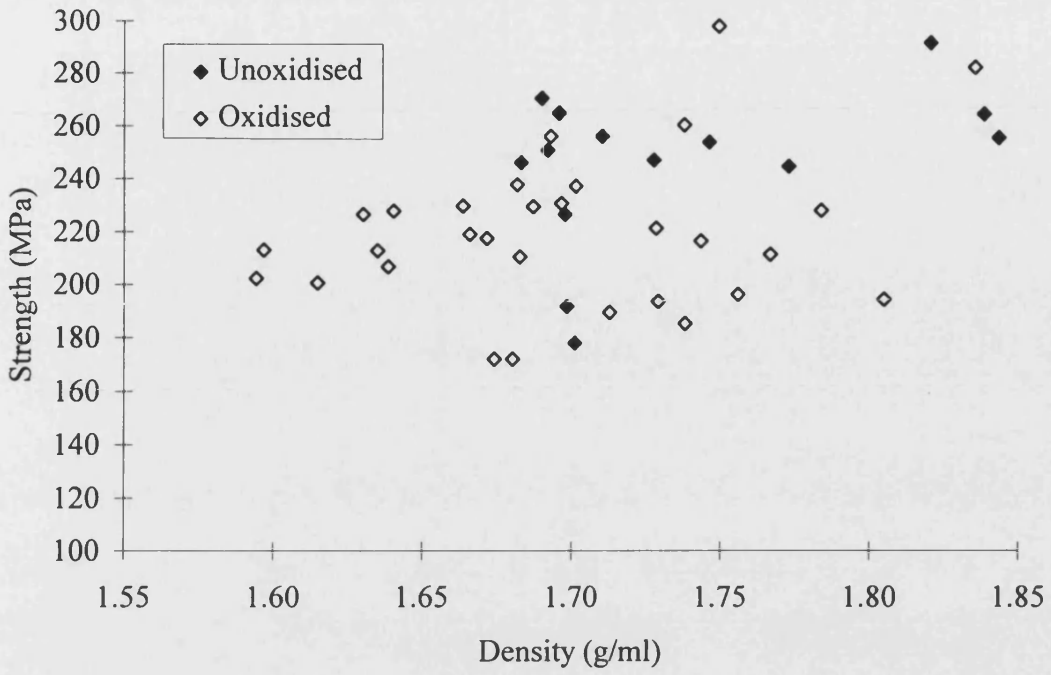

Figure 123. Plot of strength as a function of density for the TGAM model material showing results for both oxidised and unoxidised samples.

Although at first glance, the data in Table 29 might suggest that there is a genuine difference between the effect of manufactured porosity and oxidation induced porosity, over the density range studied the two best fit lines are close. When account of the lack of confidence (as evidenced by the low R^2 values) in the lines is taken into account, any differences become more dubious. To test the statistical significance, or otherwise, of the differences in the data for oxidised and unoxidised material in Table 29, 95 % confidence intervals were calculated and plotted for both lines. The large degree of overlap between the confidence intervals suggests that there is no statistically significant difference between the two data sets presented here. This is mainly a reflection of the scatter in the data as indicated by the low R^2 values. This is a little surprising given the difference in the physical form of the two types of porosity, however two other factors should be considered. Firstly, both oxidised and unoxidised material contains porosity formed during manufacture. Indeed, except at high weight losses, there is very much more manufacture-induced porosity than oxidation-induced porosity in the samples, and this may mask the effect of the latter. Secondly, only a

small number of samples have been tested which causes a lack of confidence in best fit lines, and large confidence intervals.

Similar plots for DAMZZ, STANN and DAMZN are shown in Figure 124, Figure 125 and Figure 126 respectively. The results of linear regression analyses for DAMZZ, STANN and DAMZN are given in Table 30, Table 31 and Table 32 respectively.

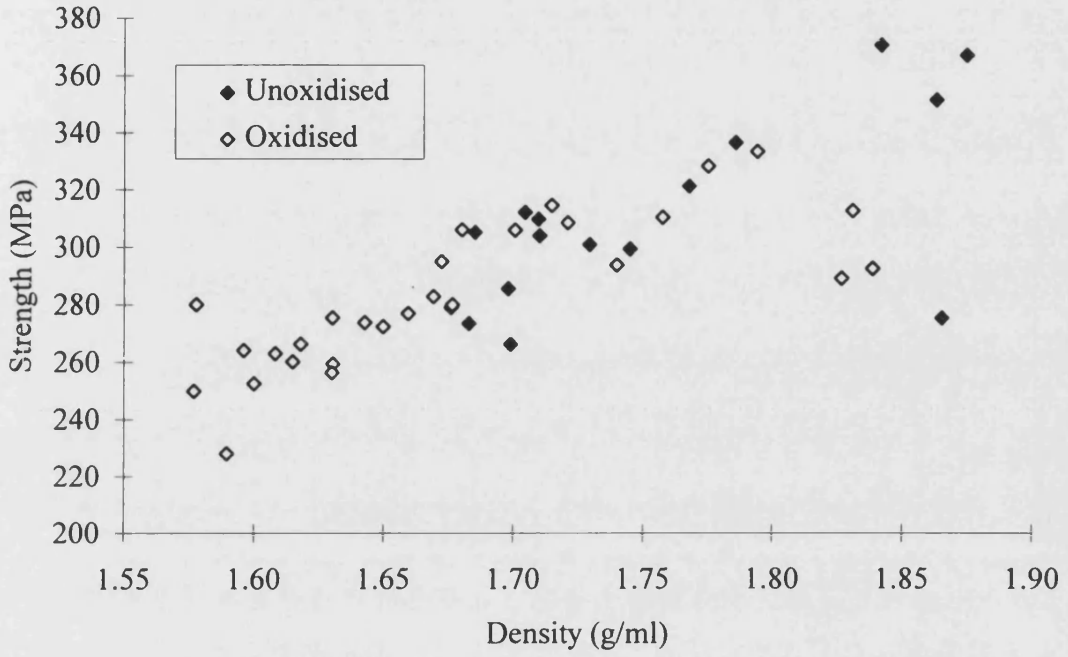

Figure 124. Plot of strength as a function of density for oxidised and unoxidised DAMZZ material.

Material	Intercept *(c)*	Coefficient *(m)*	R^2	Sig. Diff.
DAMZZ ox	-136.6	250	0.608	
DAMZZ unox	-211.0	298	0.424	No
DAMZZ all	-192.9	285	0.605	

Table 30. Results of linear regression analysis on the strength vs density data for DAMZZ material. Sig. Diff. indicates a lack of overlap between the 95 % confidence intervals in the best fit lines for oxidised and unoxidised material.

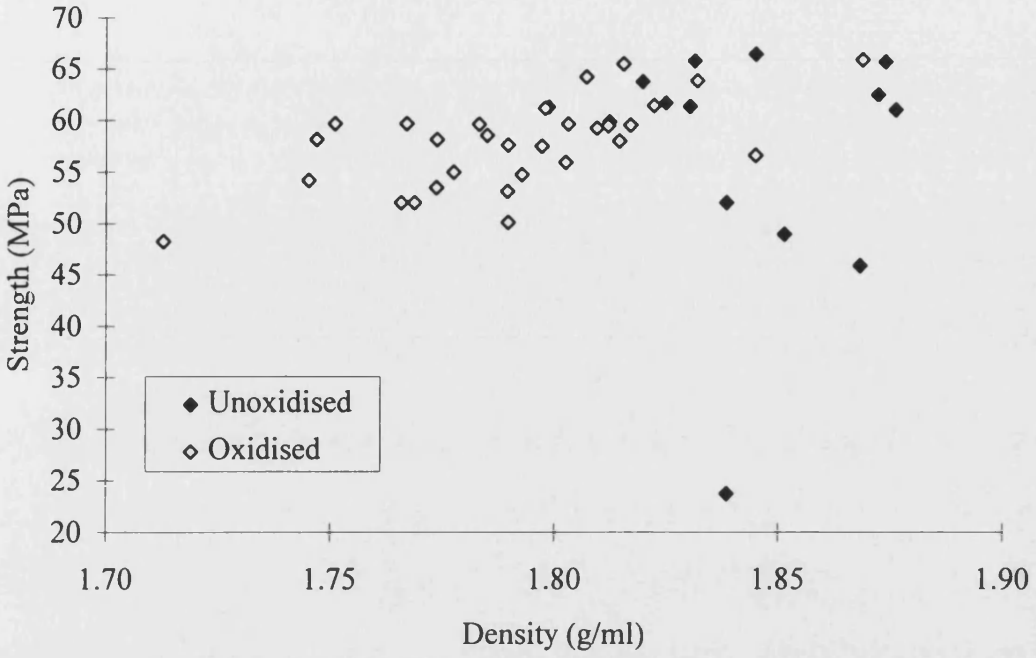

Figure 125. Plot of strength versus density for oxidised and unoxidised STANN model material.

Material	Intercept *(c)*	Coefficient *(m)*	R^2	Sig. Diff.
STANN ox	-95.5	86	0.397	
STANN unox	122.9	-36	0.006	No
STANN all	-0.5	32	0.028	

Table 31. Results of linear regression analysis on the strength vs density data for STANN material. Sig. Diff. indicates a lack of overlap between the 95 % confidence intervals in the best fit lines for oxidised and unoxidised material.

The results of the regression analysis suggest no significant differences in the effects on strength of the two types of porosity for any of the model materials. This implies that strength can be regarded as directly related to density irrespective of the proportions of the two types of porosity. However it should be remembered that only a small number of tests have been performed and that the range of density studied is small.

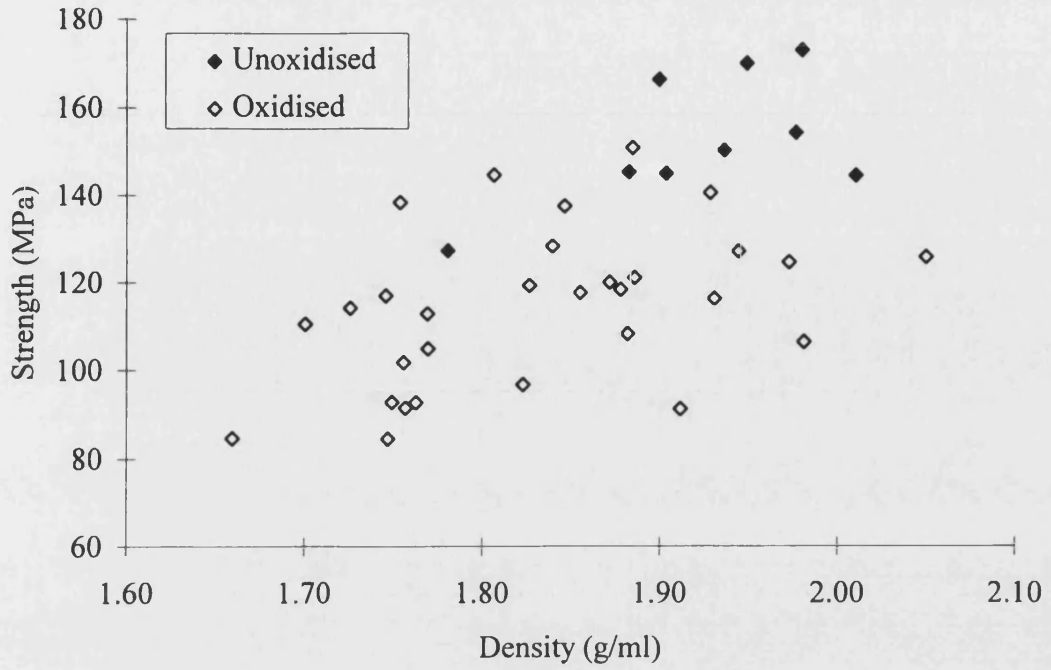

Figure 126. Plot of strength as a function of density for oxidised and unoxidised DAMZN material.

Material	Intercept *(c)*	Coefficient *(m)*	R^2	Sig. Diff.
DAMZN ox	-31.6	80	0.173	
DAMZN unox	-87.3	125	0.339	No
DAMZN all	-137.8	141	0.325	

Table 32. Results of linear regression analysis on the strength vs density data for STANN material. Sig. Diff. indicates a lack of overlap between the 95 % confidence intervals in the best fit lines for oxidised and unoxidised material.

12.3.3. Influence of oxidation on the modulus of the model materials

The modulus of the materials tested in edgewise flexure was calculated from the slope of the linear loading portion of the graphs of stress versus strain. The stress was calculated from the simple beam equation (Equation 28, page 151) and the strain was measured directly using strain gauges. The modulus reported here is equivalent to the Young's modulus. This is another important advantage of edgewise flexural testing

over flatwise flexure. By definition, the Young's modulus must be independent of the stacking sequence of the fibre layers in the composite. In a flatwise flexural test however, the modulus of a laminated composite material is dependent on stacking sequence since the individual plies are different distances from the neutral axis and are subject to different stress intensities. As a result the measured modulus should be reported as the flexural modulus. By contrast, in edgewise flexure the measured modulus is unaffected by stacking sequence since all the plies are subject to the full range of stress intensities (both tensile and compressive). Therefore the measured modulus is equivalent to the Young's modulus.

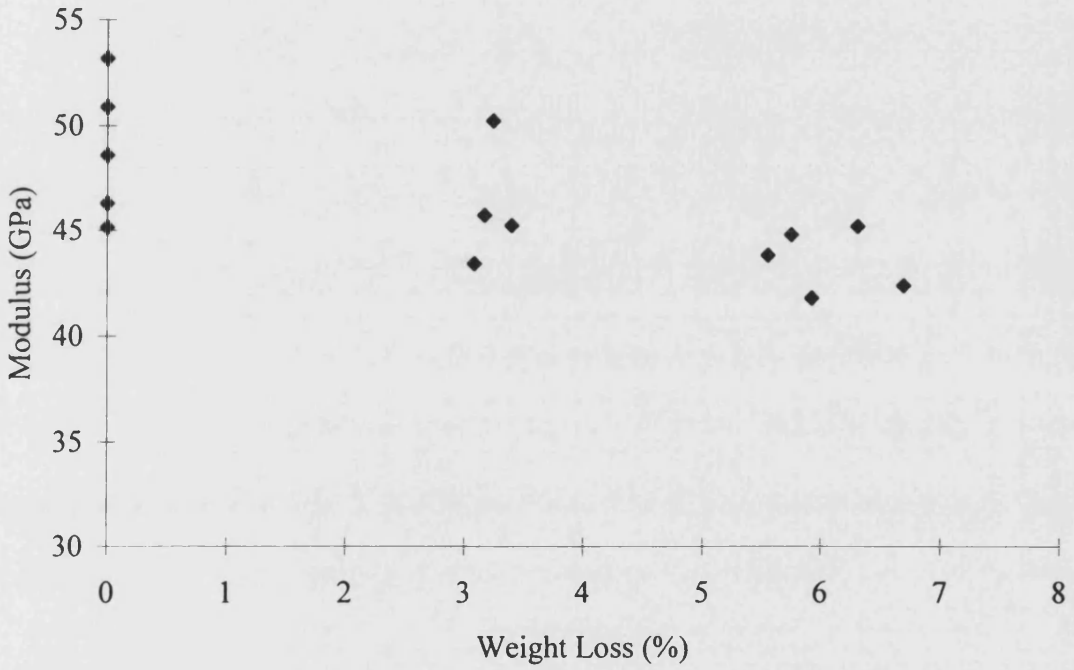

Figure 127. Plot showing the dependence of modulus on weight loss for the TGAM model material.

Figure 127 shows the modulus of the TGAM model material as a function of oxidative weight loss. Although there is a large degree of scatter in the data, a broad negative correlation can be seen. As with the strength data, linear regression was found to adequate for identifying trends in the modulus data (using R^2 values for comparison) and so was used throughout. Figure 128 and Figure 129 show modulus versus weight

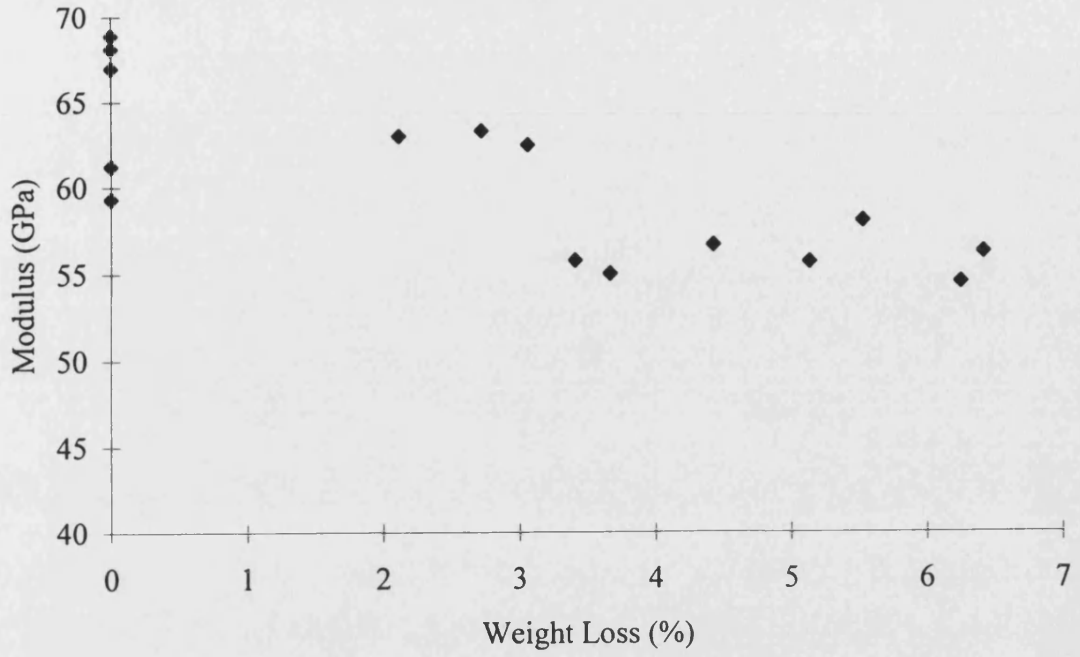

Figure 128. Graph showing the relationship between modulus and weight loss for the DAMZZ model material.

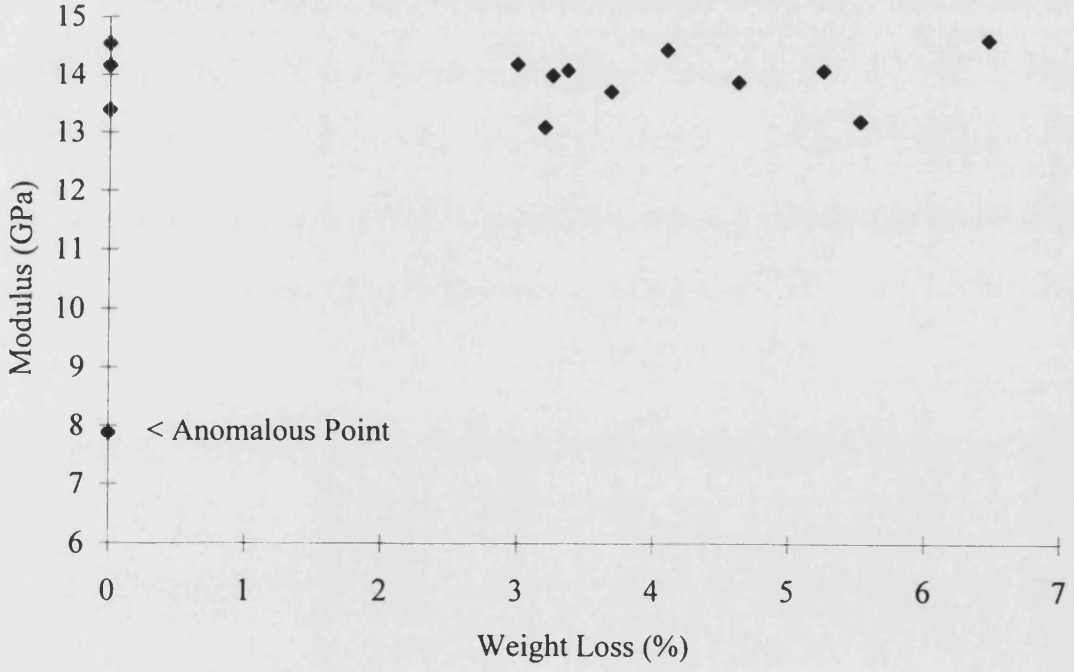

Figure 129. Plot showing the effect of oxidative weight loss on the modulus of the STANN model material.

loss plots for DAMZZ and STANN material respectively, and Table 33 shows the results of linear regression of these data for all three materials.

If the results for TGAM and DAMZZ are compared it is clear that the effect of oxidation is to reduce the modulus of both materials by a similar amount. There is some evidence however, that the reduction in modulus is slightly greater in the case of DAMZZ. This could be attributed to the substitution of 90° continuous fibre layers with 90° staple fibre layers in DAMZZ although the evidence is not strong enough for this conclusion to be confidently drawn.

Material	Intercept *(c)*		Coefficient *(m)*		R^2	Modulus at 6% wt loss	Modulus reduction at 6% wt loss
	Mean	St Dev	Mean	St Dev		(GPa)	(%)
TGAM	48.8	3.97	-0.86	0.97	0.466	43.6	10.6
DAMZZ	64.9	5.00	-1.61	1.36	0.618	55.3	14.8
STANN	12.6	2.81	0.29	0.75	0.148	14.3	-13.8
STANN*	13.9	0.96	0.01	0.25	0.001	14.0	-0.3

Table 33. Table showing the results of linear regression analysis on the modulus versus weight loss data for the model materials. The row for STANN* represents linear regression on the data excluding the anomalous point showing a modulus of approximately 8 GPa at 0 % weight loss.

Linear regression of the data for the STANN material shows that, unlike for the other materials, a broad positive relationship exists between modulus and weight loss, implying that oxidation increases the modulus of the material. This is counter-intuitive, and if the plot of the modulus versus weight loss data is inspected (Figure 129) it is clear that the reason for this is the effect of the anomalous point on the regression. Therefore, a second linear regression was performed excluding this point. The results are shown in Table 33 and is denoted STANN*. These results suggest that oxidation has negligible effect on the modulus, however caution must be exercised.

The strength data for tests on STANN where strain gauges were used also suggested a positive correlation, but when the data from tests both with and without strain gauges were analysed, a broad downward trend could be seen. Since samples with high strength also tend to exhibit a high modulus, it is likely that the upward trend in modulus is just an artefact of the testing technique. Unfortunately the modulus of samples without strain gauges could not be accurately assessed, and so the validity of this assertion cannot be tested.

Interestingly, the percentage reductions in modulus at 6 % weight loss for both the TGAM and DAMZZ materials are similar to the reductions in strength (Table 28) at the same weight loss. If the materials are approximately Hookean, this implies that for both the strain to failure is constant across the range of oxidative weight loss studied here.

As with the strength data, the plots of modulus versus weight loss take no account of the variations in the density of the samples. Plots of modulus as a function of density for TGAM, DAMZZ and STANN are shown in Figure 130, Figure 131 and Figure 132

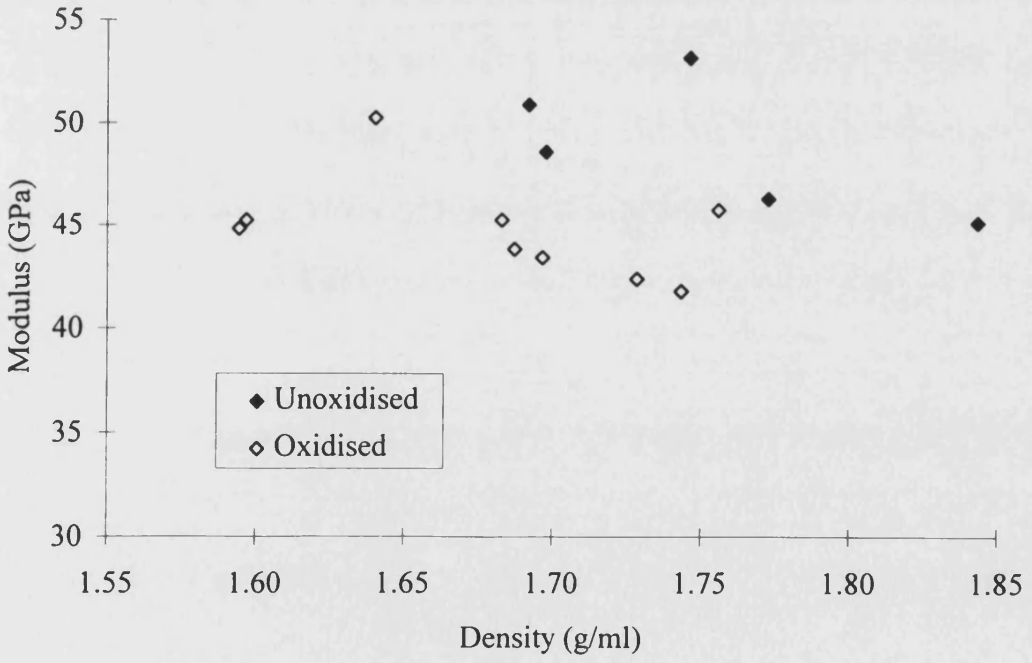

Figure 130. Plot of modulus against density for the TGAM material, showing both oxidised and unoxidised samples.

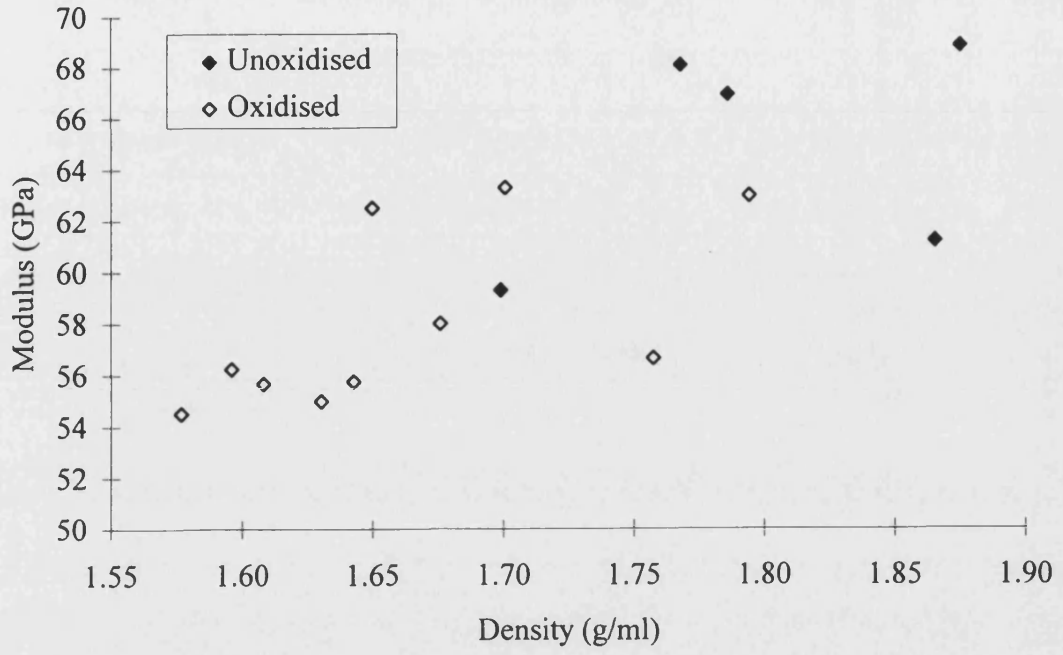

Figure 131. Plot of modulus as a function of density for oxidised and unoxidised samples of DAMZZ material.

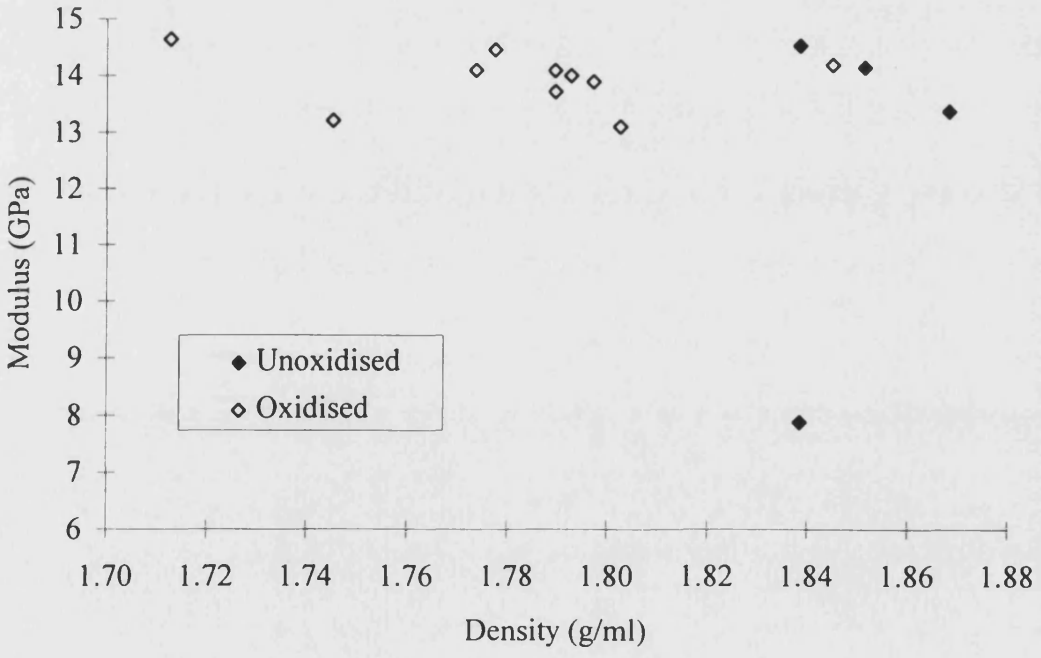

Figure 132. Plot of modulus against density for STANN material in oxidised and unoxidised conditions.

respectively. In these figures the data for oxidised and unoxidised samples have been plotted separately. Linear regression (to fit Equation 51) has been performed on all the data, and the results are given in Table 34.

Material	Intercept *(c)*	Coefficient *(m)*	R^2	Sig. Diff.
TGAM ox	75.4	-18	0.194	
TGAM unox	108.7	-34	0.451	No
TGAM all	49.9	-2	0.002	
DAMZZ ox	7.1	31	0.379	
DAMZZ unox	23.6	23	0.150	No
DAMZZ all	-6.1	39	0.563	
STANN ox	18.2	-2	0.030	
STANN unox	-136.9	81	0.134	No
STANN all	32.4	-10	0.072	

Table 34. Results of linear regression analysis of the modulus versus density data for three model materials. Regression has been performed on the data for oxidised material (ox), unoxidised material (unox) and all available data (all) for each material. A "No" in the Sig. Diff. column indicates no significant difference between the ox and unox trend lines at 95 % confidence level.

The small number of data points makes the interpretation of any trends in the dependence of modulus on density quite difficult (Figure 130). No clear trend can be established from this plot, but linear regression performed on all the data suggests that variation in density has little effect on the modulus (as evidenced by the low slope of the trend line) over the range of density studied. Interestingly, linear regression on the oxidised and unoxidised data suggests that there is a slight negative correlation for both data sets. This seems extremely unlikely. However, the small number of data points and large degree of scatter conspire to produce large confidence intervals in both trend lines. Hence it has been found that there is no statistical difference (at the 95 % confidence level) in the effects of manufactured porosity (unoxidised samples) and oxidation induced porosity on the modulus of the material.

Figure 131 shows a clear positive correlation indicating that samples of DAMZZ material with a higher density exhibit higher modulus. This is the expected result and is confirmed by linear regression (Table 34). Linear regression analysis of the data for unoxidised and oxidised material, shows that in both cases there is a positive correlation between density and modulus. However, large confidence intervals mean that the differences between the two trend lines are not statistically significant. Hence, based on these data, there is no difference in the effects of porosity included at manufacture and that added as a result of oxidation.

Figure 132 shows the modulus versus density for the STANN model material. It seems clear that the modulus is relatively unaffected by density over the range studied, particularly if the point at approximately 8 GPa, 1.84 g cm^{-3} is regarded as an anomaly. It therefore also suggests that porosity arising from manufacture, or produced during oxidation has no discernibly different effect on the modulus of the material. Microstructural investigations showed that the result of oxidation was to degrade the fibre-matrix interface and that oxidation proceeded into the fibre (Section 12.2.3.). That this has no effect on modulus, and minimal effect on strength, suggests that in STANN the transfer of stress across the fibre-matrix interface and into the fibre, is not important to the performance of the material. In other words, the modulus and strength of the material arise almost exclusively from the contributions of the matrix.

12.3.4. Influence of oxidation on the strain to failure of the model materials

The strain to failure of a sample was equated to the value of the surface strain at the time of the first significant reduction in load as a result of gross failure processes. As such, it takes no account of the nature of the failure after this point or any subsequent stepwise load reductions.

When plotted against oxidative weight loss, the strain to failure data for TGAM show (Figure 133) a high degree of scatter and a reasonably constant value in the range 0.45 to 0.63 % over the range of weight loss studied. When performed on these data (Table 35), linear regression confirms this inference by producing a best-fit line with a very low slope. However, the large confidence intervals mean that the confidence in the best-fit line is low.

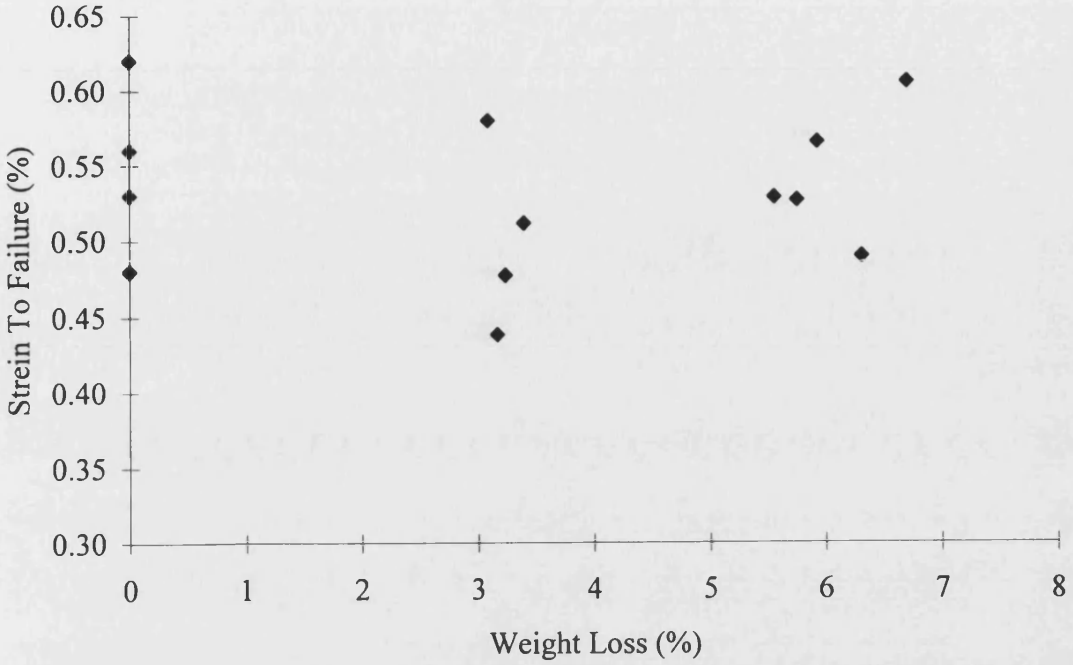

Figure 133. Strain to failure of the TGAM model material, plotted as a function of the percentage oxidative weight loss.

The effect of oxidation on the strain to failure of DAMZZ is shown in Figure 134. Again, these data show a large degree of scatter. However, linear regression (Table 35) suggests that there is a weak negative relationship between strain to failure and weight loss. Thus it can be concluded that oxidation has a slightly deleterious effect on the strain to failure of DAMZZ.

The relationship between weight loss and strain to failure for the STANN model material (Figure 135) shows a maximum at around 3 % weight loss. Although this phenomenon should be treated with some caution, an explanation for its occurrence can be found if the other data are reviewed. It should be remembered that the strain to failure could only be measured in tests where strain gauges were used. Bearing this in mind, the strength data for tests conducted using strain gauges on STANN (Figure 121) also shows a slight maximum at around 3 % weight loss. Given that the modulus of STANN was found to be relatively constant across the range of weight loss studied (Figure 129) it follows that a corresponding maximum should be seen in the strain to failure data. This arises from the fact that a high strength implies a high strain to

Material	Intercept *(c)*		Coefficient *(m)*		R^2	Strain to failure at 6% wt loss	Strain to failure reduction at 6% wt loss
	Mean	St Dev	Mean	St Dev		(%)	(%)
TGAM	0.532	0.086	-0.0002	0.022	0.0001	0.530	0.2
DAMZZ	0.539	0.046	-0.0058	0.012	0.192	0.504	6.4
STANN	0.462	0.079	0.0110	0.022	0.245	0.497	-7.4

Table 35. Results of linear regression analysis of the strain to failure versus weight loss data for TGAM, DAMZZ and STANN.

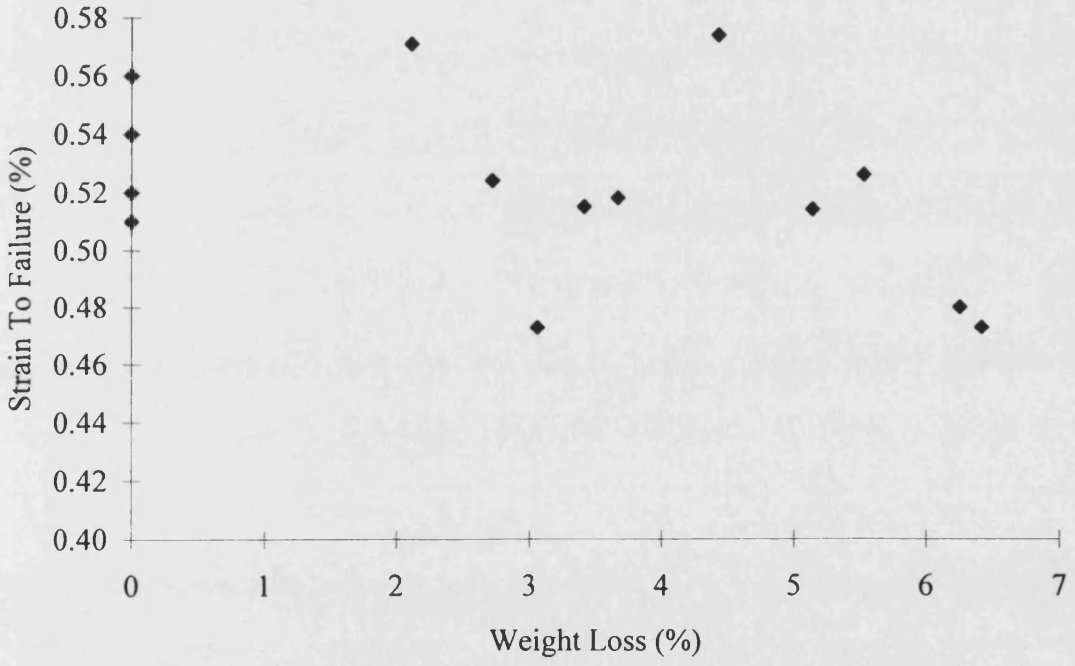

Figure 134. Plot showing the influence of weight loss on the strain to failure of DAMZZ material.

failure, if the modulus is non-variable. One possible physical explanation for the initial increase in strain to failure at low weight losses, arises from the microscopical

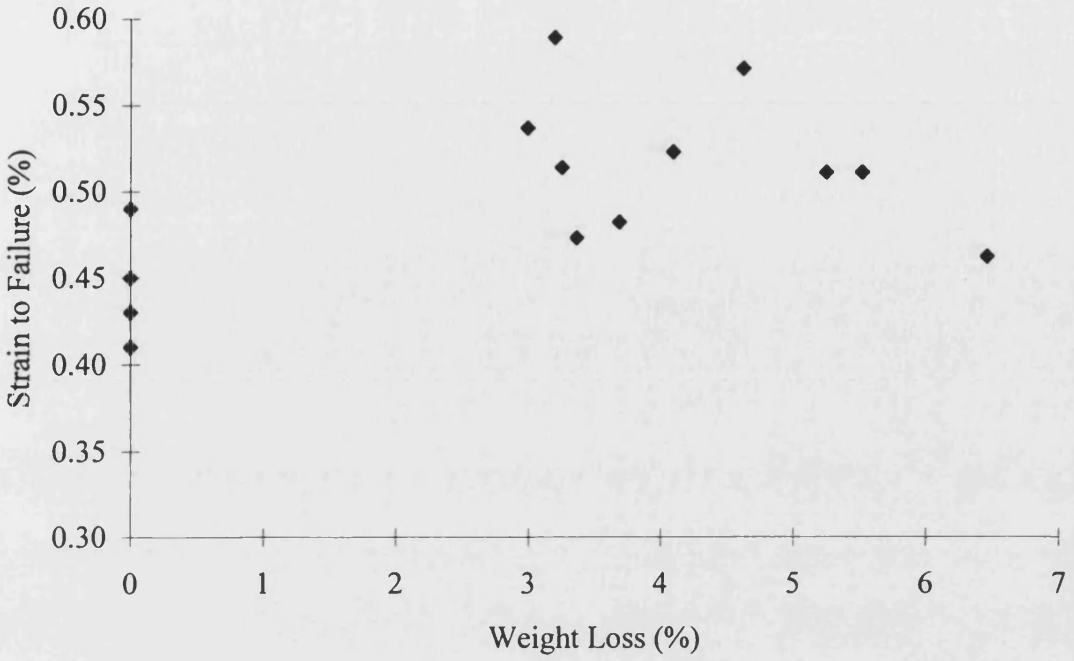

Figure 135. Strain to failure as a function of weight loss for the STANN model material.

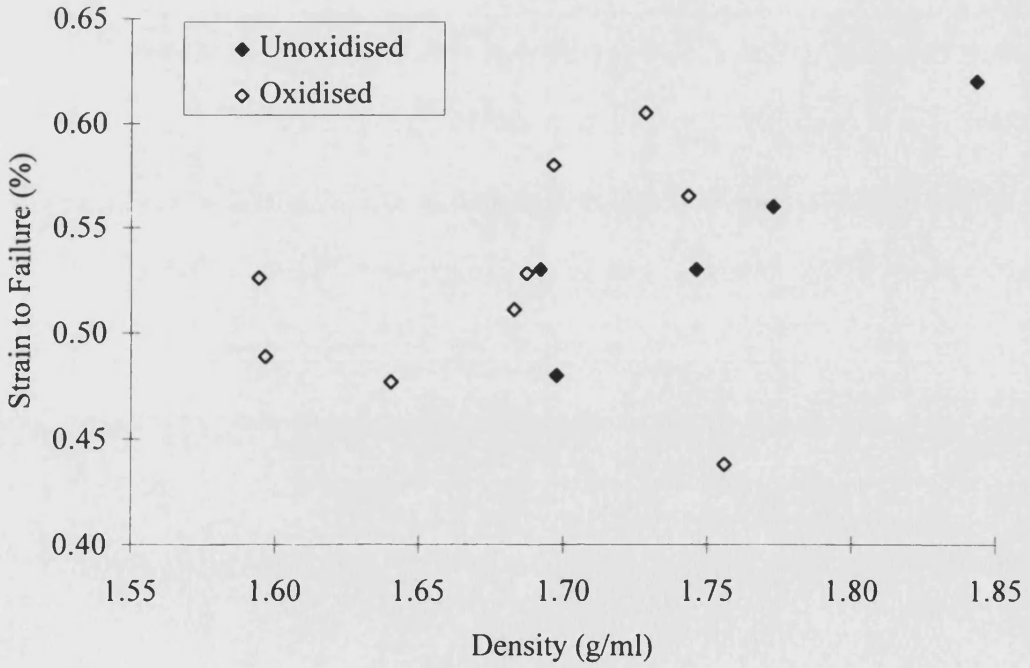

Figure 136. Strain to failure as a function of density for TGAM material in oxidised and unoxidised conditions.

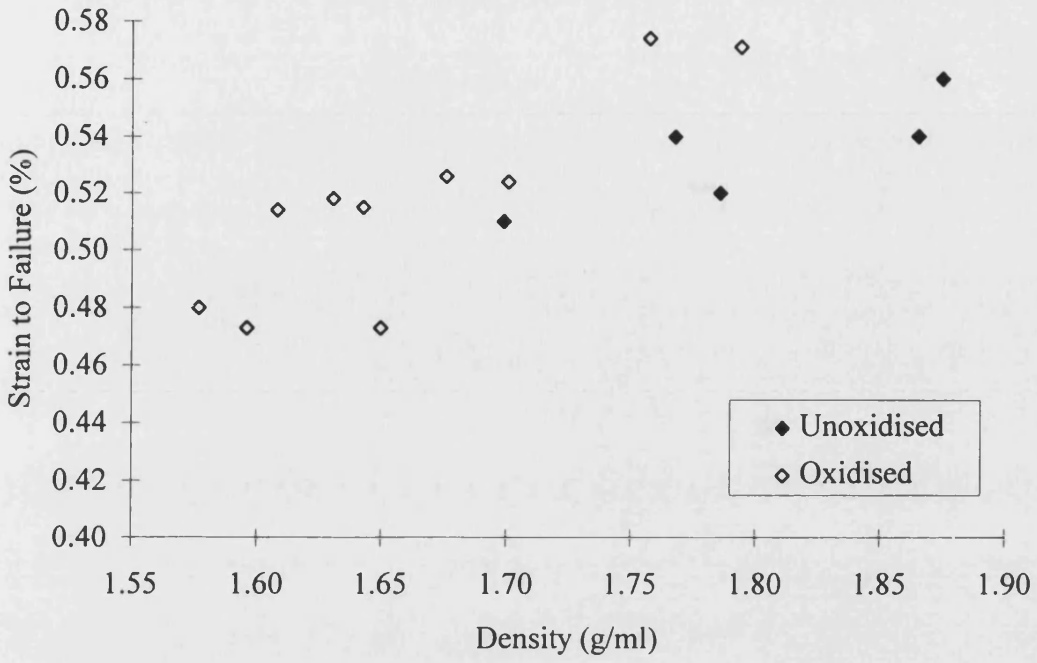

Figure 137. Plot showing the effect of variation in density on the strain to failure of DAMZZ.

Material	Intercept *(c)*	Coefficient *(m)*	R^2	Sig. Diff.
TGAM ox	0.197	0.195	0.048	
TGAM unox	-0.787	0.780	0.844	No
TGAM all	-0.089	0.364	0.230	
DAMZZ ox	-0.225	0.446	0.762	
DAMZZ unox	0.132	0.224	0.702	No
DAMZZ all	0.088	0.225	0.585	
STANN ox	-0.701	0.684	0.350	
STANN unox	0.585	-0.076	0.001	No
STANN all	0.957	-0.256	0.048	

Table 36. Results of linear regression analysis of the strain to failure versus density data for three model materials. Regression has been performed on the data for oxidised material (ox), unoxidised material (unox) and all available data (all) for each material. A "No" in the Sig. Diff. column indicates no significant difference between the ox and unox trend lines at 95 % confidence level.

evidence of pseudo-plastic behaviour in unoxidised 90° staple fibre layers which was shown in Figure 89 (page 194). The development of porosity at the fibre-matrix interface could aid the deformation processes which seem to occur in the matrix phase and hence increase the amount of deformation which could occur before failure. This would, in turn, increase the strain to failure.

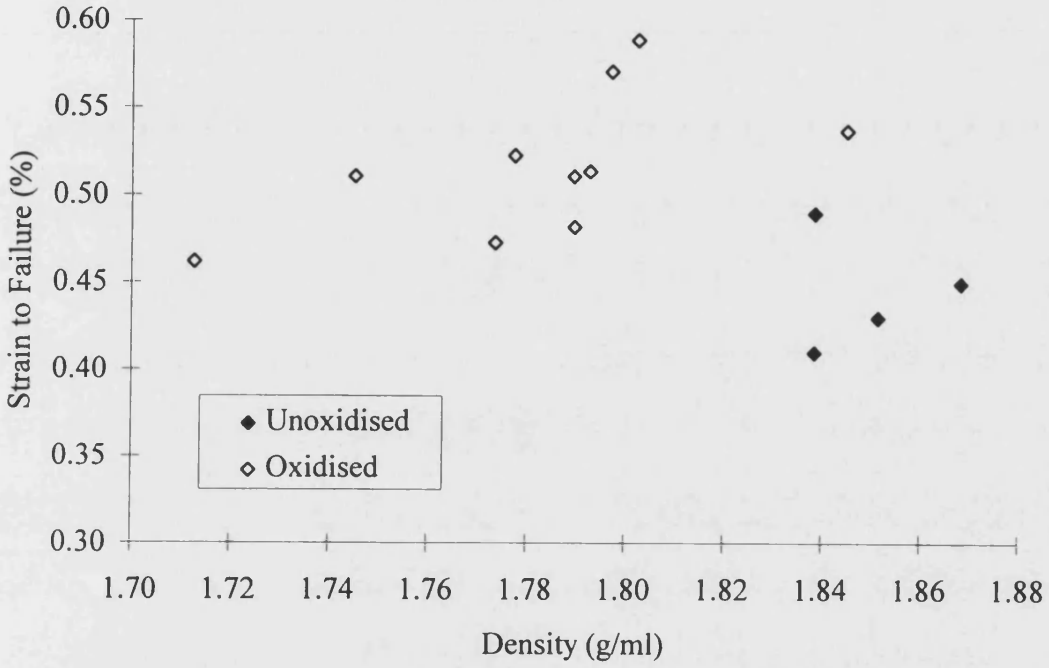

Figure 138. Strain to failure of the STANN material, plotted as a function of density.

Figure 136 and Figure 137 show the strain to failure data plotted as a function of density for TGAM and DAMZZ respectively. Both these plots suggest a broad positive correlation between strain to failure and density. Also, in both there is a slight difference between the data for oxidised and unoxidised material, with an oxidised sample exhibiting a greater strain to failure than an unoxidised sample of similar density. However, linear regression and significance analysis (Table 36) reveals that the difference is not statistically significant at the 95 % confidence level.

A plot of strain to failure against density for STANN (Figure 136) shows no clear trend. Such is the scatter in the data, that no reliable conclusions can be drawn from them. However, this plot does show a more clear difference between the oxidised and

unoxidised data than was seen for the other materials. This implies that the effects on strain to failure of porosity included at manufacture, and that caused by oxidation, are different. However, linear regression analysis shows that, as for the other materials, this perceived difference is not statistically significant at the 95 % confidence level.

12.3.5. Influence of oxidation on the stored energy at failure of the model materials

Here, the stored energy at failure refers to the total energy which has been expended in order to produce strain during the test. The value is calculated by integration of the total area under the stress versus strain curve.

The results for TGAM, Figure 139, show a shallow decrease in the stored energy at failure as a result of increasing weight loss. This is expected since, in oxidised material, less solid material remains for the storage of energy. Linear regression (Table 37) also suggests that a weak negative correlation exists, although confidence in the fitted line is low ($R^2 = 0.128$).

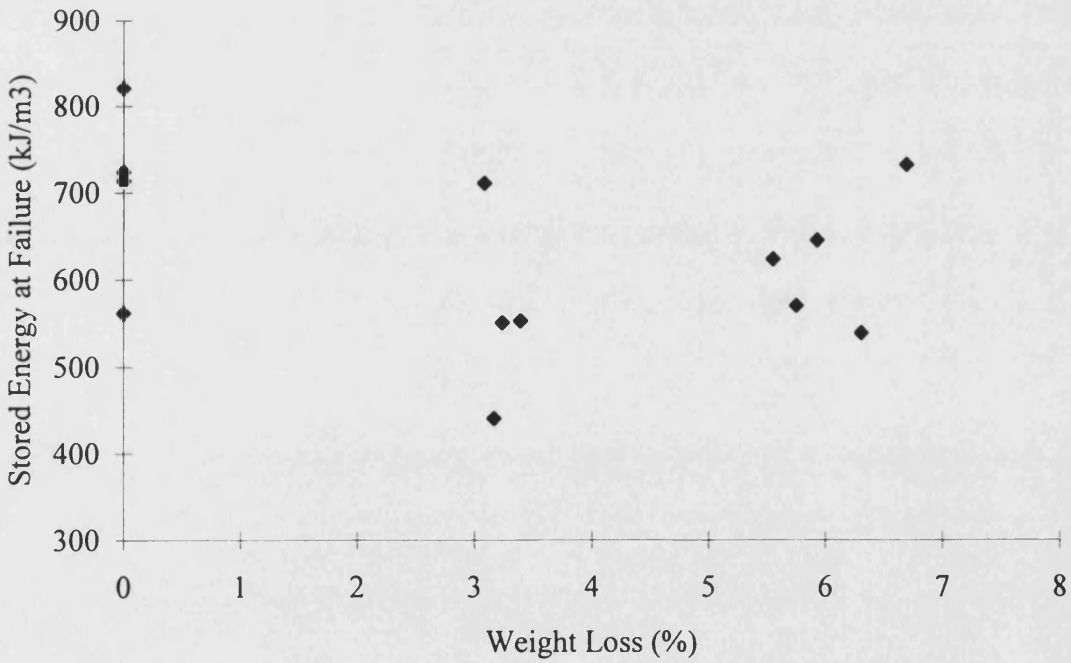

Figure 139. Graph showing the stored strain energy at failure as a function of weight loss for TGAM material.

Although there is a large amount of scatter in the data, the plot of strain energy at failure versus weight loss for DAMZZ (Figure 140) also shows a broad downward trend. Linear regression (Table 37) also suggests that this relationship exists, although once again, the confidence in the best-fit is low. It is proposed that this correlation is observed for the same reason as is was seen in TGAM.

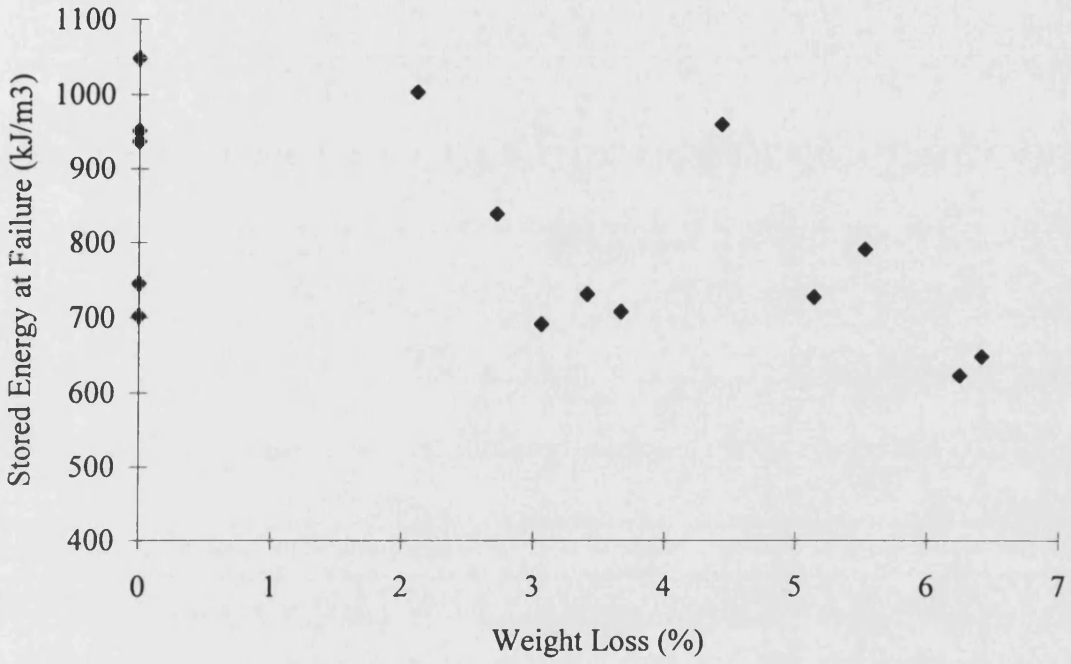

Figure 140. Plot showing the stored energy at failure of DAMZZ as a function of weight loss.

The strain energy at failure of the STANN material as a function of weight loss (Figure 141) shows a maximum at about 3 % weight loss similar to that seen in some of the other data collected for this material. This should not be surprising since the physical properties measured (strength, modulus, strain to failure and stored energy at failure) are all intimately connected. However, as with the other data, the warnings about the interpretation of this data also apply here.

A plot of stored energy at failure as a function of density of TGAM (Figure 142) shows a relatively clear positive correlation. This is expected as dense samples (of fixed volume) contain more material than samples of low density and hence have a greater energy storage capacity. This is akin to the argument to explain a similar

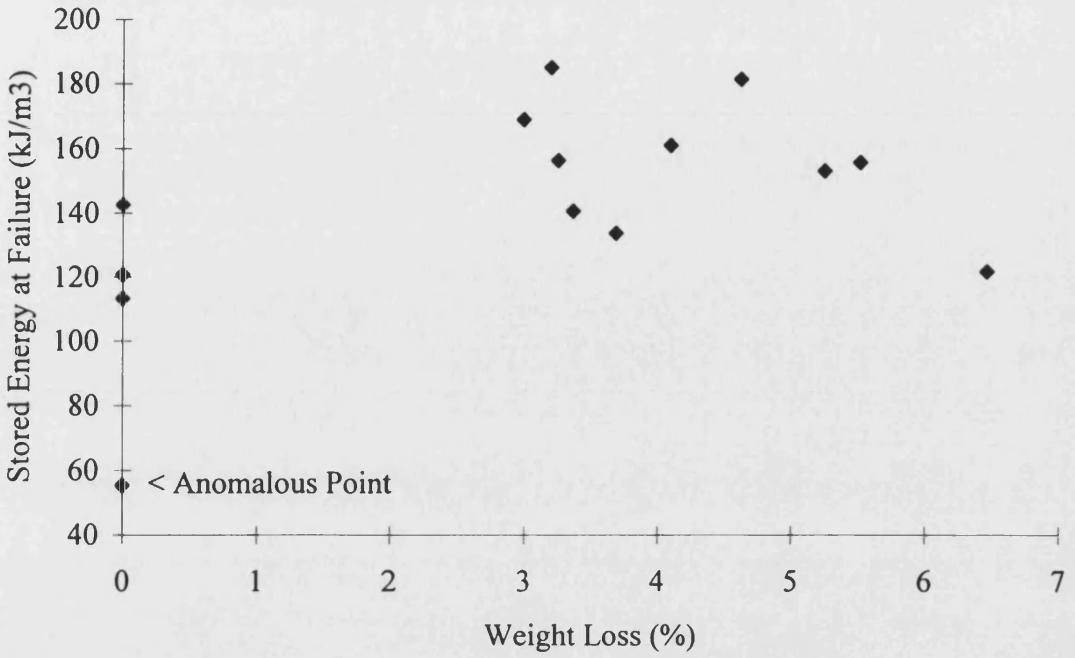

Figure 141. Plot showing the relationship between stored energy at failure andd weight loss for STANN.

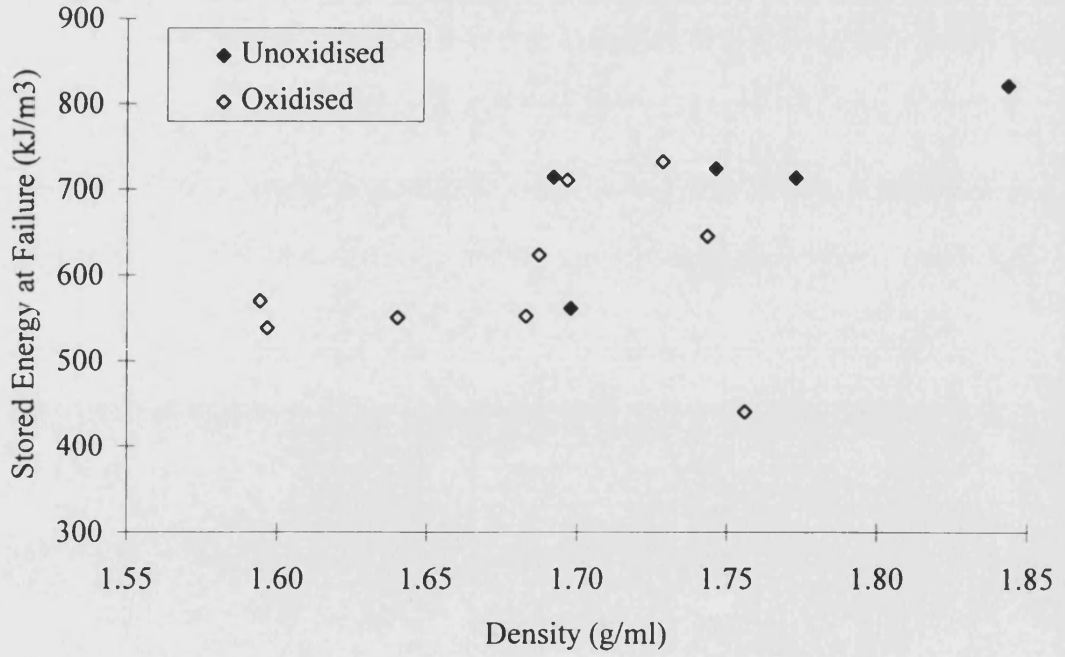

Figure 142. Graph showing stored energy at failure as a function of density for the TGAM material.

correlation between stored energy at failure and weight loss, except that density is a more accurate measure of the amount of material in a sample than weight loss, and hence here the argument might be considered more valid. Linear regression of this data has been performed and confirms the positive correlation (Table 38).

Material	Intercept *(c)*		Coefficient *(m)*		R^2	Stored energy at failure at 6% wt loss (kJm^{-3})	Stored energy reduction at 6% wt loss (%)
	Mean	St Dev	Mean	St Dev			
TGAM	679	157	-14	41	0.128	595	12.4
DAMZZ	894	194	-30	54	0.278	712	20.3
STANN	119	52	7.6	14	0.261	141	-18.7

Table 37. Results of linear regression performed on the stored energy at failure versus weight loss data for TGAM, DAMZZ and STANN.

Although Figure 142 shows no obvious differences between the relationship between stored energy at failure and density of oxidised and unoxidised samples, linear regression was performed on both data sets along with a test for any significant differences. As is clear from Table 38, no statistically significant difference was found.

Linear regression also permits the calculation of a further property of the material, namely the gravimetric energy density at failure. This is the stored energy at failure expressed per unit mass, and is equal to the slope of the best-fit line. For TGAM the gravimetric energy density is 867 mJg^{-1}. However, it is obvious that the true relationship between stored energy at failure and density should pass through the origin. The results of linear regression when this constraint is included are also shown in Table 38 and give a gravimetric energy density for TGAM of 373 mJg^{-1}. Because of the way in which it is calculated, this figure is likely to be more realistic and is useful for the comparison of different materials.

Material	Intercept *(c)*	Coefficient *(m)*	R^2	Sig. Diff.
TGAM ox	81.8	306	0.040	
TGAM unox	-1335.1	1166	0.605	No
TGAM all	-842.9	867	0.316	
TGAM all*	0	373	0.214	

Table 38. Results of linear regression analysis of the stored energy at failure versus density data for TGAM. The row labelled TGAM all* shows the results of regression on all data with the line constrained to passing through the origin.

It is possible to check which of these results is more valid by a simple calculation. If it assumed that the material behaves in an approximately Hookean manner, then the volumetric energy density, U_v, is;

$$U_v \approx \frac{1}{2}\sigma_f \varepsilon_f \qquad \textit{Equation 52}$$

Where σ_f and ε_f represent the failure stress and strain respectively . If this is divided by the density of the material, an approximate gravimetric energy density it produced. Using average values of failure stress, failure strain and density for TGAM (240 MPa, 0.53 % and 1.7 gcm^{-3}) the theoretical gravimetric energy density is 374 mJg^{-1}. This is strong evidence that constraining the best-fit line to passing through the origin is the more valid approach.

The plot of stored energy versus density for DAMZZ (Figure 143) shows a positive correlation, with no discernible differences between the oxidised and unoxidised data. Both these conclusions are confirmed by linear regression (Table 39). This analysis produces a gravimetric energy density of 1080 mJg^{-3} for regression where the best fit line was not constrained to passing through the origin, and 474 mJg^{-3} where it was. Using values of 300 MPa, 0.52 % and 1.72 g cm^{-3} for failure stress, failure strain and density respectively, and assuming Hookean behaviour, Equation 52 predicts a gravimetric energy density of 453 mJg^{-3}.

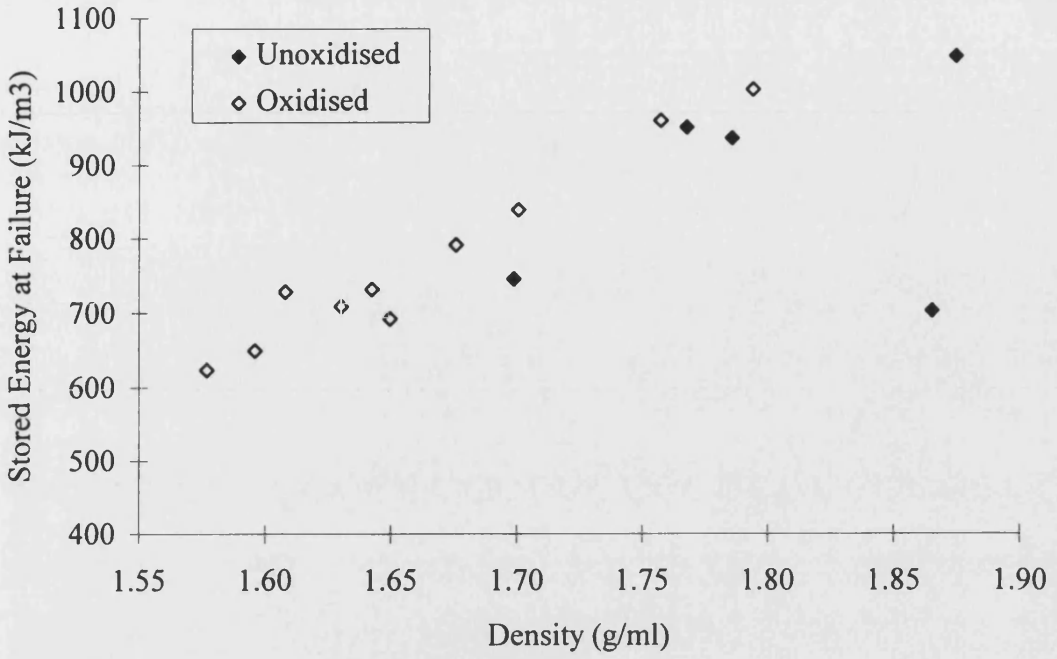

Figure 143. Plot of stored energy at failure as a function of density for the DAMZZ model material.

Material	Intercept *(c)*	Coefficient *(m)*	R^2	Sig. Diff.
DAMZZ ox	-2168.5	1769	0.955	
DAMZZ unox	-94.6	540	0.072	No
DAMZZ all	-1036.9	1080	0.552	
DAMZZ all*	0	474	0.378	

Table 39. Results of linear regression analysis of the stored energy at failure versus density data for DAMZZ. The row labelled DAMZZ all* shows the results of regression on all data with the line constrained to passing through the origin.

As with that for DAMZZ, the plot of stored energy versus density for STANN (Figure 144) shows a positive correlation, with no discernible differences between the oxidised and unoxidised data. Again, both these conclusions are confirmed by linear regression (Table 40). Linear regression of the data without the constrain of the line to passing through the origin, produces the nonsensical value of gravimetric energy

density of -192 mJg^{-3}. However, using the constraint produces the much more sensible value of 79 mJg^{-3}. Using values of 57 MPa, 0.50 % and 1.78 g cm^{-3} for failure stress, failure strain and density respectively, and assuming Hookean behaviour, Equation 52 predicts a gravimetric energy density of 80 mJg^{-3}.

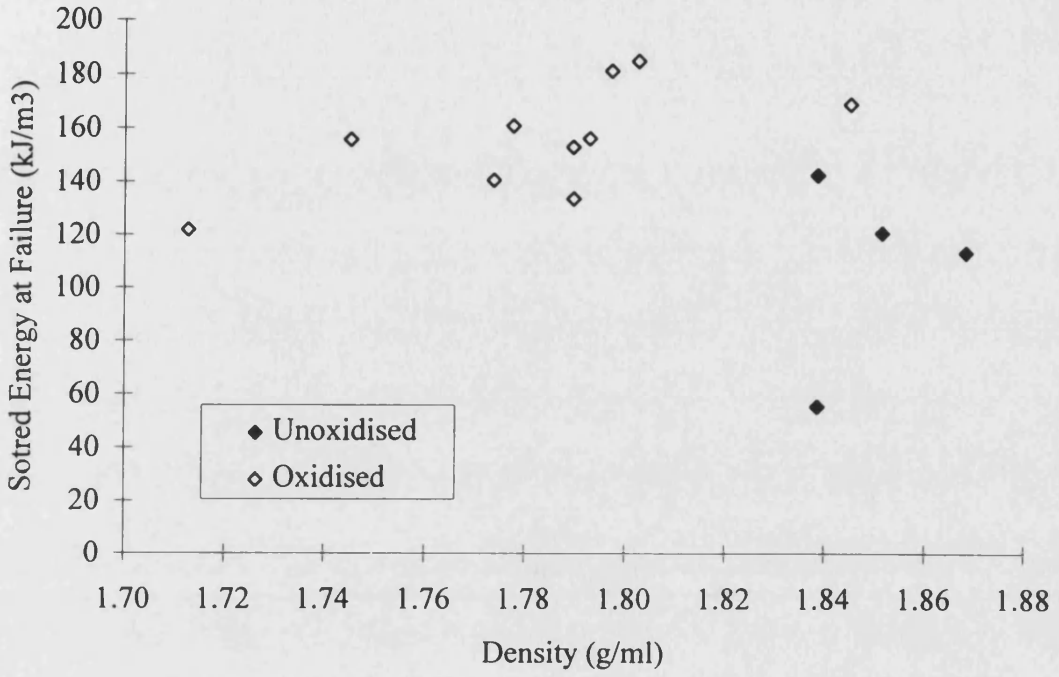

Figure 144. Plot of stored energy at failure versus density for STANN.

Material	Intercept *(c)*	Coefficient *(m)*	R^2	Sig. Diff.
STANN ox	-502.3	369	0.421	
STANN unox	-894.8	542	0.042	No
STANN all	487.8	-192	0.063	
STANN all*	0	79	0.005	

Table 40. Results of linear regression analysis of the stored energy at failure versus density data for STANN. The row labelled STANN all* shows the results of regression on all data with the line constrained to passing through the origin.

Hence the gravimetric energy density is greatest in DAMZZ (474 mJg^{-3}), least in STANN (79 mJg^{-3}) and intermediate in TGAM (373 mJg^{-3}). This implies that more energy is stored at failure in pure continuous fibre than in pure staple, but that a mixture of continuous fibre and staple, allows greater energy storage than either of the pure forms alone.

12.3.6. Influence of oxidation on the value of k for the model materials

Previously it has been discussed that, although accurate, strain gauges are expensive and sometimes difficult to use. The concept of k, the correction factor was introduced which allowed the determination of strain from total centre point deflection to be made with a fair degree of confidence. However, it was noticed that the value of k was different for the various materials tested in the unoxidised state. Therefore, the correction factor could only be used after it had been calculated from experimental data. Hence, it is only really useful if a large number of tests are to be conducted, as, once k is known from the first few tests, it can be used in the remainder without the need for strain gauges.

Given that k was dependent on the type of material under examination, there seemed no reason to suggest that k should be constant if the material was oxidised. However, if a relationship between k and a conveniently measured property, such as density or weight loss, could be found, k could still be used to simplify testing. To investigate this, k values were derived for all the tests conducted using strain gauges.

Figure 145 and Figure 146 show plots of k as a function of weight loss and density respectively, for TGAM, DAMZZ and STANN materials. It is clear that in all six of the graphs presented in these two figures, there is a large degree of scatter and no clear trend to the data. Consequently, the correction factor k cannot be predicted for these materials from the weight loss or density of a sample. This means either that the idea of the correction factor must be abandoned for oxidised materials or that another easily measured property which can predict the k value must be found. Unfortunately, the large scatter of these data also calls into question the validity of the use of k for tests on unoxidised material.

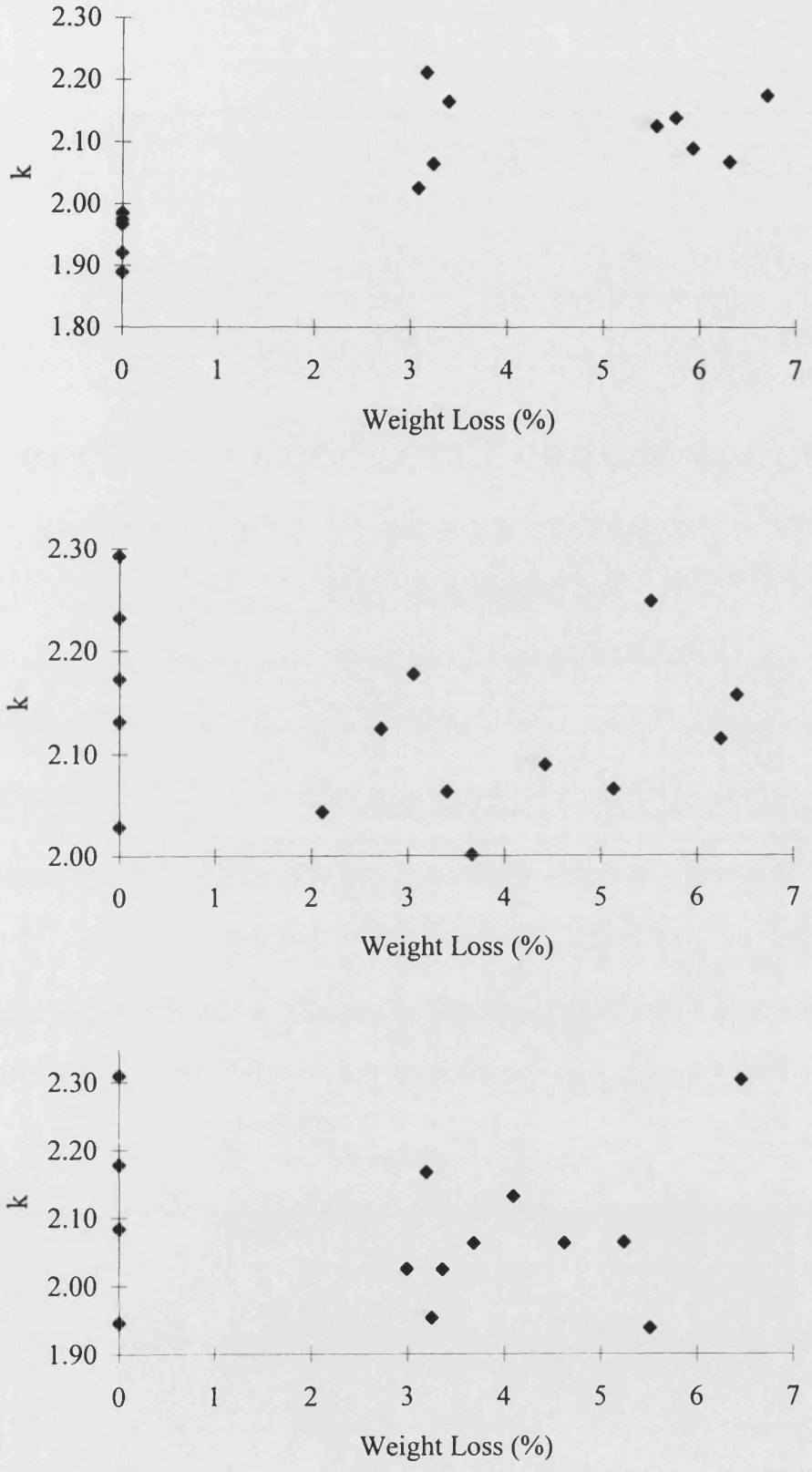

Figure 145. Three plots showing the lack of useful correlation between *k* and weight loss for TGAM (top), DAMZZ (middle) and STANN (bottom).

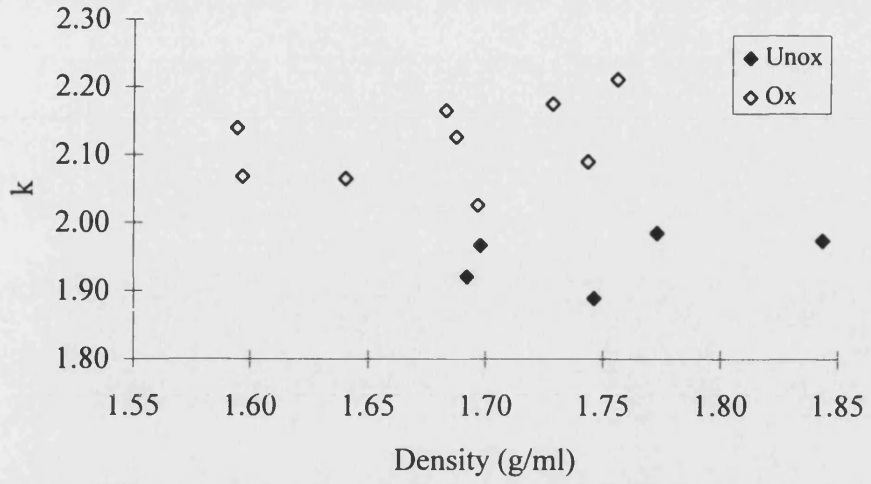

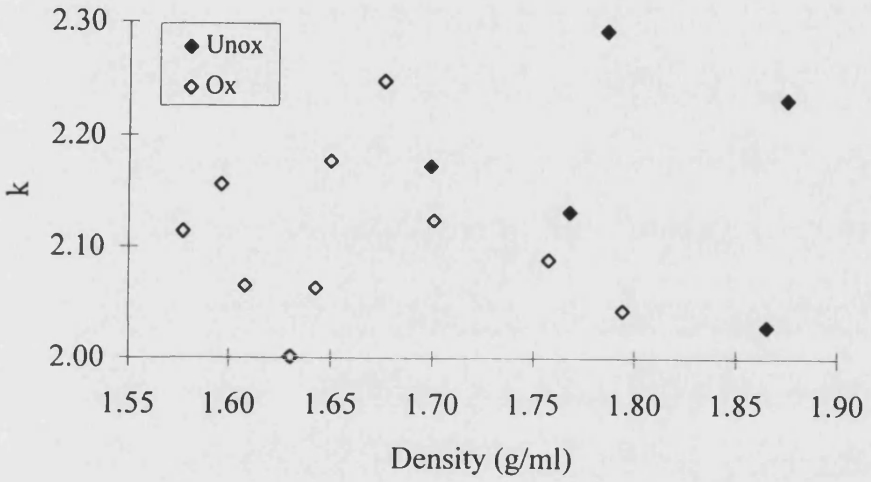

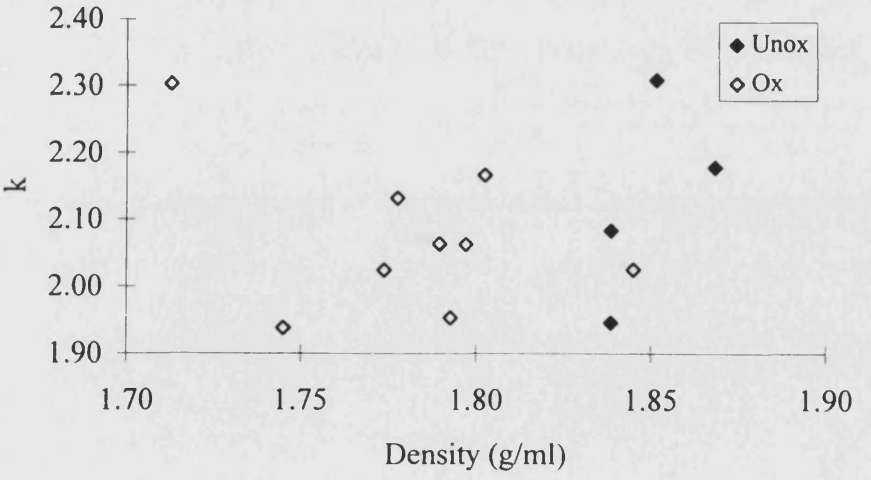

Figure 146. Three plots showing the lack of correlation between *k* and density for TGAM (top), DAMZZ (middle) and STANN (bottom).

12.4. Conclusions and summary

During this investigation it has been found that oxidation in an atmosphere of CO_2 provides a convenient method for a controlled reaction with uniformity of oxidation. It has been assumed that a low oxidation temperature will produce a more uniform pattern of oxidation due to the lower reaction rate, although this has not been experimentally verified. A temperature of 900 °C is the minimum temperature which will produce oxidation at a rate high enough to produce the low weight losses used here in a practical timescale. For shorter investigations, or those carried out to higher weight losses, higher temperatures may be necessary. Even in the slow, controlled oxidation regime used in this investigation, it was found that oxidation to exact weight losses was impossible, with an accuracy in predicted weight loss of ±1 weight percent being typical. Also, it was found that the pattern of oxidation was not entirely uniform. Although surface burn-off producing dimensional change did not occur, optical microscopy revealed that oxidation was most severe in the surface layer. Therefore it can be concluded that the structure of the material makes it very difficult for truly uniform oxidation to be achieved.

Conclusive evidence has been found from optical and electron optical microscopy, that the effect of oxidation on all of the model materials investigated is to degrade the fibre-matrix interface. There are four reasons for this. Firstly, the fibre-matrix interface is a region of high disorder which makes is thermodynamically less stable and hence more reactive. Second, shrinkage during manufacture causes the interface to contain residual stresses which also increase reactivity. Thirdly, this same shrinkage, which arises from the volumetric shrinkage associated with graphitisation of the fibres after CVI, can cause shrinkage cracks. While most of these are observed a short distance into the matrix sheath, some have been seen at the fibre-matrix interface. It is possible that cracks too small to be seen using optical microscopy exist at the fibre-matrix interface. These could provide easy access for the oxidative gas, and hence would be preferentially oxidised. Finally, EDAX has shown that the fibre-matrix interface often contains impurities, particularly sodium and potassium compounds, which are know to have a catalytic effect on the oxidation of carbon. When combined, these four factors make the interface by far the most easily oxidised region of the composite. Following oxidation of the interface it has been shown that

oxidation proceeds by attacking the fibre. This produces ever-widening crescent shaped pores at the interface and hence weakens the fibre-matrix bond.

In general, oxidation had a detrimental effect on the mechanical properties of the model materials tested. However, the magnitude of the decrease in performance was not as great as those found by researchers studying other carbon-carbon composites. There are two possible explanations for this: the differences between the materials, or differences in the test method. The first of these is possible but the fact that the performance of the materials is about twice as good as that found by other workers means that this is unlikely to be the sole cause. In other works, the conventional flatwise flexure test was used. It is known that in laminated carbon-carbon composite materials this commonly induces failure by an interlaminar shear mechanism. However, in published works, a description of the exact nature of the failure mode is often omitted. In the edgewise flexure test the effect of oxidation on the tensile strength is assessed, but in flatwise flexure the true tensile strength is often underestimated due to premature failure by interlaminar shear. Hence the flatwise test really estimates the effect of oxidation on the shear strength unless the failure mode is truly tensile. It is likely that the effect of oxidation on the tensile and shear strengths will be different and so this could be a contributing factor to the differences in results between those presented here and those in the open literature.

The strength of the STANN model material initially increased on oxidation to show a broad maximum at around 3 %weight loss. However this was only seen if data from tests using strain gauges were plotted. When all available data was plotted a broad decline in strength was seen as for the other materials. This plot also indicated that the strength of unoxidised STANN was adversely affected by the application of strain gauges, and it was this which produced the apparent peak. This effect was not seen with any of the other materials, and the reasons for this are unknown. The most plausible, although still tenuous, explanation is that the unoxidised samples tested with strain gauges were inherently flawed before testing. This could be true, particularly as these samples were all made from the same original block of model composite material.

Plots of mechanical properties against density, with oxidised and unoxidised material considered as different data sets, indicated that there were some slight differences in the relationships for these two sets for some properties of some of the materials. This

indicated, that in these cases, the effect of porosity included during manufacture and that induced by oxidation were different. This was confirmed by optical microscopy which showed that manufactured porosity was located between matrix sheaths, whereas oxidative porosity occurred at the fibre-matrix interface. However, regression analysis of the data showed that none of the differences between the data sets for unoxidised and oxidised material were statistically significant at the 95 % confidence level.

In attempting to rationalise the results of testing oxidised material, it was found that simple analysis based on the rule of mixtures for the constituent layers did not adequately describe the behaviour of the materials. It is therefore concluded that the effect of oxidation on the mechanical properties of a material depends not only on the effects within layers, but also on the interactions between them. In this way, the effects of oxidation are more complex than the effects of changing the fibre layer types or proportions. Further work is required in this area before a full understanding of the way oxidative effect and microstructure interact and affect one another.

The effect of oxidation on the fracture surfaces was to cause increased roughness indicating that more crack deflection had taken place. In 90° fibre layers little change was observed, although there was evidence that more cracking in the fibre-matrix interface region occurred. However, significant changes were seen in 0° fibre layers. In contrast to the largely planar fracture surfaces of the unoxidised material, oxidised material showed evidence of fibre pullout. At low levels of oxidation the pulled out material consisted of several fibres, but at higher weight losses the individual fibres were seen. This is a direct consequence of the weakening of the fibre-matrix bonding by oxidation.

13. CONCLUSIONS

13.1. Examination and testing of ex-service material

The examination of ex-service material proved difficult for two main reasons. Firstly, the fibre architecture of the commercial material is complex. This makes the microstructure difficult to understand fully and also makes it impossible to produce samples for testing which are identical. The second problem is that it is impossible to assess the "age" of the material. It was found that chronological age and number of landing cycles were not adequate determiners of material "age" (where "age" is a measure of the proportion of useful life experienced). This is due to the different conditions to which the aircraft brakes are subject during their service life causing differences in the extent of useful service life.

Compressive testing of ex-service material showed that the compressive test was relatively ineffective at revealing changes in strength of the material. Although no clear trend of compressive strength as a function of service life could be found, samples from close to the inside and outside edges of a failed disc showed low strengths. A broad positive correlation between density and compressive strength was also found for the commercial ex-service material. Density measurements showed that the discs which had not failed were of higher density close to the outside edge. This is attributed to the manufacturing process as the disc preform will tend to have higher density near its edges. During final machining much more material is removed from the inner edge than from the outer, and this leaves the final position of the outer edge within the zone of high density. It was also found that failed discs exhibited significantly decreased density at both the inner and outer edges. Optical microscopy revealed that the decrease in density was due to the occurrence of additional porosity and this was attributed to the effect of oxidation. The effect was particularly distinct at the inside edge where the pattern of oxidation was identical to that seen in laboratory oxidised material. The reduced strength in these regions is attributed to the effects of oxidation and was intimately related to the reduced density.

Some ex-service discs showed evidence of slot widening. This causes a reduction in the length of tenons, and hence a reduction in the amount of material bearing the shear stresses between the swept area and the tenon. It is proposed that this wear of the

tenons could be a mechanism by which discs fail in service. Examination of tenons from structural torque tests, samples from compressive testing and surfaces subject to blunt indentation, have shown that it is possible to form a surface film on these carbon-carbon composites without large displacement sliding contact. Optical microscopy showed that this film consisted of distinguishable pieces of fibre and fine particles of matrix-derived material. Blunt indentation revealed that the quality of the film improved with increasing load and number of loading cycles. Evidence was found for the detachment of this film from the substrate which lead to the conclusion that cyclic film formation and detachment could be the cause of slot widening. This is a novel wear process for carbon-carbon composites since it does not involve sliding contact as the principal film formation process.

Full scale testing of whole discs by the structural torque method has shown that failure under excessive load occurs by splitting along the boundaries between cloth plies in the composite. This type of failure has been called "broomstick failure" as a consequence of the resemblance of the fracture pattern to the head of a broom. Due to machining inaccuracies and hence non-uniform load distributions, the use of a modified structural torque test was unable to reveal the microstructural characteristics of damage accumulation prior to gross failure. A mathematical argument has been used to demonstrate that extreme machining accuracy is required if uniform load distribution between the tenons is to be achieved.

13.2. Flatwise and edgewise flexure

The main practical difficulty associated with flexural testing is the determination of strain. It has been suggested that the strain can be calculated from the crosshead displacement, or more strictly, from the displacement of the loading rollers with respect to the support rollers. However, it has been shown that this calculation is likely to be erroneous. The true strain can be calculated from the true centre point deflection, however this calculation also relies on conformity of the specimen to simple geometry during testing. Strain gauges were found to be a simple and effective way of accurately measuring the surface strain and hence were used extensively in this work.

Initial investigations confirmed that flatwise flexure cannot be used to measure the tensile strength of the materials with the geometry used in this work. This was due to

premature failure by an interlaminar shear mechanism. This is a well known effect in laminated carbon-carbon composites and is difficult to avoid even at high span to depth ratios. The effect illustrates the large difference between the tensile strength and the interlaminar shear strength for these materials.

The occurrence of interlaminar shear failure in these materials was eliminated by avoiding the coincidence of shear forces and weak planes. This was achieved by testing the specimen on edge in a test called the edgewise flexure test. This test produced true measures of the tensile strength since the failure mode was tensile. The edgewise method also had another advantage over the flatwise method. In flatwise flexure the stiffness of the specimen is dependent on the stacking sequence of the cloth layers within it. Hence the modulus must be reported as the flexural modulus. By contrast, the stiffness of the sample in edgewise flexure is independent of stacking sequence and so the measured modulus can be reported as the Young's modulus.

13.3. Testing of model materials

The concept of reducing the complexity of the commercial material by designing a series of simpler model materials to duplicate the effects of the various fibre layers has been shown to work quite well. Several types of model, laminated carbon-carbon composites were made utilising the two basic elements of the commercial material, unidirectional continuous fibre layers, and chopped fibre layers (staple) with preferred fibre orientation. The designs of the model materials and the notation used are described in Section 9.1. page 125.

Edgewise flexural testing has been conducted on a number of model materials and it proved possible to analyse the results using a simple rule of mixtures concept. This has shown that the strength of a carbon-carbon composite material is most strongly influenced by the inclusion of continuous fibres which are well oriented with respect to the applied stress. In addition to this, it has been found that continuous fibres are also present in materials with a high modulus. Of course, it should be remembered that the strength and stiffness of continuous fibre layers arises as a result of the properties of both the fibre and the matrix, the latter showing considerable orientation with the fibre direction. Of the other fibre layer types, only 0° staple material (i.e. with preferred fibre orientation parallel with the long axis of the sample) seemed to offer any reasonable properties. Layers containing continuous or short fibres

orientated perpendicular to the long axis of the sample (90° fibre layers) were found to have very poor mechanical properties. That the 0° staple material has significantly worse mechanical properties than 0° continuous fibre material implies that good mechanical properties rely on good fibre orientation and high fibre content. In 0° continuous fibre there is not only more fibre, but also the fibres are more closely aligned with the axis of the applied stress as a result of their more regular spatial arrangement.

The fracture mode in 0° fibre layers was across the fibres, and hence they had to be broken for the crack to grow. The resultant fracture surface was fairly flat but where fibre pullout did occur it was greatest in continuous fibre layers and generally consisted of groups of fibres and not individual fibres. The fracture surface in 90° fibre was very flat due to the crack path which was between adjacent matrix sheaths. The low strength and modulus of these layers suggest that the bonding between these adjacent sheaths is relatively weak. Evidence of pseudo-plastic behaviour was occasionally found in 90° staple fibre layers with multiple matrix cracking and evidence of deformation of the matrix phase provided by optical microscopy. This might go some way to explaining the relatively large departure from linearity in the load versus deflection curves for the STANN material which was made up entirely of 90° staple fibre layers.

13.4. Effects of oxidation

Despite significant effort, it has been found that the control of uniformity of oxidation of the material is difficult. Although specific weight loss values could be achieved relatively consistently, microscopic analysis revealed that the oxidation was most severe in the region close to the surface. This implies that the reaction was, at least partially, under diffusion control. That some evidence of oxidation was found through the complete thickness however, shows that the attempt to produce uniform oxidation was successful to some extent. More uniform oxidation might be achieved if lower temperatures and flow rates were used and the oxidative atmosphere was a mixture of carbon monoxide and carbon dioxide rather than pure carbon dioxide.

Conclusive evidence has been found that under the conditions used, oxidation preferentially attacks the fibre-matrix interface. It is suggested that this is due to a combination of structural disorder, residual stresses, and the presence of small scale

manufacture-induced porosity and catalytic impurities in these regions. EDAX has revealed the presence of impurities such as sodium and potassium at the surface of fibres suggesting that some catalysis of the oxidation reaction occurs at the fibre-matrix interface. Oxidative attack has been shown to progress preferentially into the fibre, leaving the matrix sheath relatively unaffected. The microstructural effect of oxidation is to produce crescent-shaped porosity in the region of the surface of the fibre. As oxidation progresses, these pores become wider and extend along the length of the fibre. SEM analysis has shown that the remaining fibre becomes pointed as a result of this attack. The angle of the point is small, indicating that the oxidative attack proceeds much more quickly along the fibre-matrix interface than it does into the fibre. This elongated porosity may aid through-thickness oxidation by providing a route for gas transport into the bulk.

Generally, oxidation had a deleterious effect on the mechanical properties of the materials. However, the magnitude of the reduction in properties was smaller than previously reported for other carbon-carbon composite materials. This is assumed to be a function of the good performance of the material, and the novelty of the test, with the latter possibly being more significant. It was found that the materials which made best use of the properties of the fibre, i.e. those with 0° continuous fibre, showed significant reductions in strength and modulus as a result of low levels of oxidation. By contrast, the all staple material STANN, showed a minimal reduction from which it can be concluded that in this material the strength of the fibre-matrix bond is relatively unimportant, and that the lack of bonding between the matrix sheaths is the property limiting factor.

Plots of mechanical properties against density revealed that in some materials, and for some properties, the effect of porosity originating from the manufacturing process and that resulting from oxidation were slightly different. This is reasonable as the manufactured porosity tends to be large and located between matrix sheaths, whereas oxidation porosity tends to be small and located at the fibre-matrix interface. However, subsequent regression analysis showed that the observed differences were not statistically significant.

The role of the microstructure on determining the oxidation behaviour has not been precisely defined. The fact that the oxidation is worst at the surface of the samples indicates that the oxidative gas is being prevented from completely penetrating the

sample. It has been found that oxidation attacks fibre-matrix interfaces, and that the attack progresses relatively rapidly along the fibre direction. Therefore it is proposed that the inclusion of long fibres which emerge at the surface of the sample might provide easy access for the oxidative gas to the core after a small amount of oxidation has taken place. This effect might not be so severe in composites containing shorter fibres.

Weakening of the fibre-matrix bond by oxidation has caused an increase in the occurrence of fibre-matrix debonding in all layers. The effect was most noticeable in 0° fibre layers. Here, as oxidation proceeded, more fibre pullout was observed. Also, at higher weight losses, the pullout of individual fibres occurred rather than pullout of groups of fibres. Evidence for this was found in both optical and electron optical analysis.

The correction factor k has been introduced, and is defined as a constant factor allowing the conversion of total centre point deflection in a four-point bending test directly into true surface strain. Unfortunately it has been found that the correction factor k varies with oxidation level in a non-predictable manner. Therefore little confidence can be had in strains calculated by this method. Indeed, the scatter in the values of k for oxidised materials has cast doubt over the validity of its use even for unoxidised materials.

13.5. Implications of results for disc and disc material design

The structural torque testing programme and subsequent mathematical analysis of the distribution of load between the tenons suggest that the performance of the discs could be improved if the machining tolerances were improved. Of course, perfection in machining could never be achieved, but more uniform stress distribution at the beginning of the life of the disc would reduce the amount of material lost and damage accumulated during initial bedding-in.

Evidence has been found for pseudo-plastic behaviour of staple fibre layers where the fibre direction is predominantly perpendicular to the applied stress. This effect could be utilised in the load bearing faces of tenons to absorb some of the machining inaccuracies.

Tenon wear by slot widening could be reduced if detachment of the surface film formed could be prevented. It seems likely that the film will only become detached

under conditions where zero load is applied. If a method could be found of retaining some load on the tenon face even when the brakes are not being used this might clamp the film to the substrate and reduce wear. During the time when the undercarriage is down, i.e. when the aircraft is on the ground, this could be achieved by maintaining some braking pressure between taxi snubs. At other times the force could be supplied by a small spring inserted between the non-load bearing faces of the tenon and torque tube which would result in light pressure at the load bearing faces.

Mechanical testing of model composites with various fibre architectures has shown that the highest strength is achieved by the inclusion of continuous fibre parallel to the applied stress. Structural torque testing has shown that tenon failure occurs by interlaminar debonding and shear across the junction between the tenon and the swept area. The combination of these two results suggests that the tenons and immediate area surrounding them should be made entirely of continuous fibre. Also, to reduce interlaminar failure, a three dimensional structure should ideally be adopted. Of course, the implementation of both of these suggestions would be costly but may provide significant performance gains. In the commercial material, staple fibre layers are used to reduce the cost of the composite by reducing the fibre content. The mechanical testing has shown that the inclusion of correctly oriented staple fibre layers provides a performance benefit over the inclusion of poorly oriented continuous fibre. Indeed, even poorly oriented staple out performs poorly oriented continuous fibre. This suggests that continuous fibre should only be included where it is well aligned with the applied stress. Where it would not be well aligned it can be replaced with well aligned staple fibre, or if this is not practical, with poorly aligned staple. Both of these suggestions would simultaneously improve material performance and reduce material cost.

Oxidation of the materials has shown the general trend that properties of the weaker materials are less affected by oxidation. This is because they rely less heavily on the fibre-matrix bond for their physical properties. However, despite the greater proportional reduction in properties of the stronger materials, they still have superior mechanical properties at low weight losses than the weaker materials. Hence there is no benefit in using materials which are initially weaker on the grounds that they offer improved performance after oxidation.

Overall, it has been shown that oxidation has a deleterious effect on the mechanical properties, in particular strength, of the materials. Therefore, the rather obvious conclusion that oxidation should be avoided, can be drawn. One of the ways in which the oxidation of the discs could be reduced is by restricting the access of the oxidative gas (air). This could be achieved to a certain extent if the open spaces between the discs and the surrounding structures were reduced in size, or better still, eliminated completely. Ideally though, the whole braking system should be environmentally sealed. This is impractical as it adds to the cost and weight of the braking system, increases inspection and servicing difficulties and reduces the vital thermal transfer between the brakes and the atmosphere.

It has been shown that the fibre-matrix interface is preferentially attacked by oxidation in these materials and it has been proposed that part of the reason for this is the occurrence of catalytic impurities in this region. The oxidation resistance of the material could therefore be improved if the source of these impurities could be isolated and eliminated. It is also known that many catalytic elements are found in common aircraft cleaning agents. It is therefore suggested that great care be exercised when cleaning aircraft, to prevent these cleaning agents coming into contact with the braking system.

When considering changes and improvements which could be made to the material it should be remembered that the mechanical and oxidative characteristics form only part of the viability criteria of a commercial product . Amongst the other factors which need to be considered are the practicality of manufacture, thermal characteristics, weight and of course most importantly, cost.

14. FURTHER WORK

This work has provided a useful insight into the world of carbon-carbon composites used in aircraft brakes. While many questions have been answered, some areas justify further investigation.

For development of this material to be made, it would be very useful to have a greater understanding of the kinetics of the oxidation process. This could further elucidate the nature of the complex relationship between microstructure, fibre architecture and oxidation behaviour. These experiments could also investigate the differences in effect between oxidation in carbon dioxide and oxidation in air. Of importance to the inhibition of oxidation is an understanding of the nature of gas transport within the materials. There are two primary routes by which oxidative gasses can enter the core of a carbon-carbon composite component: through the network of pre-existing open porosity or through the porosity created at the fibre matrix interface by oxidation. Oxidation kinetics studies could be conducted on material with no emergent fibre, i.e. no fibre which intersected with the surface of the sample. In this case the oxidative gas could only penetrate the sample via the open porosity. It would also be interesting to observe the microstructural pattern of oxidation in this material since no fibre-matrix interfaces would be immediately available for oxidative attack. How oxidation effects the mechanical properties of this material is also of interest. It is suggested that long fibre carbon-carbon composites without emergent fibres might retain a greater proportion of its mechanical properties than equivalent continuous fibre composites with emergent fibres. The effect of intentionally introducing oxidative catalysts into the materials would be another area of useful investigation. The catalyst could be introduced during lay-up at the fibre-matrix interface, or after manufacture to the surface of the open porosity. In this way the influence of the catalyst on the location of the initiation and progression of the oxidative attack could be assessed.

It is possible that a further path by which oxidative gasses can gain access to the core of the material, is via the circumferential shrinkage cracks seen in the matrix sheaths and occasionally close to the fibre-matrix interface. These arise from volumetric shrinkage of the fibre during the graphitisation stage of manufacture which takes place after CVI deposition of the matrix material. To assess the influence of these cracks on the oxidation behaviour of these composites, equivalent materials could be made using

fibres which have been graphitised prior to matrix deposition. Hopefully these materials would not contain these shrinkage cracks and by comparison with similar materials made in the conventional fashion the effect of their omission could be discovered.

An obvious area which requires further investigation is the effect of higher weight losses. Here the range of weight loss studied was between 0 % and about 6 %. Oxidation to higher weight losses, for example up to around 40 % weight loss, would improve the understanding of the effects of oxidation on the mechanical properties. It would be of particular interest to discover how accurately the results from low levels of oxidation predict the effects of higher weight loss. Here it has been assumed that the relationship between mechanical properties and weight loss approximately follow a linear form, although commonly an exponential form is assumed. There is actually little justification for this based on the data collected. It seems possible that in the materials with a low fibre content, a change in the property-weight loss dependence might be observed at weight losses corresponding to the oxidation of all the fibres.

An easy investigation could be conducted into additional material orientations. This would not require the production of any further model materials as the samples could be produced from the material which has already been made. Samples of STATT (staple thirty thirty), STAFF (staple forty five forty five) and STASS (staple sixty sixty) for example could easily be made and investigation into the strengths and effects of oxidation on these materials would indicate the true influence of fibre orientation. Similarly, tests on TAGM in orientations where the fibre direction was inclined at various angles to the long axis of the specimen would elucidate similar relationships in continuous fibre.

There are two areas in which finite element analysis would be beneficial. The first is in describing the stress state experienced by tenons subject to loading from torque in the swept area. Initially the modelling could assume a homogeneous material and later the model could be developed to include features of the commercial material such as the cloth laminates and the effect of service conditions such as thermal expansions. Understanding of the stress state in service is an essential part to the development of better disc design.

The second area is the four point bending test. In flatwise bending, finite element analysis which included the effect of point stresses under the loading rollers, might

help to clarify the reason for failure by delamination even at high span to depth ratios. It is suggested that delamination could occur as a result of stress fields associated with the loading rollers and hence delamination can initiate below the point at which the shear stress as a result of bending is high enough to induce failure. This may be the reason for failure by delamination at high span to depth ratios where it should not arise. Finite element models of the edgewise flexure test need to be created so that the stress state in the test can be understood. Of particular importance is the interaction between the layers in the material. Perhaps, when the test is understood in more depth, it will be adopted as the standard test method for carbon-carbon composites.

15. REFERENCES

[1] B. Harris, "*Engineering composite materials*", The Institute of Metals, (1986).

[2] B. McEnaney, in "*Carbon Materials for Advanced Technologies*", edited by T.D. Burchell, Elsevier, in press.

[3] I.A.S Edwards, in "*Introduction to Carbon Science*", edited by H. Marsh, Butterworths, (1989).

[4] R.E. Franklin, *Crystallite growth in graphitising and non-graphitising carbons, Proc. Roy. Soc.*, **A209**, p 196; cited by Edwards[3].

[5] J.D. Buckley, "*Carbon-carbon, An overview*", *Ceramic Bulletin*, **67**, 2, pp364-368, (1988).

[6] P.R. Becker, "*Leading-edge structural material system of the space shuttle*", *Ceramic Bulletin*, **60**, 11, pp1210-1214, (1981).

[7] G. Savage, "*Carbon-carbon composites*", Chapman and Hall, (1993).

[8] "*Advanced Materials Technologies Report 8, Carbon-Carbon Composites*", C.H. Kline & Co, (1987); cited by G. Savage[7].

[9] T.J. Hutton, "*The friction and wear of carbon-carbon composites for aircraft brakes*", PhD thesis, University of Bath, (1996).

[10] T.P. Newcomb and R.T. Spurr, "*Braking of road vehicles*", Chapman and Hall, (1967).

[11] T.P. Newcomb, "*Braking of road vehicles*", I Mech E Conference Publications, (1976).

[12] S. Awasthi and H.L. Wood, "*C/C composite materials for aircraft brakes*", *Advanced Ceramic Materials*, **3**, 5, (1988).

[13] B. Broquere, "*The SEPCARB carbon-carbon materials, friction materials*", *Proceedings of the 4th international conference and exhibition for high performance materials*", pp253-260, (1983).

[14] I.L. Stimpson and R. Fisher, "*Design and engineering of carbon brakes*", *Phil. Trans. R. Soc. Lond. A*, **294**, pp583-590, (1980).

[15] J.R. Barber, *Proc. R. Soc. Lond. A*, **312**, pp381, (1969); cited by Stimpson *et al*[14].

[16] F.R. Kennedy and F.F. Ling, *ASME, paper 73,* LUB 6, (1973); cited by Stimpson *et al*[14].

[17] J.W. Weaver, *"Advanced materials for aircraft brakes", Aero. J.,* **76,** pp695-698, (1972).

[18] T.L. Ho, M.B. Patterson and F.F. Ling, *"Effect of frictional heating on brake materials", Wear,* **30,** pp73-91, (1974).

[19] C.R. Thomas, in *"Essentials of carbon-carbon composites"*, edited by C.R. Thomas, The Royal Society of Chemistry, (1993).

[20] E. Fitzer, in *"Carbon fibres filaments and composites"*, edited by J.L. Figueiredo, C.A. Bernardo, R.T.K. Baker and K.J. Huttinger, Kluwer Academic, (1990); cited by Chung[22].

[21] J.V. Milanski and H. Katz (eds), *"Handbook of reinforcements for plastics",* Van Nostrand Reinhold, (1987); cited in Savage[7].

[22] D.D.L. Chung, *"Carbon fiber composites"*, Butterworth-Heinemann, (1994).

[23] J. Delmonte, *"Technology of carbon and graphite fibre composites",* Van Nostrand Reinhold, (1981); cited by Savage[7].

[24] G. Henrici-Olivé and S. Olivé, in *"Industrial developments (Advances in polymer science,* **51**), Springer-Verlag, (1983); cited by Savage[7].

[25] E. Fitzer and D.J. Muller, *Carbon,* **13,** p 163.

[26] M. Guigon, A. Overlin and G, Desarmot, *Fibre Sci. and Tech.*, **20**, 177, (1984); cited by Savage[7].

[27] A. Fordeaux, R. Perret and W. Ruland, *Proc. Int. Conf. on carbon fibres, their composites and applications,* Plastics and Polymer Conference Supplement no. 5, Plastics Inst. P57, (1971); Cited by Savage[7].

[28] E.J. Walker, in *"Essentials of carbon-carbon composites"*, edited by C.R. Thomas, The Royal Society of Chemistry, (1993).

[29] W.V. Kotlensky, *Chem. Phys. Carbon,* **9,** 173, (1973);cited by Savage[7].

[30] K.E. Spear, *Pure Appl. Chem.,* **54,** pp1297, (1982); cited by Savage[7].

[31] J. Hill, C.R. Thomas and E.J. Walker, *Ext. Abs. 11th Biennial Conf. On Carbon,* Am. Chem. Soc., p 278, (1973).

[32] P.J. Hacker, *Private communication,* (1998).

[33] S. Kimura, S. Kasuya and E. Yasuda, *Proc. Int. Symp. Of Factors in Dens. And Sintering of Ceramics,* Japan, p 229, (1978); cited by Savage[7].

[34] B. McEnaney and T. Mays, in *"Essentials of carbon-carbon composites"*, edited by C.R. Thomas, The Royal Society of Chemistry, (1993).

[35] W.V. Green, J. Weertman, and E.G. Zukas, *Mater. Sci. Eng.*, **6**, p 199, (1970); cited by McEnaney and Mays[34].

[36] E. Fitzer and B. Terwiesch, *Carbon*, **10**, p 383, (1972); cited by McEnaney and Mays[34].

[37] C.R. Thomas and E.J. Walker, in *"Proceedings of the 1st International Conference on Materials in Aerospace"*, Royal Aeronautical Society, London, p 138, (1986); cited by McEnaney and Mays[34].

[38] M.S. Dresselhaus, G. Dresselhaus, K. Suigihara, I.L. Spain, and H.A. Goldberg, *"Graphite Fibres and Filaments"*, Springer Verlag, (1988).

[39] *Carbon Fibre Reinforced Carbon*, Schunk promotional brochure.

[40] H. Marsh and K. Kuo, in *"Introduction to Carbon Science"*, edited by H. Marsh, Butterworths, (1989).

[41] P.L. Walker Jr., F. Rusinko Jr. and L.G. Austin, *Advan. Catalysis,* **11**, p133, (1959); cited by Marsh and Kuo[40].

[42] J.L. Figueiredo and J.A. Moulijn in, *"Carbon and Coal Gasification"*, Martinus Nijhoff, (1986).

[43] B.P. Jalan and Y.K. Rao, *Carbon,* **16**, pp 175-184, (1978).

[44] C. Kröger, *Z. Angew. Chem.*, **52**, p 129, (1939); cited by Jalan and Rao[43].

[45] P.L. Walker Jr., M. Shelef and R.A. Anderson, *Chemistry and Physics of Carbon*, **4**, p 128, (1968).

[46] D.W McKee, *Chemistry and Physics of Carbon,* **16**, pp 1-118, (1981).

[47] J.A. Arthur, *Trans. Faraday Soc.,* **47**, p 164, (1951); cited by Hayhurst and Parmar[48].

[48] A.N. Hayhurst and M.S. Parmar, *Chemical Engineering Science,* **53**, 3, pp 427-438, (1998).

[49] J.F. Grifiths and J.A. Barnard, *"Flame and Combustion"*, Blackie, (1995); cited by Hayhurst and Parmar[48].

[50] P.L. Walker Jr., J.F. Rakszawski and G.R. Imperial, *J. Phys. Chem.*, **63**, p 140, (1959); cited by McKee[46].

[51] H. Harker, *Proceedings of the Fourth Conference on Carbon,* Pergamon, (1960); cited by Jalan and Rao[43].

[52] W.J. Stephen, *"The Inhibition by Carbon Monoxide of the Reaction Between Graphite and Carbon Dioxide at High Pressures"*, PhD Thesis, University of Bath, UK, (1984).

[53] D.W. McKee, *Carbon*, **25**, 4, pp 551-557, (1987).

[54] S. Goto, K.H. Han and G.R. St. Pierrre, *Trans. I.S.I.J.*, **26**, pp 597-603, (1986).

[55] O.P. Bahl, T.L. Dhami and L.M. Manocha, *Proc. 19th Biennial Conf. on Carbon*, pp 310-311, (1989).

[56] J. Lahaye, F. Louys and P. Ehrburger, *Carbon*, **28**, 1, pp 137-141, (1989).

[57] B. Dacic and S. Marinkovic, *Carbon,* **25**, 3, pp 409-415, (1987).

[58] P. Ehrburger, J. Lahaye and C. Bourgeois, *Carbon*, **19**, pp 7-10, (1981).

[59] J. Rodríguez-Mirasol, P.A. Thrower and L.A. Radovic, *Carbon*, **33**, 4, pp 545-554, (1995).

[60] J.E. Brocklehurst, *Chemistry and Physics of Carbon*, **13**, Marcel Dekker, (1977).

[61] I.M. Pickup, *The Influence of Thermal Corrosion on the Mechanical Properties of Nuclear Graphites*, PhD Thesis, University of Bath, UK, (1984).

[62] J.L. Wood, R.C. Bradt and P.L. Walker, *Carbon*, **18**, p 179, (1980).

[63] I.M. Pickup, B McEnaney and R.G. Cooke, *Carbon*, **24**, p 535, (1986).

[64] P. Crocker, *Structural Effects of Oxidation of Carbon-Carbon Composites*, PhD Thesis, University of Bath, UK, (1991).

[65] J.X. Zhao, R.C. Bradt and P.L. Walker, *Carbon*, **23**, 1, pp 9-13, (1985).

[66] P. Crocker and B. McEnaney, *Carbon*, **29**, 7, pp 881-885, (1991).

[67] N. Hawkins, *Proc. 2nd Conf. on Ind. Carbon and Graphite*, Society of Chemical Industry, p 355, (1966); cited by Brocklehurst[60].

[68] J.E. Brocklehurst, R.G. Brown, K.E. Gilchrist and V.Y. Labaton, *J. Nucl. Mater.*, **35**, p183, (1970); cited by Brocklehurst[60].

[69] J.A. Board and R.L. Squires, *Proc. 2nd Conf. on Ind. Carbon and Graphite*, Society of Chemical Industry, p 289, (1966); cited by Brocklehurst[60].

[70] C. Rounthwaite, G.A. Lyons and R.A. Snowdon, *Proc. 2nd Conf. on Ind. Carbon and Graphite*, Society of Chemical Industry, p 299, (1966); cited by Brocklehurst[60].

[71] R.H. Knibbs and J.B. Morris, *Proc. 3rd Conf. on Ind. Carbon and Graphite*, Society of Chemical Industry, p 297, (1971); cited by Brocklehurst[60].

[72] C. Ahearn and B. Rand, *Carbon*, **34**, 2, pp 239-249, (1996).

[73] H. Amariglio and X. Duval, *Carbon*, **4**, p 323, (1966).

[74] R.J. Donaldson, P.J. Whelan and T.B. Walker, *Proc. European Carbon Conference "Carbon '96"*, pp 545-546, (1996).

[75] D.W. McKee, C.L. Spiro, P.G. Kosky and E.J. Lamby, *Proc. 16th Biennial Conf. and Carbon*, pp 156-157, (1983).

[76] D.W. McKee, *Carbon*, **8**, pp 623-635, (1970).

[77] K.L. Luthra, *Carbon*, **26**, 2, pp 217-224, (1988).

[78] E.B. Bines, in *Essentials of Carbon-Carbon Composites*, edited by C.R. Thomas, The Royal Society of Chemistry, (1993).

[79] *Engineering Properties of Selected Ceramic Materials*, edited by J.F. Lynch *et al.*, The American Ceramic Society, (1966).

[80] M.H. Battey, *Mineralogy for Students 2nd Edition*, Longman, (1981); cited by Neighbour[81].

[81] G.B. Neighbour, *Microstructural Processes Leading to Fracture in Nuclear Graphites*, PhD Thesis, University of Bath, UK, (1993).

[82] P.J. Goodhew and F.J. Humphreys, *Electron Microscopy and Analysis*, Taylor and Francis, (1988).

[83] P. Grivet, *Electron Optics*, Pergamon, (1965).

[84] J.W.S. Hearle, J.T. Sparrow and P.M. Cross, *The Use of the Scanning Electron Microscope*, Pergamon, (1972).

[85] M.H. Loretto, *Electron Beam Analysis of Materials*, Chapman and Hall, (1994).

[86] S. Wischnitzer, *Introduction to Electron Microscopy*, Pergamon, (1981).

[87] B.D. Cullity, *X-ray Diffraction*, Addison-Wesley, (1959).

[88] P.E.J. Flewitt and R.K. Wild, *Physical Methods for Materials Characterisation*, Institute of Physics, (1994).

[89] H.P. Klugg and L.E. Alexander, *X-ray Diffraction Procedures for Polycrystalline and Amorphous Materials*, Wiley, (1973).

[90] DD ENV 658-2 (1993), *Advanced Technical Ceramics - Mechanical Properties of Ceramic Matrix Composites at Room Temperature, Part 2 - Determination of Compressive Strength.*

[91] M. Hartley and B. McEnaney, *Ext. Abs. European Carbon Conference*, p 210, (1996).

[92] M. Hartley and B. McEnaney, *Abs. An Open Discussion on Current Issues in Nuclear Graphite and Carbon Topics*, Meeting of the British Carbon Group, (1996).

[93] N. Murdie and M. Wood, *Ext. Abs. European Carbon Conference*, p 415, (1996).

[94] B.D. Leigh and B. McEnaney, *Extended Abstracts of Carbon '97*, pp 538-539, (1997).

[95] T. Fend and J. Goring, *Ceram. Trans.*, **46**, pp 165-176.

[96] H. Mahfuz, P.S. Das and S. Jeelani, *Ceram. Eng. Sci. Proc.*, **13**, pp 449-468.

[97] *Carbon fibre reinforced carbon*, Schunk promotional brochure.

[98] R. Morrell, *British Ceramic Transactions*, **94**, 1, pp 1-9, (1995).

[99] A.E.J. Forno, W.P. Byrne, R.K. Varma and R. Morrell, *Compressive testing of continuous fibre reinforced ceramic matrix composite materials*, Report DMM (C) 61, National Physical Laboratory, (1993); cited by Morrel[98].

[100] ASTM 3410-87, *Test method for compressive properties of unidirectional crossply fibre-resin composites.*

[101] G.A Schoeppner and R.L. Sierakowski, *J. Compos. Technol. Res.*, **12**, 1, pp 3-12, (1993); cited by Morrell[98].

[102] S. Mall, R.P. Vozzola and L.P. Zawada, *J. Am. Ceram. Soc.*, **72**, 7, pp 1175-1178, (1989).

[103] *The Essentials of Strength of Materials and Mechanics of Solids I*, Research and Education Association, (1989).

[104] J.M. Gere and S.P. Timoshenko, *Mechanics of Materials*, PWS Publishing Company, (1997).

[105] A.C. Ugural and S.K. Fenster, *Advanced Strength and Applied Elasticity*, Prentice-Hall International, (1995).

[106] J. Case, Lord Chilver and C.T.F. Ross, *Strength of Materials and Structures*, Edward Arnold, (1983).

[107] G.D. Quinn and R. Morrell, *J. Am. Ceram. Soc.*, **74**, 9, pp 2037-2066, (1991).

[108] B. McEnaney, *Private communication*, (1998).

[109] P.D. Copp, J.C. Dendis and S. Mall, *Journal of Composite Materials*, **25**, pp 593-608, (1991).

[110] J.P. Den Hartog, *Strength of Materials*, Constable and Company, (1949).

[111] F.I. Baratta, in *Methods for Assessing the Structural Reliability of Brittle Materials, ASTM STP 844*, edited by S.W. Freiman and C.M. Hudson, American Society for Testing and Materials, pp 194-222, (1984).

[112] S. Timoshenko and J.N. Goodier, *Theory of Elasticity*, McGraw-Hill, (1951).

[113] C.C. Chamlis, *Analysis of the Three Point Ben Test for Materials with Unequal Tension and Compression Properties, NASA TN D7572*, National Aeronautical and Space Administration, (1974); cited by Baratta[111].

[114] D.G. Ashwell, *Journal of the Royal Aeronautical Society*, **54**, pp 708-715, (1950); cited by Baratta[111].

[115] R.C. Newnham, *Proceedings of the British Ceramic Society*, **25**, pp 281-293, (1975); cited by Baratta[111].

[116] N.A. Weil, *Studies of Brittle Behaviour of Ceramic Materials,* TR 61-628, Part II, U.S. Air Force, Applied Sciences Division, Wright-Patterson Air Base, Ohio, April 1962, pp 38-42; cited by Baratta[111].

[117] B. Hammant, *Composites*, pp 246-249, (December 1971).

[118] *Strain Gage Applications on Composites*, Applications Note, Measurements Group Inc. (1988).

[119] *Strain Gage Measurements on Plastics and Composites*, Report, Measurements Group Inc.

[120] B.D. Leigh and B. McEnaney, *Extended Abstracts of Carbon '98*, pp 605-606, (1998).

[121] A. Steffen, C.-J. Johansson and E.-W. Wormuth, *Holz als Roh- und Werkstoff*, **55**, pp 245-253, (1997).

[122] N, Baldassino, M. Ballerini, A. Ceccotti and R. Zanuttini, *Proceedings of International COST 508 Wood Mechanics Conference*, pp 366-379, (1996).

[123] T.F. Shupe, C.Y. Hse, L.H. Groom and E.T. Choong, *Forest Products Journal*, **47**, 9, pp 63-69, (1997).

[124] E.J. Biblis, *Ann. Sci. For.*, **53**, pp 1167-1175, (1996).

[125] American Society for Testing and Materials, *Standard method of static tests of timbers in standard sizes*, D 198-84, (1991).

[126] American Society for Testing and Materials, *Standard Test Method for Moduli of Elasticity And Fundamental Frequencies of Carbon and Graphite Materials by Sonic Resonance*, C 747-93, (1988).

[127] H.W. Chang and S.K. Rhee, *Carbon*, **16**, 14, (1978).

[128] A.G. Evans, F.W. Zok and J. Davis, *Comp. Sci. Technol.*, **42**, pp 3-24, (1991).